

Characterising blast loading from non-spherical charges in the near-field

Christian A. Langran-Wheeler

A thesis submitted in partial fulfilment of the requirements for the degree of Doctor of Philosophy

The University of Sheffield

Faculty of Engineering

School of Mechanical, Aerospace and Civil Engineering

12th April, 2026

Abstract

Near-field blast loading from non-spherical explosive charges differs markedly from that of equivalent spherical charges, yet the extent and spatial character of these differences remain poorly quantified. This has significant implications for blast-resistant design and threat characterisation, where spherical equivalence is commonly assumed but may be inadequate for elongated charges at close range. Whilst far-field blast waves from all charge geometries converge towards a spherical form, early-time near-field loading is highly dependent on charge geometry and orientation. This work provides, for the first time, a detailed spatial and temporal dataset against which theoretical and computational predictions can be assessed.

Experiments were conducted at the Characterisation of Blast Loading (CoBL) facility, University of Sheffield, measuring reflected pressure–time histories from 200 g C4 cylindrical charges (7:1 length-to-diameter ratio) at a cleared standoff of 250 mm. Orientations spanned radial to axial, including intermediate inclinations of 22.5°, 45° and 67.5° and end-detonated variants of the radial and axial configurations. An array of up to seventeen Hopkinson pressure bars enabled simultaneous measurement of localised loading at discrete positions, capturing its spatial variability and temporal development across the target face. Results were compared with equivalent spherical charges to quantify the influence of geometry and orientation on reflected pressure and specific impulse.

Charge orientation profoundly influences near-field loading. Radially oriented cylinders impart approximately twice the total impulse of an equivalent sphere to the measurement area, whilst axially oriented charges impart approximately half, a four-fold difference between the cylindrical extremes. The transition is non-monotonic: 45° and 67.5° orien-

tations produce lower total impulse than even the axial case, attributed to measurement positions lying within a bridging wave zone between the primary radial and end wave regions. Repeatability is high for total impulse, though considerable localised variability occurs at individual positions, consistent with chaotic near-field processes.

Acknowledgements

Many people have generously given me huge amounts of support in getting to the submission of this thesis. This is a short message to identify them but fullness of my heartfelt thanks I owe to them and others I am not able to convey in writing.

Firstly, Professor Andy Tyas and Professor Sam Rigby, their support and belief in me was crucial to the completion of this work. Their knowledge, insight and passion for the subject is inspirational and my greatest work came through conversations with them.

Professor Sam Clarke for getting me started, the opportunities he gave me and doors he opened are undoubtedly the reason I ended up here. You've been a great mentor and friend and I blame you for all the hard work that came from it; no regrets.
Doctors Andrew Barr and Ben Fuller for their help and technical support from the start. They made the office fun and taught me so much along the way. The technical staff at Buxton for their help running the experimental tests, especially Roy Mellor.

Dr Catie Stephens for funding the project and her friendly hospitality during my stay in Mississippi. Robert Walker for the wonderful conversations, his enthusiasm and experience is unparalleled and it has been an honour to work with him. Doctors Green and Vanhinsbergh for support outside of the academic.

Finally, my family for their patience and support, I love you all.

Kit Wheeler,

Friday 9th October, 2026.

Contents

Abstract 1
Acknowledgements 3
Contents 4
List of Figures 6
List of Tables 10

1 Introduction 13
1.1 Background and motivation . . . 13
1.2 Scope of the thesis . . . 15
1.3 Thesis Outline . . . 15
1.4 Published Work . . . 16

2 Literature Review 18
2.1 Introduction . . . 18
2.2 Explosive loading . . . 18
2.2.1 Defining explosions . . . 18
2.2.2 Shock wave formation . . . 19
2.2.3 Blast wave parameters . . . 19
2.2.4 Reflected pressures . . . 20
2.2.5 TNT equivalence . . . 20
2.2.6 Scaling laws . . . 21
2.2.7 Semi-empirical blast prediction . . . 22
2.2.8 ConWep . . . 22
2.2.9 Blast pressure measurement methods . . . 23

2.3 Explosive consistency and variability . . . 32
2.3.1 Variability in explosives . . . 32
2.3.2 Consistency and predictability of explosives . . . 33
2.4 Non-spherical charges . . . 35
2.4.1 Overview . . . 35
2.4.2 Shock wave structure . . . 36
2.4.3 Cylindrical testing . . . 36
2.4.4 Initiation location . . . 39
2.4.5 Charge shape persistence . . . 39
2.5 Numerical modelling . . . 39
2.5.1 LS-DYNA . . . 39
2.5.2 EOS . . . 40
2.5.3 Numerical domains . . . 42
2.6 Summary . . . 43

3 Experimental Methodology 44
3.1 Far-field testing . . . 44
3.1.1 Testing instrumentation . . . 45
3.1.2 Shot plan . . . 45
3.2 Near-field apparatus and data acquisition . . . 46
3.3 Near-field test arrangement . . . 50

4 Experimental Results 57
4.1 Spherical tests . . . 57
4.2 Cylindrical tests – Radial (0°, 0°) . . . 59
4.2.1 Test results . . . 60
4.2.2 Compiled results . . . 71
4.3 Cylindrical tests – Radial (0°, 0°) – End detonated . . . 79
4.3.1 Test Results . . . 79
4.3.2 Compiled results . . . 85
4.4 Cylindrical tests – Radial 45° (45°, 0°) . . . 90
4.4.1 Test Results . . . 90
4.4.2 Compiled results . . . 96
4.5 Cylindrical tests – Inclined (0°, 22.5°) . . . 101
4.5.1 Test Results . . . 101
4.5.2 Compiled results . . . 110
4.6 Cylindrical tests – Inclined (0°, 45°) . . . 115
4.6.1 Test Results . . . 115
4.6.2 Compiled results . . . 125
4.7 Cylindrical tests – Inclined (0°, 67.5°) . . . 130
4.7.1 Test Results . . . 130
4.7.2 Compiled results . . . 140

4.8 Cylindrical tests – Axial (0°, 90°) . . . 145
4.8.1 Test Results . . . 145
4.8.2 Compiled results . . . 154
4.9 Cylindrical tests – Axial (0°, 90°) – End detonated . . . 161
4.9.1 Test Results . . . 161
4.9.2 Compiled results . . . 167
4.10 Summary . . . 168

5 Numerical modelling **173**
5.1 2D Numerical model setup – Spherical . . . 173
5.1.1 Spherical results . . . 174
5.2 2D Numerical model setup – Radial . . . 176
5.2.1 Radial results . . . 176
5.3 2D Numerical modelling – Axial . . . 178
5.3.1 Axial results . . . 179
5.4 3D Numerical Modelling . . . 180

6 Discussion **183**
6.1 Validity of experimental results . . . 183
6.2 Variability of localised loading . . . 184
6.3 Consistency of experimental data . . . 190
6.3.1 Total impulse . . . 191
6.3.2 Experimental spatial variation of loading . . . 203
6.3.3 Impulse distributions . . . 206
6.4 Numerical modelling . . . 207
6.4.1 Axial . . . 207
6.4.2 Radial . . . 211

7 Conclusions **216**

8 Recommendations for future work **220**

9 Appendix **232**

List of Figures

2.1 Compiled blast parameters from TNT explosive trials. 23
2.2 Measured and predicted wave forms from (Rickman & Murrell 2006). 33
2.3 Reflected pressure time signals at varying stand-offs. 34
2.4 Total impulse over a 100 mm radius recording area. 35
2.5 Primary and secondary shock waves emanating from a cylindrical explosive. 36

3.1 Arena test setup of hemispherical charges against the continuous blockwork wall, (Rigby et al. 2015b) 45
3.2 Compiled far-field pressure and impulse histories and semi-empirical predictions. 47
3.3 Schematic of the *Characterisation of Blast Loading* apparatus. 48
3.4 Plan view of CoBL's instrumented area. 49
3.5 Schematic of the charge orientations. 51
3.6 Illustration of the instrumented array relative to the cylindrical charges. . . 54
3.7 Instrumented array orientations overlaid with expected blast wave geometry. 55
3.8 Photographs of experimental setup. 56

4.1 Test-averaged reflected pressure and specific impulse histories. 58
4.2 Compiled peak reflected pressure and peak specific impulse versus radial ordinate. 60
4.3 Reflected pressure time histories for test T006. 62
4.4 Specific impulse time histories for test T006. 63
4.5 Reflected pressure time histories for test T007. 65
4.6 Specific impulse time histories for test T007. 66

4.7 Reflected pressure time histories for test T019. 68
4.8 Specific impulse time histories for test T019. 69
4.9 Series-averaged reflected pressure and specific impulse histories. 70
4.10 Reflected pressure time histories for radial cylindrical charges. 72
4.11 Specific impulse time histories for radial cylindrical charges. 74
4.12 Peak reflected pressures for radial cylindrical charges. 76
4.13 Peak specific impulses for radial cylindrical charges. 77
4.14 Reflected pressure time histories for test T010. 80
4.15 Specific impulse time histories for test T010. 81
4.16 Reflected pressure time histories for test T012. 83
4.17 Specific impulse time histories for test T012. 84
4.18 Reflected pressure time histories for end-detonated radial cylindrical charges. 86
4.19 Specific impulse time histories for end-detonated radial cylindrical charges. 87
4.20 Peak reflected pressures for end-detonated radial cylindrical charges. 88
4.21 Peak specific impulses for end-detonated radial cylindrical charges. 89
4.22 Reflected pressure time histories for test T008. 91
4.23 Specific impulse time histories for test T008. 92
4.24 Reflected pressure time histories for test T009. 94
4.25 Specific impulse time histories for test T009. 95
4.26 Reflected pressure time histories for 45° radial cylindrical charges. 97
4.27 Specific impulse time histories for 45° radial cylindrical charges. 98
4.28 Peak reflected pressures for 45° radial cylindrical charges. 99
4.29 Peak specific impulses for 45° radial cylindrical charges. 100
4.30 Reflected pressure time histories for test T020. 102
4.31 Specific impulse time histories for test T020. 103
4.32 Reflected pressure time histories for test T021. 105
4.33 Specific impulse time histories for test T021. 106
4.34 Reflected pressure time histories for test T023. 108
4.35 Specific impulse time histories for test T023. 109
4.36 Reflected pressure time histories for 22.5° inclined cylindrical charges. . . . 111
4.37 Specific impulse time histories for 22.5° inclined cylindrical charges. 112
4.38 Peak reflected pressures for 22.5° inclined cylindrical charges. 113
4.39 Peak specific impulses for 22.5° inclined cylindrical charges. 114
4.40 Reflected pressure time histories for test T024. 116
4.41 Specific impulse time histories for test T024. 118
4.42 Reflected pressure time histories for test T026. 120
4.43 Specific impulse time histories for test T026. 121
4.44 Reflected pressure time histories for test T027. 123
4.45 Specific impulse time histories for test T027. 124
4.46 Reflected pressure time histories for 45° inclined cylindrical charges. 126
4.47 Specific impulse time histories for 45° inclined cylindrical charges. 127
4.48 Peak reflected pressures for 45° inclined cylindrical charges. 128

4.49 Peak specific impulses for 45° inclined cylindrical charges. 129
4.50 Reflected pressure time histories for test T028. 131
4.51 Specific impulse time histories for test T028. 133
4.52 Reflected pressure time histories for test T030. 135
4.53 Specific impulse time histories for test T030. 136
4.54 Reflected pressure time histories for test T031. 138
4.55 Specific impulse time histories for test T031. 139
4.56 Reflected pressure time histories for 67.5° inclined cylindrical charges. . . . 141
4.57 Specific impulse time histories for 67.5° inclined cylindrical charges. 142
4.58 Peak reflected pressures for 67.5° inclined cylindrical charges. 143
4.59 Peak specific impulses for 67.5° inclined cylindrical charges. 144
4.60 Reflected pressure time histories for test T016. 146
4.61 Specific impulse time histories for test T016. 147
4.62 Reflected pressure time histories for test T017. 149
4.63 Specific impulse time histories for test T017. 150
4.64 Reflected pressure time histories for test T032. 152
4.65 Specific impulse time histories for test T032. 153
4.66 Reflected pressure time histories for axial cylindrical charges. 155
4.67 Specific impulse time histories for axial cylindrical charges. 156
4.68 Peak reflected pressures for axial cylindrical charges. 157
4.69 Peak specific impulses for axial cylindrical charges. 158
4.70 Reflected pressure and specific impulse traces averaged at the four symmetrical, non-central radial ordinate of axial cylindrical tests and an average. . 160
4.71 Reflected pressure time histories for test T014. 162
4.72 Specific impulse time histories for test T014. 163
4.73 Reflected pressure time histories for test T015. 165
4.74 Specific impulse time histories for test T015. 166
4.75 Reflected pressure time histories for end-detonated axial cylindrical charges. 168
4.76 Specific impulse time histories for end-detonated axial cylindrical charges. . 169
4.77 Peak reflected pressures for end-detonated axial cylindrical charges. 170
4.78 Peak specific impulses for end-detonated axial cylindrical charges. 171

5.1 Spatial pressure plots from 2D numerical model of sphere. 174
5.2 Reflected pressure and specific impulse of 2D axi-symmetric numerical model of spherical charge. 175
5.3 Reflected pressure and specific impulse of experimental tests and 2D axi-symmetric numerical model. 175
5.4 Fringe plots. 177
5.5 Relative time of arrival. 178
5.6 Reflected pressure and specific impulse of numerical model and experimental axial cylinder tests. 179
5.7 Pressure distribution plots from 2D numerical model of axial cylinder charge. 180

5.8 Pressure distribution plots from 3D numerical model of axial cylinder charge. 182

6.1 Frequency analysis of the central bar pressure trace from Test T004. 185
6.2 Compiled peak reflected pressure and peak specific impulse versus radial ordinate. 186
6.3 Total impulse development of spherical blast tests. 192
6.4 Total impulse development of radial cylindrical blast tests. 193
6.5 Total impulse development of radial cylindrical blast tests, end detonated. . 194
6.6 Total impulse development of radial cylindrical blast tests. 195
6.7 Total impulse development of 22.5° inclined cylindrical blast tests. 196
6.8 Total impulse development of 45° inclined cylindrical blast tests. 197
6.9 Total impulse development of 67.5° inclined cylindrical blast tests. 198
6.10 Total impulse development of axial cylindrical blast tests. 199
6.11 Total impulse development of axial cylindrical blast tests, end detonated. . 200
6.12 Total impulse development of all blast tests. 201
6.13 Peak reflected pressure and peak specific impulse from spherical blast tests and average profile. 204
6.14 Peak reflected pressure and peak specific impulse of radial cylinder and axial cylinder blast tests with spherical comparison. 205
6.15 Interpolated peak specific impulse surface plots for spherical and radial cylindrical charges. 206
6.16 Interpolated peak specific impulse surface plots for spherical, radial cylindrical and axial cylindrical charges. 208
6.17 Temporal development of total impulse. 209
6.18 Peak specific impulse of axial cylindrical blast tests, average and numerical modelling 210
6.19 Peak reflected pressure of axial cylindrical blast tests, average and numerical modelling 211
6.20 Temporal development of total impulse for experimental and numerical modelling of radial cylinders. 212
6.21 Peak reflected pressure and peak specific impulse of aligned radial cylindrical blast tests and numerical modelling. 214
6.22 Peak reflected pressure and Peak specific impulse of perpendicular radial cylindrical blast tests and numerical modelling. 215

List of Tables

2.1 Comparison of techniques for measuring reflected blast loading. 31
2.2 JWL equation of state parameters for C4, taken from Dobratz & Crawford (1985). 41

3.1 Summary of far-field tests for 312.5 g hemispheres of C4. 46
3.2 Summary of far-field test results and semi-empirical predictions for 312.5 g hemispheres of C4. 48
3.3 Summary of experimental tests conducted 53
3.4 Summary of near-field test arrangements used in this study. 54

6.1 Relative standard deviation of peak reflected pressure and peak specific impulse for all charge orientations. 187

9.1 Summary of peak reflected pressure, peak specific impulse and time to peak pressure for all experimental tests. 233
9.2 Summary of peak total impulse for all experimental tests. 242

Glossary of Abbreviations

- **ALE** – Arbitrary Lagrangian-Eulerian
- **BOS** – Background Oriented Schlieren
- **C4** – Composition 4
- **CoBL** – Characterisation of Blast Loading
- **DIC** – Digital Image Correlation
- **DoD** – Department of Defense
- **EOS** – Equation of State
- **FEM** – Finite Element Modeling
- **HE** – High Explosive
- **HFPBNM** – High Fidelity Physics-Based Numerical Modelling
- **HPB** – Hopkinson Pressure Bar
- **HSV** – High-Speed Video
- **JWL** – Jones-Wilkins-Lee
- **MaCE** – Mechanisms and Characterisation of Explosions
- **PDV** – Photonic Doppler Velocimetry
- **PE4** – Plastic Explosive 4
- **RSD** – Relative Standard Deviation
- **TNT** – Trinitrotoluene
- **UFC** – Unified Facilities Criteria
- **VFM** – Virtual Fields Method

Chapter 1

Introduction

1.1 Background and motivation

Designing structures to withstand extreme loads from high explosive (HE) blast is a challenge to security engineers. As with any structural design, a key input is the mechanical load which the structure must resist. Thus, accurate quantification of the loading generated when the blast wave from a high explosive detonation impinges on a structure has been a topic of interest for the blast research community for decades.

Currently, there are three broad means by which these loads may be predicted:

1. Empirical findings from experimental work
2. Simplified physically-based predictive relations, possibly calibrated against empirical data
3. High Fidelity, Physically Based Numerical Modelling (HFPBNM)

Each of these approaches has advantages and disadvantages. Experimental work, if accurately conducted, is the gold standard, being what happens in the 'real' world. However, direct experimental measurements of blast loading are often difficult to make accurately, and the tests are expensive to conduct. Simplified models (sometimes called 'Fast Running Engineering Models', or FREMs) are quick and cheap to run, but are generally limited in

the range of input variables which they can deal with. Numerical modelling is highly flexible on the input variables they can accommodate (charge size, position, shape, chemistry and geometry of the space/obstacles around it) and, assuming computational power is available, relatively inexpensive to run. But ideally, some degree of experimental validation of the outputs is required.

Advances have been made across all these approaches in recent years. In particular, the rapid increase in computational power and affordability has resulted in HFPBNM of HE blast becoming a standard capability in any blast security engineering process. However, the availability of high quality, reliable experimental data for validation of the outputs has not always kept pace.

Many analyses are based on relatively simple input assumptions, often based on the idea that the explosive charge is spherically shaped and detonated in a free air environment, or hemi-spherically shaped and set on a rigid floor, such that the resulting effects extend only into a half-space. Also, the assumption is often made that the measurements of the resulting blast pressure are taken sufficiently far from the detonation point such that a well-characterised air shock wave is the transmission mechanism, and complications associated with the initial expansion of the detonation products are essentially irrelevant (this region, where the shock wave has fully detached from outer surface of the detonation product cloud, is often termed "far-field" blast). These assumptions simplify the modelling process, and semi-empirically based FREMs exist which have been shown to give excellent predictions of the key blast wave parameters, when compared to a large body of experimental tests. e.g. (Rigby et al. 2014, Farrimond et al. 2022).

The situation is less clear when considering non-spherical geometries of charges. Physically-based FREMs do not exist, because the asymmetry of the arrangement makes it too difficult to define the properties of the blast waves from a closed-form shock analysis. HFPBNM approaches can deal with these situations, but there is a very limited amount of high quality experimental data to validate the models' predictions.

These drawbacks are further amplified if we wish to investigate blast loading very close to a detonation, where the violent expansion of the detonation products may be a direct vector of the energy transferred to a target. This is an extremely challenging environment both for modelling and for experimental work. The resulting pressures are measured in the 10s–100s MPa, sometimes more. Pressure transients will vary greatly over durations of a few microseconds. Additionally the physics of the problem are complex, with high power chemical reactions needing to be modelled, along with the resulting interaction between the high energy detonation products, the surrounding air, and, eventually, the target structure. As a result, whilst HFPBNM has been used extensively for predicting loading in these scenarios, this has been done with little experimental work to interrogate the efficacy of the modelling approaches.

1.2 Scope of the thesis

In order to address this lack of experimental data, an experimental facility was developed at the University of Sheffield Blast and Impact Laboratory, Buxton, Derbyshire, UK. This facility, described in detail in Chapter 3, enables the measurement of spatial and temporal variations in the loading experienced by an effectively rigid target, when exposed to the blast load from a very near-field detonation. This Characterisation of Blast Loading (CoBL) facility has been used by University of Sheffield researchers to obtain results from detonations of spherical charges of 50-250g mass at distances of 70-400 mm from the recording surface (Rigby et al. 2015a, Tyas et al. 2016). The results have been compared against FREM and HFPBNM predictions, which have been shown to be reasonably accurate, considering the caveats noted above.

What has been lacking up until now has been an experimental study of the effect of using non-spherical explosive charge shapes, and the ability of HFPBNM to accurately predict the resulting loads. This thesis presents an attempt to fill this gap, based on work conducted by the candidate and funded by the US Army Engineer Research and Development Center (ERDC), Waterways Research Station, Vicksburg, Mississippi, USA. The study comprised CoBL experimental tests which embraced both highly non-spherical charge shapes and near-field conditions alongside HFPBNM of the same events, using the well-established LS-DYNA code. Comparisons of the experimental and numerical findings are made, with the conclusion being that the numerical models capture some, but not all of the key features of the experimental data.

To summarise therefore, the objectives of this study are:

1. To investigate mechanisms of blast loading from detonations of highly non-spherical HE charges in the near-field, through the collection of reflected pressure time histories.

2. To assess, within the limits of available computational resources, the capability of industry-standard hydrocode finite element modelling to reproduce the experimentally observed near-field blast load parameters from non-spherical charges, and to identify the deficiencies and limitations of current numerical approaches for these complex loading scenarios.

1.3 Thesis Outline

The structure of the thesis is as follows:

Chapter 1 Introduction

This chapter briefly sets out the context of this study and the structure of the thesis.

Chapter 2 Literature Review

This chapter sets out the basic principles of blast load mechanics, scaling, predictive methods, experimental measurement techniques, consistency, and differences between

spherical and non-spherical blast wave formation. The chapter concludes that there is a lack of detailed high quality experimental data on non-spherical, near field blast loading, and hence, currently an inability to interrogate the efficacy of numerical modelling.

Chapter 3 Experimental Methodology

This chapter introduces the characterisation of far-field blast loading using standard arena tests, and near-field blast loading using the aforementioned CoBL apparatus. This chapter also details adaptations to the CoBL testing methodology to facilitate testing with long, cylindrical explosive charges supported close to the reflecting surface.

Chapter 4 Experimental Results

This chapter details results from spherical and cylindrical near-field blast testing. Results are presented in individual pressure-vs-time and impulse-vs-time history form, as well as being compiled and plotted as a function of distance along the reflecting surface to facilitate comparison between spheres and cylinders in different orientations to the target. This chapter completes **Objective 1**.

Chapter 5 Numerical Modelling

This chapter details the setup of the hydrocode finite element models in both two and three dimensions, describing the methods and parameters used.

Chapter 6 Discussion

In this chapter, compiled results from the experimental and numerical studies are compared. This chapter completes **Objective 2**.

Chapter 7 Conclusions

In this chapter, the main findings of the thesis are summarised.

Chapter 8 Recommendations for Future Work

This chapter explores the wider context of the research and sets out future research in light of the main findings of this thesis.

1.4 Published Work

Some of the work set out in this thesis has been summarised in the following international journal paper, and two leading international conference papers, written in collaboration with colleagues at University of Sheffield and senior engineers at ERDC, facilitated by a month-long technical visit to ERDC in 2018:

Langran-Wheeler C, Rigby, Clarke SD, SE, Tyas A, Stephens, CS, and Walker RE. Near-field spatial and temporal blast pressure distributions from non-spherical charges: Horizontally-aligned cylinders. *International Journal of Protective Structures* **12**(4) 492–516, 2021

Langran-Wheeler C, Tyas A, Rigby, SE, Stephens, CS, Clarke SD and Warren JA. Charac-

terisation of reflected blast loads in the very near-field from non-spherical explosive charges. In *Proceedings of the 17th International Symposium on the Interaction of the Effects of Munitions on Structures*, Bad Neuenahr, Germany, October 2017.

Langran-Wheeler C, Tyas A, Rigby, SE, Stephens, CS, Clarke SD and Walker RE. Reflected blast loads from long cylinders in the near-field. In *Proceedings of the 18th International Symposium on the Interaction of the Effects of Munitions on Structures*, Panama City Beach, FL, USA, October 2019.

Chapter 2

Literature Review

2.1 Introduction

2.2 Explosive loading

2.2.1 Defining explosions

An explosion is a sudden and violent release of energy, resulting from various physical or chemical processes. They are characterised by the formation of a blast wave as the intense energy interacts with the surrounding medium.

Explosions can be caused in many different ways but generally fall into three categories;

1. Chemical Explosions

   Chemical explosions involve a rapid chemical reaction in a detonation or deflagration style as a pressure or flame front moves through the explosive material. The detonation can be initiated in one of five ways; shock, impact, thermal, friction or static electrical discharge. The exothermic reaction converts the explosive into a gas that, at the time of detonation, inhabits the same volume of the explosive. This gas at high pressure and temperature seeks to expand into the surroundings and defines the blast wave containing the reacted gases and shockwave. In 'free air' the pressure

differential drives the blast wave out to displace the adjacent air, at rates exceeding the speed of sound. The reaction of the explosive products during the detonation, and subsequently as the detonation products mix with the surrounding air and react with the available oxygen, drive the blast wave.

2. Nuclear Explosions

   Nuclear explosions represent the culmination of intricate atomic reactions, specifically involving either fission and or fusion processes. The change of element by alteration of atomic nucleus, accompanied by the liberation of a significant amount of energy, manifests as thermal energy and radiation. The energy release is accompanied by additional neutrons that, if they induce further fission reactions in nearby nuclei, lead to a self-sustaining chain reaction.

3. Mechanical Explosions

   Mechanical explosions happen when the structural integrity of a system or vessel is compromised, leading to the rapid discharge of stored energy. Such occurrences are notably observed in pressurised systems, including boilers, pipelines, and gas cylinders, wherein the contents undergo a rapid release consequent to structural rupture. Similarly, in the context of flywheel explosions, instances arise wherein abrupt material failure induces the rapid release of the system's kinetic energy. The phenomenon of tire explosions encapsulates the characteristic of both aforementioned types.

2.2.2 Shock wave formation

A shock wave is formed as the pressure wave of the explosion reaches the surrounding air. The compressible nature of air changes the acoustic properties when sufficiently pressurised, i.e., propagation velocity is proportional to pressure. This allows the pressure front to travel at supersonic velocities, and the peak of the pressure profile is able to 'catch up' with the front of the wave. This creates the characteristic near-instant rise in pressure termed a shock front.

The shock front is the leading edge of the blast wave as the gases expand, in what is classified as the 'near field' region of the explosion. As the gases cool and approach thermodynamic equilibrium, the shock front is able to outpace the detonation product cloud and the shock/blast wave continues to propagate away from the source without being driven. The shock wave rapidly loses energy as it propagates in all directions until the shock front has insufficient magnitude to travel at super sonic speeds where it transitions into behaving as an acoustic wave (or sound wave), and has little destructive power.

2.2.3 Blast wave parameters

At a fixed location from an explosion, the blast wave exhibits a near-instantaneous increase of pressure from the ambient air pressure (denoted as p_0) to the maximum peak overpressure

($p_{so,max}$). Subsequently, there is a temporal decay back to the ambient pressure, the duration of which is identified as the positive phase duration (t_d). The subscript 'so', for 'side-on', designates incident pressure values, representing the pressure experienced in an area not restricting the flow behind the shock front or by a shock wave propagating parallel (or 'side-on', hence the term), to a reflective surface. The term 'overpressure' denotes the pressure increase beyond normal atmospheric conditions induced by the blast wave.

As the pressure decays past the ambient level it concludes the primary positive phase duration and the negative phase begins. The negative phase is caused by the over expansion of the detonation products leaving an area of rarefaction. This rarefaction wave follows the shock wave/positive phase and creates a period (t_{d-}) of negative pressure, with peak amplitude $p_{so,min}$.

The arrival time of a blast wave is given the symbol t_a, and the term specific impulse relates to the cumulative temporal integral of the pressure history, $i_{so,max}$ and $i_{so,min}$ for the peak values of positive and negative phase incident specific impulse respectively (i.e. the definite integrals over the entire positive and negative phases respectively).

2.2.4 Reflected pressures

When the shock front impinges on a boundary, be it a solid surface, liquid or region of sufficiently dense air, the wave is either partially or fully reflected. Assuming perfect/full reflection, the pressure is magnified in the region and the reflection coefficient C_r defines the increase; $C_r = p_r/p_{so}$ where p_r is the reflected overpressure.

The Rankine-Hugoniot jump conditions constitute a set of equations formulated to describe the relationship in fluid states experienced either side of a travelling shock front. They provide a rigorous mathematical framework for the analysis of fluid behaviour in scenarios characterised by rapid changes induced by shock phenomena. The equations show that for weak shocks where the overpressure is small compared to the atmospheric pressure the $C_r \approx 2$, but for strong shocks where the overpressure is considerably larger than the ambient pressure $p_{so} >> p_r$ the C_d reaches a maximum of 8. These are theoretical and for ideal gases, C_r can reach 20 in practical terms, when real gas effects are accounted for (Army Matriel Command Alexandria VA 1974).

2.2.5 TNT equivalence

TNT (Trinitrotoluene) equivalence serves as a metric to standardise the comparison of the yield of high explosives to that of TNT. As a reference explosive, TNT has well-defined properties, making it a reliable benchmark for assessing the energy release of other explosive materials. This concept enables a systematic and standardised evaluation of the potential destructive capacity of various high explosives, contributing to informed decision-making in military and industrial applications.

High explosives exhibit considerable diversity in composition and performance, necessitating

a unified metric for comparative analysis and to calculate the blast parameters. In practical terms, a TNT equivalence value of 1 signifies that the explosive in question possesses the same explosive power as an equivalent charge of pure TNT, whereas TNT equivalence values greater than 1 are associated with explosives more powerful and/or energetic than TNT and values less than 1 are associated with explosives less powerful/energetic. This metric, crucial in military planning and industrial applications, enables straightforward assessments of the relative impact and safety considerations associated with different explosive materials. While TNT equivalence is a valuable tool for standardisation, it is imperative to acknowledge that each explosive material may exhibit unique characteristics, and the measure serves as a practical simplification for comparative purposes within the field of explosives engineering and safety. A nuanced understanding of TNT equivalence is pivotal for evaluating the potential consequences of high explosives in diverse applications, spanning military operations, mining, and demolition.

2.2.6 Scaling laws

Hopkinson-Cranz scaling laws, named after John Hopkinson (Hopkinson 1915) and Gerhardt Cranz (Cranz 1926), provide a scalable model that allows blast parameters to be extrapolated from one set of conditions to another facilitating the analysis of blast effects across a range of scenarios. These scaling laws, based on simple geometric ("length") scaling, and often termed 'cube-root' scaling, offer a systematic framework for understanding and predicting the effects of explosions, shocks, and impacts on structures and materials.

The scaled distance, Z, is given as;

$$Z = \frac{R}{W^{1/3}} \tag{2.1}$$

where R is the distance (in m) from the charge of mass, W (in kg TNT). Scaled distance therefore has units of $\mathrm{m/kg^{1/3}}$. The scaled distance describes the observation that a charge of characteristic dimension d produces a pressure P at a distance R, the same as a charge of dimension λd at a distance λR.

Length-based dimensions are scaled directly but parameters with a time component have a scale factor of λ: $P_1 = P_2$, $t_{a1} = \lambda t_{a2}$ and $i_1 = \lambda i_2$. The length scale on the charge dimension acts in three dimensions changing the volume v by a factor of λ^3. The charge mass ($W = \rho V$) also has a scale of λ^3 making the scale factor $W^{1/3}$ (Kinney & Graham 1985).

The scaled distance also provides a single metric to describe blast loading, incorporating mass and stand-off. It also describes the phase of the blast at the shock front which can be categorised as typically near-field or far-field, but extreme-near-field and mid-field can detail the mechanisms currently driving the blast wave.

These regions are broadly defined in Tyas (2019) as:

1. **Extreme near-field** ($Z \lesssim 0.5$ $\mathrm{m/kg^{1/3}}$)

Surface instabilities of the expanding fireball have had little time to develop: loading relatively consistent.

2. **Late near-field** ($0.5 \lesssim Z \lesssim 2.0$ m/kg$^{1/3}$)
   Surface instabilities of the expanding fireball are prominent and causing considerable structural variations in the fireball and surrounding shocked air: large variations in loading.

3. **Far-field** ($Z \gtrsim 2.0$ m/kg$^{1/3}$)
   Air shock has fully detached, local variations in structure of air shock begin to equalise: variations in loading reduce.

The work performed in this thesis largely sits in category 1 and the transition into category 2, i.e. the boundary between the extreme and late near-field.

2.2.7 Semi-empirical blast prediction

The Kingery-Bulmash (KB) blast predictions, derived from decades of seminal blast experiments, have become indispensable tools for predicting blast loads in free-air scenarios. Originating from the influential work of Kingery & Bulmash (1984), this methodology is widely regarded and has significantly impacted the field of blast analysis. The KB method employs polylogarithmic curves meticulously fitted to a comprehensive compilation of both rudimentary numerical analysis outcomes and experimental measurements, spanning a broad spectrum of events from medium-scale to large-scale explosions ($<$ 1 kg to $>$400,000 kg).

Figure 2.1 presents the compiled data from 22 individual references from studies conducted from the 1940s to the 1980s, some of which were used in the original analysis by Kingery and Bulmash. Farrimond et al. (2023) scaled the data to 1 kg hemispherical charges and plotted against the KB curves. The data holds good agreement for the three main positive phase parameters; pressure, impulse and arrival time. This is a testament to the scaling behaviour of blast waves and the quality of experimental work conducted in the field.

The KB method has emerged as a cornerstone in blast prediction practices, offering a standardised and widely accepted approach for estimating blast loads resulting from a given explosive mass at a specified distance from the target. It has played a pivotal role in the development of semi-empirical prediction tools, enabling the assessment of blast effects across diverse explosive scenarios. The versatility of the KB method is evident in its applicability to a broad range of explosive events, providing the problem is either spherical, hemispherical or, can be assumed to be either of the above.

2.2.8 ConWep

Applying the KB method, the Conventional Weapons Effects Program (ConWep) (Hyde et al. 1988, Hyde 1991) represents an extension of these methodologies. Grounded in the principles outlined in TM5-855 (US Army Engineers Waterways Experiment Station 1986,

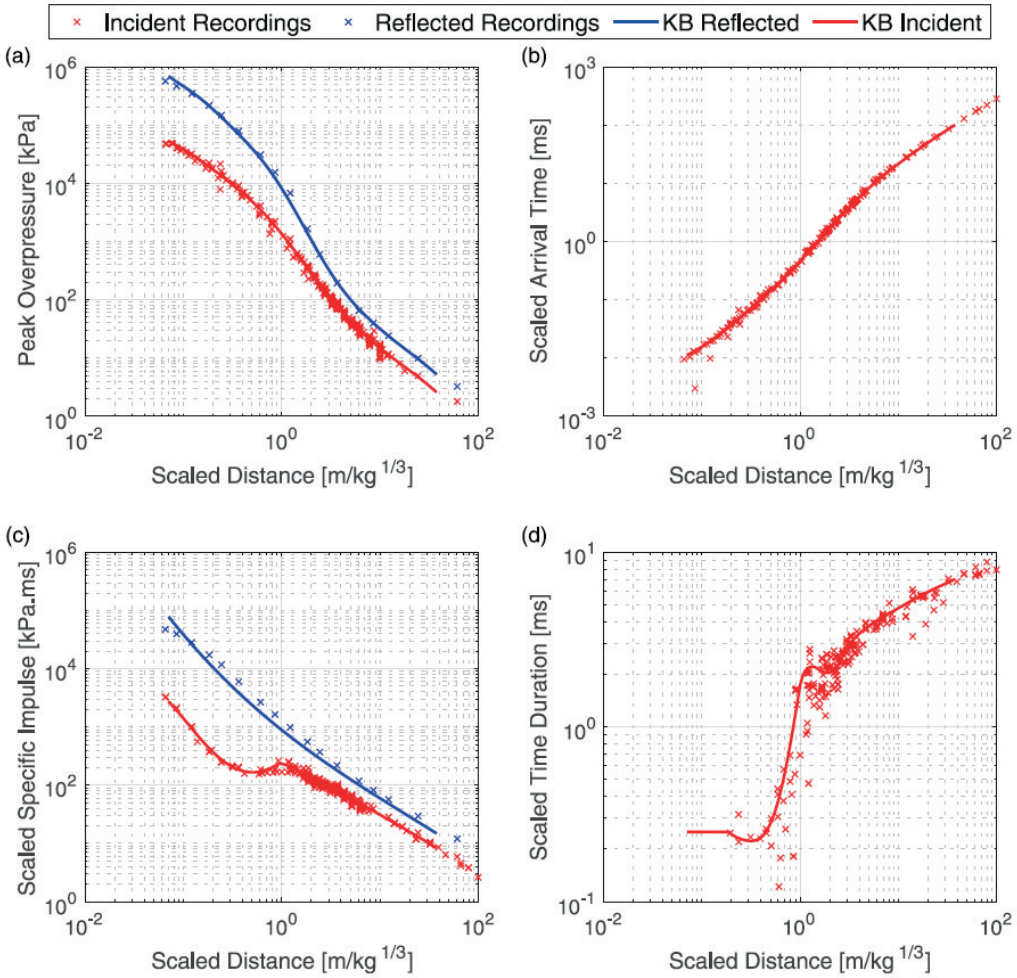


Figure 2.1: Compiled blast parameters from TNT explosive trials with varying mass as a function of scaled distance, which has been scaled to a 1 kg equivalent hemispherical charge, using a shape scaling factor of 1.8 and compared with KB predictions: (a) Peak overpressure, (b) Scaled peak specific impulse, (c) Scaled arrival time, (d) Scaled positive phase duration. Adapted from Farrimond et al. (2023).

Departments of the Army, Navy, Air Force, and the Defense Special Weapons Agency 1998), ConWep incorporates the Kingery-Bulmash curves for normal airblast shock parameters, and includes separate 'modules' to evaluate the effects from conventional weapons, as well as rudimentary methods for predicting loads on structures (Rigby et al. 2015). This integration underscores the enduring relevance and applicability of the KB method in contemporary blast analysis tools.

2.2.9 Blast pressure measurement methods

The measurement of reflected blast loading is a fundamental aspect of blast physics, structural engineering, and military research. Accurate quantification of reflected blast loading is essential for validating computational models, developing blast-resistant materials, and optimising structural design for enhanced protection. Over the years, various experimental techniques have been developed, each with distinct advantages and limitations depending

on precision, scalability, and environmental constraints.

Smoke Tracers and High-Speed Photography

Smoke trails were used to measure blast parameters by tracing the particle trajectories within blast waves, photographed using high-speed cameras to capture their movement when interacting with the blast wave. The density was determined by application of the Lagrangian conservation of mass equation and used to calculate the pressure, (Dewey 1971). Assumptions of adiabatic flow for each air element between shock fronts and ideal gas behaviour were taken and the temperature and sound speed throughout the flow were found from the pressure and density. Particle trajectories gave the particle velocity within the flow from the time derivatives. Compared with other blast measurements and with theoretical calculations, it was estimated that the technique gave blast parameters and more detailed mapping to an accuracy within 5-10% of other forms of measurement, exclusively using experimental data, at the time in the 1960s.

Impulse Plugs and Pendulums

Impulse-based measurement techniques are used to assess reflected blast loading, particularly when evaluating the total impulse transfer rather than just peak overpressure. These methods provide time-integrated force measurements, offering insights into the energy transferred from a blast wave to a structure. Two widely used impulse-based techniques include impulse plugs and impulse pendulums, both of which have distinct applications and advantages.

Impulse Plugs Impulse plugs are specially designed cylindrical or flat-surfaced elements placed in front of a blast wave to absorb and transfer impulse forces to a measurement system. Unlike traditional pressure transducers, impulse plugs capture the total impulse delivered over time rather than instantaneous pressure spikes. The impulse is typically measured by integrating the force exerted on the plug over the duration of the blast event, allowing for a more stable and robust characterisation of blast effects.

Held (1999) demonstrated the use of impulse plugs in evaluating blast profile from a squat cylindrical charge (L/D = 1.43), and demonstrated consistency of the results collected. One of the key advantages of impulse plugs is their ability to filter out transient fluctuations, providing a stable, averaged measure of blast impulse. This makes them particularly useful for scaling blast effects from small-scale experiments to real-world scenarios. However, impulse plugs are not well suited for applications requiring high-speed temporal resolution, as they do not capture detailed pressure-time histories. Additionally, their design and placement must be carefully calibrated to ensure accurate impulse transfer to the measurement system.

Impulse Pendulums and Reaction Masses Impulse pendulums provide an alternative approach to measuring reflected blast impulse, using a suspended plate or mass that swings

or is thrown in response to blast forces. The impulse delivered by the blast is determined by measuring the displacement, velocity, or angular motion of the pendulum or mass, which correlates directly with the momentum transfer from the shockwave, (Rigby & Clarke 2015). This method has been used in research settings to characterise blast loading on various materials, including armored structures and reinforced concrete panels, (Langdon & Shekhar 2020).

Studies have shown that impulse pendulums provide a direct and physically intuitive means of assessing blast impulse, particularly in large-scale field experiments where direct pressure measurements may be impractical. Unlike traditional pressure sensors, which may be overwhelmed by sensor saturation or transient wave interference, impulse pendulums offer a more resilient measurement technique for capturing the net effect of a blast wave on a structure.

However, impulse pendulums also have limitations. Accurate calibration is required to correlate pendulum motion with impulse magnitude, and environmental factors such as wind, vibrations, and secondary shock interactions can introduce errors. Additionally, impulse pendulums are less effective for measuring small-scale or localised blast effects, as they provide an overall measure of impulse rather than a spatially resolved pressure distribution.

Pressure Gauges and Overpressure Sensors

Another widely used approach involves piezoelectric and piezoresistive pressure transducers, such as those manufactured by PCB Piezotronics and Kulite. These sensors convert pressure fluctuations into electrical signals, enabling high-frequency response and spatially resolved pressure measurements. The gauge types differ in terms of their measurement principles, response times, durability, and sensitivity to environmental factors. Despite their high sensitivity and durability, these gauges provide point measurements only, meaning they might miss or record localised variations in pressure distribution in complex environments. Additionally, their accuracy is highly dependent on proper calibration, alignment and recording apparatus.

Piezoelectric-based transducers operate on the piezoelectric effect, where certain crystals, such as quartz and tourmaline, generate an electric charge proportional to applied mechanical stress. Their fast response time and high-frequency sensitivity make them ideal for blast pressure measurements, accurately capturing blast waves. With a wide dynamic range (from kilopascals to hundreds of megapascals), they capture sharp pressure spikes and wave reflections making them the preferred choice for dynamic blast analysis, (Carter et al. 2016). However, due to their high output impedance and low signal levels, they are susceptible to electrostatic and amplification noise.

Various pressure gauges have been developed to capture both free-field and reflected blast pressures, each designed to function optimally under specific conditions.

One of the most commonly used instruments for free-field blast pressure measurement is the pencil probe. These probes are designed to measure the side-on or incident pressure of an undisturbed blast wave. Their tapered design allows immediate clearing of the reflected pressure, effectively only recording the incident pressure, and minimises interference with the blast wave. However, they are susceptible to alignment errors and can be affected by thermal expansion at high temperatures.

For measuring reflected blast pressures; ground-surface transducers are commonly used, flush-mounted to a surface to directly record the reflected shockwave, (Draganić et al. 2018). Since reflected pressures are significantly higher than free-field pressures due to shockwave amplification upon impact, ground-surface transducers are designed to minimise distortion and avoid pressure signal interference. Their advantages include the ability to provide precise high-frequency reflected pressure data while offering protection against environmental and thermal interference. However, their recording duration is often limited, and they may be affected by thermal and mechanical shock seen in the near-field.

Hopkinson Pressure Bar

A Hopkinson Pressure Bar (HPB) is a robust pressure transducer comprising of a long bar instrumented with strain gauges, (Hopkinson 1914). Pressures applied to the incident face propagate down the bar as stress pulses and the resulting strain can be recorded at the gauges. The Youngs' modulus of the material is used to calculate the stress in the material and is assumed to be representative of the loading on the face at a time shift, to allow for the transmission of the stress pulse from the face to the gauge location. The geometry and the material of the bar can be designed to match the expected loading; knowing pressure range, loading time and spatial resolution.

To minimise the interference of the blast wave with the bar after the required loading, the bar must be shielded for sufficient time to allow the stress pulse to be recorded, typically behind a rigid plate. This and the length of the required bar makes it difficult to deploy in the same way as pressure gauges.

One of the major challenges in using HPB for blast pressure measurements is wave dispersion, which occurs because stress waves propagate at different velocities depending on their frequency content, (Tyas & Watson 2001, Rigby et al. 2018a). This phenomenon is particularly problematic in wide bars subjected to high-frequency wave oscillations. Higher-frequency components travel more slowly than lower-frequency components, causing the wave to spread out and distort over time, (Pochhammer 1876, Chree 1889). As a result, the sharp, well-defined blast wavefront gets broadened, making it difficult to accurately determine peak pressure, arrival time and rise time. Dispersion also attenuates high-frequency shockwave features, reducing the precision of short-duration blast events. To mitigate this issue numerical correction algorithms can be employed to attempt to reconstruct the pressure-time profile based on the received frequency and the bar's transmission properties. Despite this, wave dispersion remains a fundamental limitation,

requiring careful consideration on the blast pressure analysis.

Strain gauges have inherent high-frequency limitations that can affect their accuracy in recording blast loading. These limitations arise primarily from the gauge's response time, signal transmission, geometry and mechanical bonding characteristics. At very high frequencies, strain gauges may suffer from signal distortion, reduced sensitivity, and phase lag, making them less effective for capturing sharp pressure spikes and high-speed shockwave interactions, (Barr et al. 2023*a*). Additionally, the finite mechanical response time of the strain gauge material and adhesive layer can lead to incomplete strain transfer, especially when subjected to rapid stress waves from explosive blasts. The length of the gauge material may limit the recording of certain frequencies since strain gauges measure localised deformation. Their ability to resolve short-duration, high-speed strain events depends on their gauge length relative to the wavelength of the stress wave. If the strain gauge is too long relative to the wavelength of the strain pulse, it will act as a spatial filter, averaging out rapid strain fluctuations and reducing sensitivity to high-frequency content. This can lead to attenuation of sharp pressure spikes, making it difficult to capture precise transient stress variations in fast-rising shock waves. Conversely, shorter strain gauges have a higher spatial resolution and are better suited for measuring small-scale, high-frequency strain pulses, but they can be more susceptible to noise, delamination and installation errors.

Pairs of gauges, fitted either side of the bar, are utilised to remove the influence of bending in the stress signal and typically wired in a Wheatstone bridge assembly to average the voltages to create one recorded trace. The associated wiring, amplification and data acquisition systems must also be designed for high-frequency signals without introducing electrical noise, impedance mismatches, or filtering artifacts, which can further degrade measurement fidelity.

Optical Measurement Methods

High-Speed Video Photo-optical techniques have long been employed to capture shock front arrival times and velocities, enabling the derivation of key blast wave properties such as pressure and density through the application of the Rankine-Hugoniot jump conditions, (Dewey 1964, 1971). By correlating particle velocities with shock pressures, these methods have provided valuable insights into the behaviour of freely expanding blast waves.

Despite the advantages of modern high-speed video imaging, the intense luminosity generated during detonation can obscure critical shockwave details. Consequently, optical-based shock front tracking studies, (Mizukaki et al. 2014, Anderson et al. 2016), typically focus on the intermediate to far-field region, where the shockwave has fully detached from the fireball and propagates freely. However, within the near-field, the detonation fireball remains in close proximity to the surrounding compressed air layer, rapidly expanding in the initial phase of blast evolution, (Jenkins et al. 2013).

Rigby et al. (2020) used The Canny edge detection system to track the shock front of

the blast wave in the near-field and calculated from the velocity-radius relationship in conjunction with the Rankine-Hugoniot jump conditions the reflected pressure distributions.

Schlieren Schlieren imaging is a contrast-enhancing technique that visualises small variations in refractive index by using a collimated light source and a knife-edge filter. When light passes through a region of varying density, such as a shockwave, it is deflected at different angles due to changes in the speed of light within the medium. This method provides high-resolution, directional images of shock structures, however, Schlieren imaging requires precise optical alignment and a controlled environment.

A key advantage of Schlieren imaging is its ability to detect fine details of wave motion, including Mach stems, blast wave reflections, and boundary layer interactions. With the integration of high-speed cameras, modern Schlieren setups can capture shockwave propagation at microsecond timescales, allowing for the detailed study of transient blast events. For instance, Biss & McNesby (2014) utilised Schlieren flow visualisation and high-speed digital imaging to optically assess the temporal decay of incident blast waves in the hundreds of kilopascals (kPa) range.

Background-oriented schlieren (BOS) Unlike Schlieren imaging, BOS uses a patterned background and a high-speed camera to track small displacements of background features caused by refractive index changes in the air. By comparing these distortions using digital image correlation techniques to a tare image, BOS generates a quantitative representation of density gradients that can be used to calculate the pressure field of a blast wave.

The method is particularly advantageous for outdoor experiments, as it does not require complex optical alignment and can operate under natural lighting conditions. However, its spatial resolution is dependent on camera sensitivity, background pattern quality, and image processing algorithms.

Studies by Hargather & Settles (2007) and Hargather (2013) employed BOS techniques to establish empirical relationships between incident shock pressure and distance for various explosive compositions.

Schlieren imaging is generally unsuitable for near-field applications due to the extreme brightness of the detonation fireball, which renders the shockwave boundary indistinguishable from the surrounding air (Settles 2001). Instead, McNesby et al. (2014, 2016) employed framing and streak camera techniques to capture the fireball's outer surface dynamics and applied the Rankine-Hugoniot relations to infer near-field incident shock pressures.

Shadowgraph Shadowgraph imaging is a simpler alternative to Schlieren imaging, relying on light intensity variations rather than directional refraction to detect density gradients. Instead of using a knife-edge filter, Shadowgraph systems measure changes in brightness caused by light ray deflections, creating high-contrast images of shock structures and flow

disturbances. This technique is highly effective for tracking strong blast waves, high-speed gas expansion, and thermal effects in explosive environments. One of the major advantages of Shadowgraph imaging is its ease of implementation, as it does not require complex optical filtering or precise knife-edge alignment. This makes it particularly useful for large-scale blast testing and field experiments, where rapid setup and flexibility are required. However, Shadowgraph images often lack the directional sensitivity and fine detail resolution of Schlieren imaging, making them less suited for analysing subtle shockwave structures or weak density variations.

Digital Image Correlation A more recent advancement in blast measurement is Digital Image Correlation (DIC), which provides full-field deformation analysis of structures exposed to reflected blast waves. This optical method employs dual high-speed cameras and image processing algorithms to track displacement, strain, and structural failure in blast-loaded plates, (Curry & Langdon 2017). The main advantages of DIC include its non-contact measurement capability, high spatial resolution, and ability to analyse deformation over time. However, it requires multiple, controlled environment and lighting conditions, and extensive data processing, limiting its deployability.

Laser Doppler Velocimetry and Photonic Doppler Velocimetry Laser Doppler Velocimetry (LDV) and Photonic Doppler Velocimetry (PDV) facilitate non-contact measurement of surface velocity and displacement. Laser Doppler Velocimetry (LDV) is an advanced optical measurement technique used to determine velocity profiles of moving surfaces and fluid flow fields with high temporal and spatial precision, (Schlöffel et al. 2009). LDV plays a crucial role in analysing the kinematics of detonation waves and shock-induced motion in adjacent inert materials. The method is based on the Doppler effect, where laser light scattered or reflected from a moving surface undergoes a frequency shift proportional to the velocity of the target. A specialised variation, Photon Doppler Velocimetry (PDV), was first introduced by researchers at Lawrence Livermore National Laboratory (LLNL) in 2006 and has since become a widely used diagnostic tool for measuring free-surface velocities of shocked materials with nanosecond resolution, (Kuznetsov & Bennetts 2013).

Virtual Fields Method The Virtual Fields Method (VFM) is an advanced inverse analysis technique used in blast pressure measurements to extract material properties, stress distributions, and loading conditions from full-field deformation data. Unlike traditional point-based pressure sensors, VFM leverages high-speed imaging and Digital Image Correlation (DIC) to measure full-field strain and displacement on a test surface subjected to blast loading. By applying virtual work principles the method identifies constitutive mechanical material parameters from known loading or vice versa, (Pierron & Grédiac 2012). The method enables the estimation of pressure distributions and impulse loads without direct contact with the blast wave. This is particularly useful in complex blast scenarios, where pressure sensors may be impractical due to harsh environments, high strain rates, or non-uniform loading conditions. Recent studies have demonstrated

the effectiveness of VFM in reconstructing spatially resolved pressure fields on structures exposed to blast waves, providing valuable insights into blast-structure interactions and the development of protective materials, (Kaufmann et al. 2023). However, VFM's accuracy depends on precise high-speed image acquisition, well-calibrated deformation fields, and robust numerical processing, making it computationally intensive.

Table 2.1: Comparison of techniques for measuring reflected blast loading.

Technique	**Measurement Type**	**Pressure Range**	**Advantages**	**Limitations**
Impulse plugs	Integrated impulse	Not directly pressure-dependent; measures total impulse	Stable impulse measurement; reduces transient fluctuations; suitable for laboratory tests	Limited temporal resolution; requires precise calibration; susceptible to environmental interference
Impulse pendulums	Momentum transfer	Not directly pressure-dependent; measures global impulse transfer	Effective for large-scale experiments; resistant to sensor saturation; ideal for assessing global impulse	Affected by environmental conditions; lacks spatial resolution
Piezoelectric and piezoresistive pressure transducers	Point-based pressure measurement	1 kPa – 100 MPa	High-frequency response; precise; widely used in blast research	Requires careful calibration; susceptible to sensor damage under extreme conditions
Hopkinson pressure bar	Stress wave measurement	10 MPa – 10 GPa	Highly accurate; well-established for controlled experiments	Requires a specialised setup; limited to small-scale controlled experiments
Digital image correlation (DIC)	Full-field deformation analysis	Not pressure-based; measures strain and displacement	Non-contact; high spatial resolution; effective for structural response studies	Requires high-speed cameras, controlled lighting, and post-processing
Schlieren and shadowgraph imaging	Shock wave visualisation	Not pressure-based; visualises density gradients	Captures real-time shock wave interactions; non-intrusive	Requires specialised optical setup; not practical for field applications
Background oriented schlieren (BOS)	Full-field pressure measurement	Not pressure-based; calculates density gradients	Capable of providing detailed pressure distributions in time	Requires specialised optical setup and significant computational resource
Laser Doppler velocimetry (LDV) and photonic Doppler velocimetry (PDV)	Velocity and displacement tracking	Not pressure-based; measures velocity and displacement	Non-contact; high temporal and spatial resolution	Sensitive to environmental conditions; requires precise alignment
Virtual fields method (VFM)	Inverse analysis of full-field deformation	Not directly pressure-based; estimates distributed pressures	Non-contact; enables full-field pressure estimation from DIC data; useful for complex loading scenarios	Requires high-speed imaging; computationally intensive; dependent on accurate strain field measurements

Summary of measurement methods

The selection of an appropriate measurement technique for reflected blast loading depends on the specific research objectives, cost constraints, and environmental conditions. Impulse plugs offer a stable and integrated measure of total impulse, while pressure transducers and blast gauges provide high-frequency, point-based pressure data. HPBs remain an industry standard for high-magnitude stress wave measurements, whereas Digital Image Correlation (DIC) offers detailed structural deformation analysis. Optical and laser-based methods provide high-resolution shockwave diagnostics, and shock tubes enable repeatable testing in controlled conditions. Future advancements in sensor technology, high-speed data acquisition, and hybrid experimental-numerical methodologies will further enhance the accuracy and applicability of reflected blast pressure measurement techniques.

2.3 Explosive consistency and variability

2.3.1 Variability in explosives

While the accuracy of ConWep predictions can vary depending on the specific conditions and nuances of the blast scenario, it generally provides reasonably accurate estimations of reflected blast loading when applied within its intended range of application. Rigorous validation efforts and comparisons with experimental data have demonstrated the program's ability to capture the essential features of blast effects, and is regularly used as a preliminary check against which experimental data is validated.

Bogosian et al. (2002) conducted a meticulous examination of blast predictions by comparing them to an extensive experimental dataset, specifically focusing on the applicability of KB predictions to explosives with similar characteristics. The study revealed substantial variations, with peak pressure exhibiting fluctuations between 70–150% and specific impulse showing variations in the range of 50–130% for nominally identical far-field tests within the scaled distance range of $1 < Z < 40$ m/kg$^{1/3}$. These observed uncertainties align with similar trends identified in related studies, reinforcing the notion that as the distance from the explosive charge increases, the variability tends to diminish (Bogosian et al. 2014).

Formby & Wharton (1996) investigated the concept of TNT equivalence for a variety of hemispherical secondary explosive compositions. The findings highlighted substantial variability, approximately (±30%) for pressure and (±15%) for specific impulse, especially at large scaled distances. This collective body of literature underscores the inherent complexity and stochastic nature of blast pressure measurements (Smith et al. 1999).

Netherton & Stewart (2010) conducted a statistical analysis of the historical data used to populate the TM5-1300 (1990), concluding the variability they included gave the overly prescribed the design codes with probability of exceedence as low as 4%.

In an investigation of free-air tests involving varied charge shapes, sizes, and compositions, Stoner & Bleakney (1948) reported diminished variability in pressure, ranging between

± 0.6 and 6.5%, with a consistent reduction in variability observed as scaled distance increased. Esparza's work (Esparza 1986*a*,*b*) visually demonstrated concordance within nominally identical tests, focusing on various high explosive compositions. Tang et al. (2017) found that experimental data exhibited variability similar to earlier studies, indicating the robustness of the observed trends.

Farrimond et al. (2022) conducted a comprehensive review of historic far-field high explosive blasts noting variability observed is likely a function of scaled distance, falling into the three distinct ranges proposed by Tyas (2019), despite a parameter for it is yet to be established. Farrimond et al. (2024) conducted far-field tests and produced highly repeatable results at scaled distances greater than 3 ($Z < 3$ m/kg$^{1/3}$), with peak reflected pressure and peak specific impulse within $\pm 6 - 8\%$ and time of arrival as low as $\pm 2\%$.

2.3.2 Consistency and predictability of explosives

Moreover, studies by Rickman & Murrell (2006), Tyas et al. (2011), and Ohashi et al. (2001) reported results demonstrating reasonable agreement with KB predictions across different testing conditions and charge configurations.

Figures 2.2 and 2.3 show the pressure histories of C4/PE4 hemispherical charges reflecting off rigid vertical surfaces. Although these independent investigations were primarily designed to study the effects of clearing on the reflected pressure histories, a secondary observation was that until the relief waves arrive the pressure was seen to track very closely to the ConWep predictions.

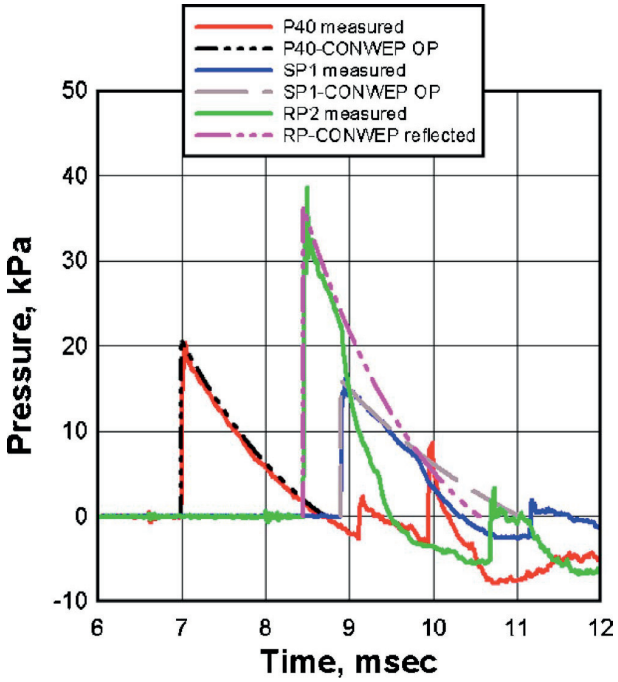


Figure 2.2: Measured and predicted wave forms from (Rickman & Murrell 2006), of a 72.6g C4 hemispherical charge at 4.116m standoff accompanied with the corresponding ConWep traces.

Rigby et al. (2014) proposed that systematic experimental and analytical errors, rather

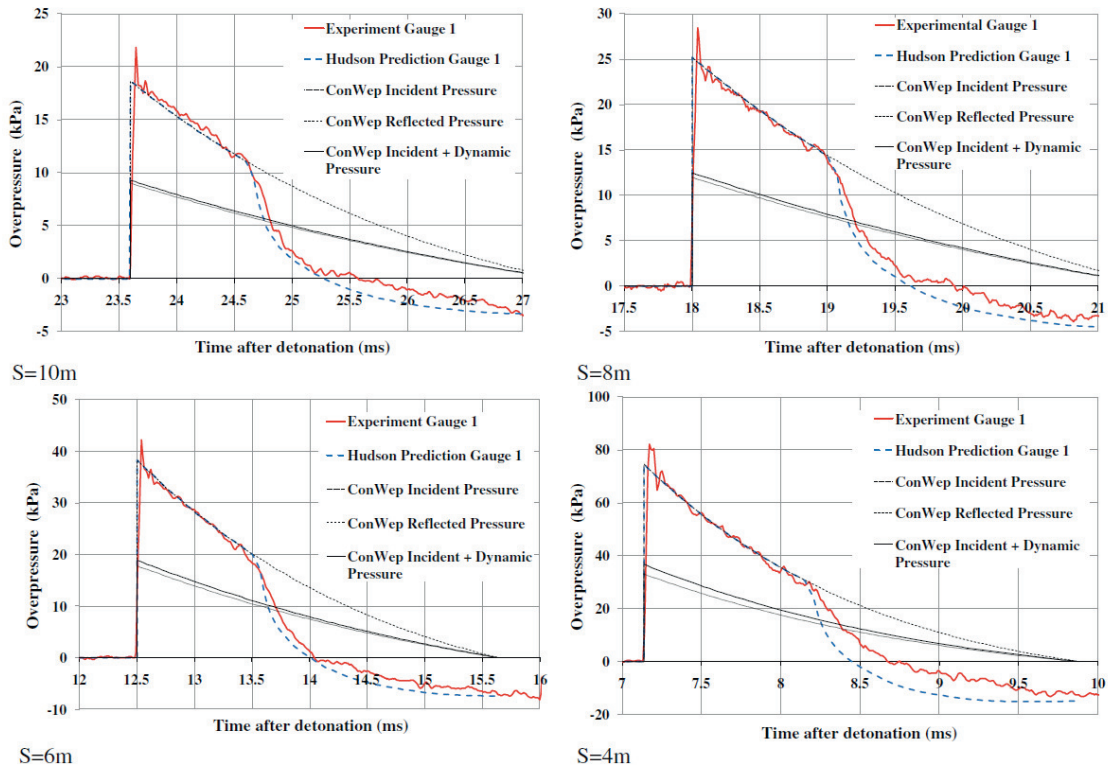


Figure 2.3: Reflected pressure time signals at stand-offs (10, 8, 6, 4m) of 250g PE4 hemispherical charges and corresponding ConWep traces, Tyas et al. (2011).

than intrinsic randomness, contribute to the documented variability in far-field blast parameters. To address these challenges, they employed an exponential 'Friedlander' curve fitting method, achieving commendable test-to-test consistency. Building on this theme, Chiquito et al. (2019) and Bogosian et al. (2019) adopted analogous methodologies, involving functional fitting curves applied to experimental data. Their efforts yielded enhanced consistency, reduced subjectivity, and further contributed to ongoing discussions regarding the refinement and validation of blast prediction models.

Farrimond et al. (2022) revisited the idea, proposed by Stoner & Bleakney (1948) and Bogosian et al. (2014), that variability levels in blast parameters differ with scaled distance. Analysing the data using two distinct methodologies, they found strong evidence supporting increased variability as the near-field is approached ($Z < 3$ m/kg$^{1/3}$), aligning with findings by Simoens & Lefebvre (2015) and the regions stipulated by Tyas (2019) in Section 2.2.6. This supports the hypothesis of scaled distance regions with prominent fireball surface instabilities, contributing to a more nuanced understanding of explosive shock front development.

Tyas et al. (2015) showed that despite the localised variability of loading onto a surface (peak pressure and specific impulse variations of upwards of 100%) the total area-integrated impulse was highly consistent (maximum variation of 5%) across a series of tests of 113g PETN spheres at 0.421m stand-off (0.760 m/kg$^{1/3}$), as shown in Figure 2.4.

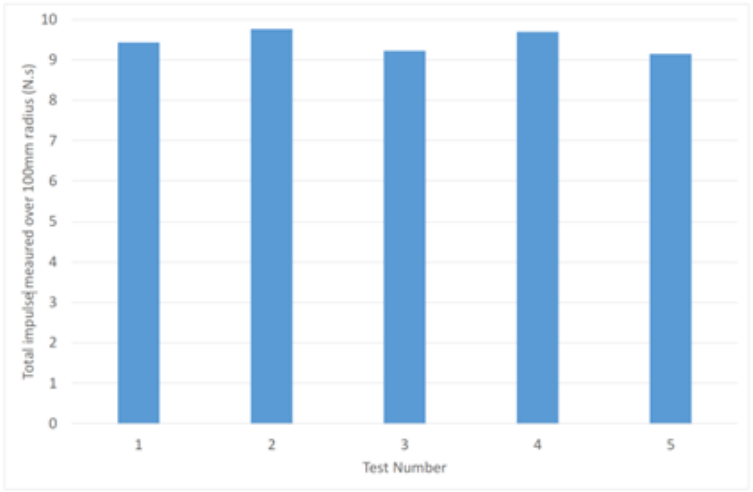


Figure 2.4: Total impulse over a 100 mm radius recording area for 5 spherical tests of 113g PETN, Tyas et al. (2015).

The blast research community exhibits a clear divide on whether free air far-field blast parameters should be deemed inherently variable. This divergence extends to the challenge of characterising these parameters for specific explosive compositions, shapes, and sizes. Borenstein & Benaroya (2009) highlight the importance of considering both extrinsic and intrinsic sources of variability, emphasising the need for a scientific understanding of both of these sources, but in particular intrinsic factors which have been studied considerably less. This recognition provides a valuable direction for the community: in order to develop reliable models accounting for extrinsic variations, a thorough understanding and quantification of intrinsic sources of variability through well-controlled scientific testing are essential.

2.4 Non-spherical charges

2.4.1 Overview

The loading imparted on structures following the detonation of a non-spherical high explosive significantly differs from that of a spherical charge, especially in the near-field, characterised by highly non-uniform (both spatial and temporal) loading and interaction with the target surface (Rigby et al. 2015a, Tyas et al. 2016). While there exist well-established tools for predicting the magnitude and distribution of loading from spherical airbursts or hemispherical surface bursts (Kingery & Bulmash 1984, US Department of Defence 2008, Hyde 1991), the characterisation of blast loading from even the simplest non-spherical charges has received considerably less attention despite their prevalence in real-world events.

Explosive devices used in terror attacks rarely assume spherical or hemispherical shapes. Yet, both engineering practice and scientific research often simplify the charge as a sphere or hemisphere due to their perfect symmetry and relative computational simplicity. It is known that blast waves from cylindrical charges differ from those from a spherical charge.

The blast community has yet to develop a comprehensive understanding of non-spherical blast effects, and has relied upon expressing them in terms of an simplified equivalent spherical charge for objective comparisons. Considering non-spherical shapes, the approach to characterising a charge is essential to reflect the non-symmetric geometric conditions of the threat.

2.4.2 Shock wave structure

A detailed visualisation and description of two primary shock waves and their interactions was offered by Wisotski & Snyer (1965). A primary shock wave radiates radially from the side of the charge (along the equatorial plane), interacting with two additional primary waves; one from each end along the axis of the charge (normal to the equatorial plane). This interaction creates bridging waves of Mach stems, as depicted in Figure 2.5. The Mach reflections travel inward behind the primary waves, giving rise to secondary shock waves, facilitating the transfer of energy from the direction of the greater primary shock wave to the lesser. This complex interplay underscores the necessity for a nuanced understanding of the distinct loading mechanisms associated with non-spherical explosive charges, reinforcing the importance of developing comprehensive models and predictive tools in this domain.

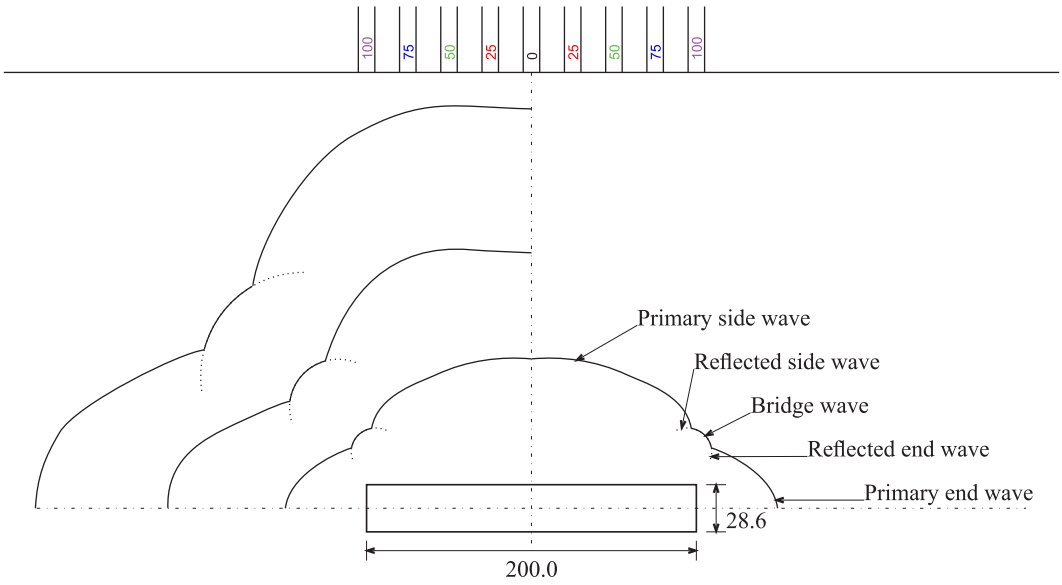


Figure 2.5: Primary and secondary shock waves emanating from a cylindrical explosive, adapted from Wisotski & Snyer (1965). Also shown are dimensions of a $L/D = 7$ cylinder and measurement locations used in this study (in mm). Numbers at each measurement location denote distance from the centre of the target.

2.4.3 Cylindrical testing

In a comprehensive analysis conducted by (Stoner & Bleakney 1948), data from 56 experimental trials were scrutinised to establish incident pressure-distance relations for free-air conditions. The study encompassed diverse charge geometries, including rectangular charges (17 tests using TNT), spherical charges (8 tests using Pentolite), and cylindrical

charges (31 tests: 5 Pentolite and 26 TNT). Notably, the determination of pressure in these trials did not involve direct measurements; rather, it was inferred from velocity-radius data compiled from various time-of-arrival piezo-electric gauges. The consideration of diverse length-to-diameter (L/D) ratios, ranging from 1.32 to 5.20, revealed a dependency on L/D. However, the authors acknowledged the limitation of insufficient tests for a statistically significant analysis. Despite this limitation, discernible distinctions emerged between spherical and cylindrical pressure-distance relations. In the near-field, the radial shock wave exhibited near-cylindrical characteristics, showcasing a slower decay than its spherical counterpart, leading to relatively higher pressures within that range.

Pronounced disparities between spherical and cylindrical pressures persisted beyond distances of 20 charge diameters, corresponding to approximately $Z > 1.8$ m/kg$^{1/3}$; the closest measurement locations in the trials. Specifically, for charges with an L/D ratio of 5.20, the pressures observed were consistently, on average, 10% higher than those associated with spherical charges. This discrepancy endured up to a scaled distance of approximately $Z = 3.0$ m/kg$^{1/3}$. The persistence of these differences in pressure characteristics underscores the enduring influence of charge geometry on the resulting blast effects.

The findings from Stoner & Bleakney (1948) illustrate the intricate dynamics governing pressure–distance relationships for different charge configurations. While the study identified clear dependencies on L/D and discernible distinctions between spherical and cylindrical pressures, the acknowledged limitation of insufficient tests emphasises the need for further comprehensive investigations to bolster the statistical robustness of these observations. The persistence of pressure differentials beyond 20 charge diameters offers a nuanced understanding of the lasting influence of charge geometry on blast effects, contributing valuable insights to the broader field of blast and impact dynamics.

Plooster (1978) undertook a comprehensive analysis utilising available experimental data to derive incident pressure-distance relationships for cylinders with varying length-to-diameter ratios (L/D). This foundational work was subsequently expanded upon with the inclusion of new experimental data, incorporating 3.6 and 7.2 kg Pentolite charges (Plooster 1982). The extended investigation covered a wider range of L/D ratios, ranging from 0.25 to 6.00, providing a nuanced exploration of the blast wave dynamics associated with cylindrical charges.

The intricacies of the blast wave profile resulting from cylindrical charges, in contrast to the spherically-symmetric nature of blast waves from spherical explosives, revealed a discernible dependency of blast loading on azimuth angle. Azimuth angle, defined as the angle between the longitudinal axis of the cylinder and the measurement axis (Esparza 1992), emerged as a critical factor influencing the blast wave characteristics. Plooster (1982) demonstrated that the orientation of the long axis of the cylinder concerning the measurement location also played a significant role, leading to localised variations in blast loading.

This nuanced understanding of the spatial variability in blast loading, determined by both

azimuth angle and cylinder orientation, contributes valuable insights into the intricate dynamics of cylindrical charge detonations. Experimental data were available for scaled distances, Z, exceeding 1.24 m/kg$^{1/3}$, providing a foundation for the analysis of blast effects in the extended distance regime. The incorporation of a diverse range of L/D ratios in the experimental setup allowed for a comprehensive exploration of how the geometrical characteristics of cylindrical charges influence the resulting blast wave and loading patterns.

Furthermore, Plooster (1978) and subsequent studies on a similar theme, showcased the applicability of Hopkinson-Cranz scaling for cylindrical charges in the far-field (Swizdak 1982). This scaling approach provides a valuable framework for predicting blast effects at distances where the blast wave tends towards a more stable and predictable form, if the critical scaled distance is identified.

More recent investigations have delved into the intricate propagation dynamics of blast waves originating from cylindrical charges, with a particular focus on their dependence on aspect ratio and scaled distance. Wu et al. (2010) conducted a comprehensive study examining the influence of length-to-diameter ratio (L/D), charge orientation, and scaled distance on blast parameters emanating from cylindrical charges. Employing finite element analysis complemented by a limited number of experiments, the study revealed intriguing observations. Specifically, Wu et al. (2010) noted that the peak reflected pressure and impulse generated by a vertically-orientated cylinder (axis perpendicular to the span of the target) surpassed those induced by a spherical charge of equal mass or a horizontally-orientated cylinder. This discrepancy underscores the profound impact of charge orientation on the blast characteristics of non-spherical charges.

Corroborating insights into the directional focus of energy from cylindrical charges are found in the works of Sherkar et al. (2016) and Artero-Guerrero et al. (2017). These studies consistently report that, for large values of L/D, the majority of energy is concentrated in the radial direction, whereas for small values of L/D, the predominant energy focus shifts to the axial direction.

Further contributing to this body of knowledge, Rigby et al. (2019a) experimentally measured near-field specific impulse distributions from both spheres and $L/D = 1/3$ cylindrical charges. Intriguingly, despite being placed three times greater distance from the target, the cylindrical charges imparted a total impulse similar to that of spherical charges of equal mass.

In the pursuit of comprehending blast phenomena from cylindrical explosives, a series of studies by Knock & Davies (2011a,b, 2013) and Knock et al. (2015) have contributed significantly. These investigations culminated in the development of empirical equations designed to predict incident blast parameters originating from both the axial and radial directions of a cylindrical explosive. Their empirical models provide valuable tools for predicting and analysing blast effects, offering insights into the complex dynamics associated with cylindrical detonations.

Simoens & Lefebvre (2015) conducted experimental measurements of mid- to far-field (0.5–2.5 m/kg$^{1/3}$) incident blast pressures emanating from cylindrical charges. The derived spherical equivalence factors, representing the mass of a spherical explosive required to impart the same load as a unit-mass of cylindrical explosive, ranged from 0.8 to 1.8 for incident pressure and from 0.6 to 1.4 for incident specific impulse. This quantification of equivalence factors provides a valuable benchmark for understanding the comparative effects of cylindrical and spherical explosives, facilitating more accurate assessments of blast consequences across various scenarios.

Recent advancements in the determination of spherical equivalence factors involve equating plate deformations using finite element analysis, as demonstrated by Rigby et al. (2021) for a range of cylindrical charges with length-to-diameter ratios (L/D) spanning 0.2 to 5.0. This approach adds a refined dimension to the quantification of equivalence factors, incorporating the intricacies of plate deformations to enhance the accuracy of predictions.

2.4.4 Initiation location

Furthermore, the initiation location of cylindrical charges has been identified as a pivotal factor influencing blast parameters, as elucidated by recent studies highlighted by Hu et al. (2018), Xiao et al. (2020a), and Xiao et al. (2020b). It was revealed that pressure levels can be significantly enhanced, up to a factor of 3.0, for centrally-detonated cylinders. This finding underscores the importance of considering not only the geometrical characteristics of cylindrical charges but also the precise location of initiation, another complication over the idealised centrally detonated perfect spheres.

2.4.5 Charge shape persistence

It is widely acknowledged that disparities in blast parameters between cylindrical and spherical charges endure up to a distance of approximately $Z \approx 4$ m/kg$^{1/3}$, as indicated by studies such as Sherkar et al. (2016), Simoens & Lefebvre (2015), and Xiao et al. (2020b). However, there exists a notable gap in our comprehensive understanding, particularly pertaining to the early and mid stages of blast wave propagation subsequent to the detonation of non-spherical charges. This knowledge gap arises from the scarcity of rigorous experimental data and investigations on near-field blast loading, with only a limited number of studies providing experimental results for non-spherical charges at scaled distances less than 1.24 m/kg$^{1/3}$ (Shi & Stewart 2015).

2.5 Numerical modelling

2.5.1 LS-DYNA

Numerical modeling emerges as an indispensable instrument in unraveling the complex phenomena inherent in explosions. LS-DYNA, a prevalent finite element analysis software, provides a robust framework for simulating explosive events and their aftermath. Finite

Element Modeling (FEM) is a numerical technique used for solving complex engineering and physical problems by dividing a complex structure or system into smaller, simpler, and finite elements. The main objective of FEM is to approximate the solution to a partial differential equation, representing the behavior of a system, by converting it into a system of algebraic equations that can be solved computationally.

LS-DYNA's effectiveness in simulating explosions stems from its handling of the intricate physics that govern such events. This encompasses the accurate representation of shockwave propagation, structural responses, and complex interactions of different materials. To enact the modeling of explosions in LS-DYNA, practitioners delineate the explosive source, the surrounding structures, and the ambient environment. Crucial parameters of the explosive material, including density, detonation properties, and energy release, are meticulously defined to mirror real-world scenarios.

2.5.2 EOS

In numerical simulations, an Equation of State (EoS) is a mathematical model that describes the thermodynamic properties of a material, particularly how its internal energy, pressure, and volume change in response to different conditions. LS-DYNA uses various Equation of State models to simulate the behavior of materials under dynamic and high-stress conditions. To account for the chemical reactions and energy release during detonation of explosive materials LS-DYNA uses the Jones-Wilkins-Lee equations of state.

JWL

The Jones-Wilkins-Lee (JWL) equation of state represents a widely used set of empirical relations in numerical modeling, specifically in the simulation of high-explosive detonations and shockwave propagation. Developed by Jones, Wilkins, and Lee, these equations provide a convenient and effective means to describe the pressure-volume relationship and chemical reaction kinetics during the detonation process of energetic materials. The equations capture the complex interplay between chemical reactions, thermodynamics, and material properties, providing a mathematical framework to simulate the evolution of pressure and volume during detonation. Significantly, within LS-DYNA's functionality is its utilisation of advanced material models, accommodating the diverse responses of materials to blast loading, encompassing deformations, fractures, and modes of failure. This feature enables engineers and researchers to assess the susceptibility of structures, optimise designs for blast resistance, and evaluate the efficacy of protective interventions.

The JWL equations typically take the form of a set of coupled differential equations, describing the rate of change of pressure and volume with respect to time. These equations are integrated into numerical simulation codes, such as LS-DYNA, to model the explosive behavior and generate realistic simulations of blast waves, shock fronts, and material response. The JWL model is particularly valuable for its ability to account for the non-linearity and complexities inherent in high-explosive detonations.

The JWL in LS-DYNA is accessed via the *EOS_JWL card, and is defined by the following expression (Lee et al. 1968):

$$p = A\left(1 - \frac{\omega}{R_1 V}\right)e^{-R_1 V} + B\left(1 - \frac{\omega}{R_2 V}\right)e^{-R_2 V} + \frac{\omega E}{V} \tag{2.2}$$

where A, B, R_1, R_2 and ω are constants, V is the volume and E is the specific internal energy as before. Density, ρ, detonation velocity, D, and Chapman-Jouguet pressure, P_{CJ}, of the explosive are defined in the *MAT_HIGH_EXPLOSIVE_BURN material model and control the programmed detonation of the explosive. Material properties and EOS parameters used in the numerical model are summarised in Table 2.2, where the JWL parameters for C4 are taken from Dobratz & Crawford (1985).

Table 2.2: JWL equation of state parameters for C4, taken from Dobratz & Crawford (1985).

*EOS_JWL			*MAT_HIGH_EXPLOSIVE_BURN		
Parameter	Value	Unit	Parameter	Value	Unit
A	609.77E9	Pa	ρ_0	1601	kg/m^3
B	12.95E9	Pa	D	8193	m/s
R_1	4.50	–	P_{CJ}	28.00E9	Pa
R_2	1.40	–			
ω	0.25	–			
E_0	9.00E9	Pa			

Linear EOS

To model the surrounding air in a domain a *MAT_NULL material model and a linear polynomial equation of state. *MAT_NULL serves a specialised purpose as a material model designated for regions or components where detailed material behaviour is not a primary focus. Essentially acting as a null material placeholder, *MAT_NULL introduces no specific material response, making it particularly useful in situations where the material's effects are either negligible or not important.

One of the distinctive features of the *MAT_NULL equation of state is its computational efficiency, avoiding complex material computations and thereby contributing to the overall speed of simulations. This makes it particularly advantageous in scenarios where the primary focus lies on other aspects of the simulation, such as structural interactions or the imposition of boundary conditions.

The linear polynomial equation of state in LS-DYNA serves as a mathematical model to describe the thermodynamic characteristics of materials experiencing dynamic loading conditions. This EOS is recognised for its simplicity and effectiveness in capturing essential material responses without introducing unnecessary intricacies. In the linear polynomial EOS, pressure is articulated as a linear function of volume, offering a straightforward portrayal of material behavior during dynamic processes.

*EOS_LINEAR_POLYNOMIAL:

$$p = C_0 + C_1\mu + C_2\mu^2 + C_3\mu^3 + (C_4 + C_5\mu + C_6\mu^2)E \tag{2.3}$$

where $C_0, C_1, C_2, C_3, C_4, C_5, C_6$ are constants, $\mu = \rho/\rho_0 - 1$, ρ and ρ_0 are the current and initial densities of air respectively, and E is the specific internal energy. The ideal gas equation of state can be simulated by setting $C_0 = C_1 = C_2 = C_3 = C_6 = 0$, and $C_4 = C_5 = \gamma - 1$, where $\gamma = 1.4$ is the ratio of specific heat for air:

$$p = (\gamma - 1)E\rho/\rho_0 \tag{2.4}$$

The initial atmospheric pressure is controlled by the specific internal energy (E), set to 253.4 kPa representing 101.4 kPa.

2.5.3 Numerical domains

The Multi-Material Eulerian/Arbitrary Lagrangian-Eulerian (MM/ALE) solver within LS-DYNA constitutes a computational methodology tailored for the dynamic simulation of materials undergoing extreme conditions, particularly in scenarios characterised by substantial deformations, intricate material interactions, and material failure. This solver adeptly manages problems involving multiple materials through the integration of Eulerian and Arbitrary Lagrangian-Eulerian (ALE) formulations. The Eulerian framework employs a fixed grid to describe materials, proving advantageous in scenarios involving fluid flow or extensive material deformations. At the same time, the ALE formulation allows the grid to move with the material, adapting to its deformation, before being 'advected' back to its original position.

Noteworthy within the MM/ALE solver is its proficiency in handling problems featuring multiple material interfaces and interactions. The solver employs Lagrangian elements to model the behaviour of individual materials, with these elements moving with the material to accurately represent deformation. Lagrangian elements are particularly well-suited for modelling the behaviour of solid structures. Eulerian elements, on the other hand, remain fixed in space, describing material behaviour within an Eulerian reference frame. This approach is particularly beneficial for simulating fluid flow or situations with substantial material deformation.

Operating within the explicit dynamics framework, LS-DYNA's MM/ALE solver excels in capturing transient phenomena, making it well-suited for problems involving short-duration, high-impact events. Applications of the MM/ALE solver span impact analysis, crash simulations, blast and explosion modelling, forming processes, and material failure studies. Its ability to handle multiple materials and intricate interactions positions it as a valuable tool for a broad spectrum of engineering simulations, (Hallquist 2006).

2.6 Summary

1. The disparity in blast loading characteristics between spherical and cylindrical charges is most pronounced in the near-field. As the driving mechanisms approach equilibrium, the pressure within the shock wave is anticipated to transition towards a spherical wave, with this convergence occurring at undetermined scaled distances in the far-field. This underscores the critical need for a comprehensive understanding of these dynamic processes to accurately predict blast effects.

2. The experimental datasets for cylindrical charges is marked by data covering various cylindrical ratios, yet there exists an under-explored territory, especially for long cylinders and specific L/D ratios. The limited spatial resolution in experimental datasets highlights a notable gap in research, particularly regarding near-field investigations. Bridging this gap is crucial for a holistic characterisation of blast waves in diverse charge configurations.

3. Numerical modelling has emerged as a predominant analytical tool, particularly in resilience studies for engineering applications involving non-spherical charges. However, the lack of validation for complex shapes due to a scarcity of high-quality experimental data poses a significant challenge as they remain un-validated. Establishing a robust experimental foundation becomes imperative to enhance the accuracy and reliability of numerical models, ensuring their applicability in complex scenarios.

4. Variations observed in experimental data are not inherent to the high-explosive material, and there is no fundamental difference in energy released. Instead, these variations arise from intricacies in experimental setup or data capture at discrete points within the chaotic blast wave. While the overall impulse remains constant, the introduction of non-spherical charges introduces complexity, resulting in an uneven distribution of loading spatially around the charge. This nuanced understanding is essential for comprehensively addressing the intricacies of blast dynamics in non-standard charge geometries.

Chapter 3

Experimental Methodology

All experimental work reported in this article was conducted at the The University of Sheffield Blast and Impact Laboratory in Buxton, UK.

3.1 Far-field testing

In the initial phase of the experimental test series, three arena tests were executed, following the methodology described by Rigby et al. (2015b). These experiments were specifically designed to investigate the detonation characteristics of 312.5 g hemispheres composed of Composition 4 (C4) bare high-explosive charges. The primary objectives encompassed a thorough characterisation of the behaviour and consistency of the C4 explosive, and additionally establishing its TNT equivalence. This deliberate emphasis on achieving consistency in the far-field, as corroborated by Farrimond et al. (2023), allowed attribution of any observed variations in loading during subsequent near-field testing to genuine physical features, rather than experimental error. Farrimond et al. (2024) concluded the quantification and characterisation of explosive properties is deterministic to the levels of error that they determine 'reasonable', through low-variance experimental data, of which minor features were identifying experimental setup and not inherent variability.

3.1.1 Testing instrumentation

To measure reflected pressure, a single Kulite HKM-375 7-bar pressure transducer was situated at ground level, positioned flush with the exterior of a robust 500 mm thick blockwork-covered reinforced concrete bunker wall, 3.1. The bunker wall at 4.5 m in height and extending over 10 m horizontally from the measurement location, was sufficiently large such that no clearing waves would reach the gauge during the loading duration, as documented by Tyas et al. (2011). Data recording was accomplished using Tie-Pie HAS Handyscope USB digital oscilloscopes, featuring a resolution of 14 bits and a sampling rate of 1.562 MHz. Oscilloscope triggering was facilitated through a low-voltage breakwire embedded with the detonator.

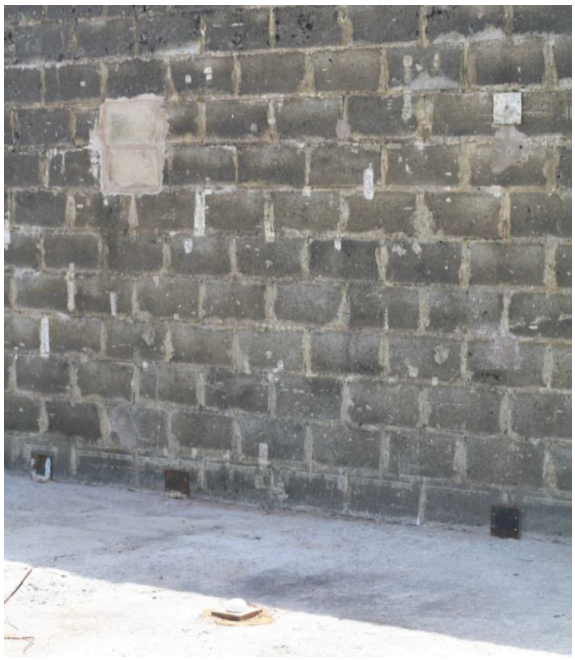


Figure 3.1: Arena test setup of hemispherical charges against the continuous blockwork wall, (Rigby et al. 2015b)

3.1.2 Shot plan

In order to ensure the repeatability and consistency of the C4 explosive intended for the investigation, a series of far-field arena tests was conducted. The primary objective of these tests was to ascertain the uniformity and expected characteristics of the C4 explosive, aligning with the parameters outlined in the existing literature, particularly as discussed by Farrimond et al. (2023). Through these far-field arena tests, we aimed to establish a reliable baseline for the behaviour of the C4 explosive, allowing for the identification and quantification of its properties including the TNT equivalence.

In total, three comprehensive tests were conducted, placing charges at stand-off distances of 2 m, 4 m, and 6 m. The explosives were centrally detonated using Nitronel MS 25 non-electronic shock-tube detonators, placed on a small steel anvil to prevent repetitive damage to the concrete ground slab.

Table 3.1: Summary of far-field tests for 312.5 g hemispheres of C4.

Test no.	Stand-off (m)	Scaled distance ($m/kg^{1/3}$)
1	2	2.947
2	4	5.894
3	6	8.842

Figure 3.2 presents the pressure and specific impulse histories for each of the three tests. The signals are plotted alongside the UFC 3-340-02 (US Department of Defence 2008) semi-empirical predictions, with the negative phase constructed using the relationships outlined by Rigby et al. (2014a), assuming a TNT equivalence of 1.20 (Bogosian et al. 2016). It is worth highlighting that the experimental timebases for the 2 m and 6 m tests underwent an adjustment of 0.1 ms for better alignment with the semi-empirical predictions, improving the clarity of the presentation.

Generally the results appear in excellent agreement, particularly in the initial phases leading up to the emergence of the secondary shockwave, a phenomenon commonly observed shortly after the initiation of the negative phase, as described by Rigby & Gitterman (2016). However, as time progresses, a discernible divergence between the observed outcomes and the predictive models becomes apparent, attributable to the omission of the secondary shock from the theoretical frameworks.

A summary of the experimental and semi-empirical blast parameters, specifically during the positive phase, is presented in Table 3.2. It is noteworthy that the determination of experimental peak pressure values were conducted by fitting an exponential decay model to the recorded traces, following the approach of Friedlander (1946). This methodological approach included the deliberate exclusion of the initial 25% of the positive phase, strategically mitigating the potential impacts of sensor ringing and any incidental electrical noise that may have inadvertently been captured during the recording process. Subsequent extrapolation back to the arrival time further refined the precision of the experimental results (Rigby et al. 2014).

The tabulated data reveal a remarkable consistency, wherein the predicted values, derived from the theoretical frameworks, consistently align with the corresponding experimental counterparts, consistently within a narrow margin of $\pm 5\%$ across the board. This tendency instils a confidence in the experimental methodology, underscoring the control and precision exercised throughout the study.

3.2 Near-field apparatus and data acquisition

Near-field tests were conducted using the *Characterisation of Blast Loading* (CoBL) apparatus (Clarke et al. 2015), as depicted in Figure 3.3. The CoBL apparatus, initially designed for measuring the output from buried explosives, has been repurposed to investigate

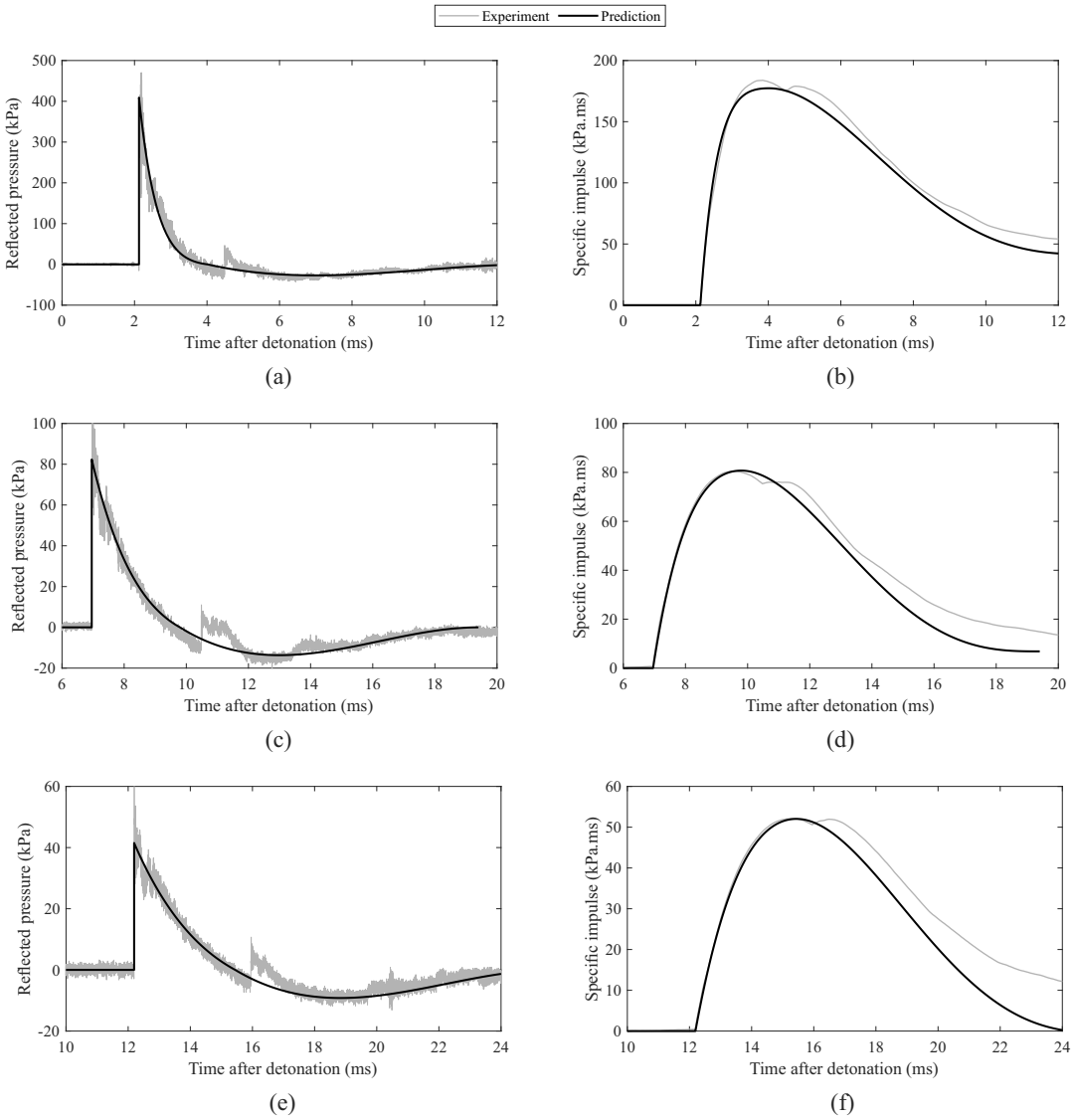


Figure 3.2: Compiled far-field pressure and impulse histories and semi-empirical predictions for 312.5 g hemispheres of C4: (a–b) 2 m stand-off; (c–d) 4-m stand-off; (e–f) 6 m stand-off.

and quantify near-field reflected blast pressures resulting from free-air explosions (Rigby et al. 2015a, 2019a, 2020, Tyas et al. 2016).

The apparatus, as utilised for this study, comprises an array of 17 Hopkinson (1914) pressure bars (HPBs), suspended vertically such that their faces lie flush with the surface of a 100 mm thick, 1400 mm diameter high-strength steel plate that acts as a nominally rigid reflecting surface, under which the explosives are detonated. The target plate is suspended from the soffits of a pair of steel fibre and bar reinforced concrete A-frames, located approximately 1 m apart, via a 50 mm thick steel 'acceptor' plate cast into the frame to enable the target plate to be affixed. Each A-frame comprises two 500 mm square columns with a 750 mm deep, 500 mm wide concrete beam spanning between the two columns.

The 3.25 m long, 10 mm diameter EN24(T) steel HPBs are formed into two perpendicular

Table 3.2: Summary of far-field test results and semi-empirical predictions for 312.5 g hemispheres of C4.

Test	Stand-off	Peak reflected pressure (kPa)			Peak specific impulse (kPa.ms)		
no.	(m)	Experiment	Prediction	% diff.	Experiment	Prediction	% diff.
1	2	418.0	409.1	2.1	183.8	177.3	3.6
2	4	86.5	82.4	4.8	80.5	80.7	0.3
3	6	42.6	41.5	2.6	52.1	52.0	0.2

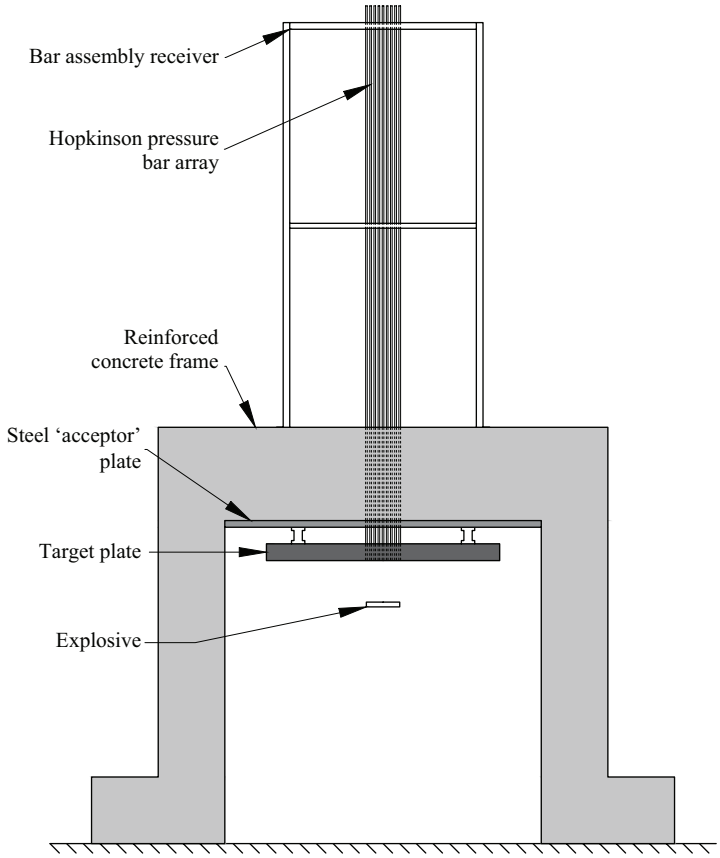


Figure 3.3: Schematic of the *Characterisation of Blast Loading* apparatus, general arrangement, after Clarke et al. (2015).

arrays of nine bars (with a common central bar: 17 bars in total) that form a cross, centred on the centre of the target plate, see Figure 3.4. The distal ends of the bars are threaded to permit fine adjustments to their height at the bar assembly receiver. The bars are located at 25 mm centres, thereby providing a 200 mm diameter instrumented region in the centre of the target plate. Spatial and temporal pressure distributions are recorded at each bar location using pairs of perimeter-mounted Kyowa KSP-2-120-E4 semi-conductor strain gauges in a Wheatstone bridge circuit to neglect any bending in the bars.

A Wheatstone bridge is a circuit used for the measurement of dynamic electrical resistance. Typically consisting of four resistive arms arranged in a diamond configuration, offering a mechanism to accurately measure unknown electrical resistances. The principle behind

the Wheatstone bridge is the attainment of electrical balance through the adjustment of variable resistances. When the bridge is in balance, the voltage difference between its junctions reaches zero, indicating equivalence in resistances.

Schematically the bridge exhibits a symmetrical, diamond-shaped configuration consisting of four resistive arms. Each arm is contains a resistor, two fixed resistors, one variable and the resistor (in this case the stain gauge), and the arrangement forms a closed loop with a voltage source applied across two opposite junctions. Perpendicular to the power source on the bridge, voltage is measured and tiny changes in resistance corresponding to strain can be recorded.

The strain gauges are located 250 mm from the loaded face of each bar and record axial stress history up to ∼1.2 ms from arrival of the stress pulse at the gauge location (Clarke et al. 2015), subjected to a theoretical bandwidth of ∼250 kHz (Tyas & Watson 2001).

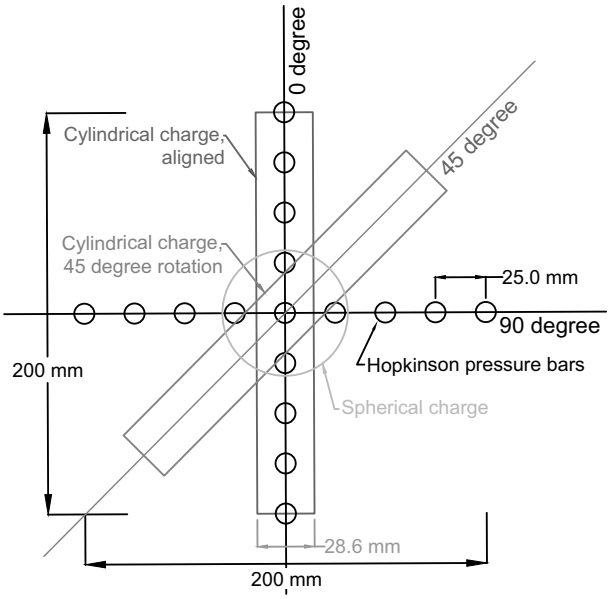


Figure 3.4: Plan view of the instrumented area indicating HPB layout and charge orientation used in the spherical, aligned cylindrical and 45° cylindrical tests [to scale].

Data was recorded using Tie-Pie HAS Handyscope USB digital oscilloscopes at 14-bit resolution with a sampling rate of 3.125 MHz. The recording process was automatically initiated through the application of TiePie's 'out window' signal trigger, which was synchronised with a low voltage (5V) break-wire wrapped around the detonator. The 'out window' trigger, activated by a discernible voltage drop beyond the typical electrical noise associated with the break-wire, precisely marked the moment of charge detonation, coinciding with the interruption of the circuit. This method ensured an accurate and synchronised initiation of the recording process, aligning with the critical event of charge detonation. A 10% 'pre-trigger' was also recorded to ensure the entire event was captured.

Recorded signals are processed to convert to stress by zeroing against the pre-trigger voltage and applying a known calibration factor. Occasionally strain gauges de-laminate from the

surface of the bars creating erroneous or nil traces, which are identified and removed from the dataset.

Time of detonation was established by scrutinising the break-wire trace for the first sign of voltage change prior to triggering, which in addition to the time taken for the stress pulse to reach the gauge location from the face of the HPB (50 μs), was subtracted from the timebase of the pressure signals in post-processing. No additional post-processing, e.g. smoothing, frequency filters and dispersion correction, is applied to the signals.

Design of CoBL

The design considerations driving the choice of elements of the CoBL apparatus were made for the initial use case as described in Rigby et al. (2014a), Clarke et al. (2015). Loading in the near-field and from buried charges required a robustness in the blast receiving elements, as the impact of projectiles (e.g. soils) abrading the plate and bars would limit the life expectancy of these components.

The use of HPB for pressure analysis has been detailed in 2.2.9, their use in a configuration to capture the spatial loading was novel. Economic factors, unknowns in the expected loading and a time-pressure component restricted the design of CoBL. The suitability of the bar diameter and length for near-field free-air testing is not optimised but offered the most suitable measurement method for the loading characterisation. The 'relatively' large diameter bar and set-back of the gauges (250 mm) contributes to the dispersion of the signal, attenuating the instantaneous shock front expected from blast waves. Excluding the very high-frequency signals, that the strain gauges are unable to pick up, the dispersed signal maintains the total loading and specific impulse calculated is considered to be truer representation with the understanding that the gradient is slightly influenced by the shock pressure arrival profile.

Given the limitations of the measurement apparatus the direct loading parameters measured should be taken with the consideration of experimental accuracy and precision. The variability of experimental data capture in the CoBL method was analysed and validated in Rigby et al. (2018b). However the comparison of CoBL data for varying, or repeated, charge threats can be highly effective at analysing blast profiles and their variance.

Years of testing and experience on the CoBL apparatus fed into the design of the next generation of near-field blast characterisation: MaCE, (Barr et al. 2023*b*).

3.3 Near-field test arrangement

Thirty-two near-field tests were conducted on the CoBL apparatus of PE4 and C4 explosives, see Table 3.3.

Twenty-nine near-field tests of C4 were performed in total: two tests using 200 g spheres (31.3 mm radius) and twenty-seven tests using 200 g cylinders (200.0 mm long, 14.3 mm

radius, $L/D = 7$); see Table 3.4. Of the twenty-nine tests, six (11, 13, 18, 22, 25, 29) failed to produce data due to either failed detonation or equipment malfunctions, with premature tripping of the recording sequence or subsequent loss of the data.

Of the twenty-one successful cylindrical charge tests;

1. Five were conducted with the cylinders parallel with the reflecting plate and the longitudinal axis aligned with one set of the HPBs, Figure 3.5-f). Three of which were centre detonated and two were detonated at one end.

2. Two were conducted with the cylinders parallel with the reflecting plate but positioned at a forty-five degree approach to the instrument array, detonated centrally.

3. Five were conducted with the cylinders perpendicular to the reflecting plate, with the longitudinal axis passing through centre of the central bar of the array, Figure 3.5-b). Three were detonated centrally and two were detonated at the distal end, furthest from the instrumentation.

4. Nine were conducted aligned horizontally to the instrumentation array, but angled between the horizontal and vertical at angles of 22.5, 45 and 67.5 degrees, Figure 3.5-c)–e). Three at each incline and all detonated centrally.

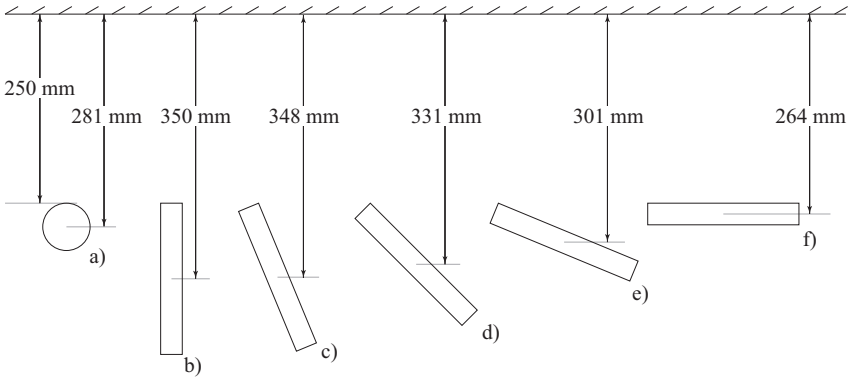


Figure 3.5: Schematic of the charge orientations relative to the target plate, illustrating the standoff distances for each configuration. A consistent 'clear' standoff of 250 mm is maintained across all charges, corresponding to a scaled distance of 0.427 m/kg$^{1/3}$. The 'to-centre' standoff distances and corresponding scaled distances vary with charge geometry and orientation as follows: spherical charges (a), 281 mm, 0.481 m/kg$^{1/3}$; axial cylindrical charges (b), 350 mm, 0.598 m/kg$^{1/3}$; inclined cylindrical charges at 22.5°, 45°, and 67.5° (c–e), 348 mm, 331 mm, and 301 mm respectively, with scaled distances of 0.595, 0.566, and 0.516 m/kg$^{1/3}$ respectively; and radial cylindrical charges (f), 264 mm, 0.452 m/kg$^{1/3}$.

The charges were set at different distances to the reflecting plate relative to the centre of mass. Constant 'clear stand-off' of 250 mm from the reflecting plate was maintained measured to the surface of the charge in each set-up. The stand-off distances to centre are given in Table 3.4 and shown in Figure 3.5. Typically stand-off is only measure to the centre of charges but considering the charge geometries (on account of the different spherical and cylindrical charge radii and cylindrical length) vary significantly in proportion to the stand-off distance it was considered prudent to make a distinction. The scaled distance

(to charge centre) are 0.452, 0.481, 0.516, 0.566, 0.595 and 0.598 m/kg$^{1/3}$ respectively for the 'to centre' standoffs of 0.264, 0.281, 0.301, 0.331, 0.348 and 0.350 m compared to the 0.427 m/kg$^{1/3}$ scaled distance calculated from the clear stand-off.

Table 3.3: Summary of experimental tests conducted

Test Number	Explosive	Charge Shape	Vertical Angle	Horizontal Angle	Detonation Location
1	PE4	Power supply failure			
2	PE4	Spherical			
3	PE4	Test Failure			
4	C4	Sphere	0°	0°	Centre
5	C4	Sphere	0°	0°	Centre
6	C4	Cylindrical	0°	0°	Centre
7	C4	Cylindrical	0°	0°	Centre
8	C4	Cylindrical	0°	45°	Centre
9	C4	Cylindrical	0°	45°	Centre
10	C4	Cylindrical	0°	0°	End
11	C4	Data saving failure			
12	C4	Cylindrical	0°	0°	End
13	C4	Data capture failure			
14	C4	Cylindrical	90°	0°	End
15	C4	Cylindrical	90°	0°	End
16	C4	Cylindrical	90°	0°	Centre
17	C4	Cylindrical	90°	0°	Centre
18	C4	Data capture failure			
19	C4	Cylindrical	0°	0°	Centre
20	C4	Cylindrical	22.5°	0°	Centre
21	C4	Cylindrical	22.5°	0°	Centre
22	C4	Charge not detonated			
23	C4	Cylindrical	22.5°	0°	Centre
24	C4	Cylindrical	45°	0°	Centre
25	C4	Data capture failure			
26	C4	Cylindrical	45°	0°	Centre
27	C4	Cylindrical	45°	0°	Centre
28	C4	Cylindrical	67.5°	0°	Centre
29	C4	Charge not detonated			
30	C4	Cylindrical	67.5°	0°	Centre
31	C4	Cylindrical	67.5°	0°	Centre
32	C4	Cylindrical	90°	0°	Centre

Table 3.4: Summary of near-field test arrangements used in this study.

Test nos.	Shape	Orientation		Detonation Location	Stand-off (m)	
		Horizontal	Vertical		Clear	To-centre
4–5	Sphere	0°	0°	Centre	0.250	0.281
6, 7, 19	Cylinder	0°	0°	Centre	0.250	0.264
8–9	Cylinder	45°	0°	Centre	0.250	0.264
20–21, 23	Cylinder	0°	22.5°	Centre	0.250	0.301
24, 26–27	Cylinder	0°	45°	Centre	0.250	0.331
28, 30–31	Cylinder	0°	67.5°	Centre	0.250	0.348
16–17, 32	Cylinder	0°	90°	Centre	0.250	0.350
10, 12	Cylinder	0°	0°	End	0.250	0.264
14–15	Cylinder	0°	90°	End	0.250	0.350

The instrumented, Hopkinson pressure bar, array occupies a fixed position relative to the target plate throughout the experimental programme, whilst the charge orientation is varied systematically between tests. Figure 3.6 illustrates the geometric relationship between the instrumented array and the cylindrical charge, with reference to the charge, for each of the tested configurations.

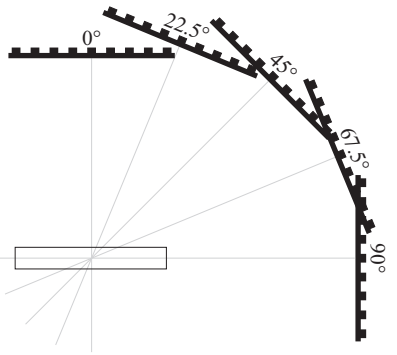


Figure 3.6: Schematic illustration of the instrumented Hopkinson pressure bar array relative to the cylindrical charge for each tested orientation. The parallel array bars are represented by the comb-like shapes, with their angular relationship to the charge axis indicated for each of the inclined configurations. The perpendicular array lies out of the plane of the illustration.

The selection of charge orientations tested in this experimental programme was informed by the expected interaction between the instrumented array and the distinct regions of the blast wave produced by a cylindrical charge. Figure 3.7, produced by merging the blast wave front schematic of Figure 2.5 with the array orientation schematic of Figure 3.6, illustrates the anticipated blast wave geometry overlaid on the array orientations. At 0°, the instrumented array lies directly within the primary side wave region, whilst at 90° it is positioned within the axial end wave region. By sampling at regular angular increments across this range, the experimental programme captures the progressive transition in loading character between these two extremes, including the bridging wave zone at intermediate inclination angles of 22.5°, 45°, and 67.5°, where the loading is governed by the complex interaction of the side and end waves rather than either in isolation.

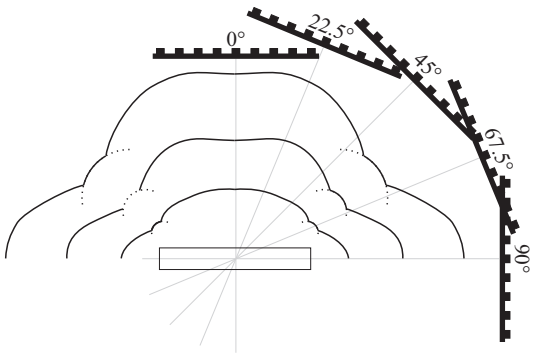


Figure 3.7: Schematic illustration of the instrumented Hopkinson pressure bar array orientations relative to the cylindrical charge, overlaid with the anticipated blast wave geometry. Produced by merging Figures 2.5 and 3.6. The characteristic lobed blast wave structure illustrates the primary side wave and axial end wave regions sampled by the 0° and 90° array orientations respectively, with the intermediate inclination angles of 22.5°, 45°, and 67.5° positioned within the bridging wave zone between these two primary regions.

The C4 bare charges were formed using bespoke 3D printed moulds, ensuring precision and consistency in charge geometry across all tests. The formed charges were suspended on an ultra-light woven glass fibre fabric (25 g/m^2), pulled taut within a steel ring fitted with adjustable legs to facilitate precise levelling and alignment beneath the target plate, as illustrated in Figure 3.8. Perpendicular self-levelling line lasers were employed to ensure accurate alignment of the cylindrical charges relative to the instrumented array.

The primary objective of the experimental configuration was to record the reflected blast loading from charges detonated in a free-air environment, minimising early interactions of the blast wave with the supporting structure. The steel ring and leg assembly were positioned to maintain an adequate clearance from the charge, reducing the potential for disturbance to the primary shock wave. The ultra-light glass fibre fabric, given its minimal areal mass, the fabric was observed to vaporise within the fireball generated by the detonation during previous test programmes, ensuring that it did not contribute to reflection or interaction with the blast wave and had a negligible influence on the measured blast parameters.

Where the fabric alone was insufficient to support the charge, a minimal cable support system was employed, with cables attached to the concrete frame, the floor, or the target plate outside of the instrumented area as required, from which the charge was braced. The cable systems were designed to be low mass and to present minimal obstruction to the blast wave path to the target plate, and, as with the glass fibre fabric, the cables are incinerated within the fireball generated by the detonation and are therefore expected to contribute negligibly to the reflected blast loading.

Where the geometry of the charge permitted, Nitronel MS 25 non-electronic shock-tube detonators were positioned in-line with the charge centre from below, providing additional support to the charge prior to testing and reducing fabric sagging. The detonators were deliberately not inserted directly into the explosive material during the charge-forming or

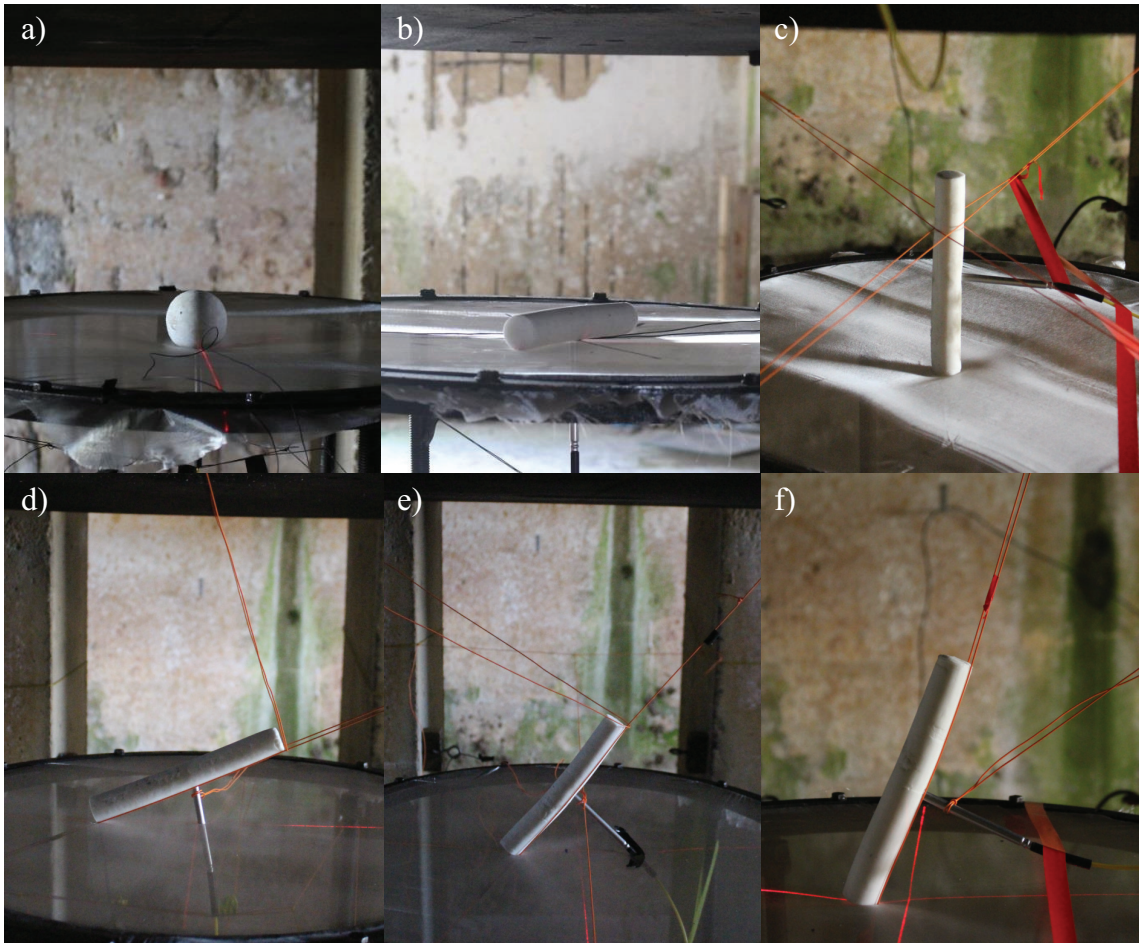


Figure 3.8: Photographs of the experimental setup illustrating the charge support and alignment arrangements for each tested configuration: a) spherical charge; b) radial cylindrical charge; c) axial cylindrical charge; d)–f) inclined cylindrical charges at 22.5°, 45°, and 67.5° respectively.

handling process. This was a considered decision to preserve the structural integrity of the charges, particularly for the cylindrical geometry where the relatively small cross-sectional dimensions of the charge relative to the detonator introduced a risk of fracturing the charge, potentially compromising the stability of the setup and resulting in a partial or failed detonation. This approach improved both the reliability of the experimental testing and the precision with which the charges could be positioned. The potential for detonator placement between the charge and target to introduce unwanted electrical noise into the experimental setup has been noted in previous experimental studies (Fay et al. 2013), and was a further consideration in the adopted arrangement.

During periods of warmer weather, the formed C4 charges were deliberately cooled prior to testing. The reduction in temperature stiffened the explosive material, improving the structural stability of the charges and, in some cases, rendering them self-supporting without the need for additional measures. This precaution ensured consistency in charge behaviour across varying environmental conditions and contributed to the repeatability of the experimental outcomes.

Chapter 4

Experimental Results

4.1 Spherical tests

The pressure and specific impulse histories obtained from the spherical charge tests are presented in Figure 4.1. To facilitate a meaningful qualitative comparison across these tests, the traces within the range of 25 to 100 mm are displayed as the test-average of the pressure and impulse histories recorded by the four bars at each radial ordinate. The pressure trace from the single central bar in each test is represented as the '0 mm' bar. This approach of averaging the pressure signals at each non-central HPB location serves a dual purpose: it enhances the visibility of general loading features that might be indiscernible when examining the trace from a single bar, and it effectively minimizes the impact of signal noise and electrical spikes without necessitating the application of a smoothing algorithm. This method preserves the fundamental physical characteristics of the applied loading.

The averaging process was executed by aligning the central bar to ensure that the time at which each pressure signal had risen to $1/3^{\text{rd}}$ of its peak value coincided across the tests under consideration. All other pressure traces were uniformly shifted by the same time to preserve variations in arrival time concerning the distance from the plate centre. It is noteworthy that, in no instance, was it required to adjust each signal by more than 6.73 μs, attesting to the precision and consistency achieved in the experimental setup.

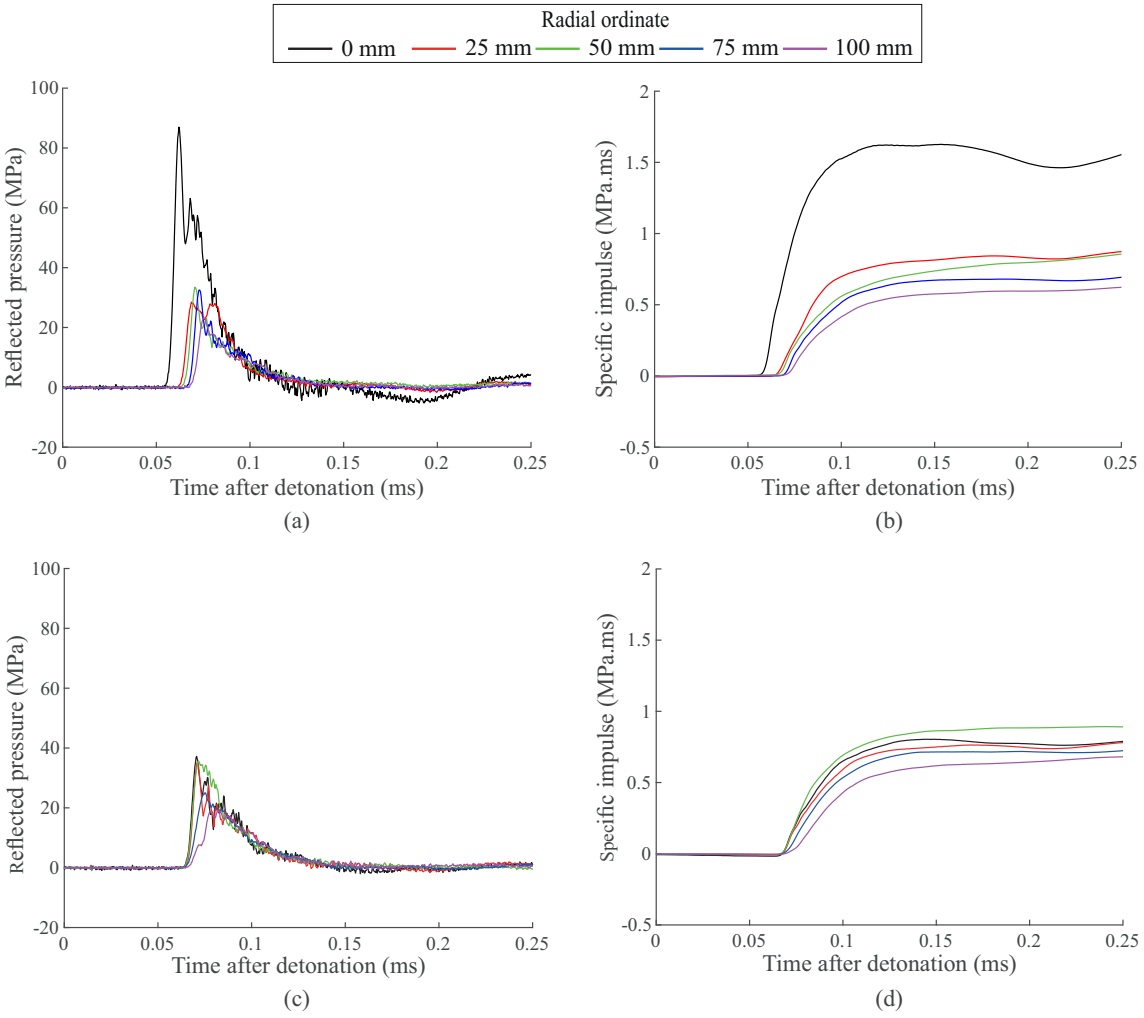


Figure 4.1: Test-averaged reflected pressure (a, c) and specific impulse (b, d) histories from detonation of 200 g spheres of C4 at 250 mm clear stand-off: (a–b) Test 4; (c–d) Test 5.

The traces of reflected pressure exhibit characteristics consistent with a typical Friedlander-type decay, displaying a discernible ascent to peak pressure followed by a relatively uniform decay to ambient pressure across all radial ordinates. At a specific time after the wave's arrival at the furthest measurement location, the loading appears to be spatially near-uniform. Noteworthy are the features associated with Pochhammer-Chree dispersion (Rigby et al. 2018a), indicating the degradation of transient pressure features with durations less than 5 μs and the emergence of spurious oscillations in the pressure traces. These phenomena are a consequence of the wave propagating through a finite-diameter bar over the distance to the location of the strain gauge. However, it is observed that the general form of the pressure pulse and the temporal evolution of specific impulse remain largely unaffected by dispersion.

This suggests that while the traces exhibit some dispersion-related effects, the overall shape of the pressure pulse and the specific impulse's temporal progression remain unaffected and does not affect the recording of peak specific impulse. Therefore the recorded specific impulse distributions are highly indicative of the true specific impulse acting on the target

face and the HPB instrumentation is adequate to act as a pressure transducer.

While the recorded pressure histories at 25–100 mm exhibit notable consistency, localised variability in blast loading is evident at the central bar. It has been proposed that the transition between "*relatively consistent loading*" in the extreme near-field and "*large variations in loading*" in the late near-field occurs around $Z \approx 0.5$ m/kg$^{1/3}$ (Tyas 2019). The results depicted in Figure 4.1 ($Z = 0.481$ m/kg$^{1/3}$) provide support for this claim. It appears that a turbulent fireball plume, likely induced by the emergence and growth of Rayleigh-Taylor (Lord Rayleigh 1882, Taylor 1950) and Richtmyer-Meshkov (Richtmyer 1960, Meshkov 1969) surface instabilities (Rigby et al. 2020), has affected the central bar in Test 4 but not in Test 5. While the central bar loading in Test 5 seems consistent with other radial ordinates, the central bar loading in Test 4 exhibits an earlier arrival time, a higher magnitude peak pressure, and generally higher pressure-time history thereafter.

Figure 4.2 illustrates the compiled results of peak reflected pressure (a) and peak specific impulse (b) in relation to the radial ordinate for the spherical charge tests, (Test 4 and Test 5). To note, the traces here refer to individual Hopkinson pressure bars (HPBs) rather than the test-averaged values discussed in previous analyses. Examining the radial ordinates within the range of 25 to 100 mm, both peak pressures and specific impulses exhibit a relatively narrow distribution around the mean values (depicted by the solid line). The results consistently fall within a range of approximately ±10 MPa for peak pressure and ±0.25 MPa.ms for peak specific impulse at each radial ordinate.

However, a distinctive influence emerges in Test 4 due to the impingement of the fireball plume on the central bar (0 mm), Figure 4.1. To ensure a fair baseline for comparing spherical loading distributions with subsequent tests involving cylindrical charges, the central bar data from Test 4 has been excluded when calculating the average distributions, as denoted by the dashed line in Figure 4.2. This exclusion is warranted given the discernible impact of the fireball plume on the central bar in Test 4. At this scaled distance, the peak loading is relatively uniform across the central 200 mm diameter of the target plate.

4.2 Cylindrical tests – Radial (0°, 0°)

The experiments involving horizontal cylindrical charges, three of which executed aligned the longitudinal axis of the charge directly beneath the centerline of one of the Hopkinson pressure bar (HPB) arrays, as illustrated in Figure 3.4. This arrangement resulted in two subsets of HPB data for each of these tests, distinguishing between arrays aligned 'parallel' and 'perpendicular' to the longitudinal axis of the charge, denoted by the 0° and 90° arrays, respectively (see Figure 3.4).

In the two remaining tests, where the cylinders were oriented at a 45° angle to the HPB arrays, each measurement location exhibited symmetry about the longitudinal axis of the charge. Consequently, this configuration produced a singular dataset from which mean values could be derived at each radial ordinate, utilising all four HPB measurements (except

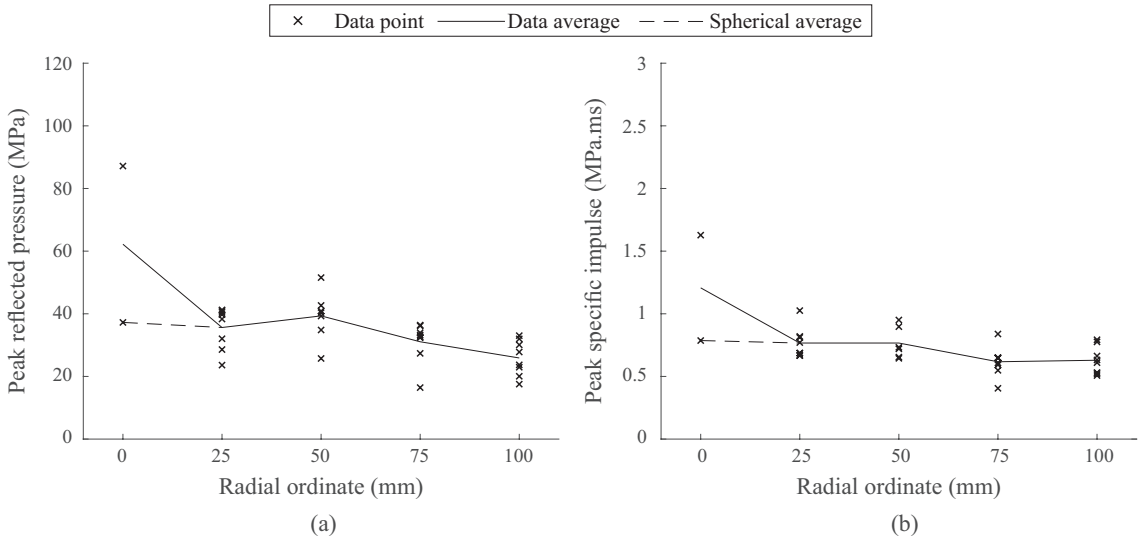


Figure 4.2: Compiled peak reflected pressure (a) and peak specific impulse (b) versus radial ordinate from detonation of 200 g spheres of C4 at 250 mm clear stand-off. The dashed line indicated the representative spherical data disregarding the anomalous data point

the central bar), similarly to the methodology applied to the spherical data. This collective approach allowed for the separate evaluation of blast loading distributions along arrays oriented at 0°, 45°, and 90°.

Figure 4.9 presents the series-averaged pressure and impulse histories from the aligned tests (Tests 6–7, 19) and the 45° tests (Test 8 and Test 9). The pressure traces depicted here represent the average at each HPB location for all tests within the series. This averaging technique enhances the clarity of the presentation and facilitates the observation of the general behaviour and temporal characteristics of the loading.

The data from Tests 6–7, 19 are further identified as parallel and perpendicular components, indicated by the small illustration in each sub-figure denoting the orientation to the HPB array from which the data are extracted.

4.2.1 Test results

T006

The reflected pressure histories recorded during Test T006 are presented in Figure 4.3. The figure is organised as a matrix of subplots arranged in four rows and two columns, where each row corresponds to a discrete radial ordinate, with increasing distance from the centre progressing from top to bottom, labelled a)–d) to denote the respective radial groupings (25, 50, 75, 100 mm). The left column presents results from bars oriented perpendicular to the symmetrical charge axis, whilst the right column presents the corresponding bars aligned parallel to the axis. In all subplots, the trace from the central bar is included alongside each measurement to provide a consistent spatial reference for comparison.

The recorded waveforms exhibit a complex structure characterised by multiple peaks and

little to no negative phase, deviating from the classical Friedlander form. For bars aligned parallel to the charge axis, an attenuation of peak reflected pressure is observed with increasing radial distance, consistent with trends identified in the spherical charge tests presented in Section 4.1, the traces also demonstrate strong repeatability across nominally identical positions within the expectations of variability in the near-field. Comparison between orientations reveals that the parallel-aligned bars at 75 mm exhibit higher peak reflected pressures than their perpendicular counterparts, recording the highest peak reflected pressure amongst all measured positions.

The specific impulse histories derived from the reflected pressure traces recorded during Test T006 are presented in Figure 4.4. Specific impulse is obtained through the temporal integration of the reflected overpressure and is presented using the same subplot arrangement as Figure 4.3, with radial position increasing from top to bottom and perpendicular and parallel orientations occupying the left and right columns respectively.

The impulse histories broadly reflect the trends observed in the pressure traces. For bars oriented perpendicular to the charge axis, the specific impulse decreases with increasing radial distance, with the exception of the 100 mm position, which deviates from this trend attributed to the later peaks in pressure. The perpendicular results exhibit impulse profiles that closely resemble that of the central reference bar, suggesting a broadly consistent loading mechanism across these positions. A notable feature of the perpendicular results is the strong convergence of the impulse traces towards the end of the period of interest (0.25 ms), where the specific impulse at all radial distances is remarkably similar. For bars aligned parallel to the charge axis, greater variation is observed between nominally identical sampling locations, and the impulse profiles exhibit markedly different temporal characteristics compared to both the central bar and the perpendicular measurements. At radial distances of 25 mm and 100 mm, the parallel-aligned bars record lower specific impulse than their perpendicular counterparts, whilst the reverse is true at 50 mm and 75 mm.

The initial rise times of the impulse histories are broadly consistent across all measurement positions and orientations, with the exception of the 100 mm parallel bar, which exhibits a markedly different early-time response. This behaviour is attributed to the geometric configuration of the charge, as the 100 mm parallel bar corresponds to a position directly above the end of the cylindrical charge, where the localised blast environment differs where the primary radial (side) wave transitions into bridging waves as predicted by Wisotski & Snyer (1965).

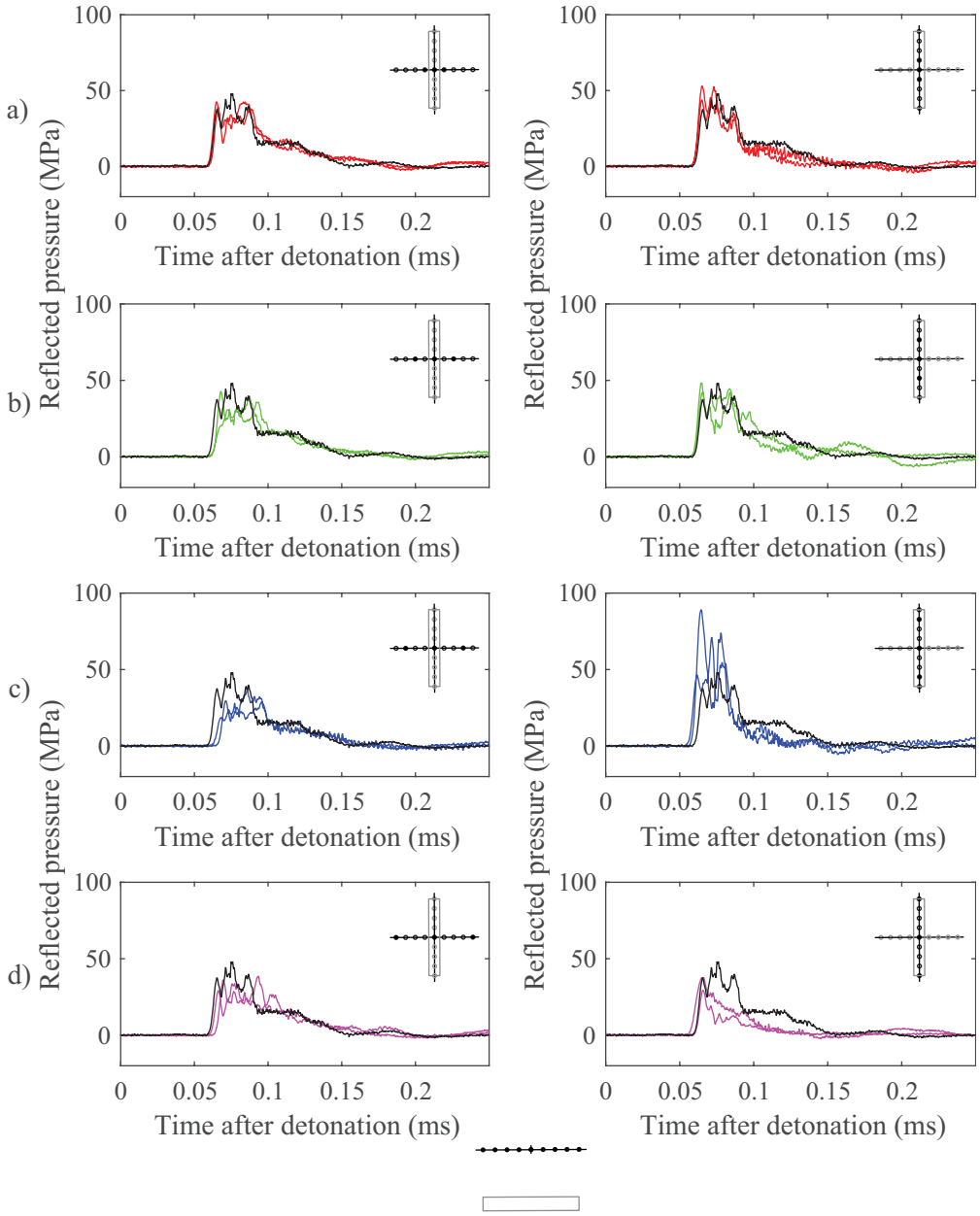


Figure 4.3: Reflected pressure time histories for test T006 (radial cylindrical charge, 0°, 0° orientation, centrally detonated). Results are shown for radial offsets of (a) 25 mm (red), (b) 50 mm (green), (c) 75 mm (blue), and (d) 100 mm (magenta), compared against the central reference measurement (0 mm, black). For each radial position, measurements are presented for perpendicular sensor arrays (left column) and aligned sensor arrays (right column). Insets indicate the relative orientation of the charge and sensor configuration.

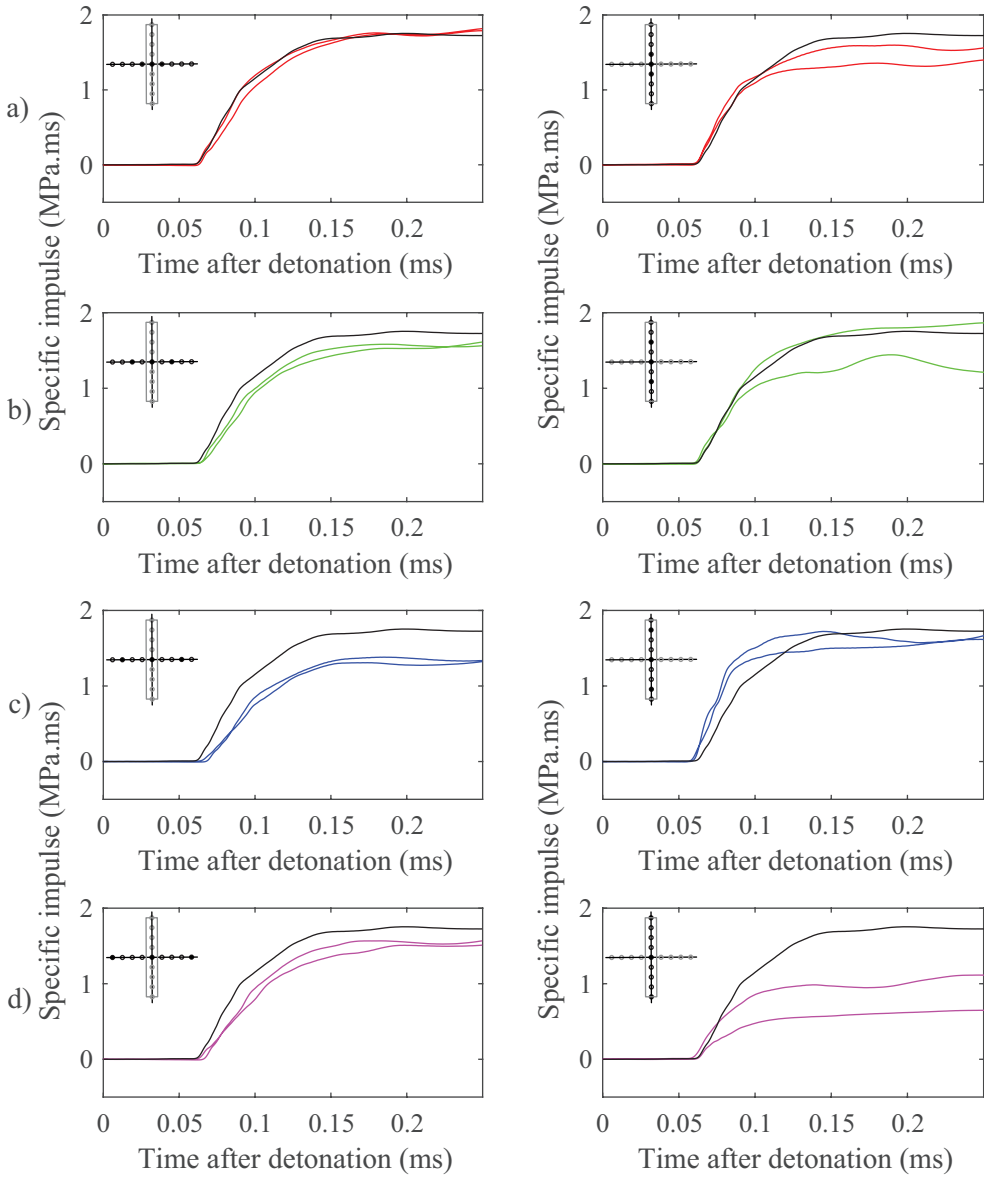


Figure 4.4: Specific impulse time histories for test T006 (radial cylindrical charge, $0°, 0°$ orientation, centrally detonated). Results are shown for radial offsets of a) 25 mm (red), b) 50 mm (green), c) 75 mm (blue), and d) 100 mm (magenta), compared against the central reference measurement (0 mm, black). For each radial position, measurements are presented for perpendicular sensor arrays (left column) and aligned sensor arrays (right column). Insets indicate the relative orientation of the charge and sensor configuration.

T007

The reflected pressure histories recorded during Test T007 are presented in Figure 4.5, using the same array configuration and subplot arrangement as described for Test T006 in Section 4.2.1. The central bar trace is included in all subplots as a consistent spatial reference.

The perpendicular results exhibit close agreement between the two bars at each radial position, demonstrating good repeatability, with pressure profiles that closely resemble that of the central bar across all measured locations. A slight reduction in peak reflected pressure is observed with increasing radial distance, consistent with the trends identified in Test T006.

The parallel results present a more varied response. At 25 mm, both bars exhibit profiles broadly similar to those of the perpendicular measurements, with good inter-bar agreement. At 50 mm and 75 mm, however, significantly elevated peak reflected pressures are recorded relative to the central bar. The highest peak pressures at the 75 mm ordinates are accompanied by a more classical decay response approaching that of a Friedlander form. At 100 mm, the two parallel bars exhibit opposing behaviours; one records a notably elevated peak pressure consistent with the trend observed at 50 mm and 75 mm, whilst the other falls below the central bar measurement. This could suggest a slight misalignment of the charge and one bar is experiencing the lower magnitude bridging waves and the other is subjected to the radial primary wave.

The specific impulse histories for Test T007 are presented in Figure 4.6. The perpendicular impulse profiles exhibit close correspondence with that of the central bar across all radial positions. Particularly strong consistency is observed at 50 mm and 75 mm, whilst the results at 25 mm and 100 mm show good alignment within a margin of error.

The parallel impulse histories exhibit considerably greater variation. At 25 mm, the impulse profiles remain broadly similar to the perpendicular measurements, consistent with the pressure observations at this position. At 50 mm and 75 mm, where elevated peak pressures with a Friedlander-like decay were recorded, the impulse histories exhibit markedly faster rise times; however, the classical pressure decay at these positions results in the impulse flattening off rapidly. At 100 mm, the divergence in pressure magnitude and profile between the two parallel bars is reflected in considerable variation in both the impulse profiles and peak specific impulse, consistent with a possible geometric influence of the charge discussed previously.

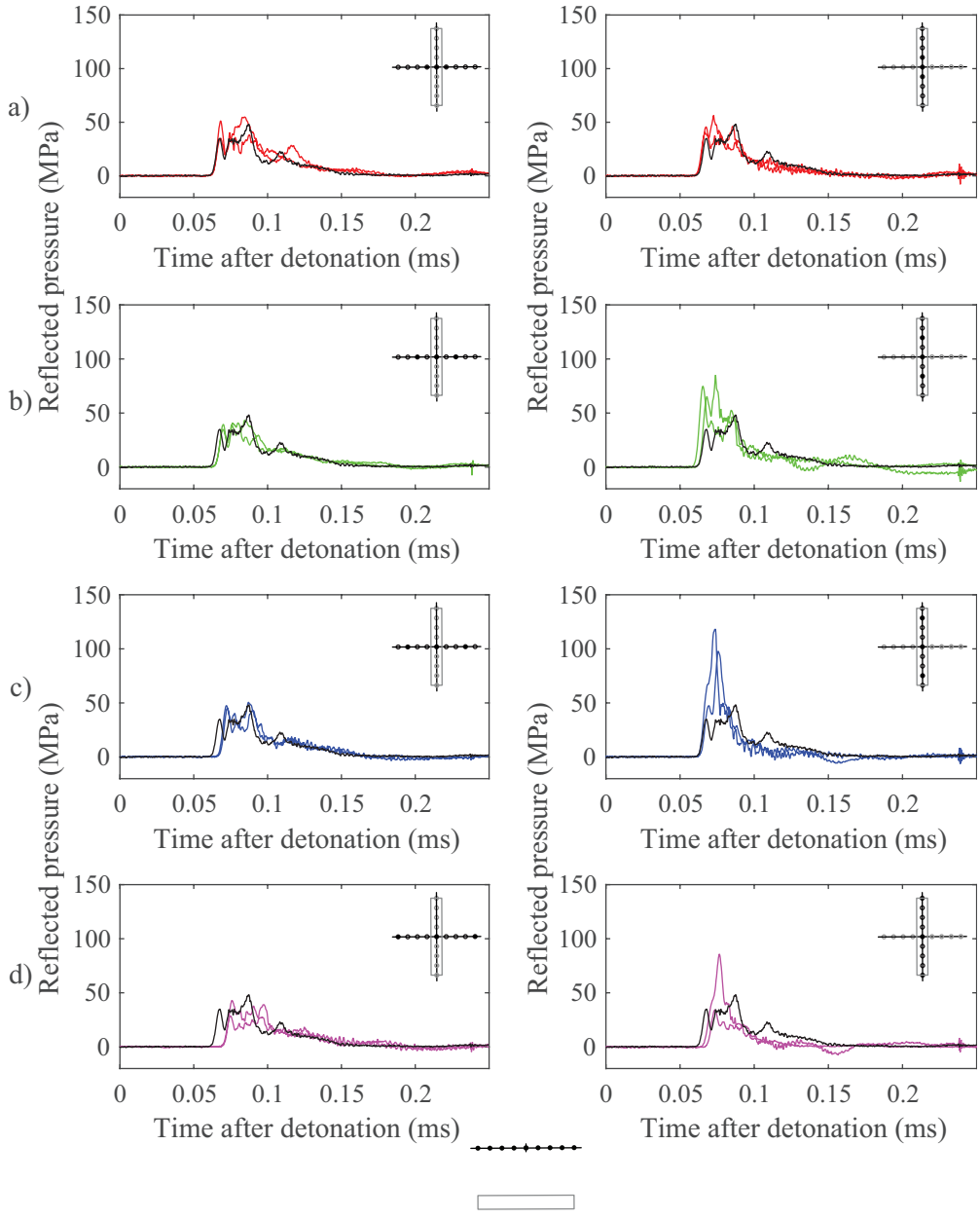


Figure 4.5: Reflected pressure time histories for test T007 (radial cylindrical charge, 0°, 0° orientation, centrally detonated). Results are shown for radial offsets of (a) 25 mm (red), (b) 50 mm (green), (c) 75 mm (blue), and (d) 100 mm (magenta), compared against the central reference measurement (0 mm, black). For each radial position, measurements are presented for perpendicular sensor arrays (left column) and aligned sensor arrays (right column). Insets indicate the relative orientation of the charge and sensor configuration.

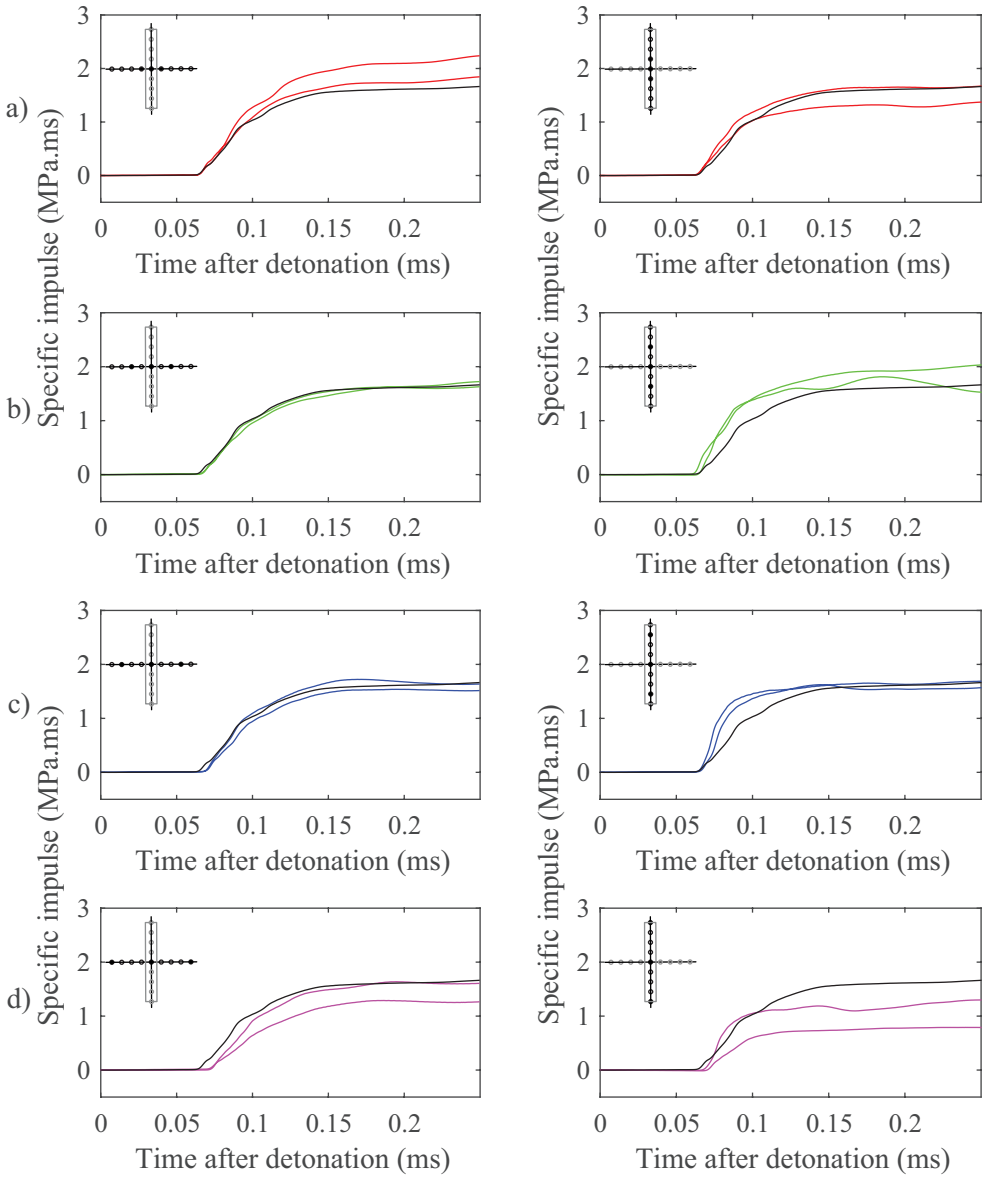


Figure 4.6: Specific impulse time histories for test T007 (radial cylindrical charge, 0°, 0° orientation, centrally detonated). Results are shown for radial offsets of a) 25 mm (red), b) 50 mm (green), c) 75 mm (blue), and d) 100 mm (magenta), compared against the central reference measurement (0 mm, black). For each radial position, measurements are presented for perpendicular sensor arrays (left column) and aligned sensor arrays (right column). Insets indicate the relative orientation of the charge and sensor configuration.

T019

The reflected pressure histories recorded during Test T019 are presented in Figure 4.7. The parallel results show broadly similar trends to those observed in Tests T006 and T007, although a comparatively lower central bar pressure results in the radial measurements appearing elevated relative to the reference. Good repeatability is observed between the two bars at each parallel position. It is noted that one of the 50 mm perpendicular bars did not record a pressure trace during this test; the failed gauge is represented in Figure 4.7 as a zero-value flat line, and the remaining trace at this position is considered representative.

The parallel results exhibit broadly consistent trends with the previous tests, with elevated peak pressures observed at 25 mm and 50 mm, differing slightly from Tests T006 and T007 where the peaks were more prominent at 50 mm and 75 mm. Poor inter-bar agreement is observed at these elevated positions, with only one of the two bars recording the higher peak pressure. The remaining perpendicular positions show good repeatability between paired traces. The 100 mm perpendicular bars again record a reduced response, consistent with the geometric influence of the charge end discussed previously.

The specific impulse histories for Test T019 are presented in Figure 4.8. The perpendicular impulse histories display greater variation in peak specific impulse than observed in the equivalent results from Tests T006 and T007, with the difference being most pronounced at the 75 mm positions. At 100 mm, the two perpendicular traces show good initial agreement before diverging from approximately 0.1 ms onwards, reflecting the influence of a prolonged positive phase on specific impulse.

The parallel impulse histories demonstrate more complex behaviour, particularly at 25 mm. One of the 25 mm parallel bars records an elevated peak pressure with a rapid Friedlander-like decay, producing a fast-rising impulse that flattens off quickly. The other bar at this position records a lower peak pressure with a longer positive phase duration, resulting in a more gradually accumulating impulse that overtakes the first at approximately 0.16 ms, thereafter remaining broadly similar. A similar disparity in rise rate is observed at 50 mm, where the bar with the higher peak pressure produces a steeper initial impulse gradient; however, unlike at 25 mm, the two traces maintain a consistent separation in magnitude throughout the period of interest. A more uniform response is observed at 75 mm and 100 mm, where the parallel impulse histories show closer agreement between paired traces.

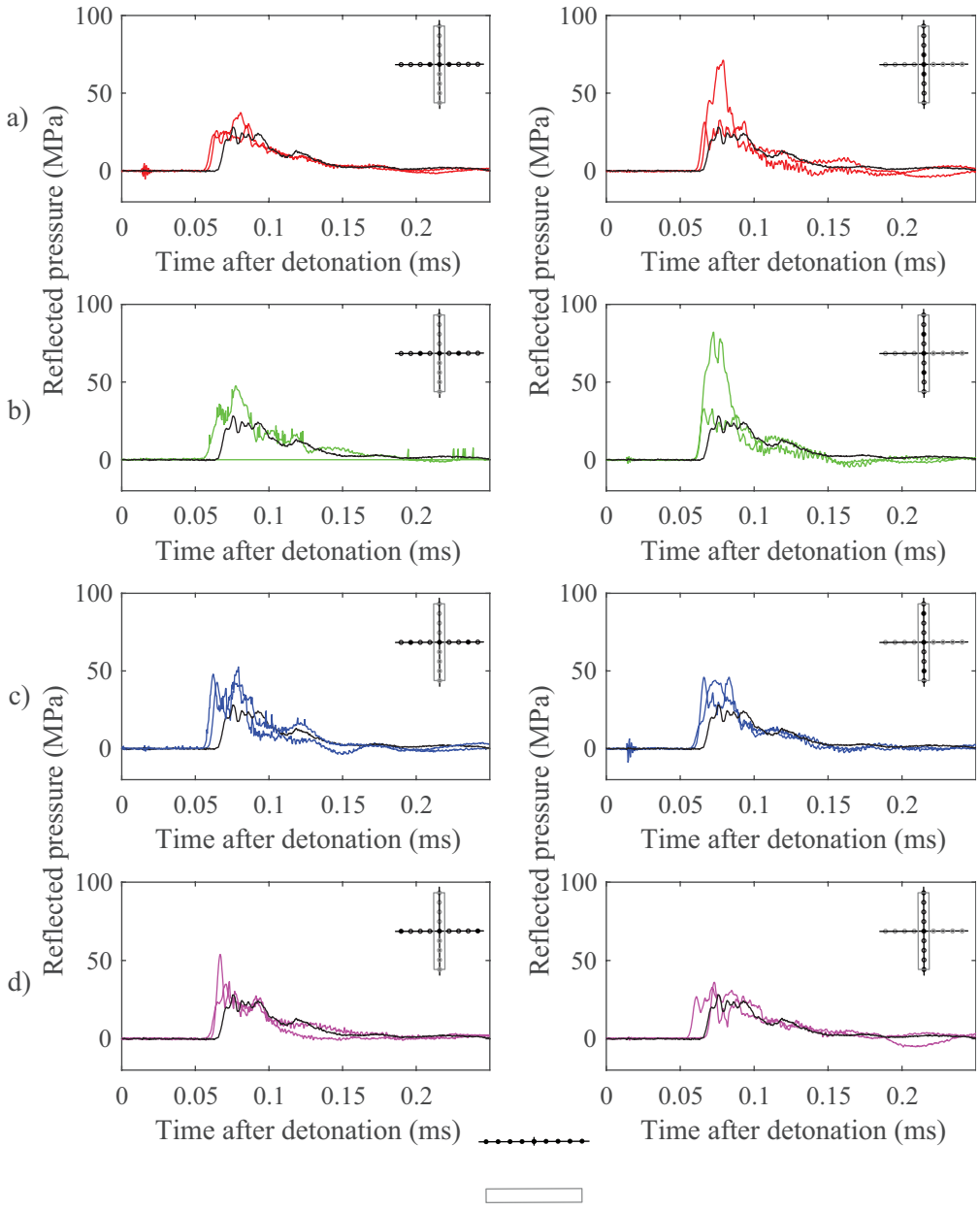


Figure 4.7: Reflected pressure time histories for test T019 (radial cylindrical charge, 0°, 0° orientation, centrally detonated). Results are shown for radial offsets of (a) 25 mm (red), (b) 50 mm (green), (c) 75 mm (blue), and (d) 100 mm (magenta), compared against the central reference measurement (0 mm, black). For each radial position, measurements are presented for perpendicular sensor arrays (left column) and aligned sensor arrays (right column). Insets indicate the relative orientation of the charge and sensor configuration.

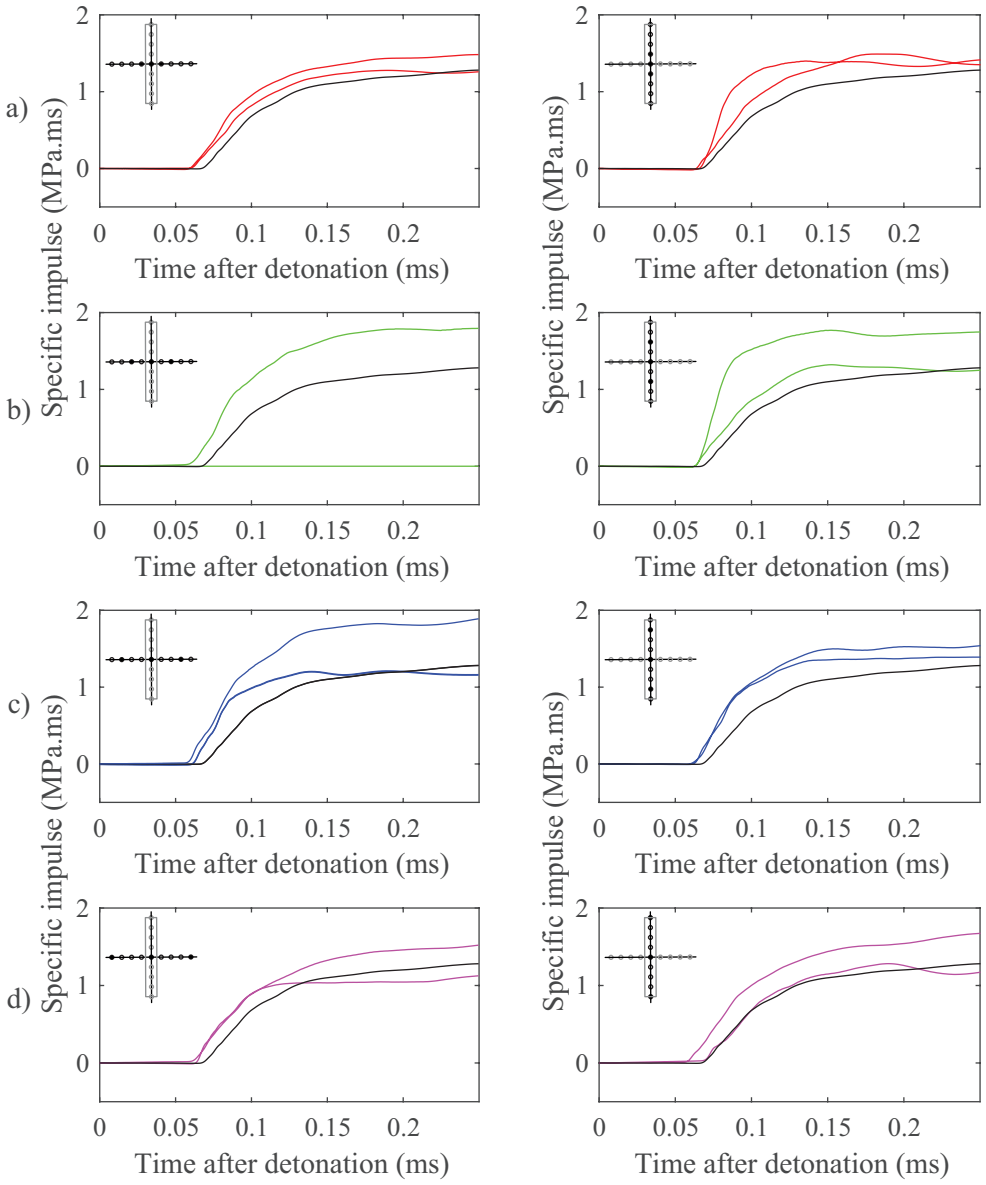


Figure 4.8: Specific impulse time histories for test T019 (radial cylindrical charge, $0°, 0°$ orientation, centrally detonated). Results are shown for radial offsets of a) 25 mm (red), b) 50 mm (green), c) 75 mm (blue), and d) 100 mm (magenta), compared against the central reference measurement (0 mm, black). For each radial position, measurements are presented for perpendicular sensor arrays (left column) and aligned sensor arrays (right column). Insets indicate the relative orientation of the charge and sensor configuration.

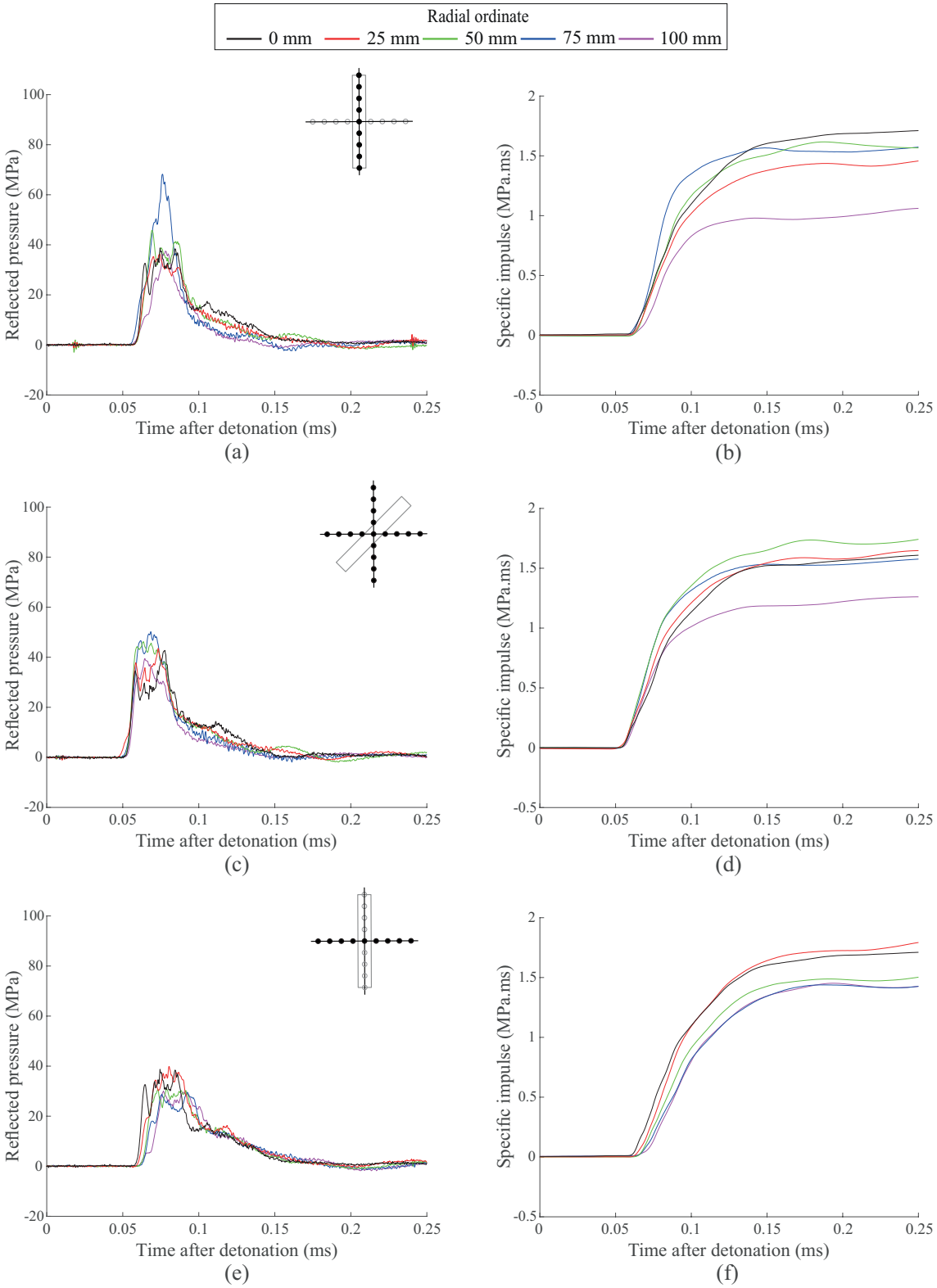


Figure 4.9: Series-averaged reflected pressure and specific impulse histories from detonation of 200 g $L/D = 7$ horizontal cylinders of C4 at 250 mm clear stand-off: (a–b) 0°; (c–d) 45°, and; (e–f) 90°. Alignment is indicated in on the respective row.

4.2.2 Compiled results

The reflected pressure histories from Tests T006, T007, and T019 are presented collectively in Figure 4.10, enabling direct comparison of the recorded waveforms across all three tests and both array orientations. The figure is arranged as a matrix of subplots. Rows a), b), and c) present the results from Tests T006, T007, and T019 respectively, whilst row d) presents an unweighted mean trace calculated from the three tests at each radial ordinate. Within each row, the left column presents the mean trace of the two perpendicular bars at each radial position, and the centre and right columns present the individual parallel array results. It is noted that for this charge orientation the parallel arrays are nominally symmetrical about the charge centre, however, the two-column format is retained for consistency with the non-symmetrical charge orientations introduced in subsequent sections. In all subplots, traces corresponding to radial offsets of 0 mm, 25 mm, 50 mm, 75 mm, and 100 mm are plotted in black, red, green, blue, and magenta respectively. The inset diagrams indicate the spatial relationship between the presented bars, the charge orientation, and the angle of the charge relative to the reflecting plate. Where a bar did not record a valid pressure trace, the corresponding zero-value trace was excluded from the averaging process prior to computation of the mean.

The comparative pressure traces presented in Figure 4.10 demonstrate a repeatability across the three tests, particularly for the perpendicular array. Tests T006 and T007 show notably consistent waveform profiles at equivalent perpendicular radial positions, characterised by a prolonged positive phase duration and close agreement in both shape and magnitude. The perpendicular results across all three tests exhibit profiles that follow that of the central bar, with a gradual attenuation in peak reflected pressure with increasing radial distance, as discussed in the individual test sections.

The parallel array results exhibit greater inter-test variability, with elevated peak pressures observed at 50 mm and 75 mm in a number of cases. The variability in these peaks across the three tests is reflected in the averaged traces in row (d), where the transient peak pressures are visibly attenuated. This is a consequence of the averaging methodology, in which all traces are time-shifted to align on the central bar arrival time prior to computation of the mean. As the transient peaks at other radial positions are not guaranteed to be coincident following this alignment, the averaging process tends to suppress their magnitude. It is important to note, however, that this attenuation is confined to the transient peak pressures and does not affect the impulse represented by the traces. The averaged waveforms remain representative of the overall loading profile and the energy delivered to the measurement positions.

The specific impulse histories from Tests T006, T007, and T019 are presented together in Figure 4.11, following the same subplot arrangement as described for Figure 4.10, with rows a)–c) corresponding to Tests T006, T007, and T019 respectively, and row d) presenting the unweighted mean across all three tests. The colour convention is retained throughout, with radial offsets of 0 mm, 25 mm, 50 mm, 75 mm, and 100 mm plotted in black, red,

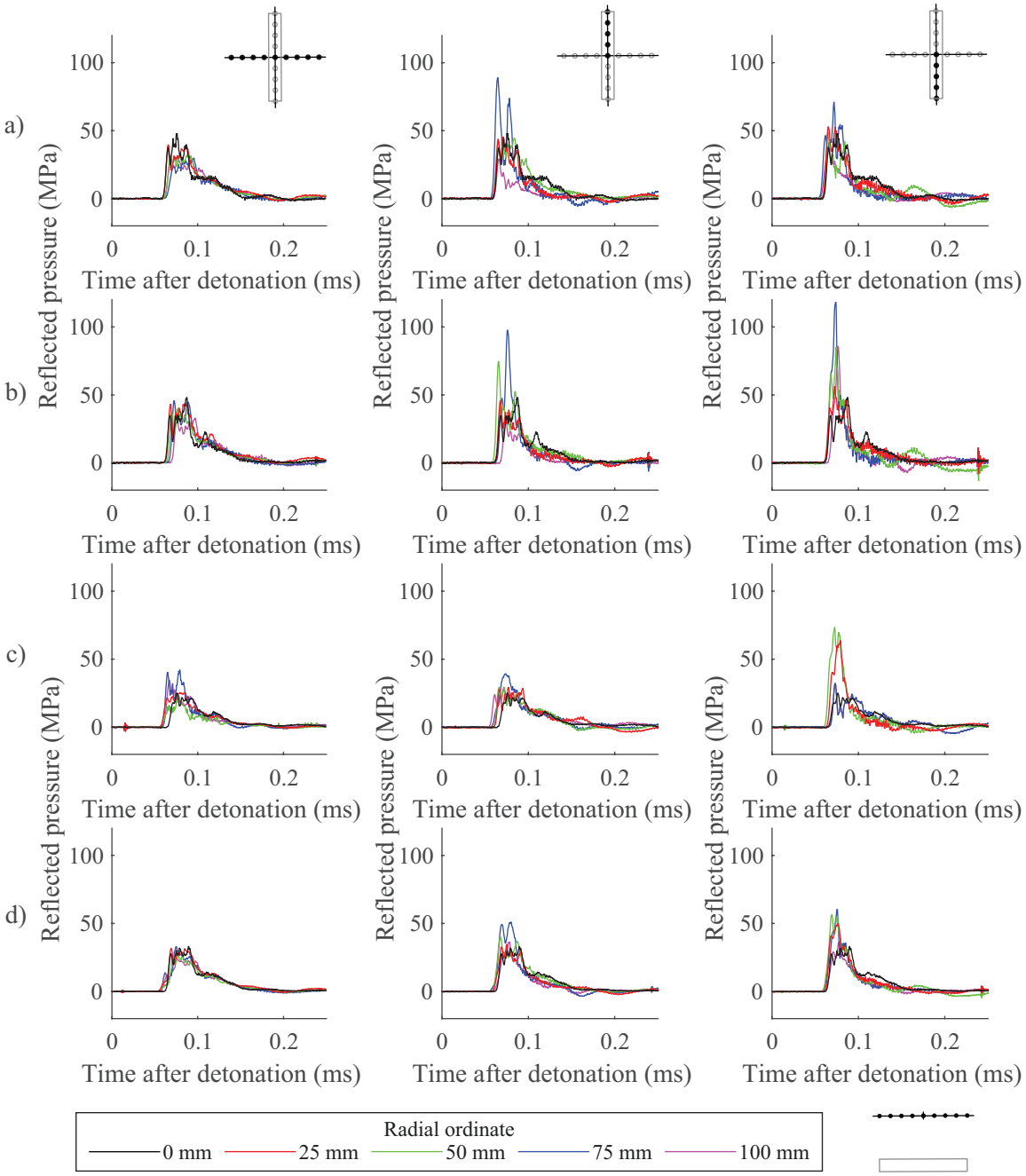


Figure 4.10: Reflected pressure time histories for radial cylindrical charges (0°, 0° orientation, centrally detonated) for tests a) T006, b) T007, and c) T019, with d) showing the average of the three tests, aligned by the arrival time at the central reference measurement (0 mm, black). Traces are shown for radial offsets of 0 mm (black), 25 mm (red), 50 mm (green), 75 mm (blue), and 100 mm (magenta). For each case, the perpendicular sensor array is presented in the left column, with the aligned array shown in the middle and right columns (opposing sides). Insets indicate the relative orientation of the charge and sensor configuration.

green, blue, and magenta respectively.

For each test, the parallel array traces, presented in the centre and right columns, are taken directly from the individual test results presented in Figures 4.4, 4.6, and 4.8, whilst the perpendicular traces, presented in the left column, represent the mean of the

two bars at each radial position. The mean traces presented in row d) are computed as the unweighted mean of the specific impulse histories above, rather than being derived from integrating the averaged pressure traces presented in Figure 4.10. Whilst both approaches are expected to yield equivalent results, the former is considered more directly representative of the measured impulse at each position. Where a bar did not record a valid trace, the corresponding zero-value trace was excluded from the averaging process prior to computation of the mean.

The averaged specific impulse histories presented in Figure 4.11 demonstrate the consistency of the loading across the three tests. The perpendicular results in row d) show a close grouping of the specific impulse traces, with the averaged mean exhibiting a tighter spread than the individual test results, reflecting the strong repeatability observed across the perpendicular array. This repeatability is particularly evident in Tests T006 and T007, with Test T019 exhibiting a slightly different response whilst remaining consistent with the general trend.

The parallel averaged results exhibit a broader spread of specific impulse across array. The 100 mm radial positions consistently record the lowest peak specific impulses, as expected from the geometric relationship between these bars and the end of the cylindrical charge. The 50 mm and 75 mm bars record the highest specific impulse amongst the radial positions, although not significantly greater than their perpendicular counterparts. The faster rise times corresponding to the peak pressures of the parallel bars at these positions are largely preserved in the averaged traces. It is noted that unlike the average pressure traces, the averaging process does not attenuate the peak specific impulse as these are present over a longer period of time; whilst the rise times are marginally affected by the time-shifting methodology, the total impulse and energy content are preserved.

The influence of the missing 50 mm perpendicular bar in T019, notable in the high value of the remaining individual trace, making the location the peak specific impulse of the test. However, this effect is largely eliminated in the cross-test average in row d) although it is given equally weighting to the other two tests where the results are already averaged. This illustrates the benefit of multiple equivalent measurements in identifying the representative trends and mitigating the influence of the inherent variability in the near-field. Similarly, the elevated 25 mm parallel trace recorded in Test T019 is present in row c) but is diminished in the cross-test average, further demonstrating the robustness of the repeated test programme in producing representative mean loading profiles.

The peak reflected pressures recorded during Tests T006, T007, and T019 are presented in Figure 4.12, arranged in four rows and two columns, with rows a)–d) corresponding to Tests T006, T007, T019, and the compiled results. The left column presents the perpendicular array results and the right column presents the parallel array results. The parallel horizontal axis spans radial offsets from -100 mm to $+100$ mm, with negative and positive values denoting the two bars at each radial position on either side of the central bar. Where a bar did not record a valid pressure trace, the corresponding data point is marked at zero

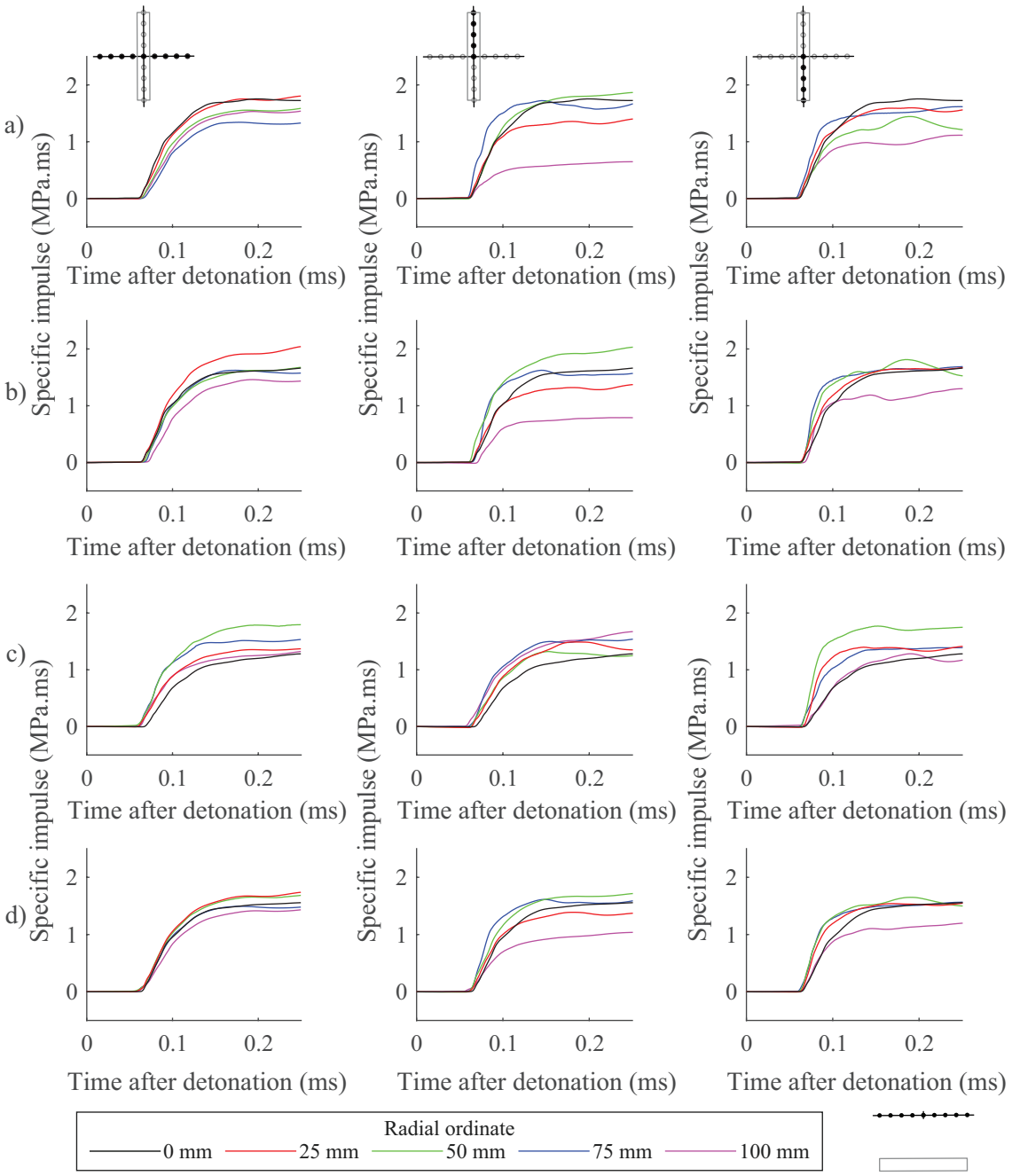


Figure 4.11: Specific impulse time histories for radial cylindrical charges (0°, 0° orientation, centrally detonated) for tests a) T006, b) T007, and c) T019, with d) showing the average of the three tests, aligned by the arrival time at the central reference measurement (0 mm, black). Traces are shown for radial offsets of 0 mm (black), 25 mm (red), 50 mm (green), 75 mm (blue), and 100 mm (magenta). For each case, the perpendicular sensor array is presented in the left column, with the aligned array shown in the middle and right columns (opposing sides). Insets indicate the relative orientation of the charge and sensor configuration.

using the same marker style as the remaining data points.

The peak pressure results provide a spatial illustration of the reflected loading distribution. For the perpendicular array, Tests T006 and T007 exhibit a consistent decrease in peak reflected pressure with increasing radial distance from the centre, whilst Test T019 exhibits

the opposite trend, with peak pressure increasing with radial distance. This divergence in T019 is consistent with the poor inter-bar agreement noted in the individual test results and is reflected in the cross-test mean in row (d), which resultantly shows a broadly uniform distribution of peak pressures across the perpendicular array, forming a solid band with relatively even spatial distribution.

The parallel array results exhibit considerably greater inter-test variability; however, a consistent spatial pattern can be established from the data. The highest peak reflected pressures are recorded at the ±50 mm and ±75 mm positions, with a significant reduction at ±100 mm, consistent with the geometric influence of the charge end discussed previously. This distribution produces a characteristic inverted 'W' profile in the cross-test mean in row (d), with elevated pressures at the intermediate radial positions and suppressed values towards centre and the extremities of the array.

The peak specific impulse values recorded during Tests T006, T007, and T019 are presented in Figure 4.13, following the same arrangement as Figure 4.12, with four rows and two columns with rows a)–c) corresponding to Tests T006, T007, and T019 respectively and row d) contains all individual results compiled together, with up to six data points per radial position. The left column presents the perpendicular array results and the right column the parallel array data. The horizontal axis spans radial offsets from −100 mm to +100 mm. Where a bar did not record a valid trace, the corresponding data point is still included as a zero value.

The perpendicular peak specific impulse results demonstrate strong spatial consistency in Test T006, with excellent agreement between the two bars at each radial position. Greater variability is observed in Tests T007 and T019, with a broader spread of values at equivalent positions. Despite this increased spread, the compiled results in row d) reveal a observable trend of decreasing peak specific impulse with increasing radial distance from the centre outwards.

The parallel array results exhibit a more even spatial distribution of peak specific impulse compared to the peak pressure results, with values remaining broadly consistent across the intermediate radial positions. A notable downturn is observed at the ±100 mm positions, except for -100 mm in T019, consistent with the geometric influence of the charge end identified throughout the preceding sections. The compiled parallel results in row d) show slightly less inter-test variability than the perpendicular equivalent, and considerably less than that observed in the peak reflected pressure data, suggesting that the specific impulse is a more stable and repeatable measure of the loading despite the variance of peak pressure in this instance. The inverted 'W' profile is also not discernable in the peak specific impulse data.

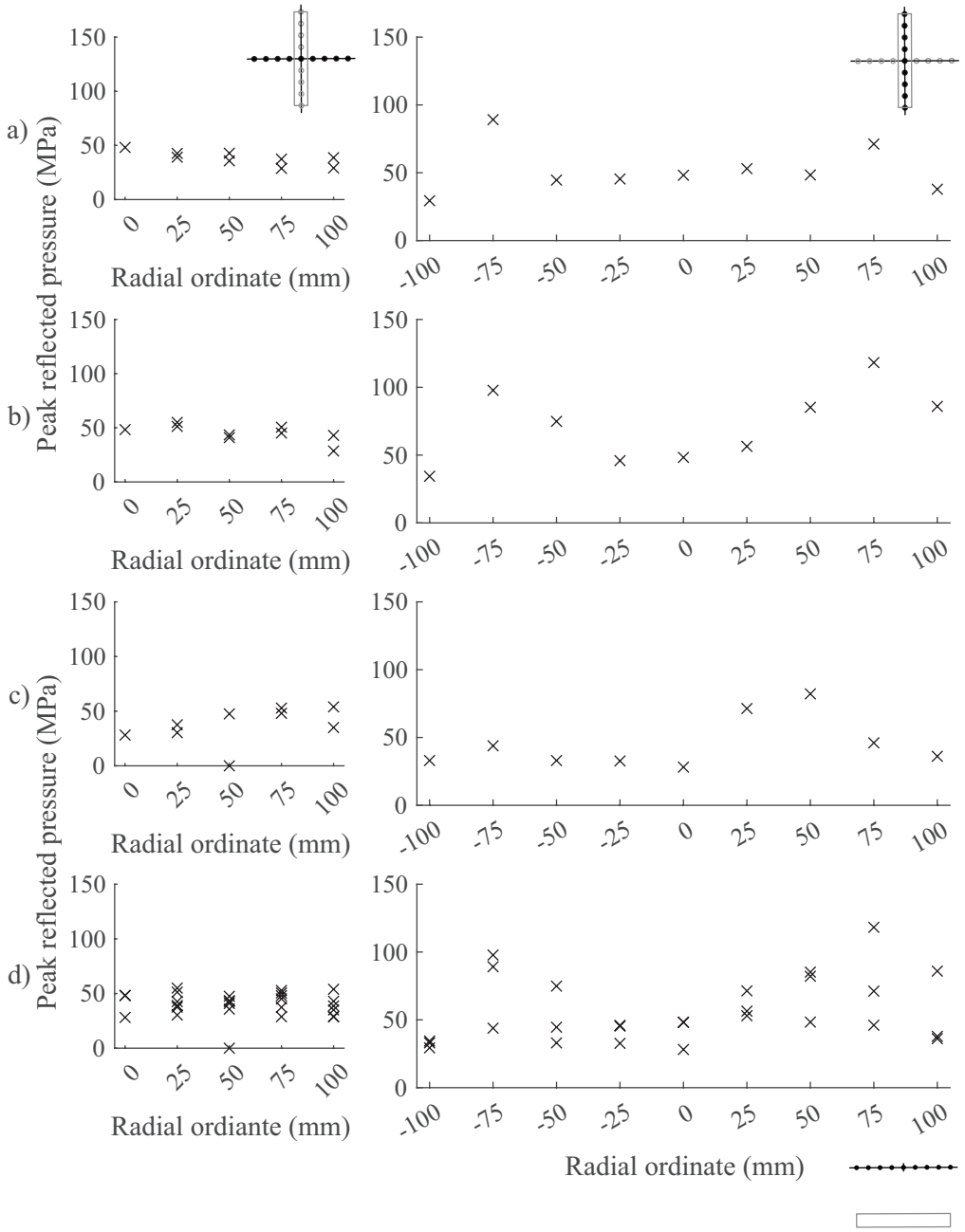


Figure 4.12: Peak reflected pressures for radial cylindrical charges ($0°, 0°$ orientation, centrally detonated) for tests a) T006, b) T007, and c) T019, with d) showing a collation of the three tests. For each case, the perpendicular sensor array is presented in the left column, with the aligned array shown in the right column. Insets indicate the relative orientation of the charge and sensor configuration.

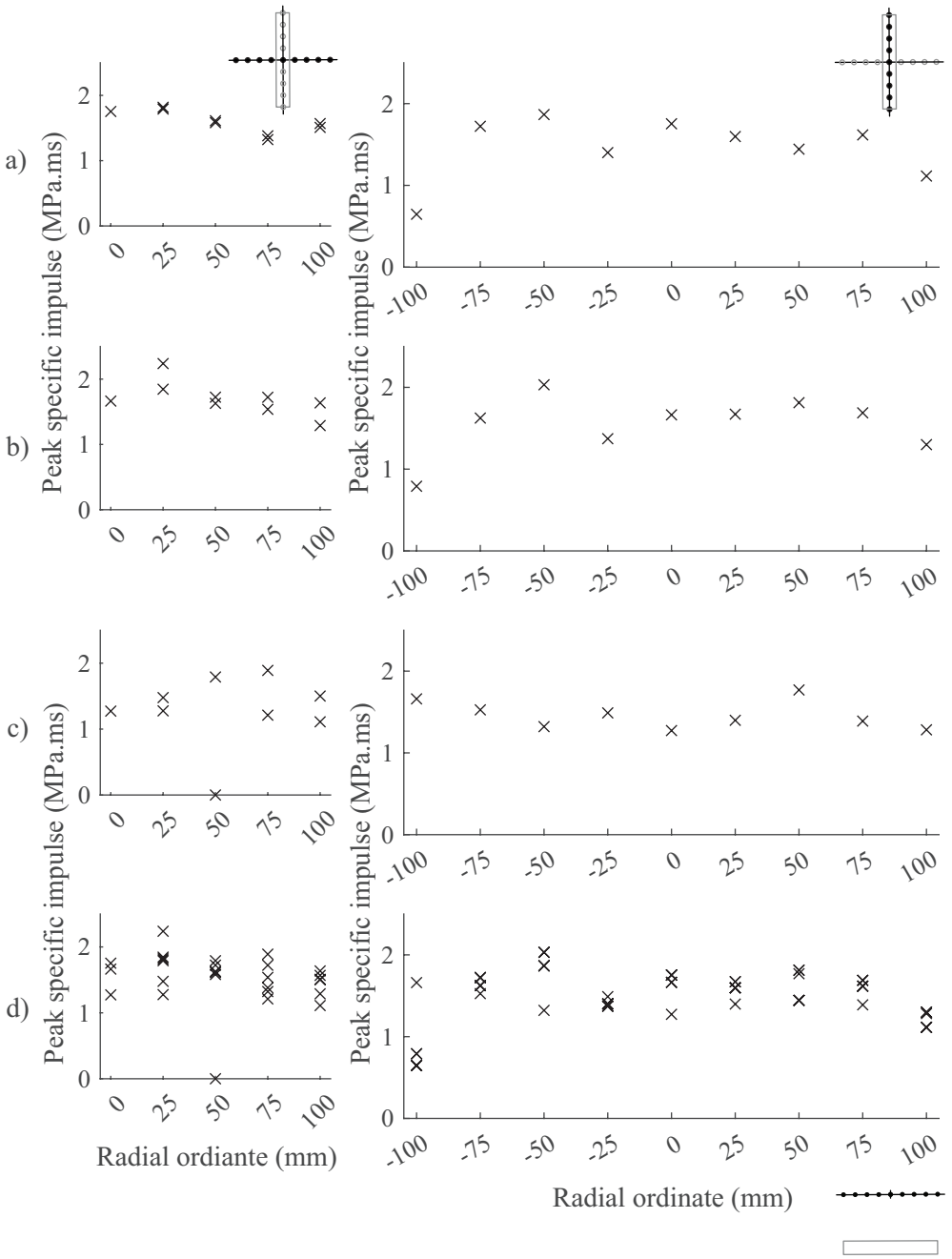


Figure 4.13: Peak specific impulses for radial cylindrical charges ($0°, 0°$ orientation, centrally detonated) for tests a) T006, b) T007, and c) T019, with d) showing a collation of the three tests. For each case, the perpendicular sensor array is presented in the left column, with the aligned array shown in the right column. Insets indicate the relative orientation of the charge and sensor configuration.

The reflected pressure histories depicted in Figure 4.9 exhibit a heightened level of complexity and magnitude compared to the well-defined Friedlander-type exponential decays observed in the spherical charge tests (Figure 4.1). Peak pressure is frequently reached after the initial shock front arrival, resulting in an irregular decay and a prolonged positive phase duration relative to the spherical loading. Consequently, a consistently higher specific impulse is recorded at all radial ordinates in comparison to the spherical charges.

As anticipated, the arrival times of the shock show broad similarities at each radial offset in the 0° orientation, with an increase observed with radial offset in the 90° orientation. Specifically, pressure traces at the 50 mm and 75 mm bar locations in the 0° orientation are approximately twice in magnitude as those at the same bar locations for the 90° orientation, while the 45° results fall approximately midway between the two for all radial ordinates, except the central bar, which is common to both 0° and 90° arrays.

At 0° orientation, the highest peak pressures are off-centred, with the 50 mm and 75 mm bars recording an average peak pressure higher than that of the central bar. These larger non-central pressures persist until approximately 0.08 ms, after which the non-central bars, particularly those at 75 mm and 100 mm from the centre, record a rapid temporal decay in pressure. This phenomenon may be attributed to localised 'clearing' or equalisation of pressures in regions outside the projected area of the charge.

The temporal development of specific impulse at the central bar initially progresses more gradually but eventually surpasses the specific impulse at the 50 mm and 75 mm bars due to prolonged high pressure between 0.10–0.15 ms, which is not present at other locations. This behaviour is also observed at the 45° orientation; however, the 50 mm and 75 mm bars record a less significant pressure increase above the central bar than those at 0° orientation. With the exception of the 25 mm bar, the peak specific impulse decreases with increasing distance from the plate centre, with the 100 mm bar recording an impulse that is approximately 30% lower than the remaining bars. In the 0° orientation tests, the 100 mm bars align exactly vertically with each end of the charge, suggesting that this location marks the transition between the radial shock wave and the lower magnitude bridging waves.

4.3 Cylindrical tests – Radial (0°, 0°) – End detonated

The following section presents the reflected pressure and specific impulse results obtained from radial cylindrical charges detonated at the end of the charge, in contrast to the central detonation point employed in the preceding tests. End detonation introduces an inherent asymmetry in the detonation wave propagation and blast wave development. This is expected to produce a directionally dependent blast environment, with the loading characteristics along the charge axis differing from those observed under central detonation. The results are presented in the same format as the preceding section. The reflected pressure and specific impulse histories for Tests T010 and T012 are presented individually, followed by the comparative figures.

4.3.1 Test Results

T010

The reflected pressure histories recorded during Test T010 are presented in Figure 4.14, using the same array configuration and subplot arrangement as described in Section 4.2.1. The central bar trace is included in all subplots as a consistent spatial reference.

The perpendicular results demonstrate good repeatability between the two bars at each radial position, with pressure profiles that closely resemble that of the central bar across all measured locations. A slight reduction in peak reflected pressure is observed with increasing radial distance, consistent with the trends identified in the centrally detonated tests.

The parallel results exhibit significant elevated peak pressures across all radial distances, with the most prominent peaks recorded at the 50 mm positions. The pressure profiles at these locations exhibit a Friedlander-like decay character, consistent with observations from the preceding centrally detonated charges. One of the 100 mm parallel bars records a considerably reduced peak pressure; whilst this is partly consistent with the geometric influence of the charge end noted in the centrally detonated tests, it is noted that under end detonation the two parallel bars at each radial position are no longer nominally identical in their geometric relationship to the detonation point, and their responses are therefore not expected to be equivalent.

The specific impulse histories for Test T010 are presented in Figure 4.15. The perpendicular impulse results exhibit good consistency between paired traces across most radial positions, with a trend of decreasing specific impulse with increasing radial distance. The exception is at 100 mm, where greater variation between the two bars is observed. The parallel impulse histories exhibit a broader spread of values than the perpendicular results, reflecting the physical asymmetry of the end detonated configuration. As the two parallel bars at each radial position occupy geometrically distinct locations relative to the detonation point, their impulse responses are not expected to correspond, and the divergence between the two traces is observed to increase progressively with radial distance from 25 mm to 100 mm.

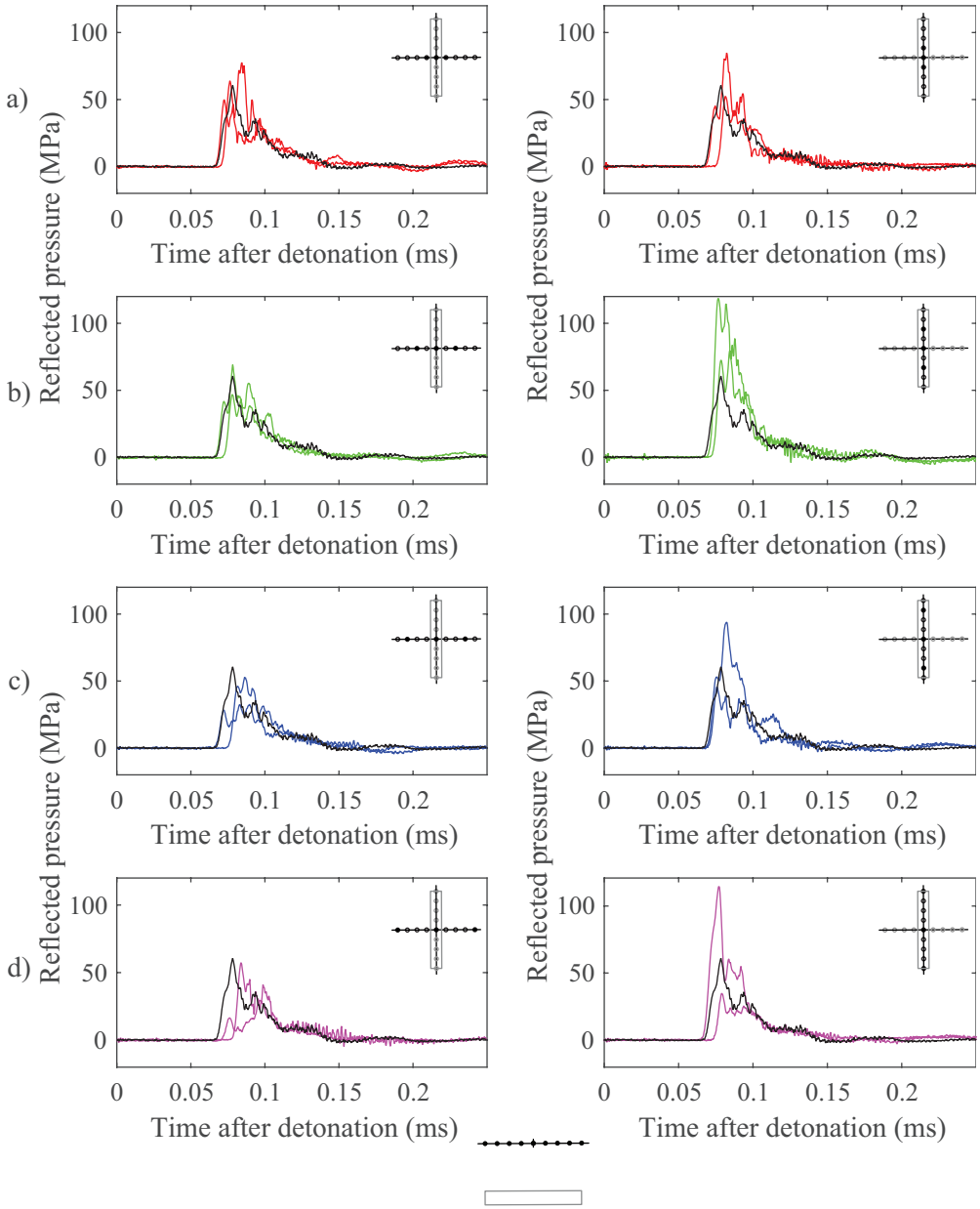


Figure 4.14: Reflected pressure time histories for test T010 (radial cylindrical charge, 0°, 0° orientation, end detonated). Results are shown for radial offsets of (a) 25 mm (red), (b) 50 mm (green), (c) 75 mm (blue), and (d) 100 mm (magenta), compared against the central reference measurement (0 mm, black). For each radial position, measurements are presented for perpendicular sensor arrays (left column) and aligned sensor arrays (right column). Insets indicate the relative orientation of the charge and sensor configuration.

The faster rise times noted in the pressure results at the elevated peak positions are reflected in the corresponding impulse histories.

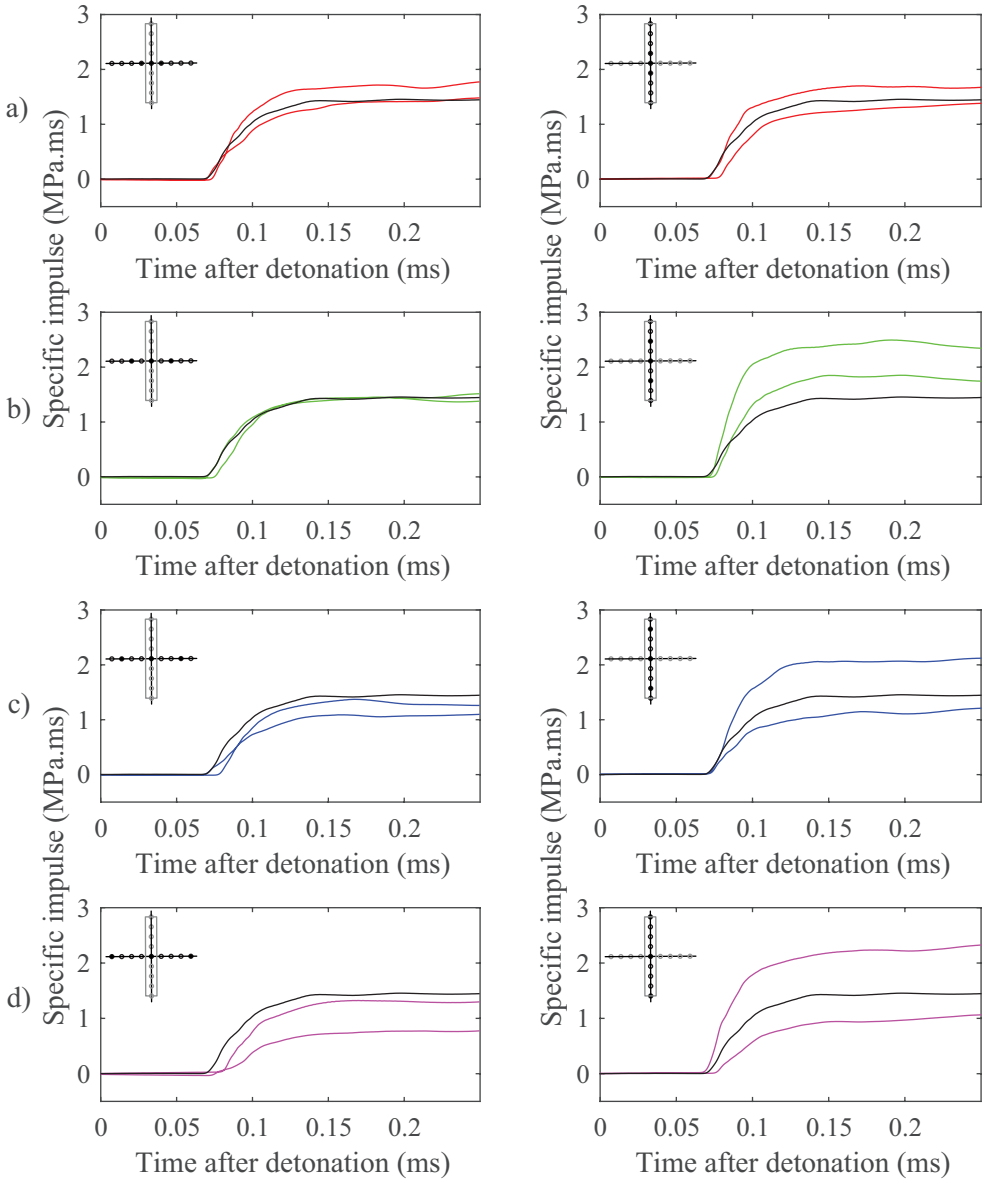


Figure 4.15: Specific impulse time histories for test T010 (radial cylindrical charge, 0°, 0° orientation, end detonated). Results are shown for radial offsets of a) 25 mm (red), b) 50 mm (green), c) 75 mm (blue), and d) 100 mm (magenta), compared against the central reference measurement (0 mm, black). For each radial position, measurements are presented for perpendicular sensor arrays (left column) and aligned sensor arrays (right column). Insets indicate the relative orientation of the charge and sensor configuration.

T012

The reflected pressure histories recorded during Test T012 are presented in Figure 4.16. It is noted that one of the 50 mm perpendicular bars did not record a valid pressure trace during this test and is represented as a zero-value flat line in the plot.

The perpendicular results exhibit broadly consistent pressure profiles across most radial positions. A notable elevated peak pressure is observed at the 25 mm position, exceeding that of the central bar and all parallel bars with the exception of the 50 mm parallel position. One of the 100 mm perpendicular bars records a considerably reduced pressure trace, consistent with a single bar exhibiting an anomalous response rather than a systematic geometric effect at this position.

The parallel results differ notably from those recorded in Test T010, with significant elevated peak pressures confined exclusively to the 50 mm bars. All other radial positions exhibit pressure profiles broadly consistent with the central bar, without the elevated peaks observed across all distances in T010.

The specific impulse histories for Test T012 are presented in Figure 4.17. As with the pressure data, the 50 mm perpendicular dead bar is represented as a zero-value trace and is excluded from any subsequent averaging. The perpendicular impulse histories exhibit good consistency across all radial positions, with a broadly even distribution of specific impulse values. The 100 mm traces show a distinct difference in profile and peak impulse, consistent with the results from T010. The parallel impulse histories exhibit strong consistency between paired traces at 25 mm, 75 mm, and 100 mm, whilst the 50 mm position records elevated specific impulse values with a large difference between the two parallel bars, consistent with the asymmetric loading expected under end detonation and the significant peak pressures recorded at this position in the pressure data.

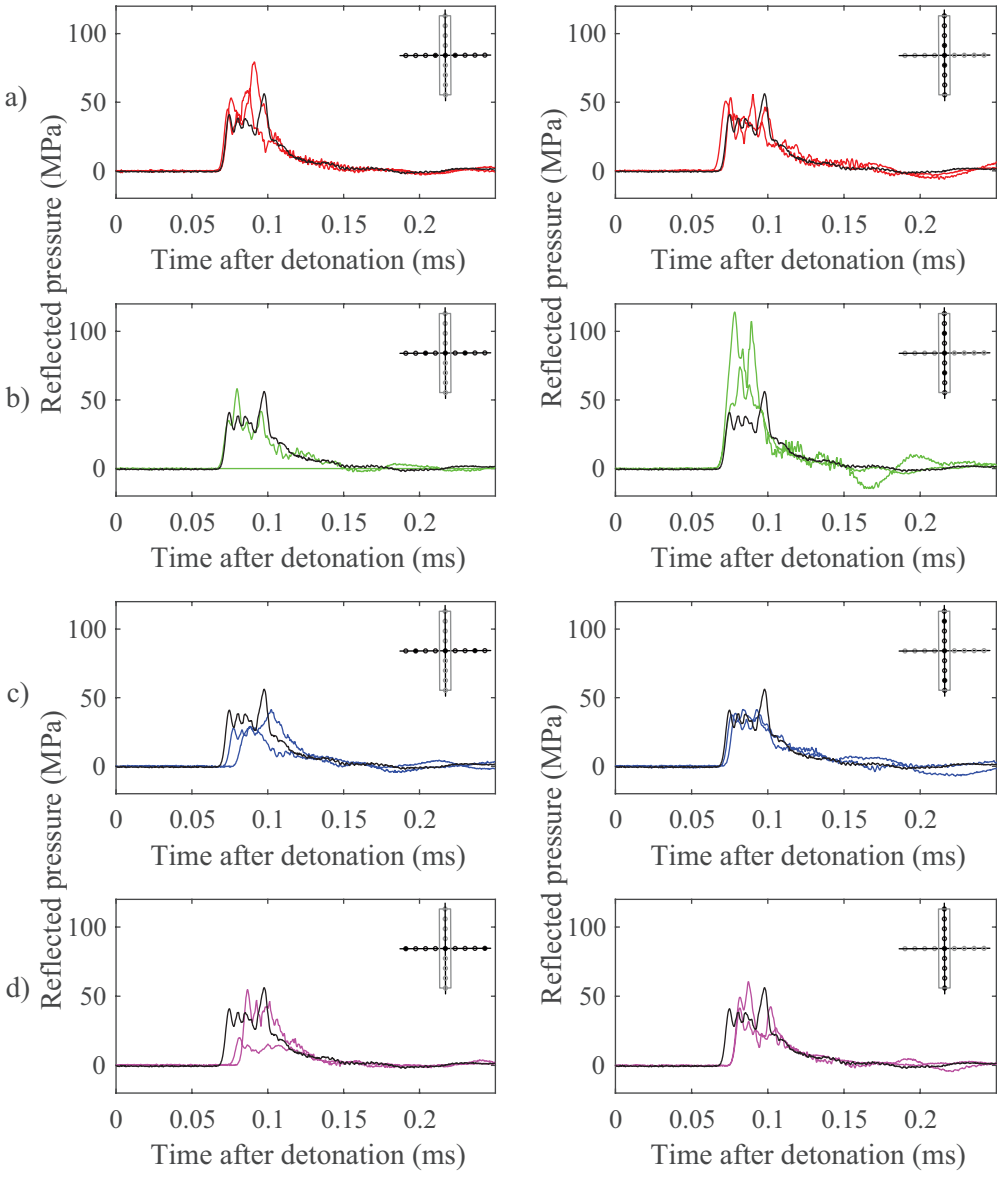


Figure 4.16: Reflected pressure time histories for test T012 (radial cylindrical charge, $0°, 0°$ orientation, end detonated). Results are shown for radial offsets of (a) 25 mm (red), (b) 50 mm (green), (c) 75 mm (blue), and (d) 100 mm (magenta), compared against the central reference measurement (0 mm, black). For each radial position, measurements are presented for perpendicular sensor arrays (left column) and aligned sensor arrays (right column). Insets indicate the relative orientation of the charge and sensor configuration.

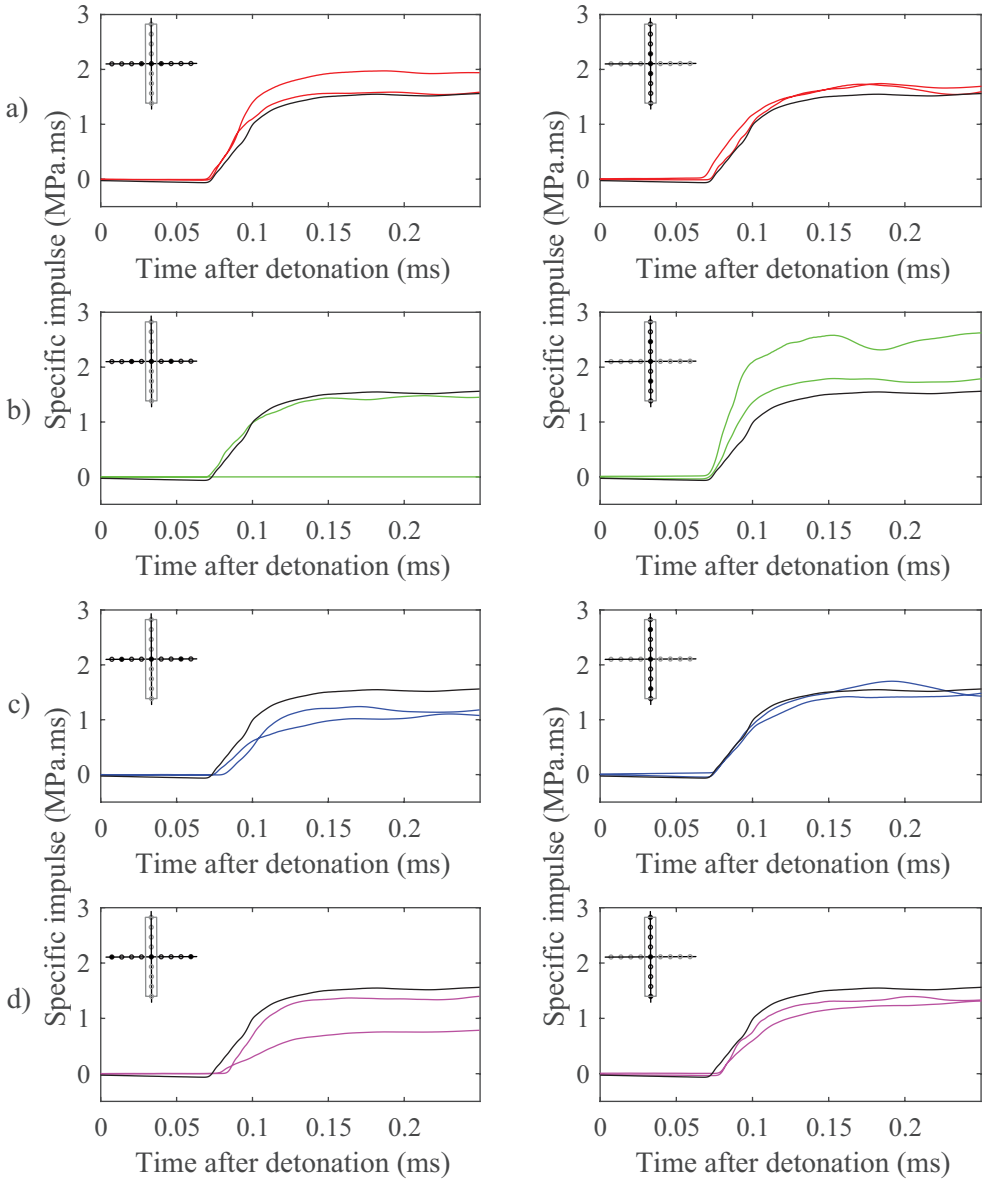


Figure 4.17: Specific impulse time histories for test T012 (radial cylindrical charge, 0°, 0° orientation, end detonated). Results are shown for radial offsets of a) 25 mm (red), b) 50 mm (green), c) 75 mm (blue), and d) 100 mm (magenta), compared against the central reference measurement (0 mm, black). For each radial position, measurements are presented for perpendicular sensor arrays (left column) and aligned sensor arrays (right column). Insets indicate the relative orientation of the charge and sensor configuration.

4.3.2 Compiled results

The reflected pressure histories from Tests T010 and T012 are presented together in Figure 4.18, following the same subplot arrangement as described for Figure 4.10, with the exception that only three rows are presented. Rows a) and b) correspond to Tests T010 and T012 respectively, and row c) presents the combined data points.

The perpendicular results exhibit consistent pressure profiles across both tests, characterised by well-defined peak to ambient decays with good repeatability between equivalent radial positions. The parallel results exhibit a more complex loading character than the perpendicular measurements, with multiple pressure peaks observed in the traces rather than the single dominant peak with smooth decay seen in the perpendicular array. Elevated peak pressures are most prevalent in the parallel traces, particularly at the 50 mm position, where significant peaks are recorded in both tests. Notably, despite the differences between T010 and T012 in the distribution of elevated peaks across radial distances, the 50 mm parallel peak pressures are well preserved in the cross-test mean in row (c).

The specific impulse histories from Tests T010 and T012 are presented in Figure 4.19, following the same arrangement as Figure 4.18. The perpendicular impulse results demonstrate good consistency in the distribution of specific impulse across both tests, with a general decline in peak specific impulse with increasing radial distance from 25 mm to 100 mm. The parallel impulse histories exhibit greater variation between radial positions, reflecting the asymmetric loading environment of the end detonated configuration. The +50 mm parallel position consistently records a strong specific impulse rise and elevated peak specific impulse across both tests, corresponding to the significant peak pressures observed at this location in Figure 4.18.

The peak reflected pressures from Tests T010 and T012 are presented in Figure 4.20. Each data point represents an individual bar measurement, with up to four data points per radial position in the left column corresponding to the two bars for the two tests. The right column presents the parallel results spanning −100 mm to +100 mm, where the negative and positive values represent physically distinct measurement locations relative to the detonation end of the charge rather than nominally identical repeat measurements. The perpendicular results exhibit a discernible trend, with the peak pressures forming a 'V' shape across the array, with higher values above the detonator, dropping off towards central bar, before rising again to the peak at +50 mm and then steeply declining at the far positions of +75 mm and +100 mm. Whilst some outliers are present, this trend is observable across both tests. The parallel results exhibit a fair spread of peak pressures with a general downward trend with increasing radial distance.

The peak specific impulse values from Tests T010 and T012 are presented in Figure 4.21, following the same arrangement as Figure 4.20. The perpendicular results demonstrate good consistency between the two tests, with the same downward trend in peak specific impulse with increasing radial distance observed across both. The parallel results exhibit a similar spatial distribution to that observed in the peak pressure data, with a 'U' shaped

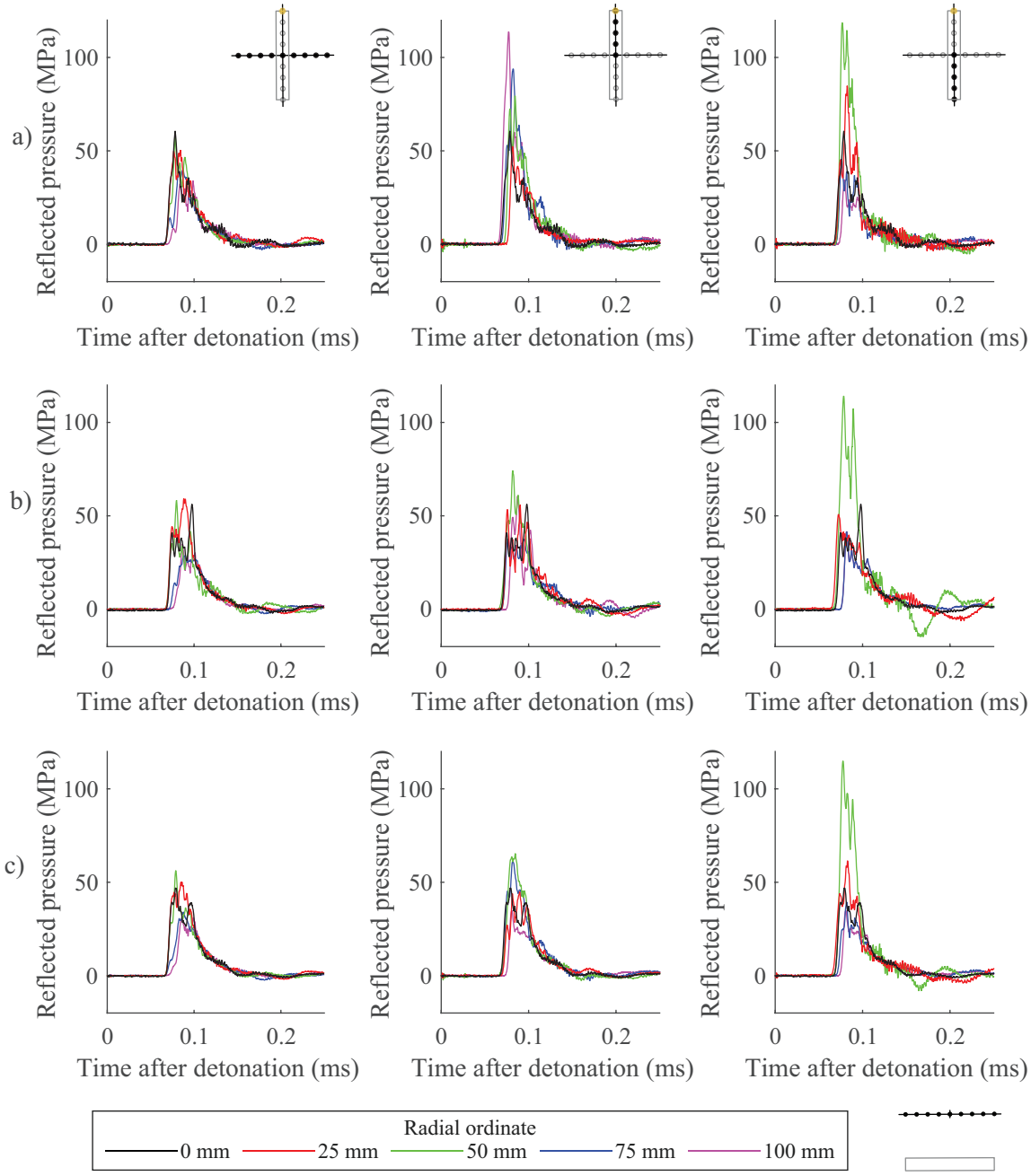


Figure 4.18: Reflected pressure time histories for radial cylindrical charges (0°, 0° orientation, end detonated) for tests a) T010, b) T012, with c) showing the average of the two tests, aligned by the arrival time at the central reference measurement (0 mm, black). Traces are shown for radial offsets of 0 mm (black), 25 mm (red), 50 mm (green), 75 mm (blue), and 100 mm (magenta). For each case, the perpendicular sensor array is presented in the left column, with the aligned array shown in the middle and right columns (opposing sides). Insets indicate the relative orientation of the charge and sensor configuration.

profile across the array and a notable reduction in peak specific impulse at the ±75 mm and ±100 mm positions.

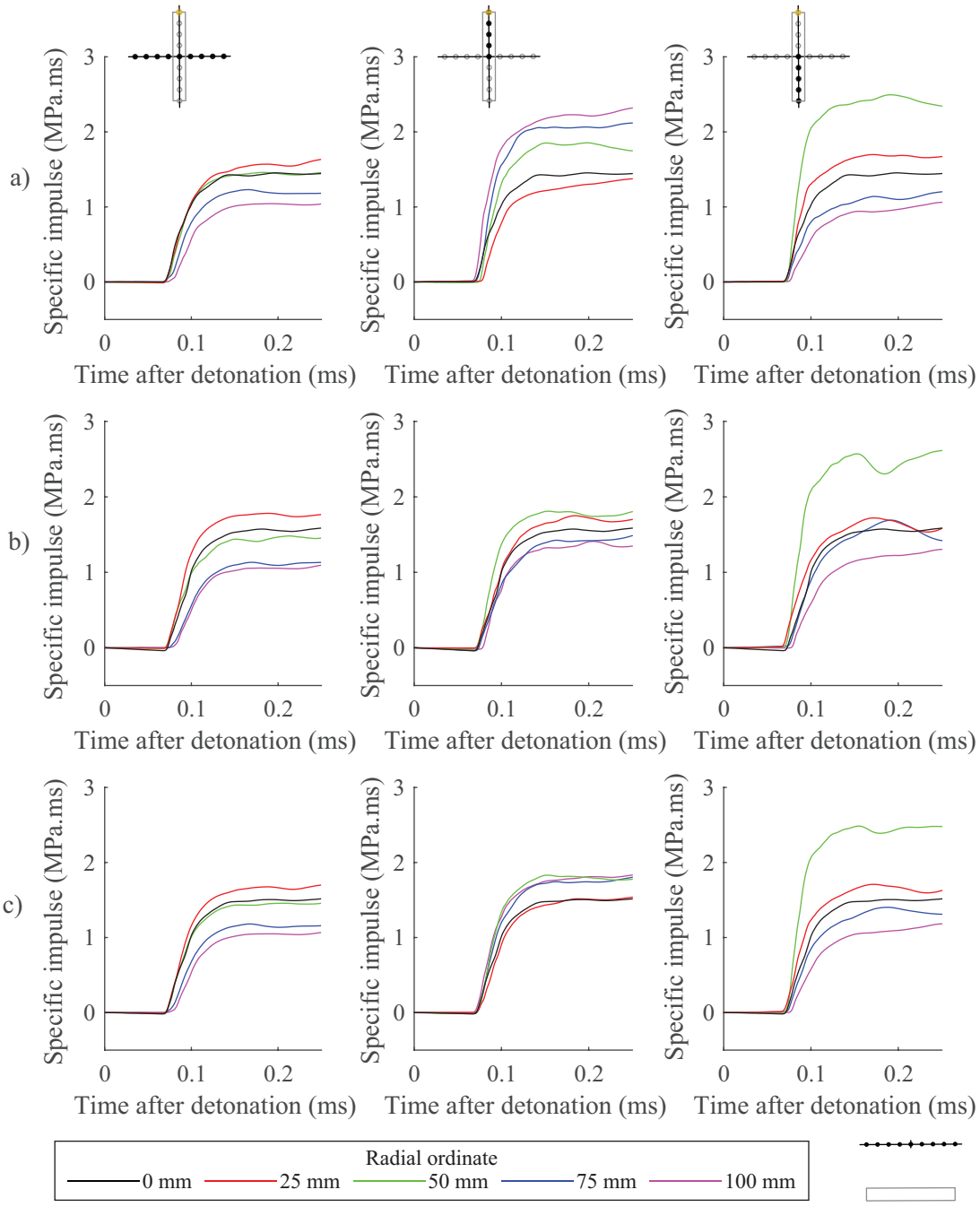


Figure 4.19: Specific impulse time histories for radial cylindrical charges (0°, 0° orientation, end detonated) for tests a) T010, b) T012, with c) showing the average of the two tests, aligned by the arrival time at the central reference measurement (0 mm, black). Traces are shown for radial offsets of 0 mm (black), 25 mm (red), 50 mm (green), 75 mm (blue), and 100 mm (magenta). For each case, the perpendicular sensor array is presented in the left column, with the aligned array shown in the middle and right columns (opposing sides). Insets indicate the relative orientation of the charge and sensor configuration.

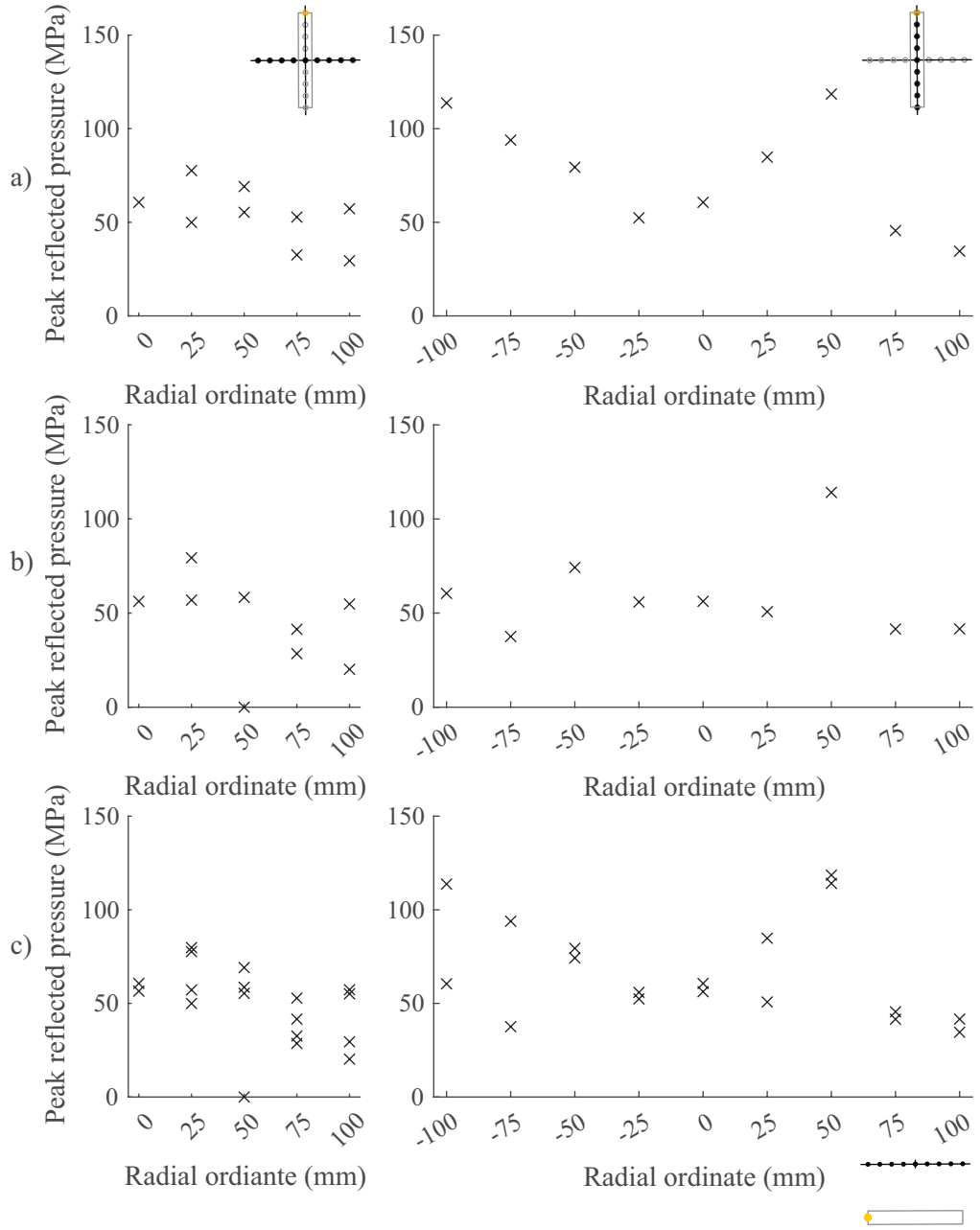


Figure 4.20: Peak reflected pressures for radial cylindrical charges (0°, 0° orientation, end detonated) for tests a) T010, b) T012, with c) showing a collation of the two tests. For each case, the perpendicular sensor array is presented in the left column, with the aligned array shown in the right column. Insets indicate the relative orientation of the charge and sensor configuration.

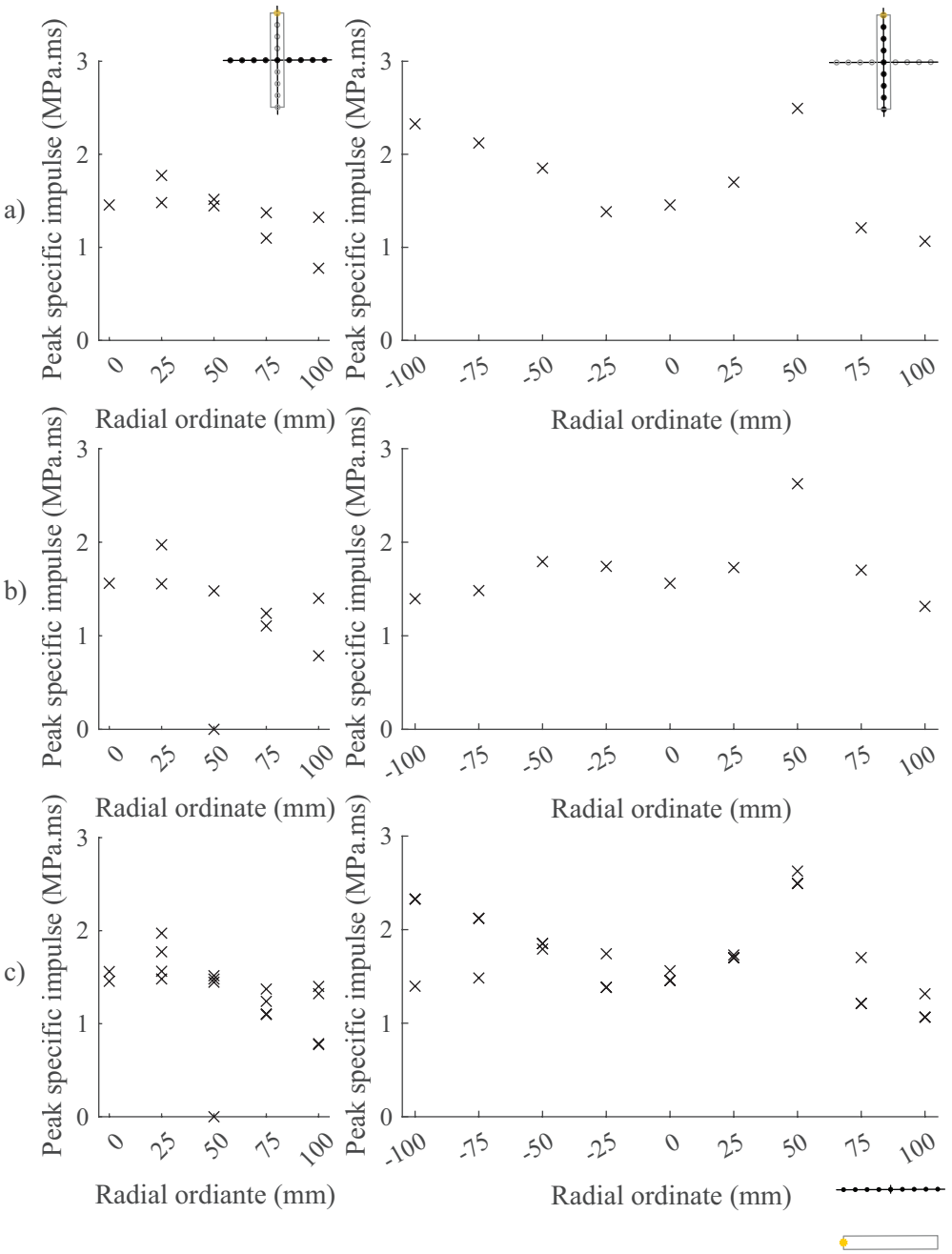


Figure 4.21: Peak specific impulses for radial cylindrical charges ($0°, 0°$ orientation, end detonated) for tests a) T010, b) T012, with c) showing a collation of the two tests. For each case, the perpendicular sensor array is presented in the left column, with the aligned array shown in the right column. Insets indicate the relative orientation of the charge and sensor configuration.

4.4 Cylindrical tests – Radial 45° (45°, 0°)

4.4.1 Test Results

The following section presents the reflected pressure and specific impulse results obtained from cylindrical charges orientated at 45° to the instrumented bar array. In contrast to the preceding orientations, the 45° configuration results in all bars within the array occupying nominally identical positions relative to the charge axis, as neither array is aligned with nor perpendicular to the charge. As a consequence, all bars at equivalent radial distances are treated as repeat measurements of the same loading condition, yielding up to four repeat measurements per radial location across the two arrays. The results are presented in the same format as the preceding sections, with the individual test figures arranged as a matrix of four subplots corresponding to radial offsets of 25 mm, 50 mm, 75 mm, and 100 mm, labelled a)–d) respectively, with the central bar trace included in each subplot as a consistent spatial reference. The comparative figures follow the same arrangement as described in the preceding sections, with a) and b) corresponding to Tests T008 and T009 respectively, and c) presenting the cross-test mean or compiled results as appropriate.

T008

The reflected pressure histories recorded during Test T008 are presented in Figure 4.22, using the same array configuration as described for the preceding tests. As all bars at equivalent radial distances are nominally identical in this orientation, the results are presented in four subplots corresponding to radial offsets of 25 mm, 50 mm, 75 mm, and 100 mm, with the central bar trace included in each subplot as a consistent spatial reference. It is noted that one of the 100 mm bars did not record a valid pressure trace during this test and is represented as a zero-value flat line in the figure.

The 25 mm bars exhibit pressure profiles closely resembling that of the central bar, with good agreement between all four traces at this position. Considerably elevated peak pressures are recorded at 50 mm, 75 mm, and 100 mm, with magnitudes reaching as much as twice that of the central bar, consistent with the elevated parallel results observed in the 0° orientation tests. Unlike the 0° results, however, the tapering off of peak pressure at 100 mm is not observed, with the two surviving bars at this position recording elevated pressures. The pressure profiles at the elevated positions exhibit a good fall off from the peak combined with an extended positive phase duration, presenting a character that resembles a combination of the parallel and perpendicular responses observed in the radial (0°, 0°) orientation.

The specific impulse histories for Test T008 are presented in Figure 4.23. Good agreement is observed between the four traces at 25 mm, consistent with the pressure results at this position. At 50 mm, 75 mm, and 100 mm, considerably greater variance is observed between the individual traces, reflecting the elevated and more complex pressure loading at these locations. Isolated negative phases are present in the records, observed once each

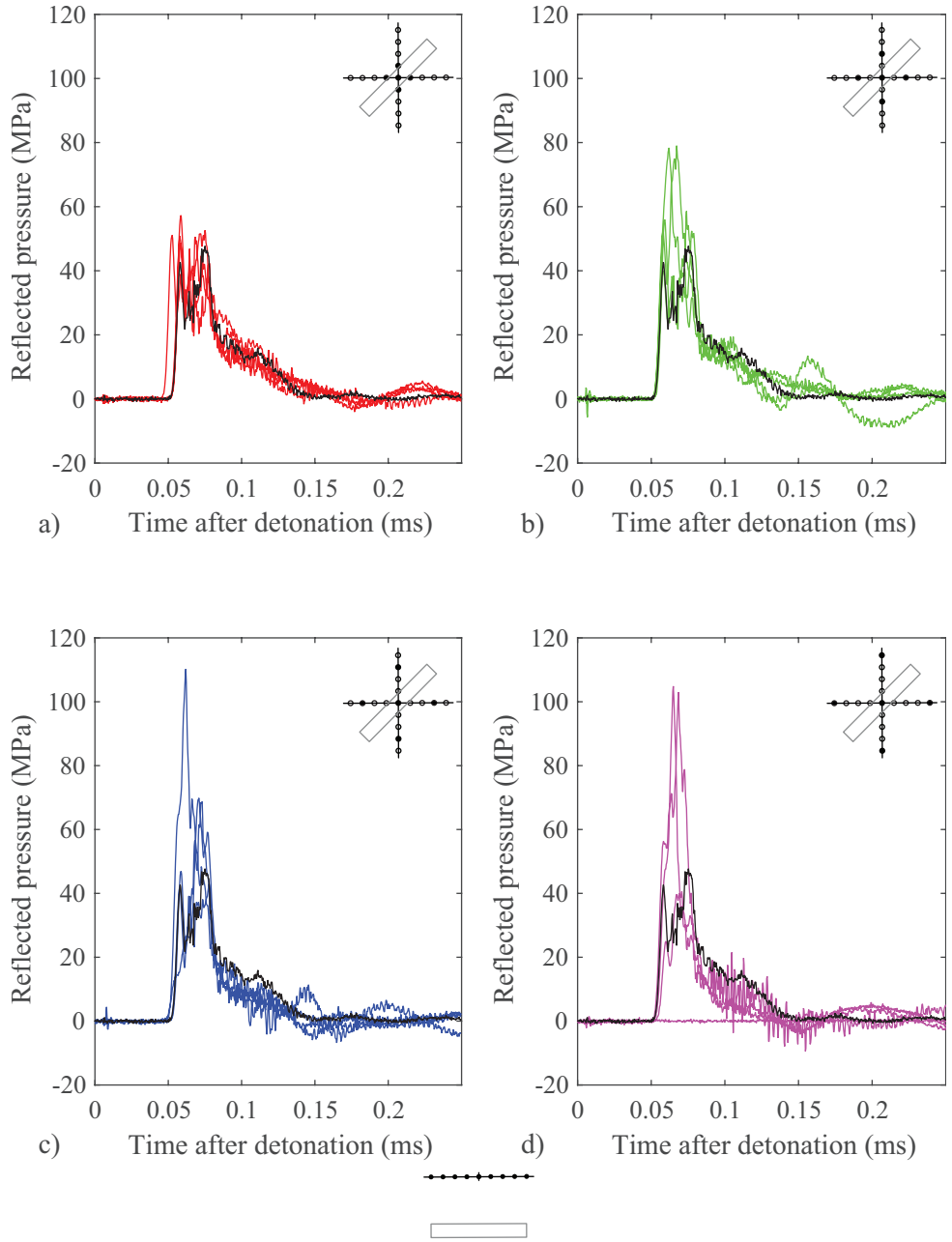


Figure 4.22: Reflected pressure time histories for test T008 (radial cylindrical charge, 45°, 0° orientation, centrally detonated). Results are shown for radial offsets of (a) 25 mm (red), (b) 50 mm (green), (c) 75 mm (blue), and (d) 100 mm (magenta), compared against the central reference measurement (0 mm, black). For each radial position, measurements are presented for perpendicular sensor arrays (left column) and aligned sensor arrays (right column). Insets indicate the relative orientation of the charge and sensor configuration.

at the 50 mm and 75 mm positions, which act to reduce the specific impulse notably from its peak value towards the end of the period of interest.

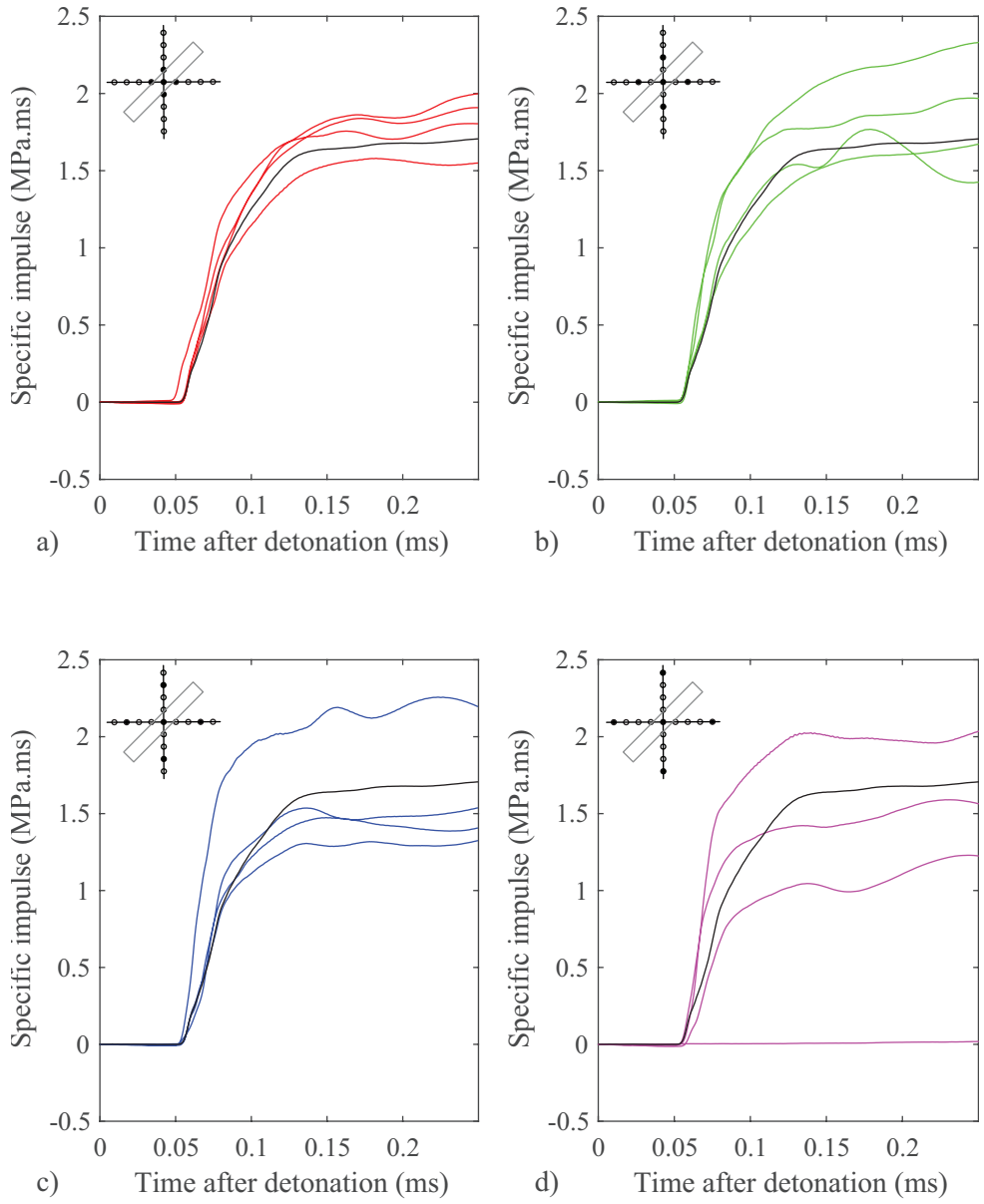


Figure 4.23: Specific impulse time histories for test T008 (radial cylindrical charge, 45°, 0° orientation, centrally detonated). Results are shown for radial offsets of a) 25 mm (red), b) 50 mm (green), c) 75 mm (blue), and d) 100 mm (magenta), compared against the central reference measurement (0 mm, black). For each radial position, measurements are presented for perpendicular sensor arrays (left column) and aligned sensor arrays (right column). Insets indicate the relative orientation of the charge and sensor configuration.

T009

The reflected pressure histories recorded during Test T009 are presented in Figure 4.24, using the same array configuration and subplot arrangement as described for Test T008. No dead bars were recorded during this test.

The pressure profiles exhibit broadly consistent maximum peak pressures across all radial distances, with the greatest peak recorded at each position being of comparable magnitude across the instrumented array. However, the agreement between the individual bar traces within each radial position is more variable. A distinguishing feature of the T009 results is the behaviour of the central bar, which records a comparatively low peak pressure but exhibits a consistently elevated pressure tail relative to the radial bar measurements, suggesting a more sustained loading at the central position.

The specific impulse histories for Test T009 are presented in Figure 4.25. Greater variability is observed between the individual traces at the 25 mm and 100 mm positions compared to the equivalent results in Test T008, whilst a better agreement is observed at 50 mm and 75 mm. The irregular influence of negative phases noted in Test T008 is largely absent in the T009 results, resulting in a cleaner set of impulse histories. Nevertheless, as with Test T008, the inter-bar variability across the radial positions makes it difficult to establish a clear trend in peak specific impulse.

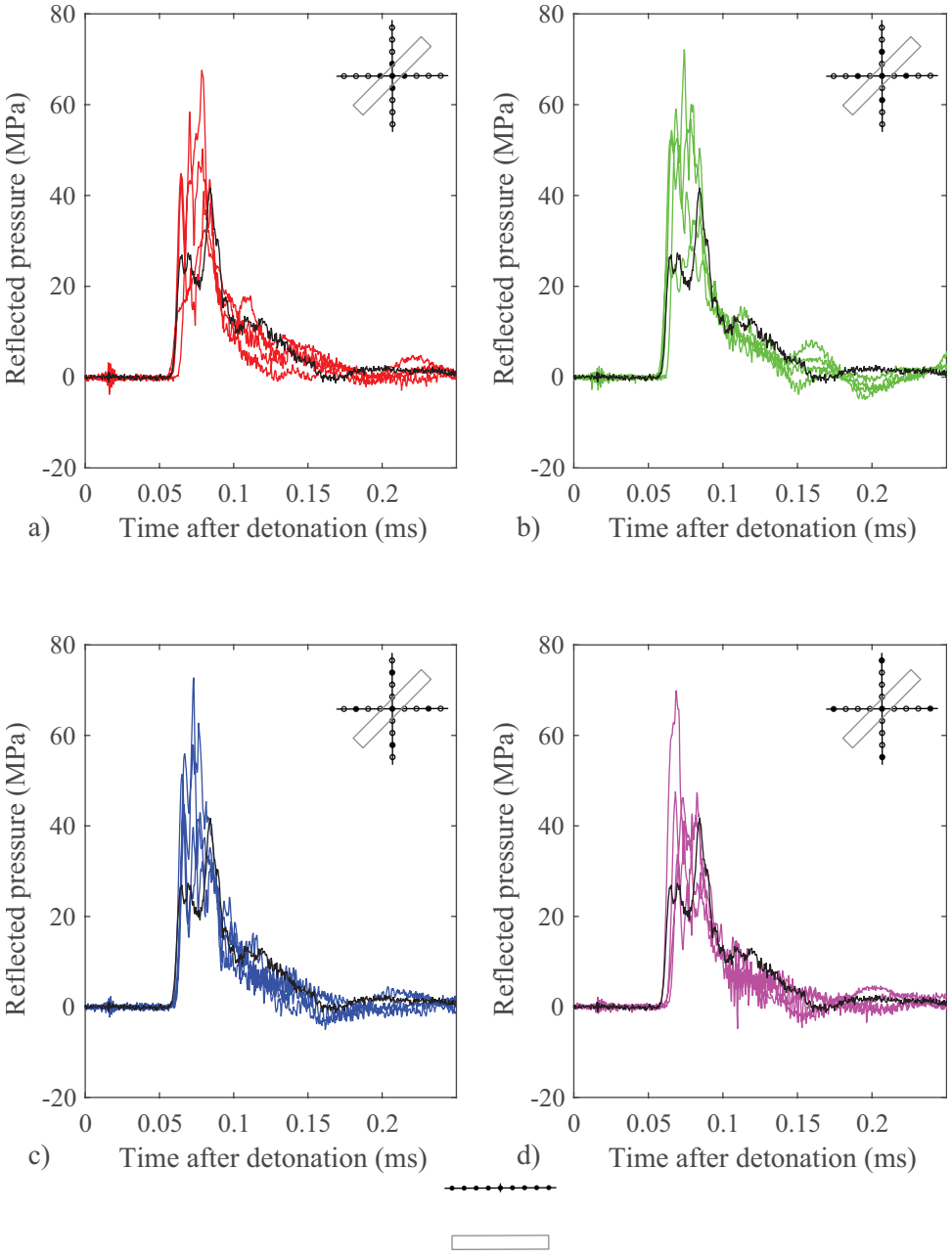


Figure 4.24: Reflected pressure time histories for test T009 (radial cylindrical charge, 45°, 0° orientation, centrally detonated). Results are shown for radial offsets of (a) 25 mm (red), (b) 50 mm (green), (c) 75 mm (blue), and (d) 100 mm (magenta), compared against the central reference measurement (0 mm, black). For each radial position, measurements are presented for perpendicular sensor arrays (left column) and aligned sensor arrays (right column). Insets indicate the relative orientation of the charge and sensor configuration.

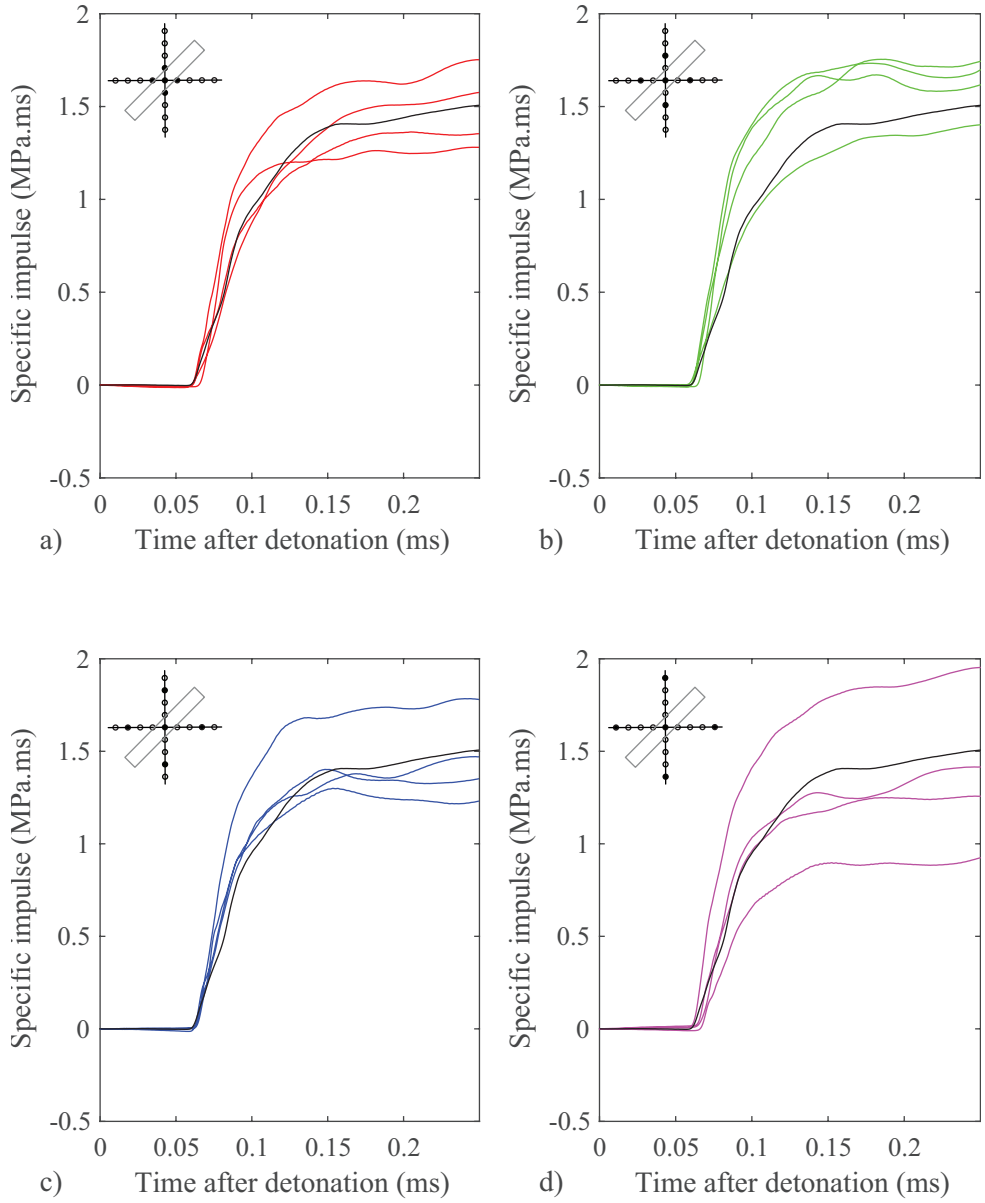


Figure 4.25: Specific impulse time histories for test T009 (radial cylindrical charge, 45°, 0° orientation, centrally detonated). Results are shown for radial offsets of a) 25 mm (red), b) 50 mm (green), c) 75 mm (blue), and d) 100 mm (magenta), compared against the central reference measurement (0 mm, black). For each radial position, measurements are presented for perpendicular sensor arrays (left column) and aligned sensor arrays (right column). Insets indicate the relative orientation of the charge and sensor configuration.

4.4.2 Compiled results

The reflected pressure histories from Tests T008 and T009 are presented collectively in Figure 4.26, following the same subplot arrangement as described for the preceding comparative figures. Graphs a) and b) correspond to Tests T008 and T009 respectively, and c) presents the unweighted cross-test mean. As all bars at equivalent radial distances are nominally identical in this orientation, each trace represents the mean of up to four bars at each radial position. Where a bar did not record a valid pressure trace, the corresponding zero-value trace was excluded from the averaging process prior to computation of the mean; with up to four bars contributing to each average, the influence of any single excluded trace on the resulting mean is correspondingly reduced.

Both tests exhibit a narrow window of elevated pressure of approximately 0.03 ms, followed by a tail of diminishing pressure across all radial distances. This tail is more prominent in Test T008, where a reduction in amplitude with increasing radial distance is observed, consistent with a clearing effect propagating inwards from the edges of the array. Whilst this feature contributes to the cross-test mean, c), its influence is diminished relative to the individual T008 result. The averaged traces in c) provide a good representation of the two individual test averages, capturing the key loading characteristics observed across both tests.

The specific impulse histories from Tests T008 and T009 are presented in Figure 4.27, following the same arrangement as Figure 4.26. The averaged traces for both individual tests present a good representation of the loading, with the 25 mm and 50 mm radial positions recording the highest peak specific impulse values. This is consistent with the extended positive phase duration observed at these positions in the pressure data, which results in a greater accumulation of specific impulse despite the elevated peak pressures recorded at the higher radial distances. The cross-test mean in c) provides a representative averaged profile across both tests.

The peak reflected pressures from Tests T008 and T009 are presented in Figure 4.28, with each data point representing an individual bar measurement and up to four data points per radial position per test. The T008 results exhibit considerable variability, with a trend of increasing peak pressure with radial distance from the centre outwards. The T009 results show a comparatively even distribution of peak pressures across the array. The compiled results demonstrate an overall trend of increasing peak reflected pressure with radial distance from the centre, reflecting the elevated loading at the outer positions observed consistently across both tests.

The peak specific impulse values from Tests T008 and T009 are presented in Figure 4.29, following the same arrangement as Figure 4.28. Both tests exhibit greater variability in peak specific impulse at positions further from the centre, whilst the compiled results reveal a complimenting trend to that observed in the peak pressure data, with the specific impulse concentrated towards the intermediate radial positions of 50 mm and 75 mm. This reflects the combined influence of the elevated peak pressures and extended positive phase

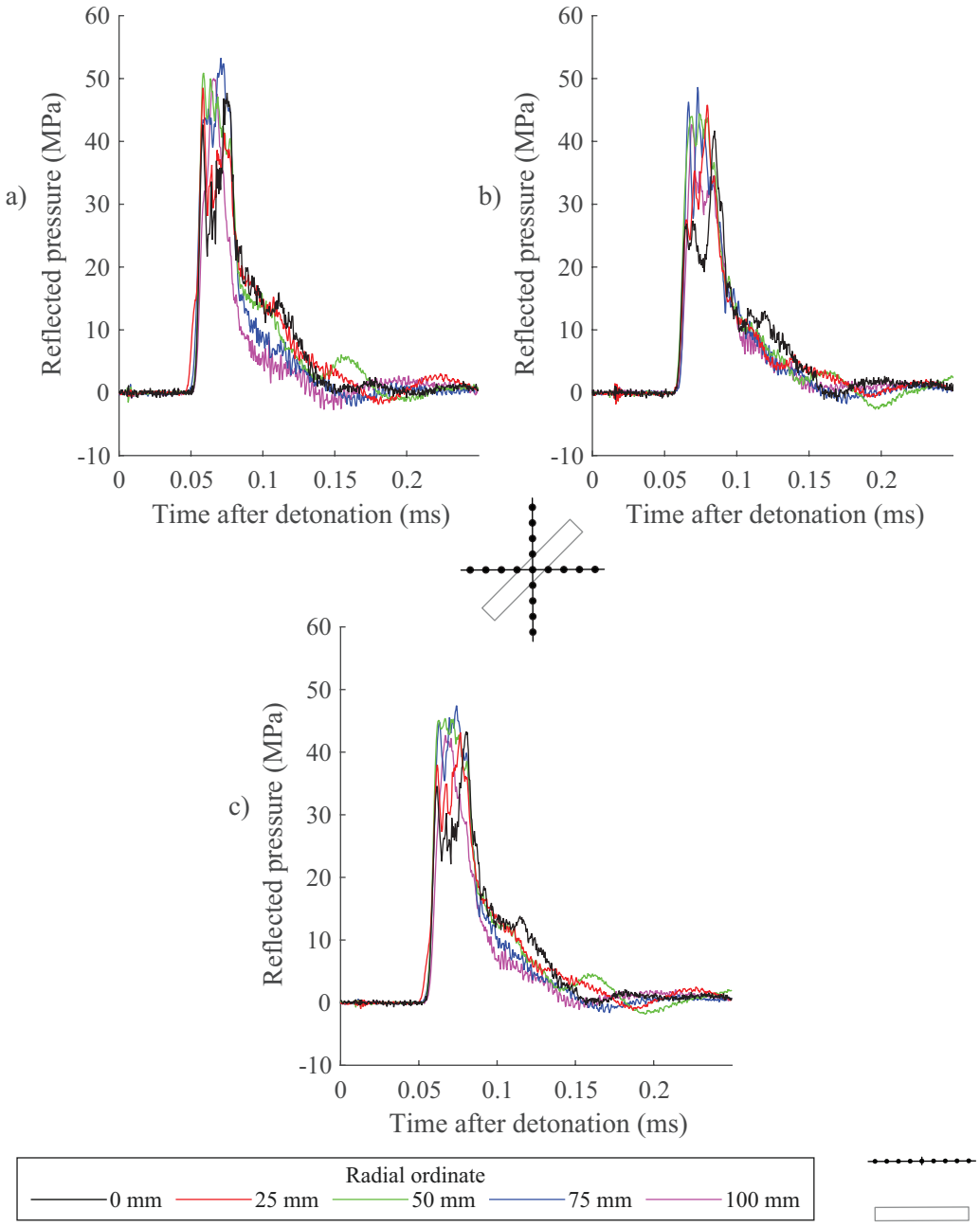


Figure 4.26: Reflected pressure time histories for radial cylindrical charges (45°, 0° orientation, centrally detonated) for tests a) T008, b) T009, with c) showing the average of the two tests, aligned by the arrival time at the central reference measurement (0 mm, black). Traces are shown for radial offsets of 0 mm (black), 25 mm (red), 50 mm (green), 75 mm (blue), and 100 mm (magenta). For each case, the perpendicular sensor array is presented in the left column, with the aligned array shown in the middle and right columns (opposing sides). Insets indicate the relative orientation of the charge and sensor configuration.

durations at these locations, resulting in a greater total energy delivery to the intermediate positions relative to the outermost bars.

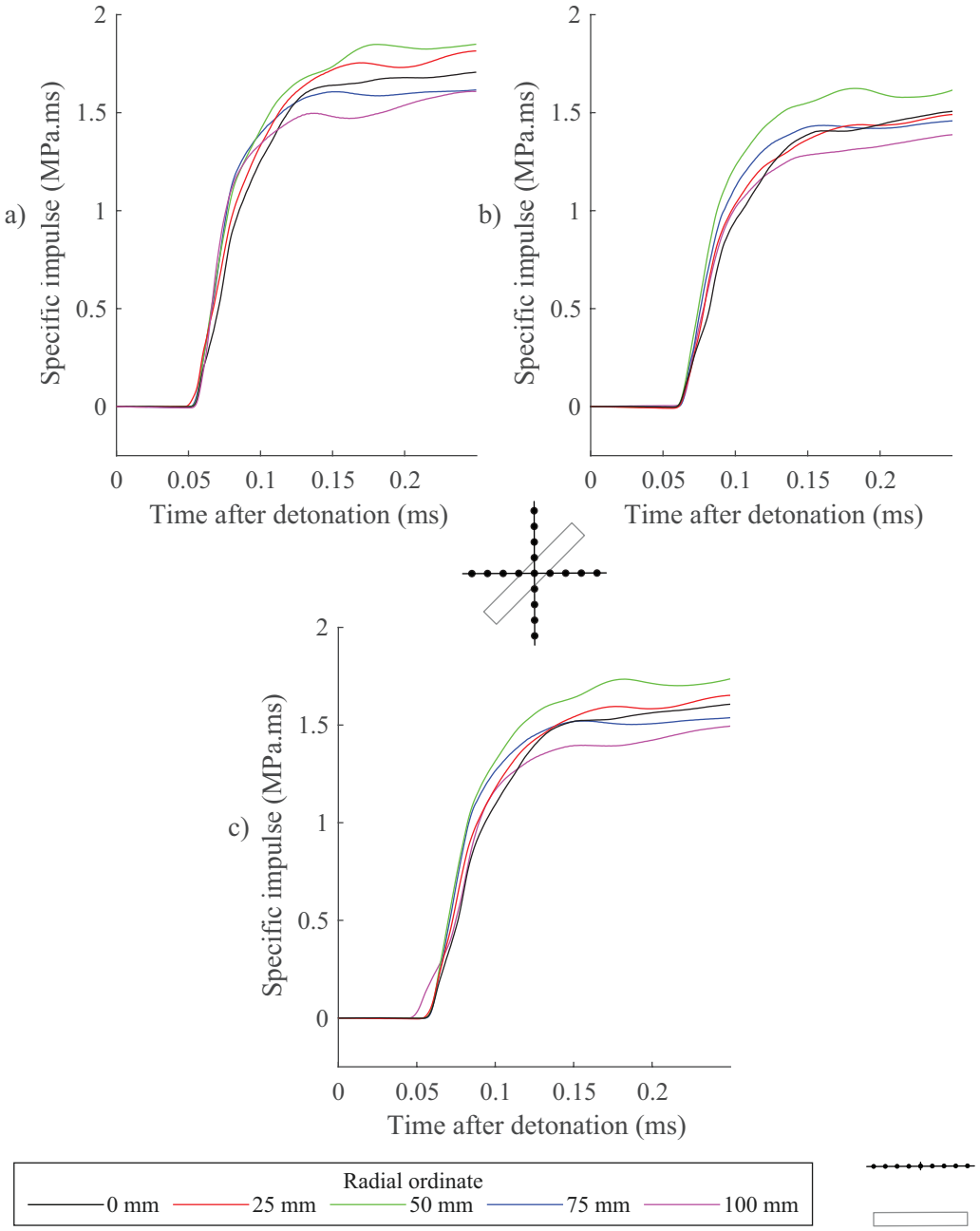


Figure 4.27: Specific impulse time histories for radial cylindrical charges (45°, 0° orientation, centrally detonated) for tests a) T008, b) T009, with c) showing the average of the two tests, aligned by the arrival time at the central reference measurement (0 mm, black). Traces are shown for radial offsets of 0 mm (black), 25 mm (red), 50 mm (green), 75 mm (blue), and 100 mm (magenta). For each case, the perpendicular sensor array is presented in the left column, with the aligned array shown in the middle and right columns (opposing sides). Insets indicate the relative orientation of the charge and sensor configuration.

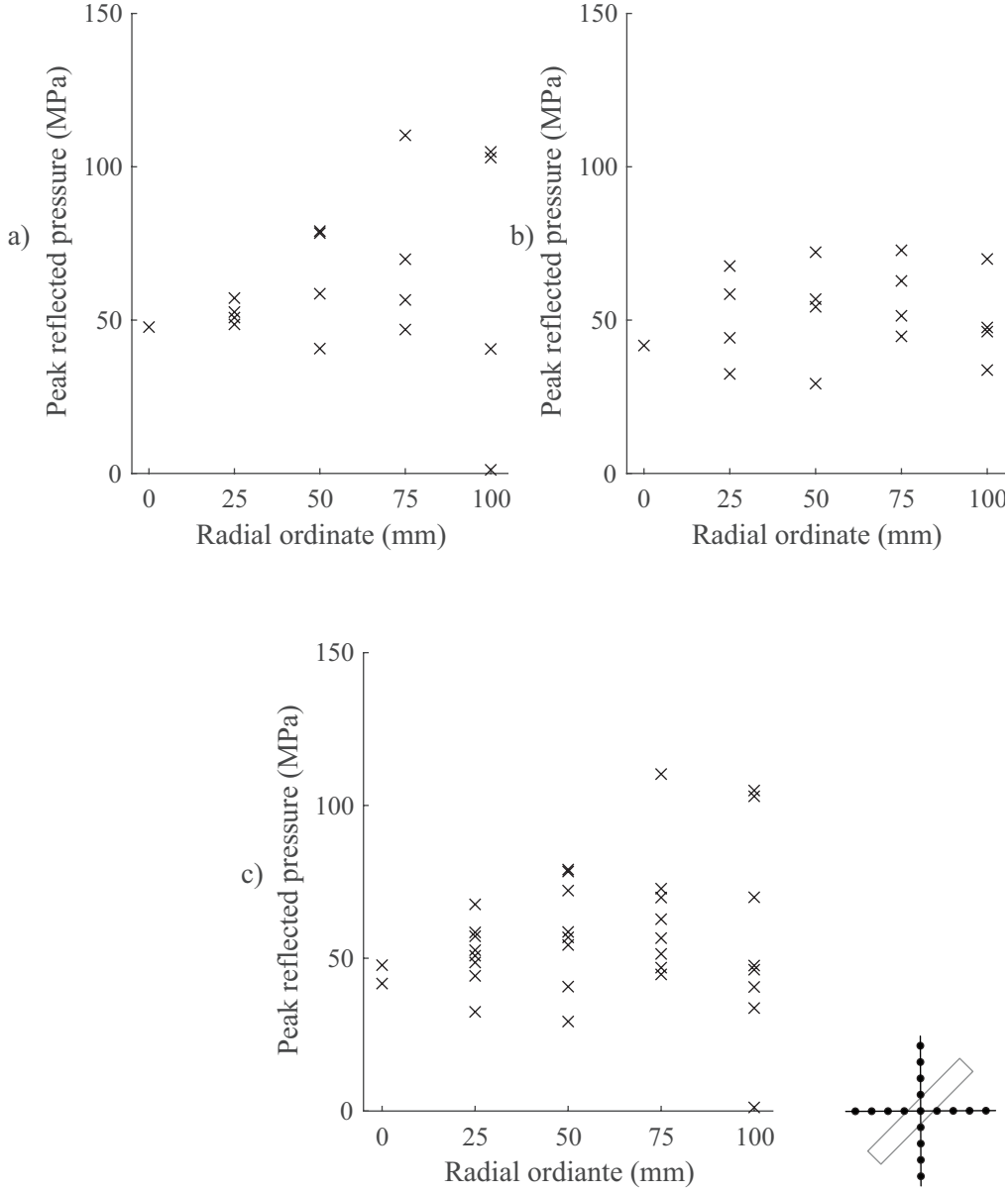


Figure 4.28: Peak reflected pressures for radial cylindrical charges ($45°, 0°$ orientation, centrally detonated) for tests a) T008, b) T009, with c) showing a collation of the two tests. For each case, the perpendicular sensor array is presented in the left column, with the aligned array shown in the right column. Insets indicate the relative orientation of the charge and sensor configuration.

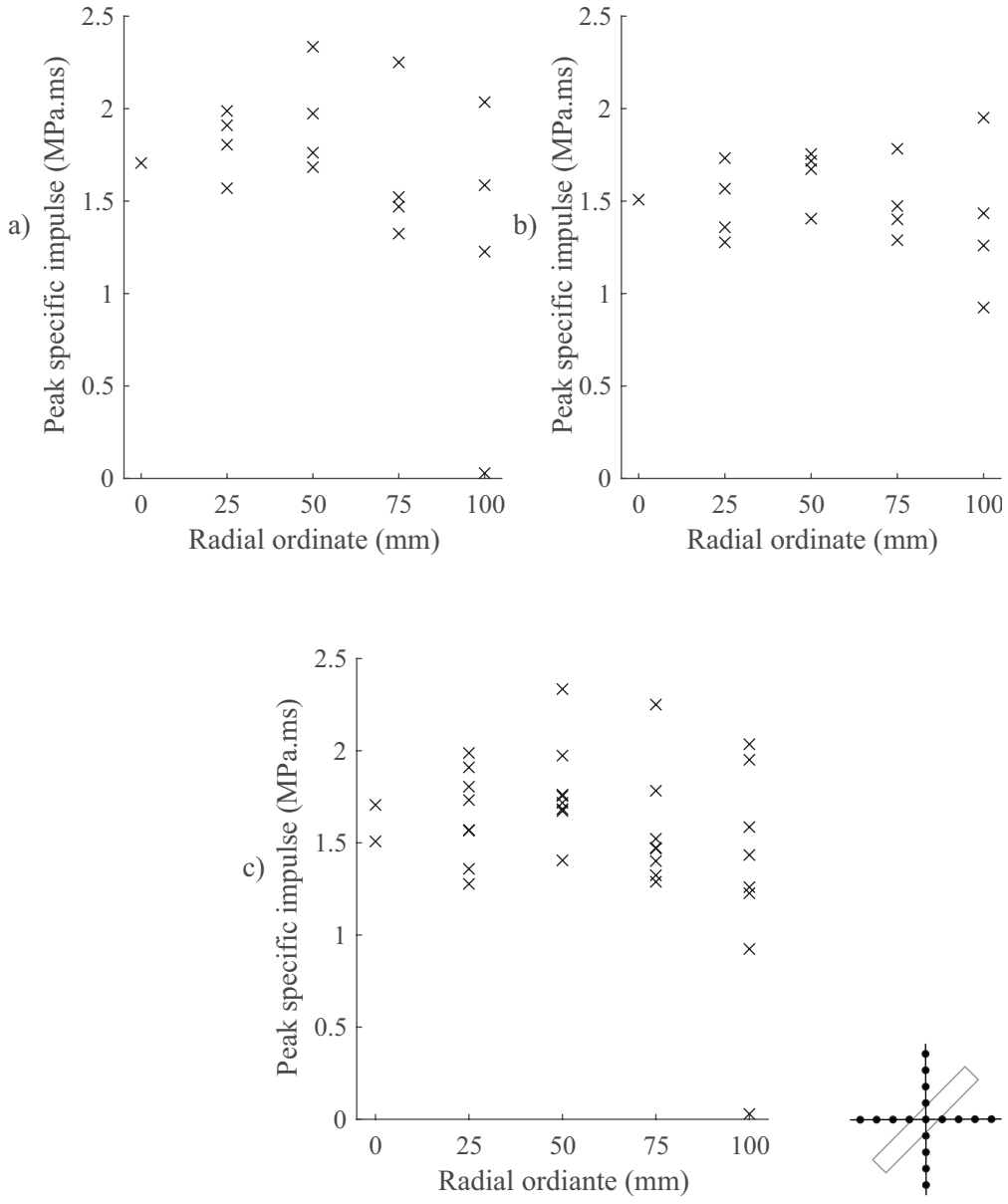


Figure 4.29: Peak specific impulses for radial cylindrical charges (45°, 0° orientation, centrally detonated) for tests a) T008, b) T009, with c) showing a collation of the two tests. For each case, the perpendicular sensor array is presented in the left column, with the aligned array shown in the right column. Insets indicate the relative orientation of the charge and sensor configuration.

4.5 Cylindrical tests – Inclined (0°, 22.5°)

4.5.1 Test Results

The following section presents the reflected pressure and specific impulse results obtained from cylindrical charges inclined at 22.5° to the reflecting plate, with the charge axis aligned at 0° to the instrumented bar array. The inclination of the charge introduces an asymmetry to the reflecting plate, such that the two parallel arrays are no longer nominally identical in their geometric relationship to the charge, whilst the perpendicular arrays remain symmetric about the charge axis. The results are presented in the same format as the centrally detonated radial tests in Section 4.2, with individual test figures arranged as a matrix of four rows and two columns, with the left column presenting the perpendicular array results and the right column presenting the parallel array results. The comparative figures follow the same four-row arrangement, with rows a), b), and c) corresponding to Tests T020, T021, and T023 respectively, and row d) presenting the cross-test mean or compiled results as appropriate.

T020

The reflected pressure histories recorded during Test T020 are presented in Figure 4.30, using the same array configuration and subplot arrangement as described for the centrally detonated radial tests. The central bar trace is included in all subplots as a consistent spatial reference. It is noted that one of the 50 mm parallel bars did not record a valid pressure trace during this test and is represented as a zero-value flat line in the figure.

The perpendicular results exhibit good repeatability between the two bars at each radial position, with all traces displaying a similar waveform character to the central bar; a moderate initial peak followed by two lesser peaks before decaying to ambient. The 50 mm position records a slightly greater peak pressure than the 25 mm and 75 mm positions, which are broadly similar to one another, whilst the 100 mm bars record the lowest peak pressures of the radial array, consistent with the shock wave attenuation at the greatest radial distance and angle of incidence with the plate.

The parallel results exhibit a notably more varied response. At 25 mm, one bar records a significantly elevated peak pressure, with the other bar recording approximately half the magnitude. This represents the only position in the parallel array where a bar arrives earlier than the central bar, consistent with its proximity to the inclined charge. At 50 mm, the surviving bar records a low pressure trace, broadly in line with the lower results at other parallel positions, whilst the dead bar is represented as a zero-value flat line. At 75 mm and 100 mm, the two parallel bars at each position exhibit notably different temporal characteristics; one trace exhibits a Friedlander-like decay from the peak, whilst the other displays a longer positive phase duration. Furthermore, the accentuated wave arrives with a notable delay relative to the central bar and bar of same radial ordinate, consistent with the asymmetric blast propagation expected from the inclined charge geometry.

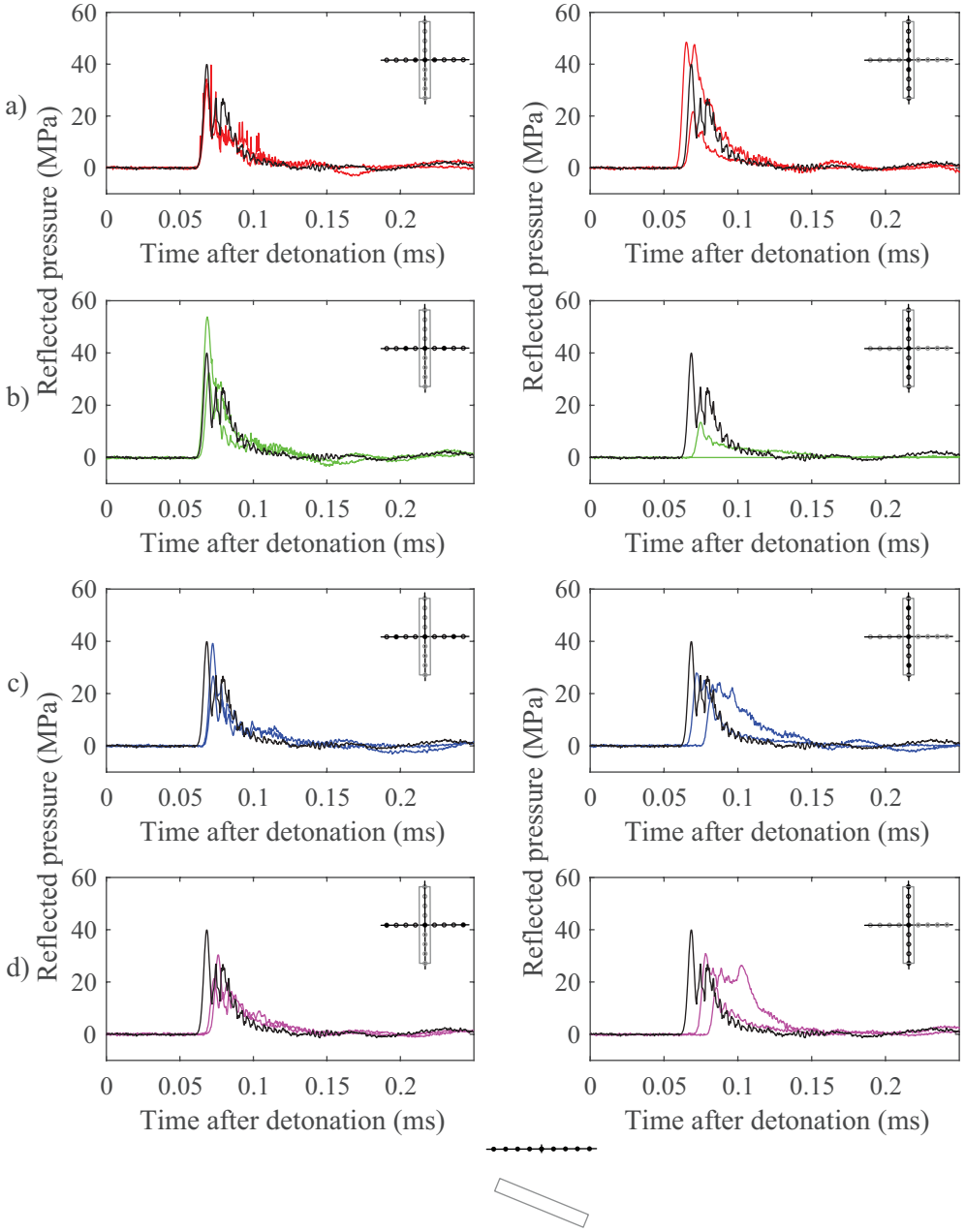


Figure 4.30: Reflected pressure time histories for test T020 (inclined cylindrical charge, $0°, 22.5°$ orientation, centrally detonated). Results are shown for radial offsets of (a) 25 mm (red), (b) 50 mm (green), (c) 75 mm (blue), and (d) 100 mm (magenta), compared against the central reference measurement (0 mm, black). For each radial position, measurements are presented for perpendicular sensor arrays (left column) and aligned sensor arrays (right column). Insets indicate the relative orientation of the charge and sensor configuration.

The specific impulse histories for Test T020 are presented in Figure 4.31. The perpendicular impulse results exhibit similar traces across all radial distances, with a subtle downward trend in peak specific impulse with increasing radial distance. The exception is at 50 mm, where a greater difference between the two bars is observed, bucking the otherwise consistent trend. The parallel impulse results exhibit considerably greater variation, with the higher

of the two traces at each position recording peak specific impulse values of approximately 150% greater than the lower trace at the same radial distance. The surviving 50 mm parallel bar follows the general trend of the lower value in the parallel array, whilst the dead bar is represented as a zero-value trace and excluded from subsequent averaging.

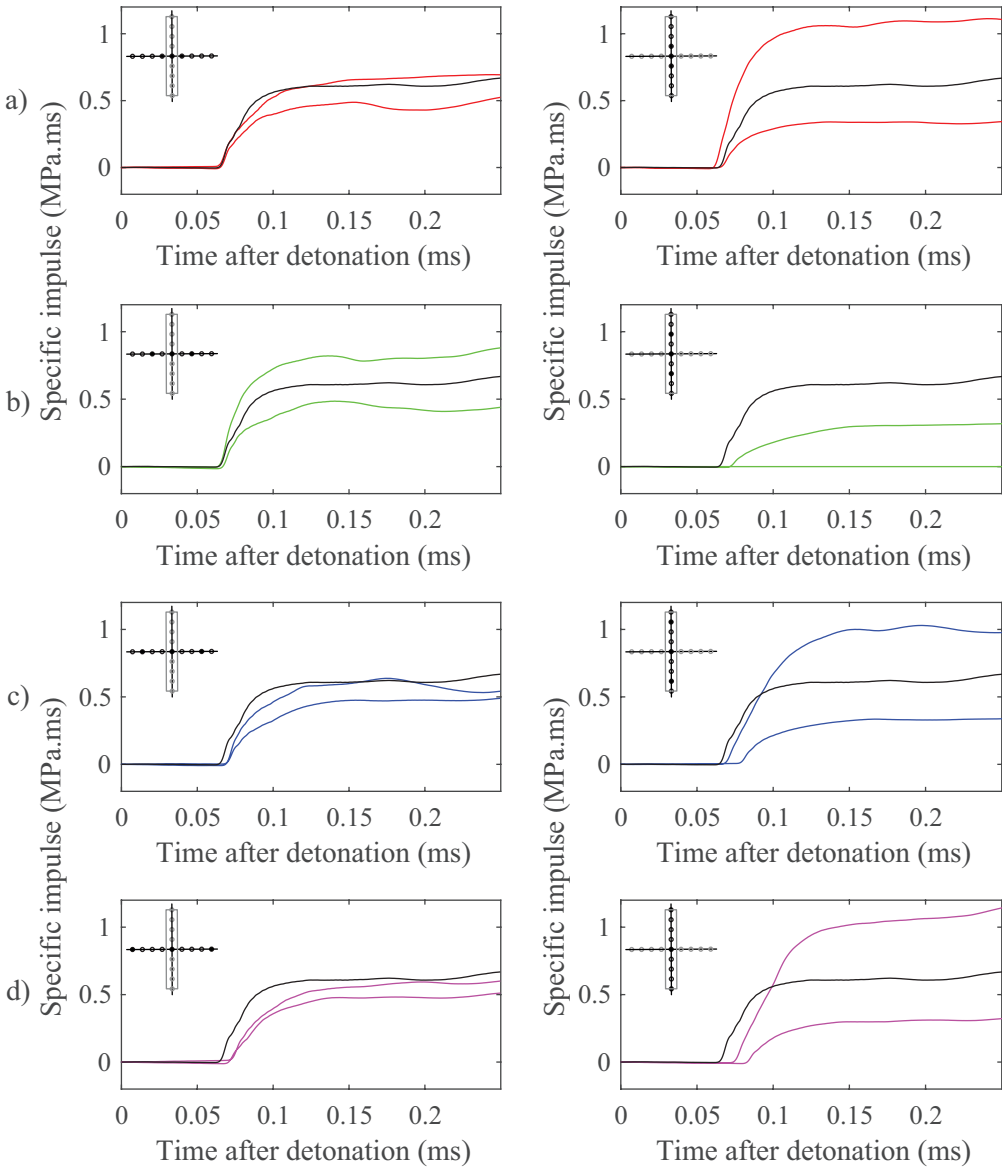


Figure 4.31: Specific impulse time histories for test T020 (inclined cylindrical charge, $0°, 22.5°$ orientation, centrally detonated). Results are shown for radial offsets of a) 25 mm (red), b) 50 mm (green), c) 75 mm (blue), and d) 100 mm (magenta), compared against the central reference measurement (0 mm, black). For each radial position, measurements are presented for perpendicular sensor arrays (left column) and aligned sensor arrays (right column). Insets indicate the relative orientation of the charge and sensor configuration.

T021

The reflected pressure histories recorded during Test T021 are presented in Figure 4.32, using the same array configuration and subplot arrangement as described for the preceding tests. The central bar trace is included in all subplots as a consistent spatial reference. It is noted that one of the 50 mm parallel bars did not record a valid pressure trace during this test and is represented as a zero-value flat line in the figure.

The perpendicular results exhibit good repeatability between the two bars at the 25 mm and 50 mm positions, with pressure profiles consistent with the waveform character observed in Test T020. Greater variation between the paired traces is observed at the 75 mm and 100 mm positions. A late arriving shock wave is observed in one of the 100 mm perpendicular traces at approximately 0.08 ms, for which no suspected cause has been identified. The strong central bar pressure recording in this test makes the radial ordinates appear relatively smaller in comparison, although the underlying trends remain consistent with those observed in Test T020.

The parallel results exhibit broadly similar characteristics to Test T020. One of the 25 mm parallel bars again records an elevated peak pressure arriving before the central bar, consistent with the same phenomenon identified in Test T020. The surviving 50 mm parallel bar exhibits no discernible shock front, presenting instead as a broad pressure hump; given the low peak pressures observed at the 75 mm and 100 mm positions, this is considered potentially representative of the genuine loading at this location rather than a gauge anomaly. At 75 mm and 100 mm, both parallel bars record low peak pressures with long positive phase durations.

The specific impulse histories for Test T021 are presented in Figure 4.33. The strong central bar pressure recording results in a peak specific impulse approximately twice that observed in Test T020, providing an adjusted reference against which the radial ordinates appear relatively lower, despite their absolute values being broadly similar to those of Test T020. The perpendicular impulse results exhibit similar traces across radial distances, with a subtle downward trend in peak specific impulse with increasing radial distance. The exception is at 100 mm, where the late arriving shock wave identified in the pressure data contributes additional impulse to one of the traces, resulting in a greater difference between the two bars at this position and a deviation from the otherwise consistent downward trend. The parallel impulse histories exhibit a similarly large difference between the higher and lower traces at each radial position as observed in Test T020, consistent with the asymmetric loading introduced by the charge inclination.

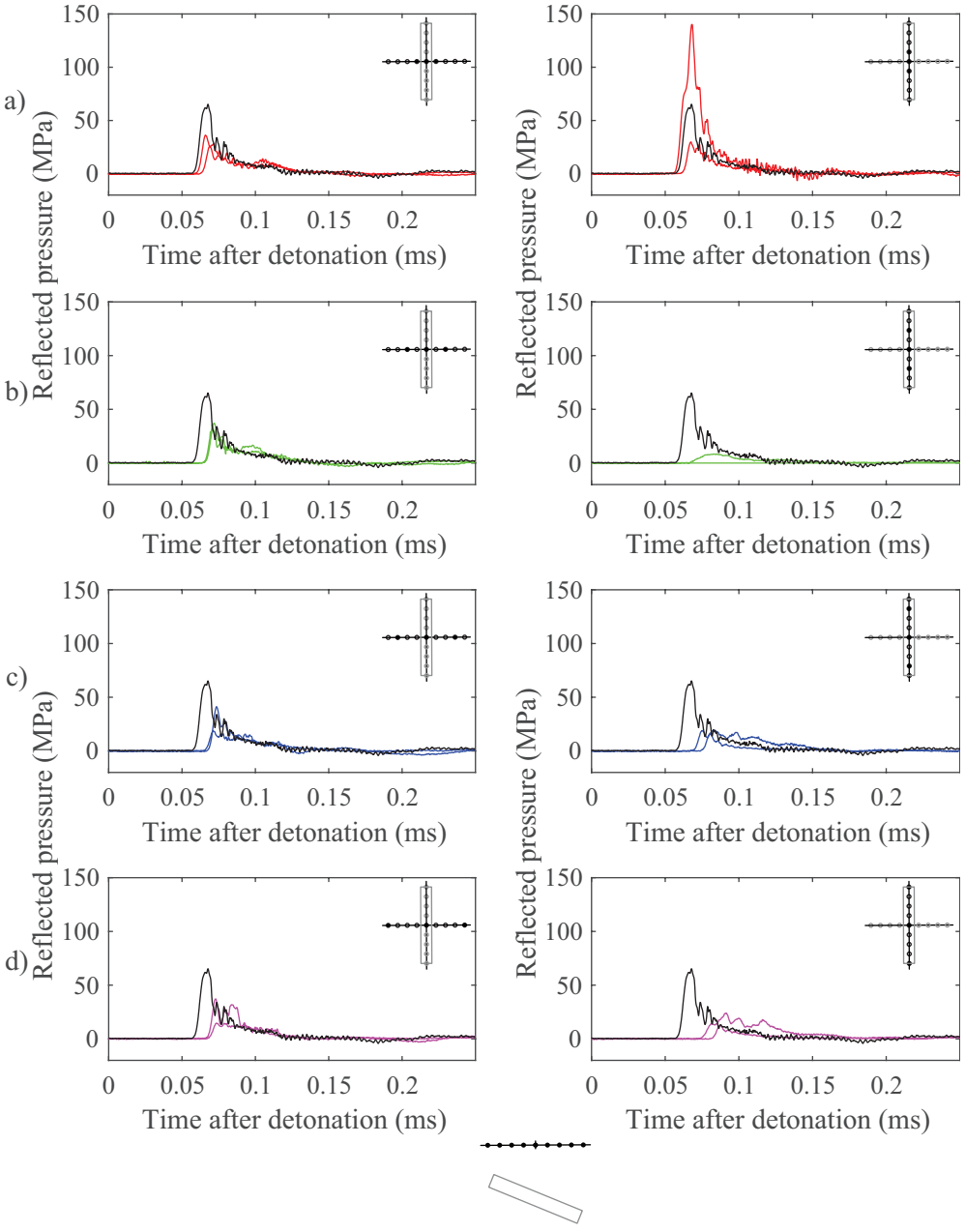


Figure 4.32: Reflected pressure time histories for test T021 (inclined cylindrical charge, $0°, 22.5°$ orientation, centrally detonated). Results are shown for radial offsets of (a) 25 mm (red), (b) 50 mm (green), (c) 75 mm (blue), and (d) 100 mm (magenta), compared against the central reference measurement (0 mm, black). For each radial position, measurements are presented for perpendicular sensor arrays (left column) and aligned sensor arrays (right column). Insets indicate the relative orientation of the charge and sensor configuration.

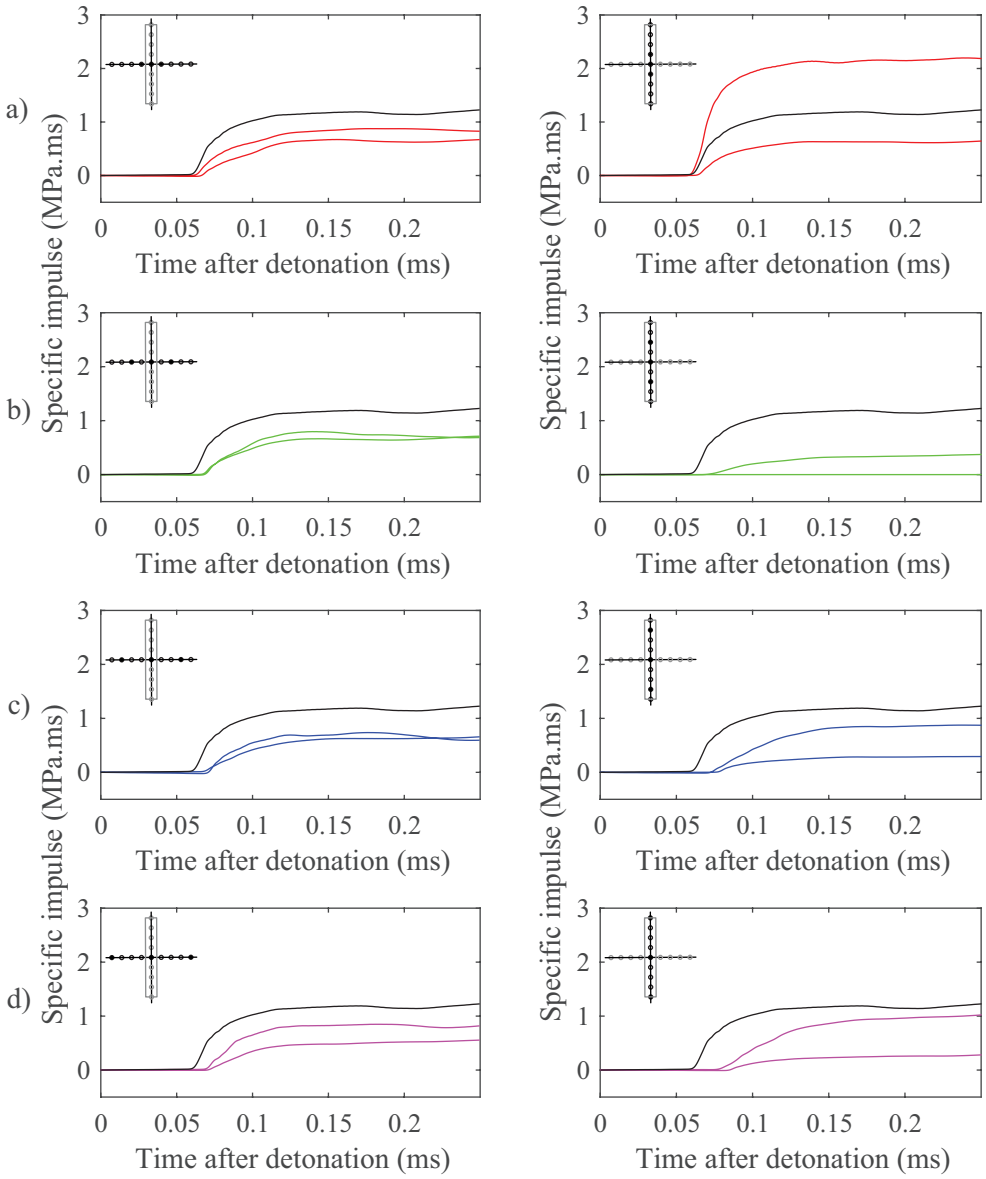


Figure 4.33: Specific impulse time histories for test T021 (inclined cylindrical charge, $0°, 22.5°$ orientation, centrally detonated). Results are shown for radial offsets of a) 25 mm (red), b) 50 mm (green), c) 75 mm (blue), and d) 100 mm (magenta), compared against the central reference measurement (0 mm, black). For each radial position, measurements are presented for perpendicular sensor arrays (left column) and aligned sensor arrays (right column). Insets indicate the relative orientation of the charge and sensor configuration.

T023

The reflected pressure histories recorded during Test T023 are presented in Figure 4.34, using the same array configuration and subplot arrangement as described for the preceding tests. The central bar trace is included in all subplots as a consistent spatial reference. It is noted that one of the 50 mm parallel bars did not record a valid pressure trace during this test and is represented as a zero-value flat line in the figure.

The perpendicular results exhibit good repeatability between the two bars at each radial position, with pressure profiles broadly consistent with those observed in previous tests, with the central bar recording a pressure magnitude comparable to that of Test T020 rather than the elevated values seen in Test T021. One of the 25 mm perpendicular bars exhibits noise on the recorded trace, manifesting as short single-sample-point spikes superimposed on the underlying waveform. The pressure profile remains discernible despite this noise and the trace is retained in the analysis, though the spurious spikes should be disregarded in the interpretation of the results.

The parallel results differ notably from those observed in Tests T020 and T021. At 25 mm, the consistently elevated early-arriving peak seen in the preceding tests is largely absent, with that bar recording a much reduced response arriving simultaneously with the central bar. At 50 mm, the surviving bar exhibits a Friedlander-like pressure profile, whilst the dead bar is represented as a zero-value flat line. At 75 mm, one bar exhibits a Friedlander-like profile consistent with the 50 mm result, whilst the other records a lower magnitude pressure wave with a longer positive phase duration and a delayed arrival relative to the central bar. At 100 mm, one bar records a large pressure wave of long positive phase duration, with a peak magnitude broadly equivalent to that of the central bar, whilst the other bar records a response consistent with the expectations established by the previous tests at this position.

The specific impulse histories for Test T023 are presented in Figure 4.35. The perpendicular impulse results exhibit profiles broadly similar to those observed in Test T020, with a consistent distribution across radial distances. It is noted that the noise present in one of the 25 mm perpendicular pressure traces artificially elevates the computed specific impulse at this position through the integration process; these results should therefore be interpreted with caution and are not considered representative of the true specific impulse at this location.

The parallel impulse results reflect the pressure observations discussed above. At 25 mm, the diminished pressure wave compared to Tests T020 and T021 results in a correspondingly reduced difference between the two parallel traces at this position. A similar impulse trace is observed at 50 mm. The anomalously large long duration pressure wave recorded by one of the 100 mm parallel bars produces a considerably elevated specific impulse relative to both the central bar and the other bar at this position.

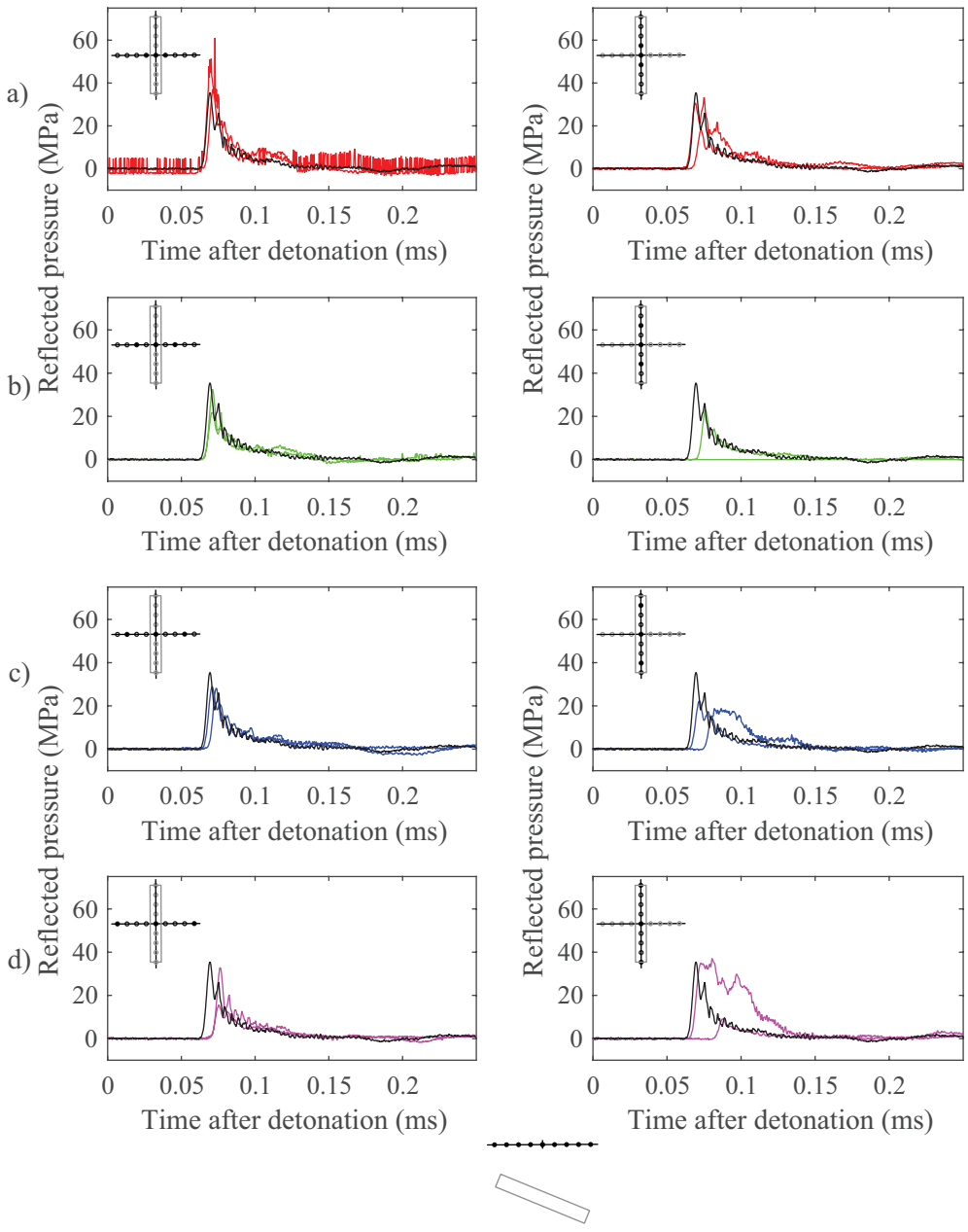


Figure 4.34: Reflected pressure time histories for test T023 (inclined cylindrical charge, $0°, 22.5°$ orientation, centrally detonated). Results are shown for radial offsets of (a) 25 mm (red), (b) 50 mm (green), (c) 75 mm (blue), and (d) 100 mm (magenta), compared against the central reference measurement (0 mm, black). For each radial position, measurements are presented for perpendicular sensor arrays (left column) and aligned sensor arrays (right column). Insets indicate the relative orientation of the charge and sensor configuration.

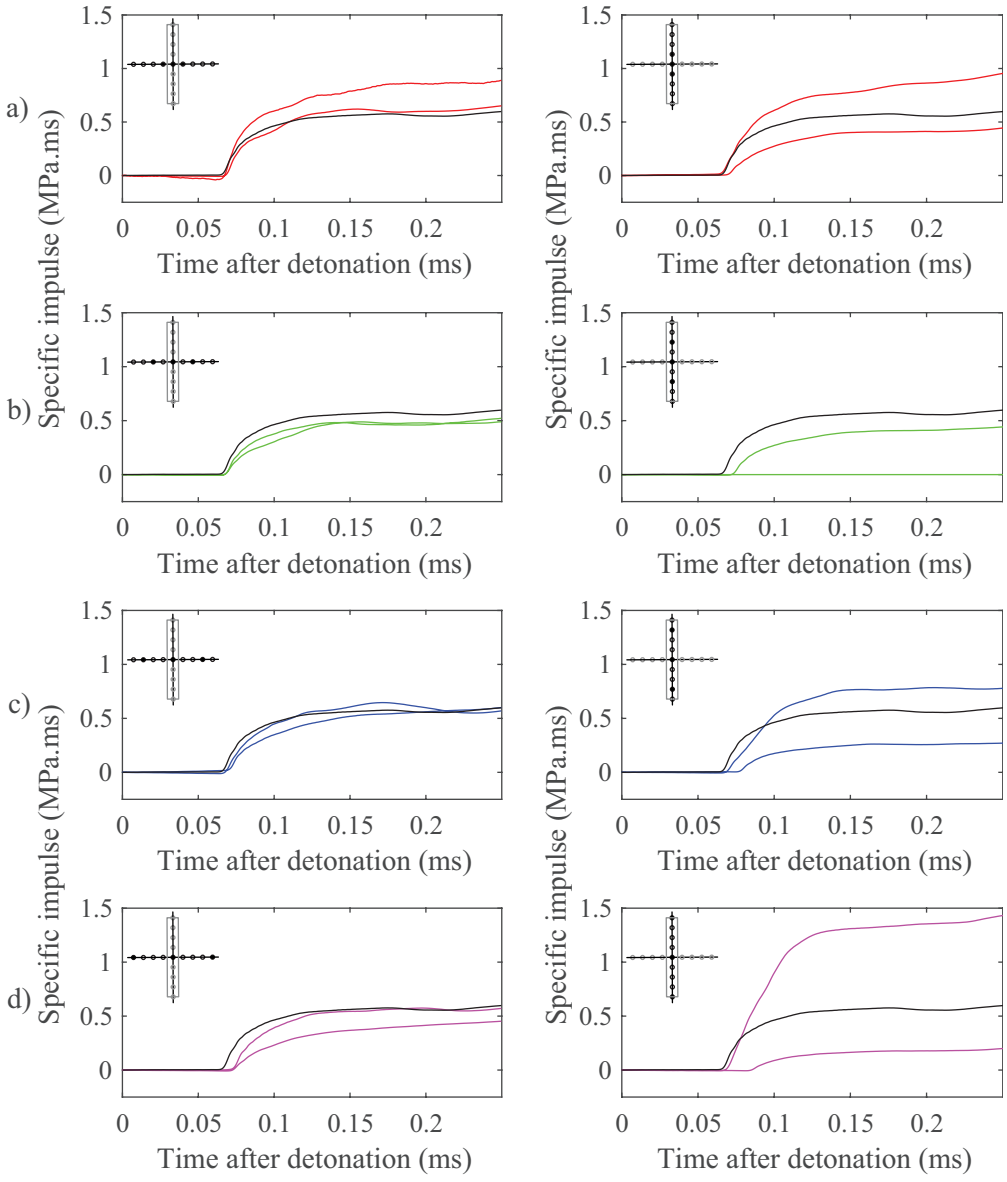


Figure 4.35: Specific impulse time histories for test T023 (inclined cylindrical charge, $0°, 22.5°$ orientation, centrally detonated). Results are shown for radial offsets of a) 25 mm (red), b) 50 mm (green), c) 75 mm (blue), and d) 100 mm (magenta), compared against the central reference measurement (0 mm, black). For each radial position, measurements are presented for perpendicular sensor arrays (left column) and aligned sensor arrays (right column). Insets indicate the relative orientation of the charge and sensor configuration.

4.5.2 Compiled results

The reflected pressure histories from Tests T020, T021, and T023 are presented collectively in Figure 4.36, following the same subplot arrangement as described for Figure 4.10, with rows a), b), and c) corresponding to Tests T020, T021, and T023 respectively, and row d) presenting the unweighted cross-test mean. The left column presents the averaged perpendicular array results, and the centre and right columns present the individual parallel array results. The + and − notation used to distinguish the two parallel columns is arbitrary but applied consistently throughout; it is noted that the charge is elevated on the − side of the array, as shown in the inset diagram.

The perpendicular results exhibit consistent pressure profiles across all three tests, with good agreement between equivalent radial positions and a waveform character broadly similar to that described for the spherical tests. The parallel results exhibit a more pronounced asymmetry between the two columns. The + parallel traces, corresponding to the side of the array further from the elevated charge, record higher and more prolonged pressure responses across all radial distances. The elevated peak pressure at the +25 mm position recorded in Test T021 is the most prominent feature of the comparative figure, dominating the individual test row and remaining clearly visible in the cross-test mean in row d).

The specific impulse histories from Tests T020, T021, and T023 are presented in Figure 4.37, following the same arrangement as Figure 4.36. The perpendicular and −parallel results exhibit consistent and comparatively low specific impulse values across the three tests, with good agreement between equivalent radial positions. The +parallel results exhibit elevated and more varied specific impulse histories, with the 25 mm and 100 mm positions consistently recording the highest peak specific impulse values across all three tests. It is noted that the +50 mm parallel bars did not record valid traces across all three tests and are therefore absent from the comparative figure at this position.

The peak reflected pressures from Tests T020, T021, and T023 are presented in Figure 4.38. The perpendicular results demonstrate a consistent slight decline in peak reflected pressure with increasing radial distance across all three tests. The parallel results exhibit a pronounced asymmetry, with a clear ramping up in peak pressure from −100 mm to +25 mm. This trend is most prominently driven by the Test T021 results, with the +25 mm position recording the highest peak pressures. The +50 mm position is absent from the compiled results due to the dead bars at this location across all three tests. The +75 mm and +100 mm positions record low peak pressures, consistent with the other side of the array.

The peak specific impulse values from Tests T020, T021, and T023 are presented in Figure 4.39, following the same arrangement as Figure 4.38. The perpendicular results exhibit a similar trend to the peak pressure data, with a consistent slight decline in peak specific impulse with increasing radial distance. The parallel results display a ramping up from −100 mm to +25 mm, a trend that is consistent across all three tests rather than being driven by a single test as observed in the peak pressure data. Notably, the +75 mm

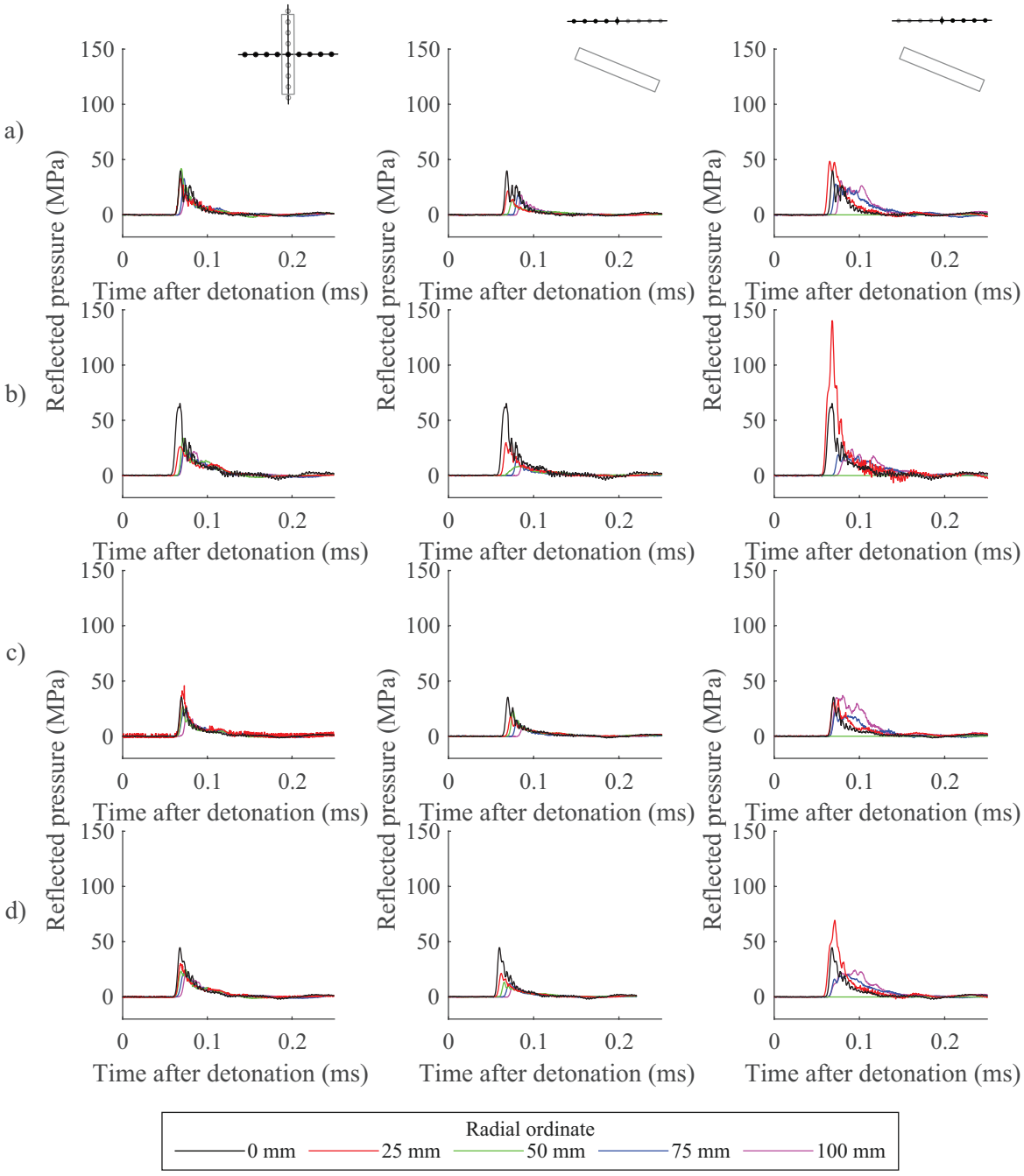


Figure 4.36: Reflected pressure time histories for inclined cylindrical charges ($0°, 22.5°$ orientation, centrally detonated) for tests a) T020, b) T021 and c) T023, with d) showing the average of the three tests, aligned by the arrival time at the central reference measurement (0 mm, black). Traces are shown for radial offsets of 0 mm (black), 25 mm (red), 50 mm (green), 75 mm (blue), and 100 mm (magenta). For each case, the perpendicular sensor array is presented in the left column, with the aligned array shown in the middle and right columns (opposing sides). Insets indicate the relative orientation of the charge and sensor configuration.

and +100 mm positions record increased peak specific impulse values relative to their peak pressures, consistent with the accumulation of impulse from the long positive phase duration pressure waves observed at these locations in the individual test results. The +50 mm position remains absent from the compiled results.

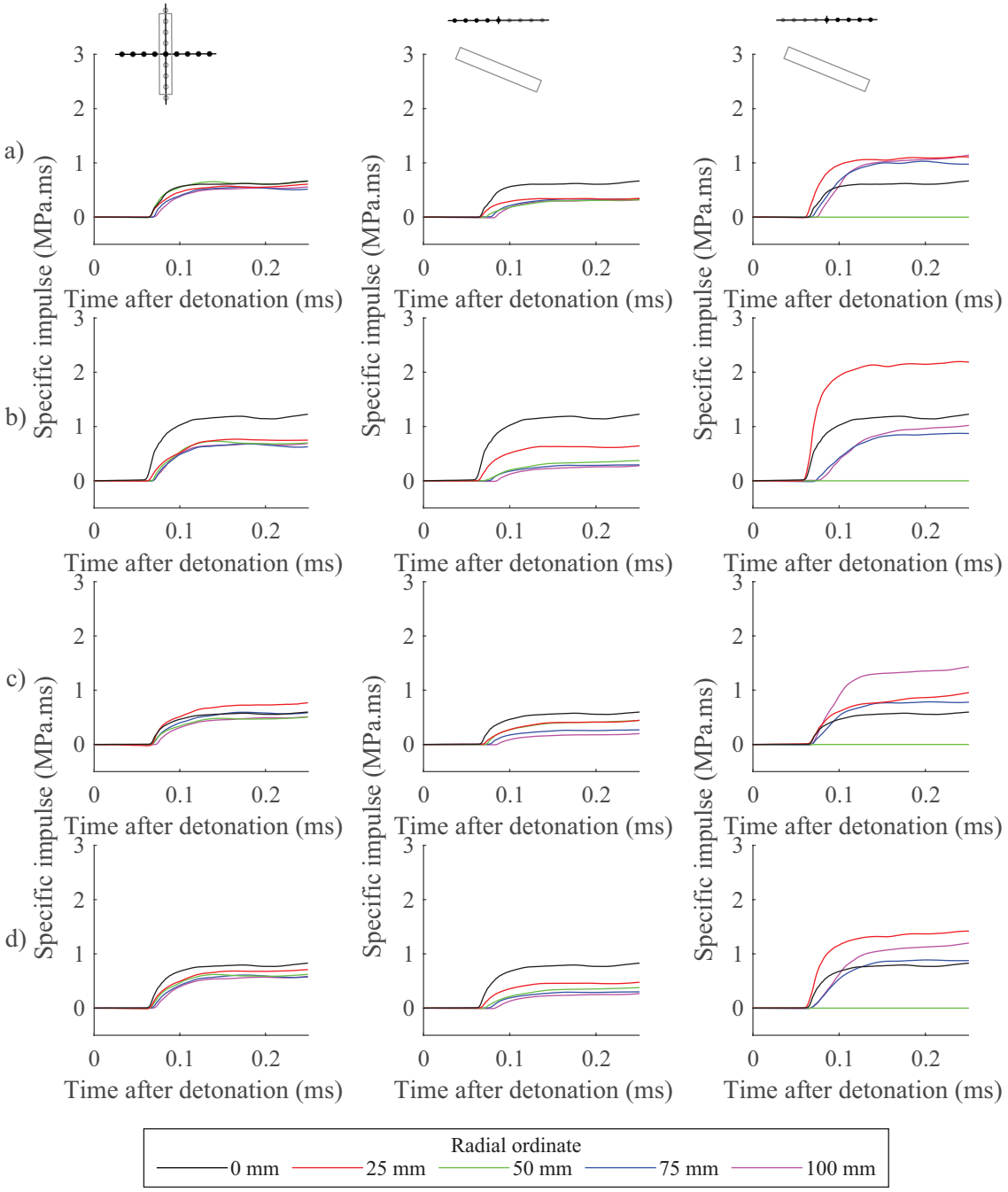


Figure 4.37: Specific impulse time histories for inclined cylindrical charges (0°, 22.5° orientation, centrally detonated) for tests a) T020, b) T021 and c) T023, with d) showing the average of the three tests, aligned by the arrival time at the central reference measurement (0 mm, black). Traces are shown for radial offsets of 0 mm (black), 25 mm (red), 50 mm (green), 75 mm (blue), and 100 mm (magenta). For each case, the perpendicular sensor array is presented in the left column, with the aligned array shown in the middle and right columns (opposing sides). Insets indicate the relative orientation of the charge and sensor configuration.

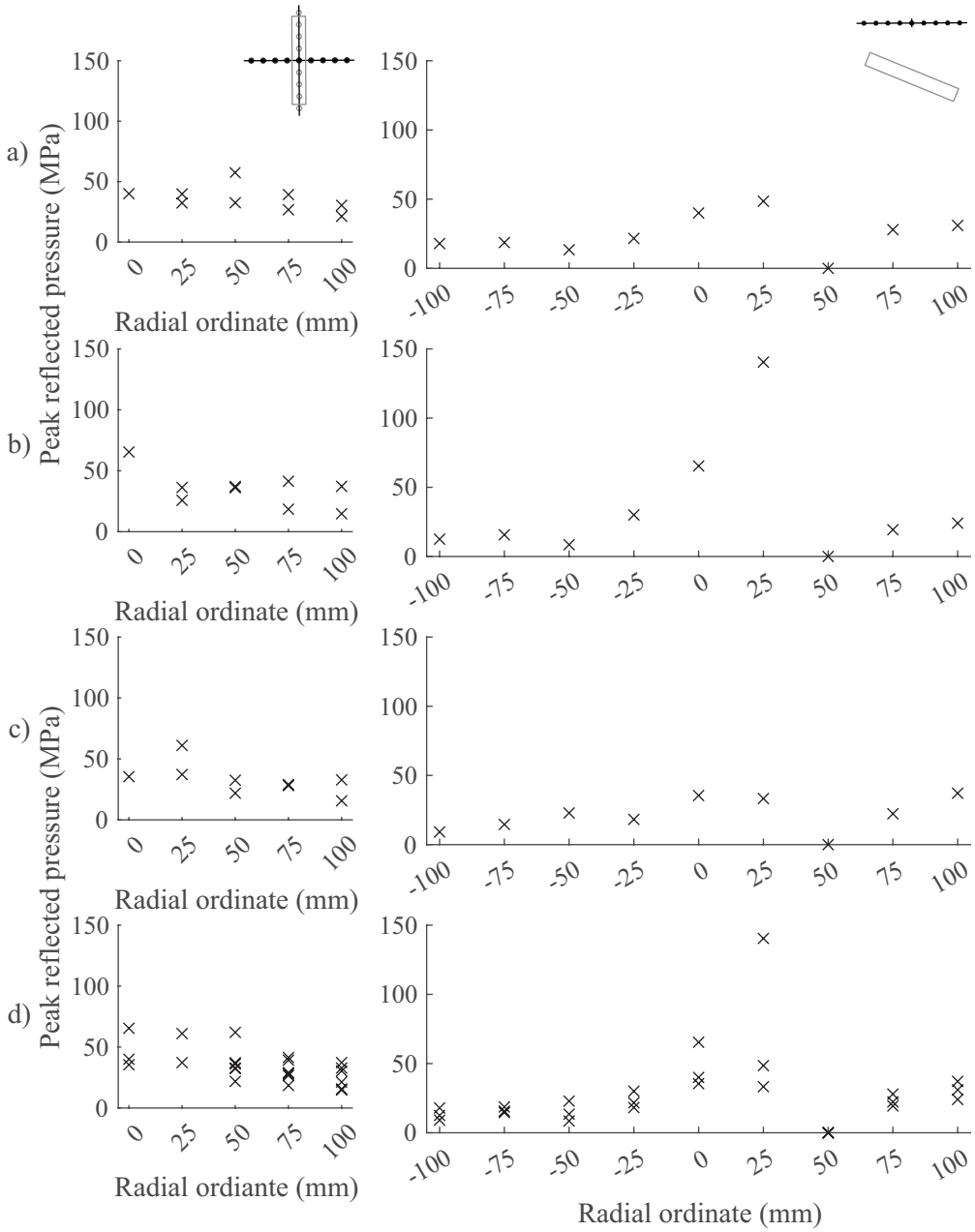


Figure 4.38: Peak reflected pressures for inclined cylindrical charges ($0°, 22.5°$ orientation, centrally detonated) for tests a) T020, b) T021 and c) T023, with d) showing a collation of the three tests. For each case, the perpendicular sensor array is presented in the left column, with the aligned array shown in the right column. Insets indicate the relative orientation of the charge and sensor configuration.

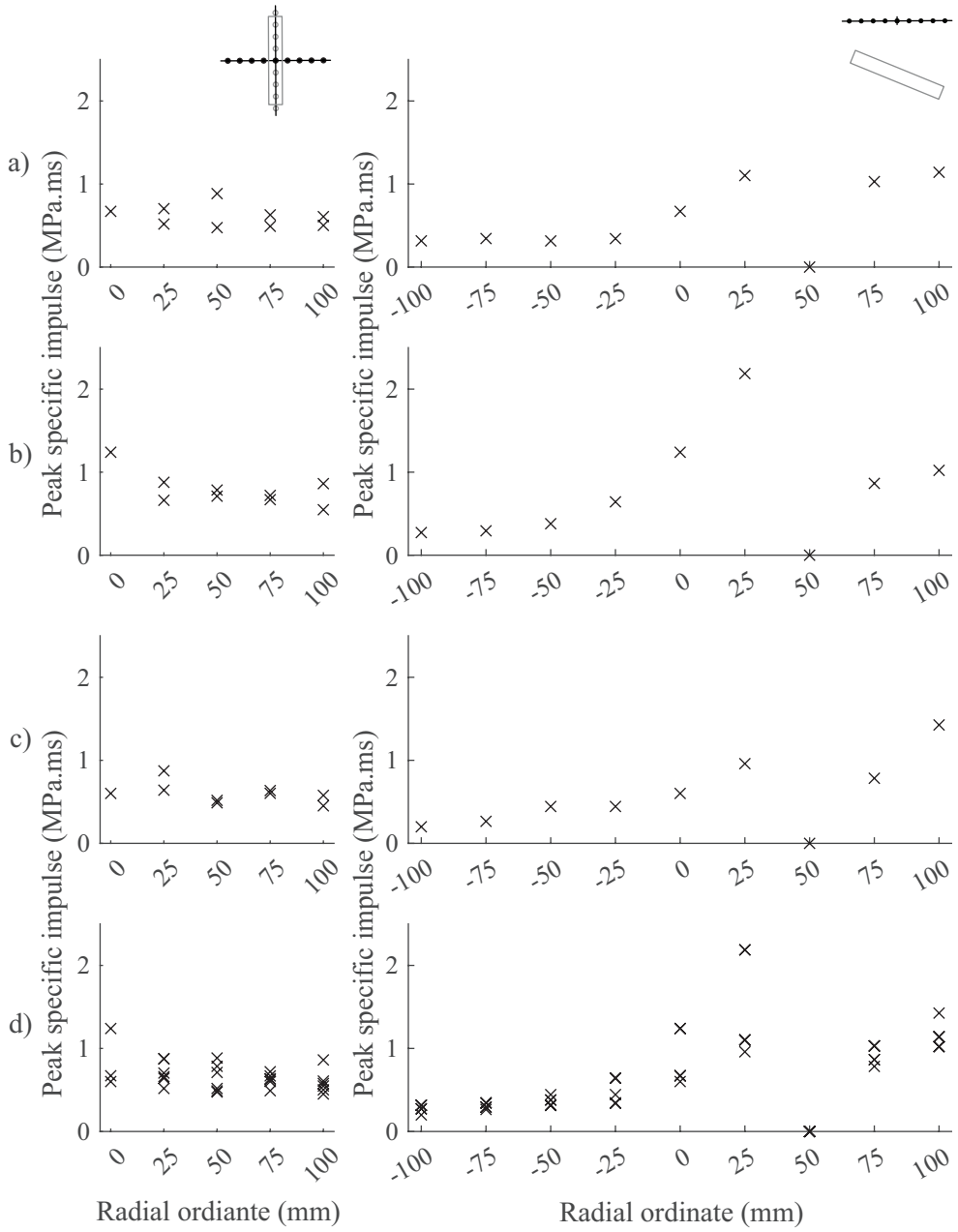


Figure 4.39: Peak specific impulses for inclined cylindrical charges ($0°, 22.5°$ orientation, centrally detonated) for tests a) T020, b) T021 and c) T023, with d) showing a collation of the three tests. For each case, the perpendicular sensor array is presented in the left column, with the aligned array shown in the right column. Insets indicate the relative orientation of the charge and sensor configuration.

4.6 Cylindrical tests – Inclined (0°, 45°)

The following section presents the reflected pressure and specific impulse results obtained from cylindrical charges inclined at 45° to the reflecting plate, with the charge axis oriented radially at 0° to the instrumented bar array. At this inclination angle, it is predicted that the measurement positions fall neither within the primary radial nor axial blast wave paths from the charge, but rather in the transitional region characterised by the interaction of the bridging and reflected waves.

4.6.1 Test Results

The results are presented in the same format as the 22.5° inclined tests in Section 4.5, with individual test figures arranged as a matrix of four rows and two columns, with the left column presenting the perpendicular array results and the right column presenting the parallel array results. The comparative figures follow the same four-row arrangement, with rows a), b), and c) corresponding to Tests T024, T026, and T027 respectively, and row d) presenting the cross-test mean or compiled results as appropriate.

T024

The reflected pressure histories recorded during Test T024 are presented in Figure 4.40, using the same array configuration and subplot arrangement as described for the preceding tests. The central bar trace is included in all subplots as a consistent spatial reference. It is noted that one of the 50 mm parallel bars did not record a valid pressure trace during this test and is represented as a zero-value flat line in the figure. The peak pressures recorded across this test are considerably lower than those observed in the preceding charge orientations, rendering the instrumentation noise more prominent relative to the signal amplitude; this should be borne in mind in the interpretation of the results.

The perpendicular results exhibit consistent arrival times across the array, with a progressive delay in shock arrival relative to the central bar with increasing radial distance. This delay is particularly consistent at the 75 mm and 100 mm positions, where both bars at each location record well-defined and repeatable arrival times. At 25 mm and 50 mm, one of the two bars at each position records a reduced peak pressure compared to its counterpart but with an earlier arrival, whilst the 75 mm and 100 mm positions exhibit good agreement between the paired traces. Despite the variation in peak magnitude at the closer radial positions, all perpendicular bars record broadly similar peak pressures across the array, with no strong trend of attenuation with radial distance.

The parallel results exhibit a more complex arrival pattern. At each radial position, one bar records a lower pressure trace arriving earlier than the central bar, with the degree of early arrival increasing with radial distance. The other bar at each position records a higher pressure trace also arriving earlier than the central bar, but to a lesser degree, with the earliness of arrival again increasing with radial distance. The dead 50 mm parallel bar

is assumed, based on the consistency of the trend across the array, to correspond to the position that would have recorded the higher of the two traces at this location.

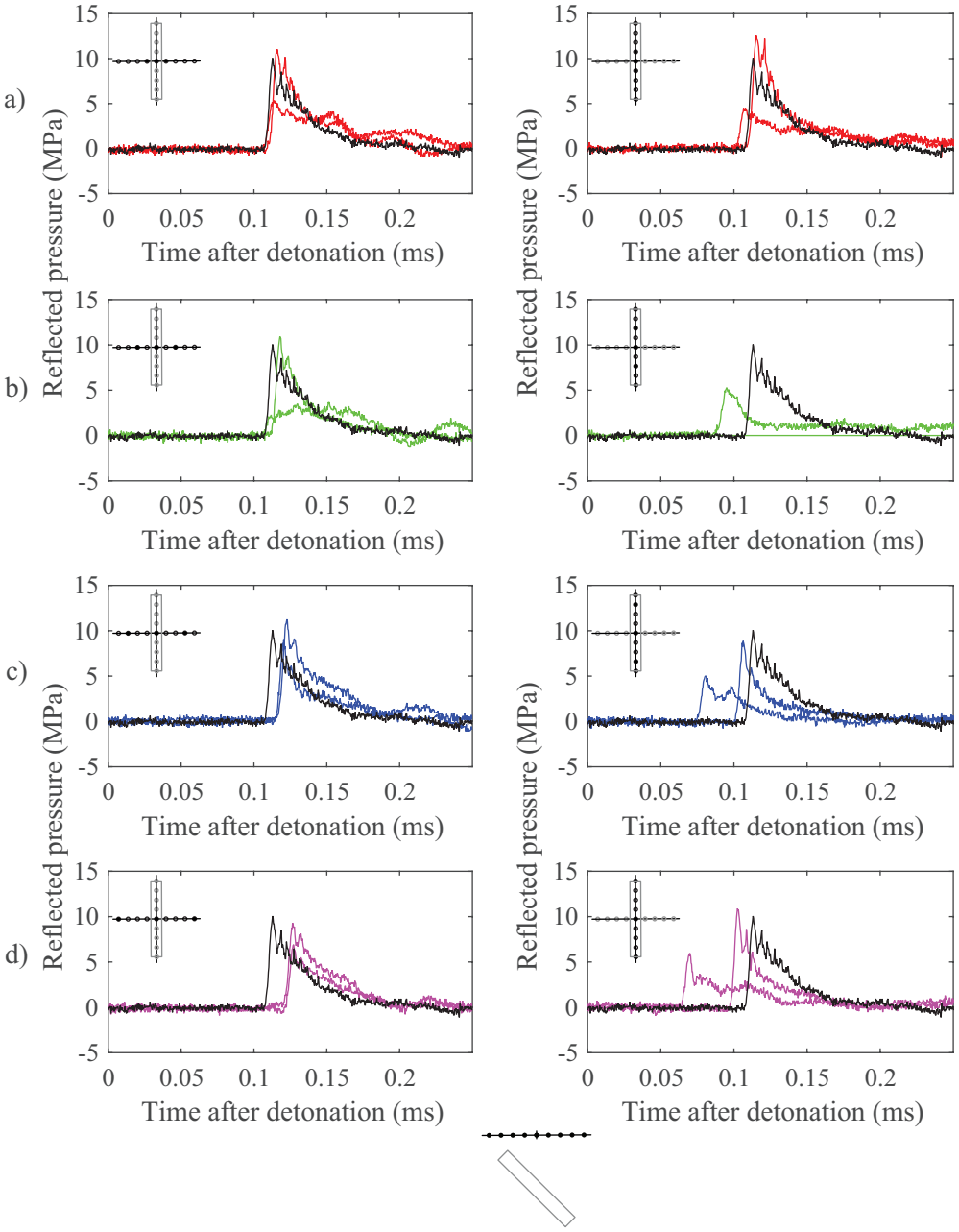


Figure 4.40: Reflected pressure time histories for test T024 (inclined cylindrical charge, 0°, 45° orientation, centrally detonated). Results are shown for radial offsets of (a) 25 mm (red), (b) 50 mm (green), (c) 75 mm (blue), and (d) 100 mm (magenta), compared against the central reference measurement (0 mm, black). For each radial position, measurements are presented for perpendicular sensor arrays (left column) and aligned sensor arrays (right column). Insets indicate the relative orientation of the charge and sensor configuration.

The specific impulse histories for Test T024 are presented in Figure 4.41. It is noted that the instrumentation noise present in the pressure traces influences the computed specific impulse prior to the shock arrival, manifesting as a non-zero impulse baseline before the

physical loading commences. This is a consequence of the low pressure magnitudes recorded in this orientation rendering the signal-to-noise ratio of the CoBL apparatus less favourable, and is not representative of a physical feature of the blast loading. This effect is most prominent in the central bar and a 75 mm perpendicular trace but is present to varying degrees across the results of this and subsequent tests at comparable loading levels.

The perpendicular impulse results exhibit good agreement between the two bars at 25 mm, although the two traces display different loading gradients, with one bar exhibiting a lower initial gradient but continuing to accumulate impulse over a longer duration. Larger variation between the paired traces is observed at 50 mm and 75 mm. The parallel impulse results exhibit a large variation between the two bars at 25 mm, consistent with the differing pressure profiles at this position, with the two traces displaying notably different gradients. At 75 mm and 100 mm, the impulse profiles exhibit an unusual character, with one bar beginning to accumulate impulse earlier and at a lower gradient, whilst the other follows a more conventional rise; despite these differences, both bars at each position converge to broadly similar peak specific impulse values by the end of the period of interest.

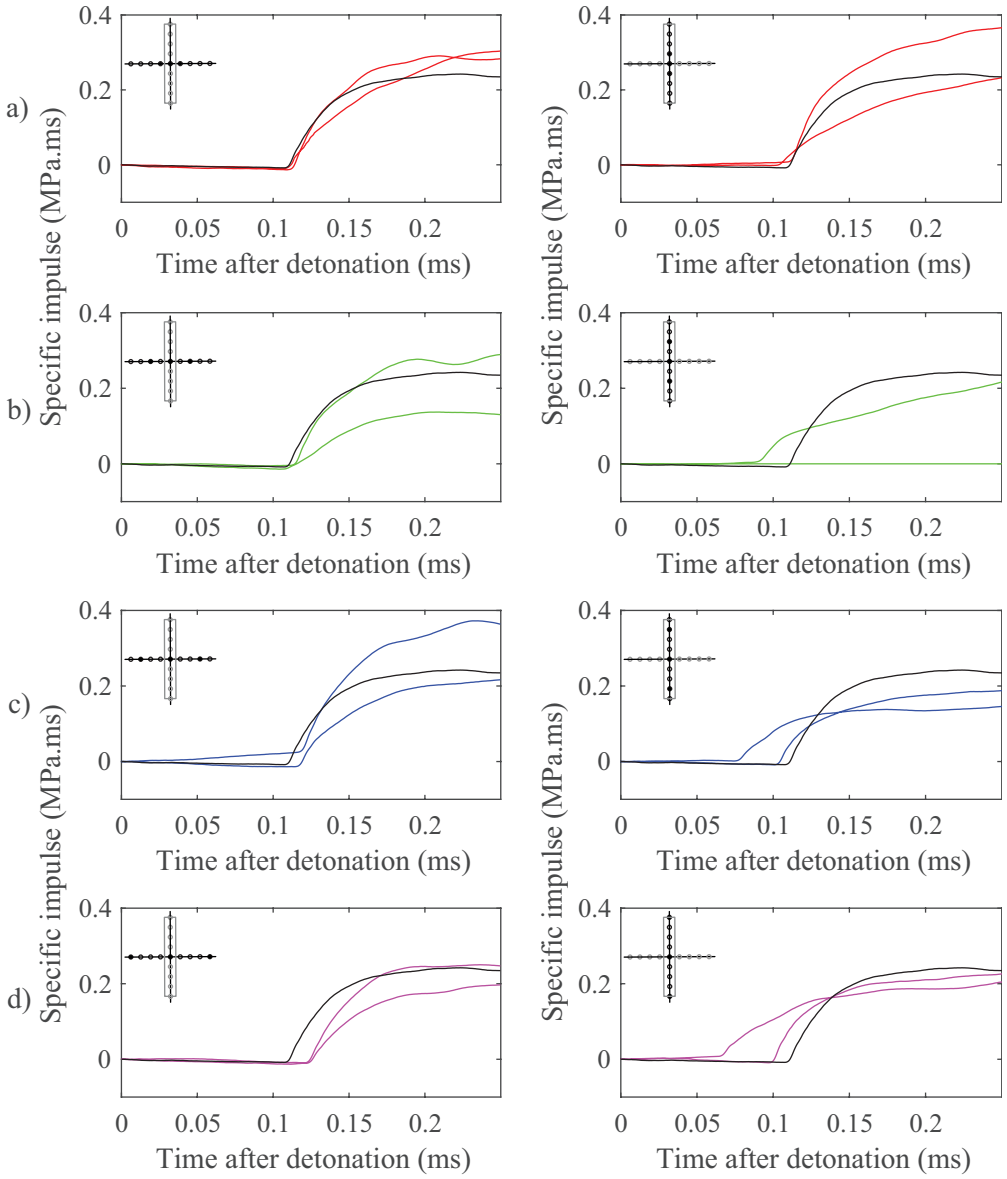


Figure 4.41: Specific impulse time histories for test T024 (inclined cylindrical charge, 0°, 45° orientation, centrally detonated). Results are shown for radial offsets of a) 25 mm (red), b) 50 mm (green), c) 75 mm (blue), and d) 100 mm (magenta), compared against the central reference measurement (0 mm, black). For each radial position, measurements are presented for perpendicular sensor arrays (left column) and aligned sensor arrays (right column). Insets indicate the relative orientation of the charge and sensor configuration.

T026

The reflected pressure histories recorded during Test T026 are presented in Figure 4.42, using the same array configuration and subplot arrangement as described for the preceding tests. The central bar trace is included in all subplots as a consistent spatial reference. It is noted that one of the 75 mm perpendicular bars did not record a valid pressure trace during this test and is represented as a zero-value flat line in the figure.

The perpendicular results exhibit broadly similar pressure profiles across the 25 mm, 50 mm, and 75 mm positions, with the surviving 75 mm trace consistent with the lower of the two traces at the closer radial positions. At 25 mm and 50 mm, one of the two bars at each position records a delayed arrival relative to its counterpart, whilst both bars at 75 mm arrive simultaneously with the central bar. At 100 mm, the two perpendicular bars exhibit notably different behaviour; one records a low pressure trace consistent with the trend established at the closer radial positions, whilst the other records an elevated peak pressure with a good initial decay followed by a prolonged positive phase duration, arriving later than the remainder of the array.

The parallel results exhibit a reversal of the arrival pattern observed in Test T024. At each radial position, the higher pressure trace arrives earlier than the central bar, whilst the lower trace arrives after it, with the degree of early and late arrival increasing with radial distance. Elevated peak pressures are recorded at the 75 mm and 100 mm positions, with values above the central bar measurement. At 25 mm and 50 mm, both parallel bars exhibit a long positive phase duration despite their comparatively lower peak pressures.

The specific impulse histories for Test T026 are presented in Figure 4.43. As noted for Test T024, the instrumentation noise influences the computed specific impulse prior to shock arrival across a number of traces, and this effect should be borne in mind in the interpretation of the results. The perpendicular impulse results at 25 mm and 50 mm exhibit a similar pattern to that observed in Test T024, with one bar displaying a lower, more gradually accumulating trace and the other exhibiting a steeper, later rising profile. At 100 mm, the impulse results reflect the pressure observations at this position, with one bar recording a low trace and the other a considerably elevated specific impulse consistent with the high pressure and prolonged positive phase recorded in the pressure data; both traces at this position are subject to noise effects. The parallel impulse results exhibit a broadly similar character to those of Test T024, with differing gradients and arrival times between the two bars at each radial position, albeit less pronounced in some cases.

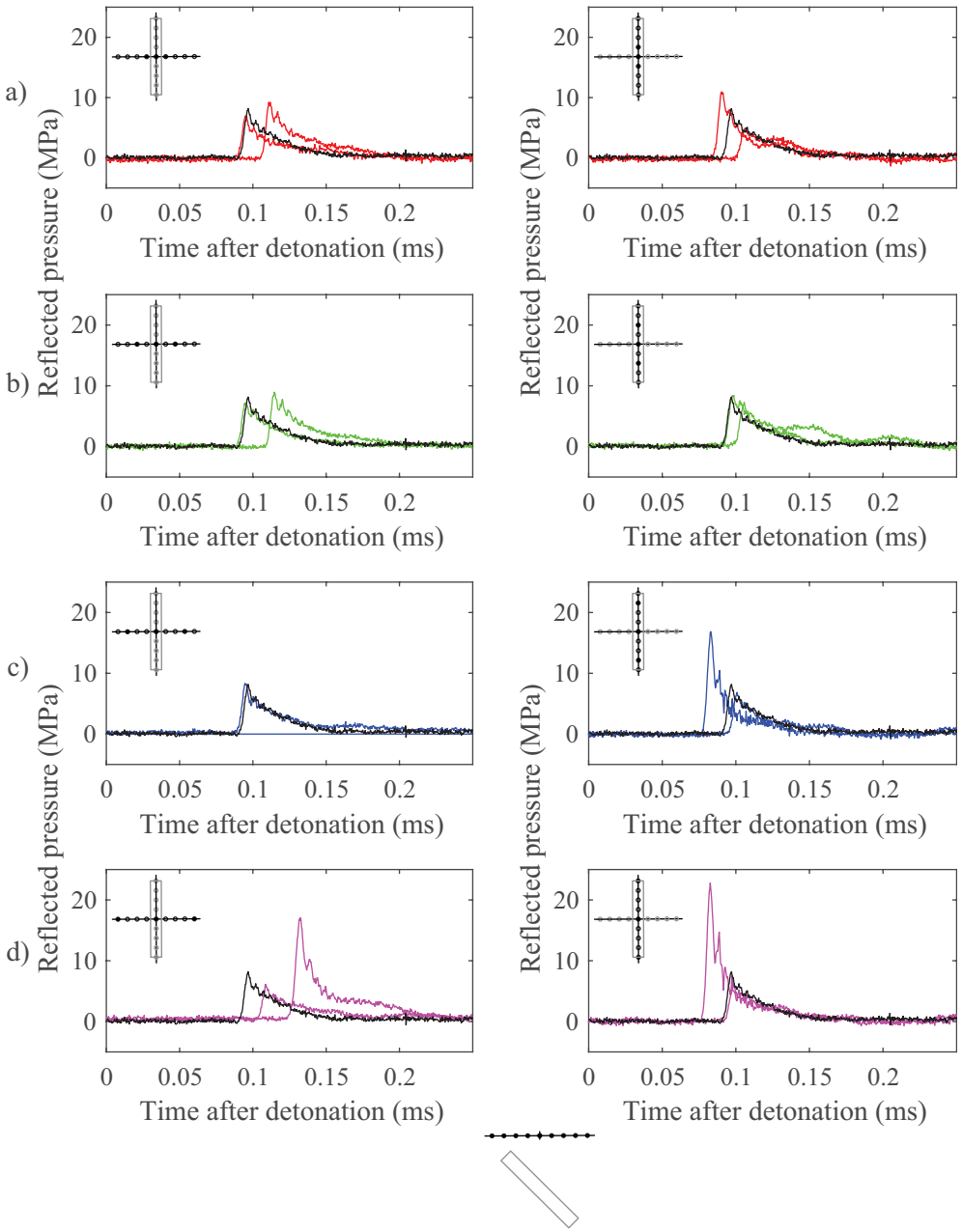


Figure 4.42: Reflected pressure time histories for test T026 (inclined cylindrical charge, 0°, 45° orientation, centrally detonated). Results are shown for radial offsets of (a) 25 mm (red), (b) 50 mm (green), (c) 75 mm (blue), and (d) 100 mm (magenta), compared against the central reference measurement (0 mm, black). For each radial position, measurements are presented for perpendicular sensor arrays (left column) and aligned sensor arrays (right column). Insets indicate the relative orientation of the charge and sensor configuration.

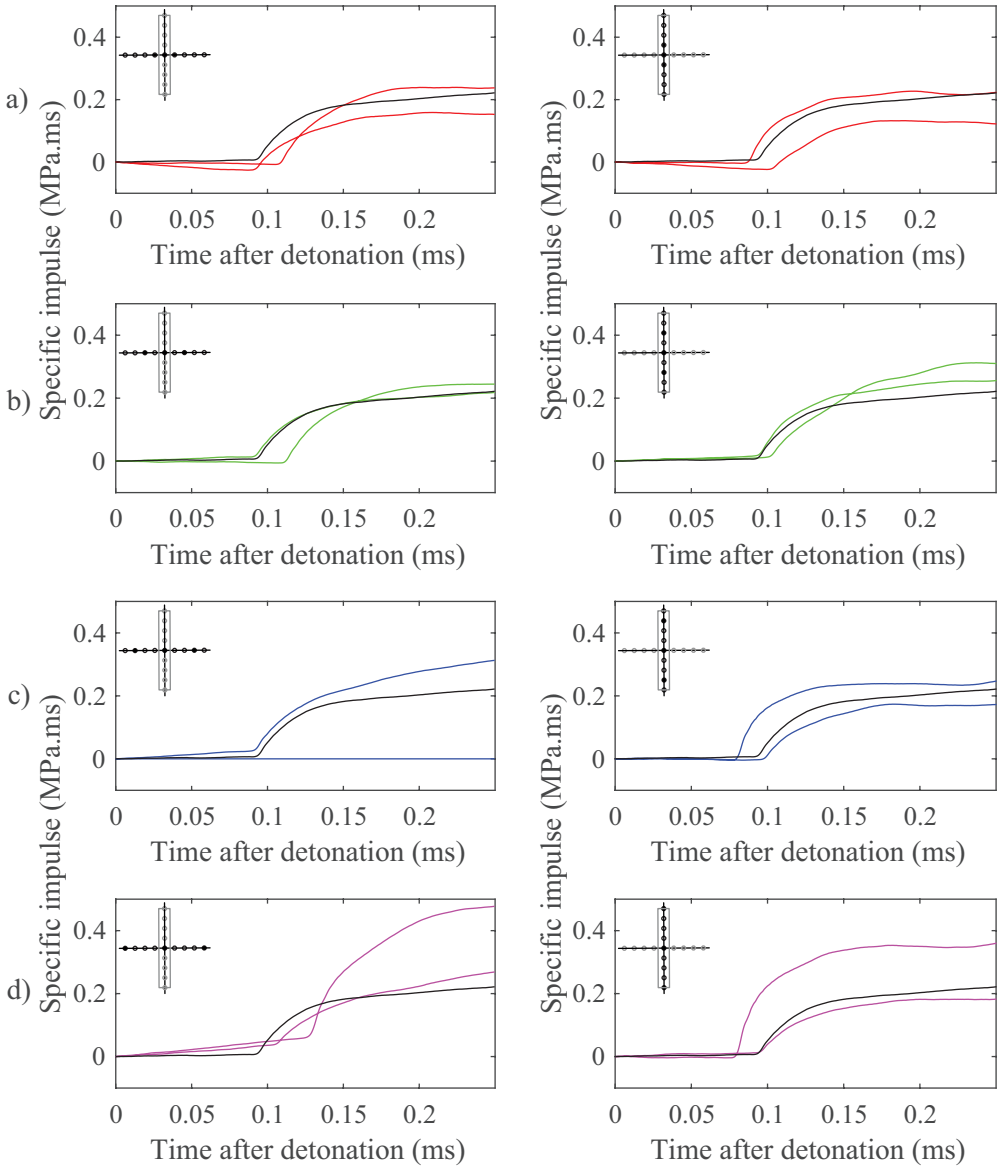


Figure 4.43: Specific impulse time histories for test T026 (inclined cylindrical charge, $0°, 45°$ orientation, centrally detonated). Results are shown for radial offsets of a) 25 mm (red), b) 50 mm (green), c) 75 mm (blue), and d) 100 mm (magenta), compared against the central reference measurement (0 mm, black). For each radial position, measurements are presented for perpendicular sensor arrays (left column) and aligned sensor arrays (right column). Insets indicate the relative orientation of the charge and sensor configuration.

T027

The reflected pressure histories recorded during Test T027 are presented in Figure 4.44, using the same array configuration and subplot arrangement as described for the preceding tests. The central bar trace is included in all subplots as a consistent spatial reference. It is noted that one of the 50 mm and one of the 75 mm perpendicular bars did not record valid pressure traces during this test and are represented as zero-value flat lines in the figure.

The perpendicular results exhibit good consistency across the 25 mm to 75 mm positions, with pressure profiles broadly similar to those observed in Tests T024 and T026, and good repeatability between the paired traces at each position accounting for the dead bars. At 100 mm, the two perpendicular bars exhibit markedly different behaviour; one records a low pressure trace with a late arrival, whilst the other records a considerably higher peak pressure also arriving later than the remainder of the array, consistent with the anomalous 100 mm behaviour noted in Test T026.

The parallel results exhibit good consistency in pressure profile shape between the two bars at each radial position, despite a progressive temporal separation between the paired traces that increases with radial distance. Elevated peak pressures are recorded at the 75 mm and 100 mm positions, consistent with the observations from Tests T024 and T026. One of the 50 mm parallel bars exhibits a long positive phase duration pressure pulse, similar in character to the long duration features observed at the 50 mm position in Test T026.

The specific impulse histories for Test T027 are presented in Figure 4.45. As noted for the preceding tests in this orientation, instrumentation noise influences the computed specific impulse prior to shock arrival and should be borne in mind in the interpretation of the results. The perpendicular impulse results exhibit broadly normal profiles across the 25 mm to 75 mm positions, consistent with the pressure observations at these locations. At 100 mm, the two traces exhibit considerably different characters, with one recording a low and gradually accumulating impulse and the other a later, more abrupt rise, reflecting the markedly different pressure profiles at this position. The parallel impulse results exhibit good consistency between the two bars at each radial position in terms of overall profile shape, with a temporal separation between the paired traces that increases progressively with radial distance. The 50 mm parallel bar exhibiting the long positive phase duration pressure pulse produces a notably elevated specific impulse relative to its counterpart at this position, consistent with the additional impulse accumulated during the extended positive phase.

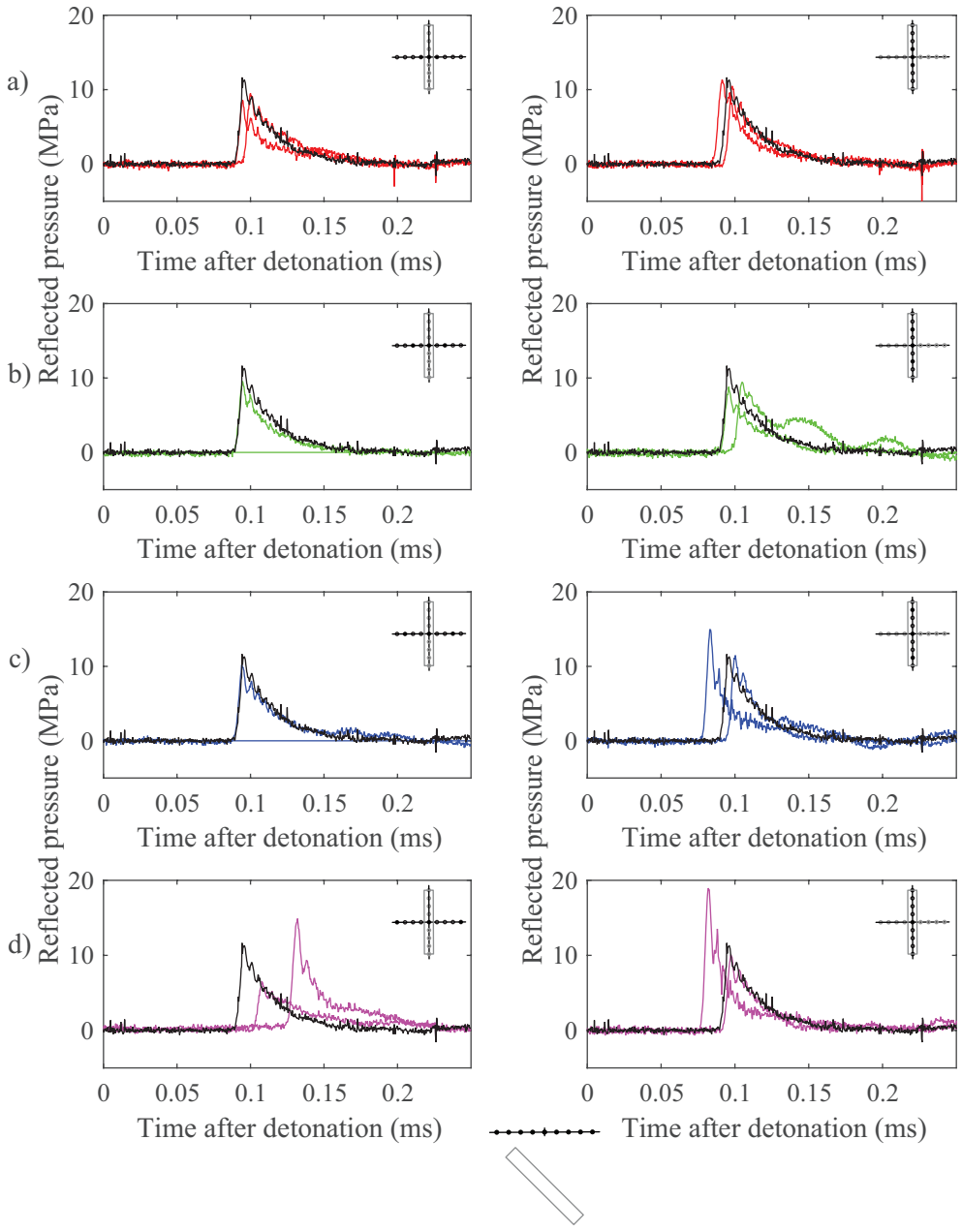


Figure 4.44: Reflected pressure time histories for test T027 (inclined cylindrical charge, $0°, 45°$ orientation, centrally detonated). Results are shown for radial offsets of (a) 25 mm (red), (b) 50 mm (green), (c) 75 mm (blue), and (d) 100 mm (magenta), compared against the central reference measurement (0 mm, black). For each radial position, measurements are presented for perpendicular sensor arrays (left column) and aligned sensor arrays (right column). Insets indicate the relative orientation of the charge and sensor configuration.

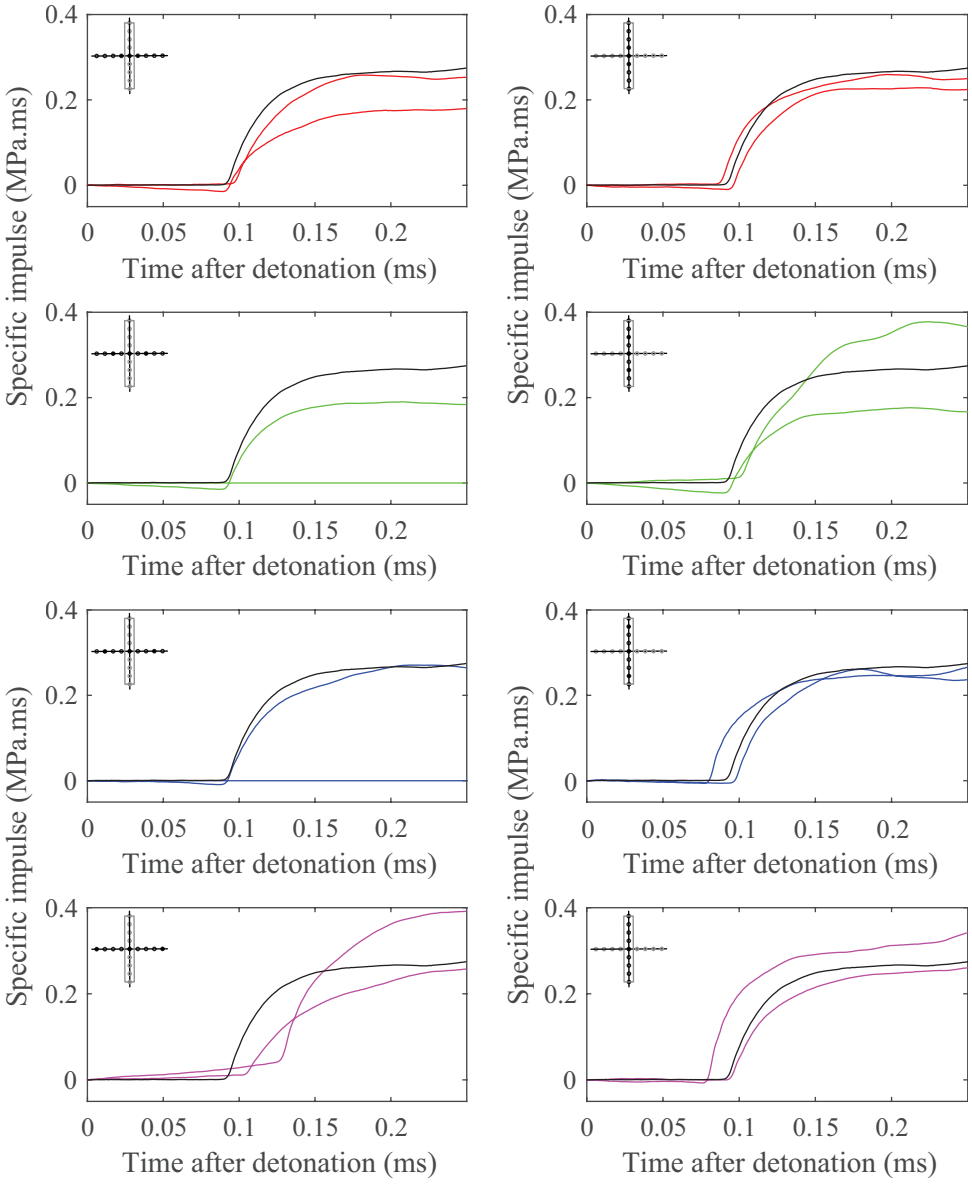


Figure 4.45: Specific impulse time histories for test T027 (inclined cylindrical charge, 0°, 45° orientation, centrally detonated). Results are shown for radial offsets of a) 25 mm (red), b) 50 mm (green), c) 75 mm (blue), and d) 100 mm (magenta), compared against the central reference measurement (0 mm, black). For each radial position, measurements are presented for perpendicular sensor arrays (left column) and aligned sensor arrays (right column). Insets indicate the relative orientation of the charge and sensor configuration.

4.6.2 Compiled results

The reflected pressure histories from Tests T024, T026, and T027 are presented collectively in Figure 4.46, following the same subplot arrangement as described for Figure 4.36, with rows a), b), and c) corresponding to Tests T024, T026, and T027 respectively, and row d) presenting the unweighted cross-test mean. The left column presents the averaged perpendicular array results, and the centre and right columns present the individual parallel array results. The + and − notation is applied consistently with the preceding inclined tests, with the charge elevated on the − side of the array.

A prominent feature of the comparative pressure results is the early arrival of the −parallel traces in Test T024, where the traces arrive in reverse distal order, with greater radial distances arriving earlier than closer positions. This behaviour is consistent with a wave propagating across the face of the reflecting plate from behind the tip of the inclined charge, producing an inverted arrival sequence relative to the conventional blast loading pattern. The late arriving elevated pressure peak at the 100 mm perpendicular position, observed in Tests T026 and T027, is sufficiently consistent between the two tests to remain visible in the cross-test mean. Similarly, the long positive phase duration pressure pulse at the −50 mm parallel position, recorded in Tests T026 and T027, is consistent between the two tests and is preserved in the averaged trace at this position in row (d). The elevated peak pressures and early arrivals of the +75 mm and +100 mm parallel traces dominate the loading character of the right column and are well preserved in the cross-test mean despite the inter-test variability.

The specific impulse histories from Tests T024, T026, and T027 are presented in Figure 4.47, following the same arrangement as Figure 4.46. The noise effects discussed in the individual test sections are most prominent in the perpendicular averaged results, introducing an unpredictable character to a number of traces prior to shock arrival. Notwithstanding these noise influences, the cross-test averages in row d) present a consistent and fairly even distribution of specific impulse across the perpendicular array. The elevated specific impulse associated with the long positive phase duration pressure pulse at the −50 mm parallel position in Tests T026 and T027 is reflected in the averaged parallel traces at this position in row d).

The peak reflected pressures from Tests T024, T026, and T027 are presented in Figure 4.48. The perpendicular results exhibit a broadly even spread of peak pressures across the array, with considerable variance at the 100 mm position, consistent with the anomalous high and low traces observed at this location in Tests T026 and T027. The parallel results exhibit a clear trend of increasing peak pressure towards the far end of the + side of the array, with the +75 mm and +100 mm positions recording the highest peak pressures, consistent with the dominant loading features identified in the comparative pressure traces.

The peak specific impulse values from Tests T024, T026, and T027 are presented in Figure 4.49, following the same arrangement as Figure 4.48. The perpendicular results exhibit a gentle trend of increasing peak specific impulse with radial distance towards

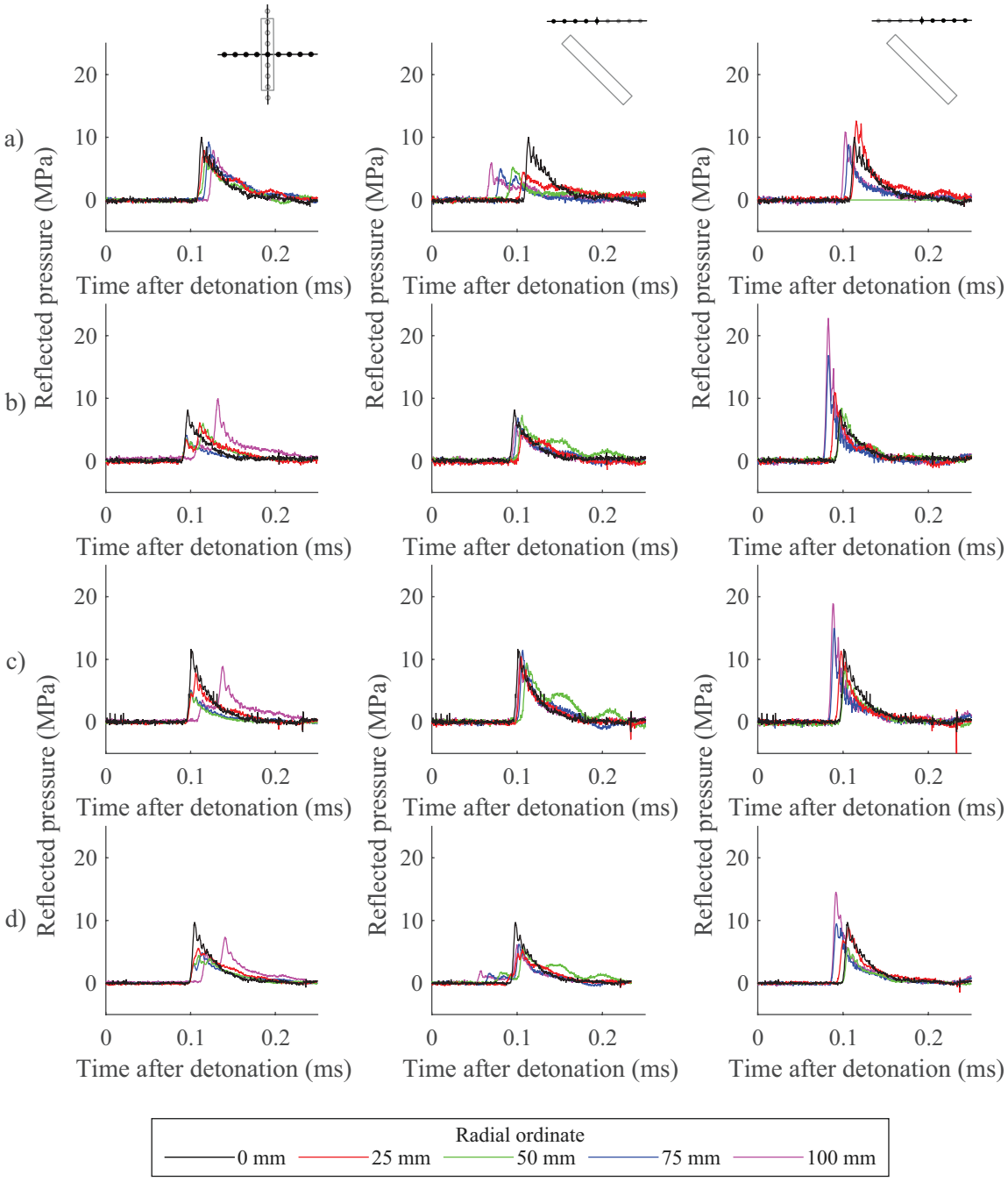


Figure 4.46: Reflected pressure time histories for inclined cylindrical charges (0°, 45° orientation, centrally detonated) for tests a) T024, b) T026 and c) T027, with d) showing the average of the three tests, aligned by the arrival time at the central reference measurement (0 mm, black). Traces are shown for radial offsets of 0 mm (black), 25 mm (red), 50 mm (green), 75 mm (blue), and 100 mm (magenta). For each case, the perpendicular sensor array is presented in the left column, with the aligned array shown in the middle and right columns (opposing sides). Insets indicate the relative orientation of the charge and sensor configuration.

the 100 mm positions, a departure from the declining trends observed in the preceding orientations; this trend is predominantly driven by the results of Tests T026 and T027. The parallel results exhibit a broadly even distribution of peak specific impulse across all radial positions, with consistently high variability throughout the array.

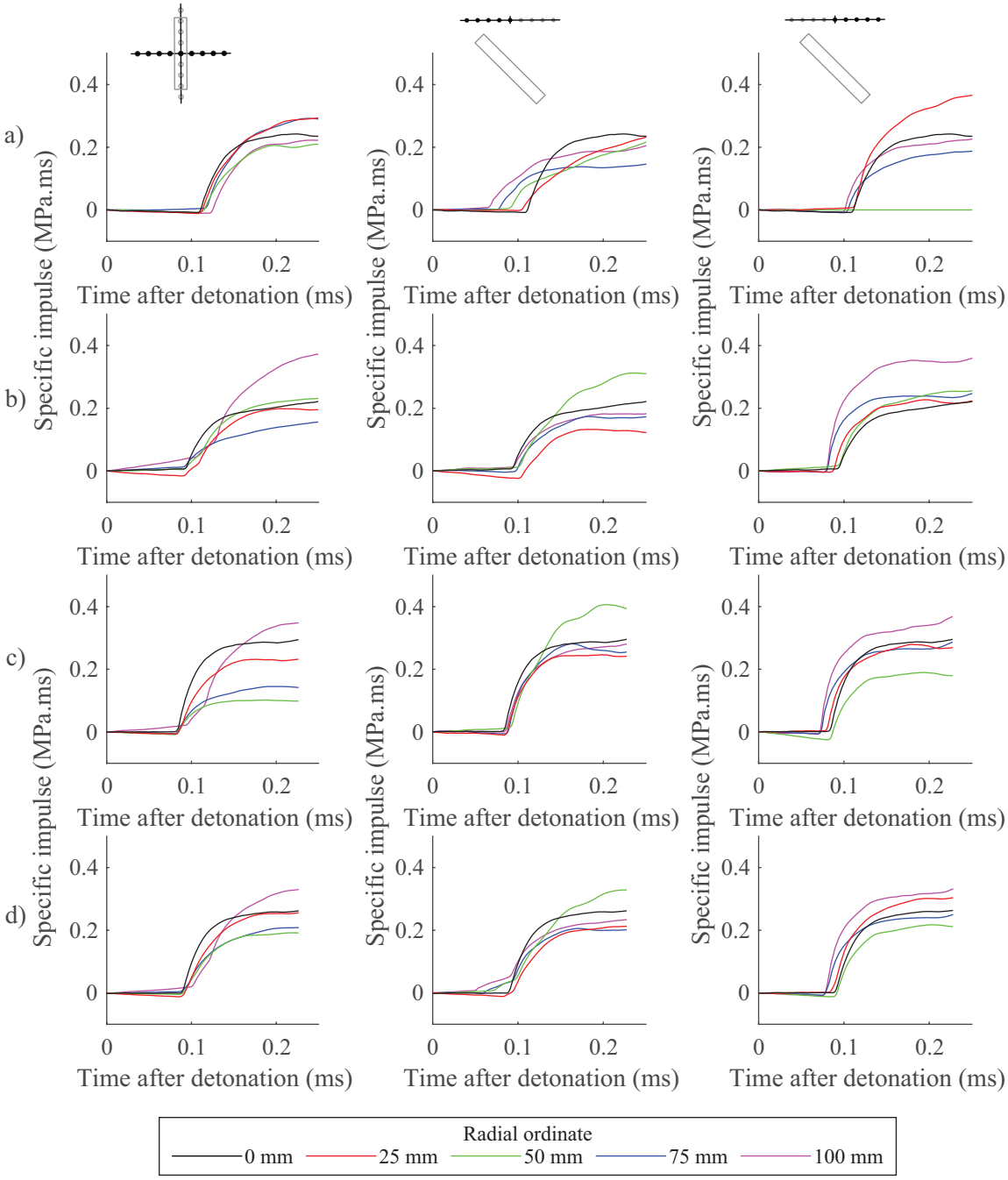


Figure 4.47: Specific impulse time histories for inclined cylindrical charges ($0°, 45°$ orientation, centrally detonated) for tests a) T024, b) T026 and c) T027, with d) showing the average of the three tests, aligned by the arrival time at the central reference measurement (0 mm, black). Traces are shown for radial offsets of 0 mm (black), 25 mm (red), 50 mm (green), 75 mm (blue), and 100 mm (magenta). For each case, the perpendicular sensor array is presented in the left column, with the aligned array shown in the middle and right columns (opposing sides). Insets indicate the relative orientation of the charge and sensor configuration.

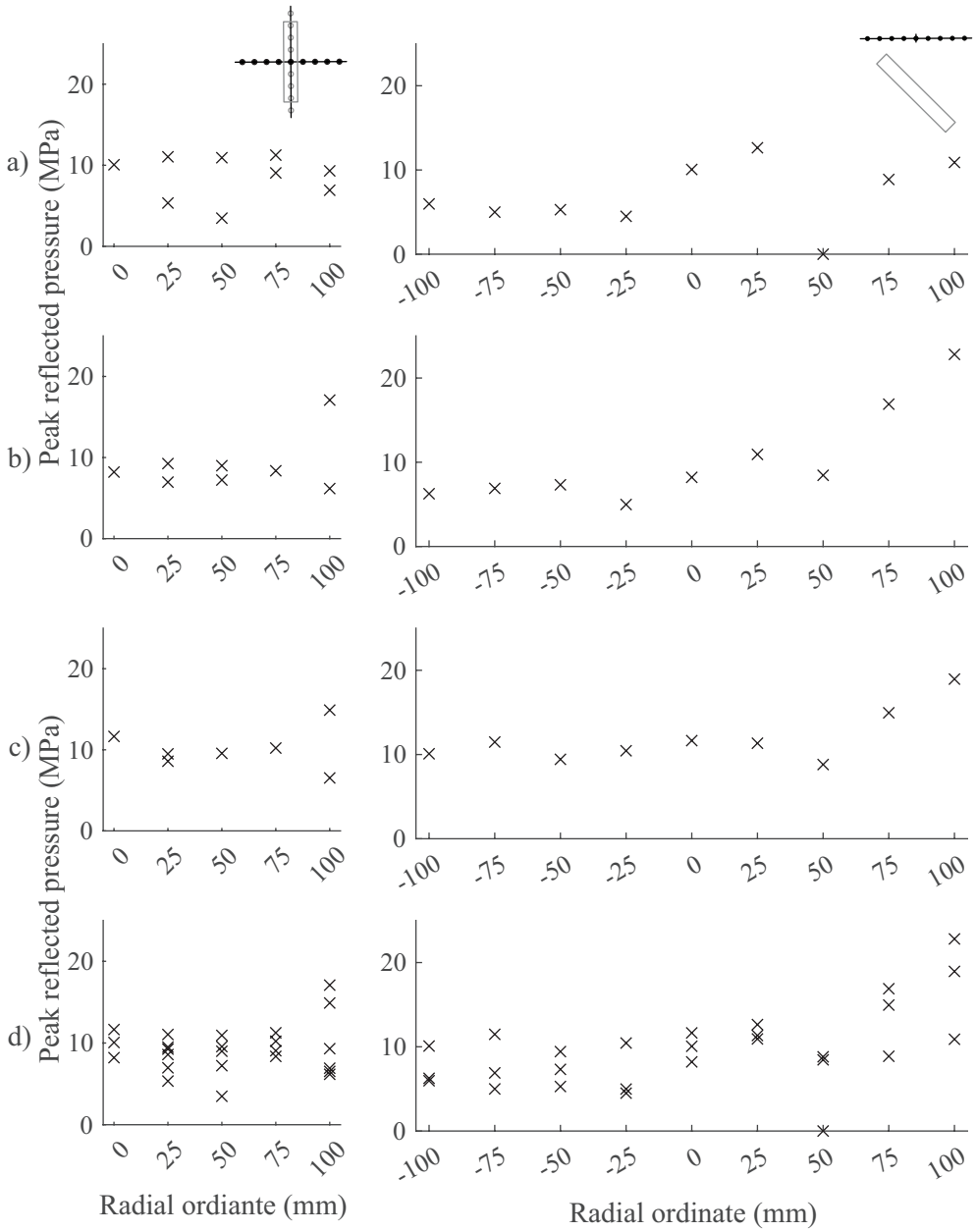


Figure 4.48: Peak reflected pressures for inclined cylindrical charges ($0°, 45°$ orientation, centrally detonated) for tests a) T024, b) T026 and c) T027, with d) showing a collation of the three tests. For each case, the perpendicular sensor array is presented in the left column, with the aligned array shown in the right column. Insets indicate the relative orientation of the charge and sensor configuration.

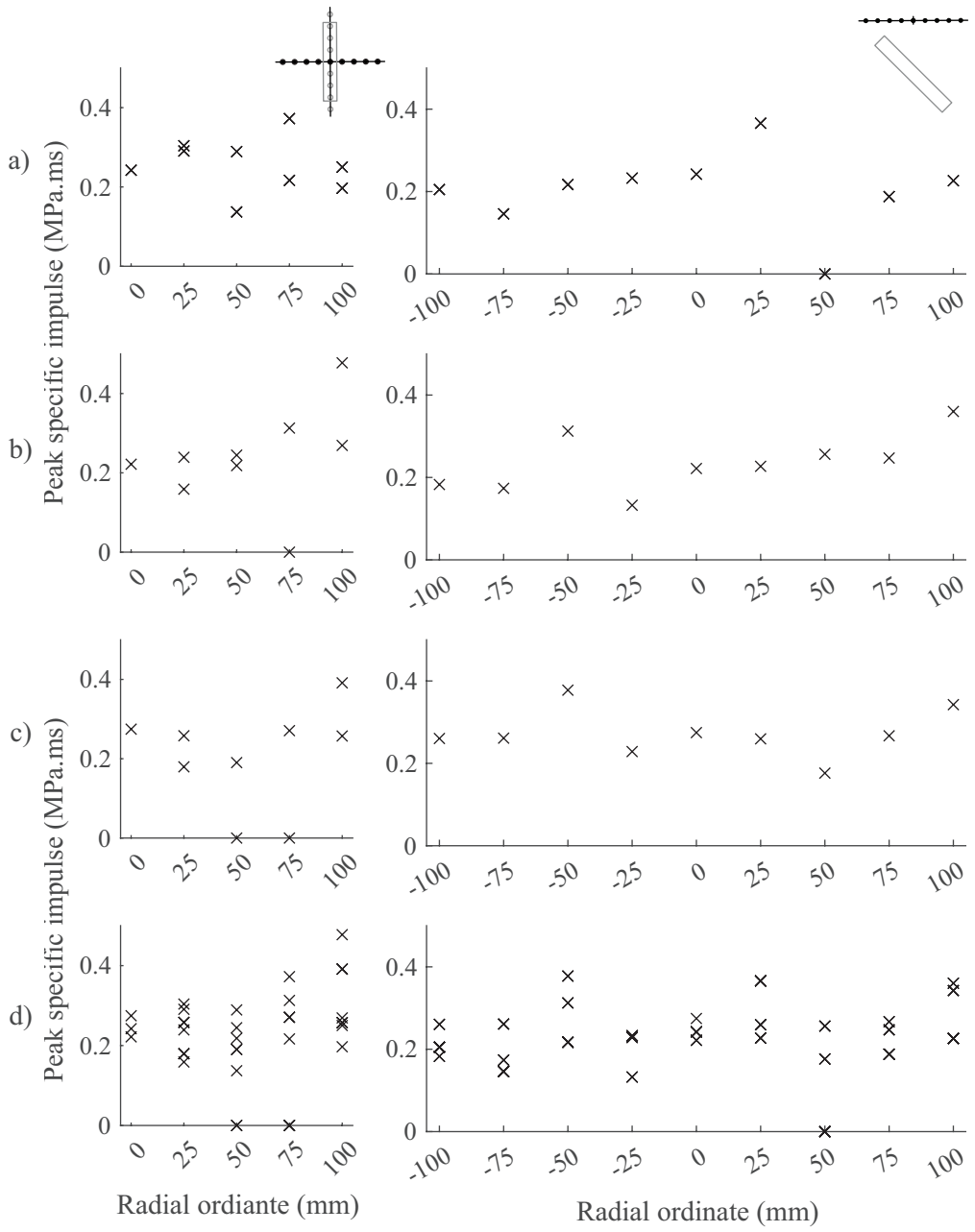


Figure 4.49: Peak specific impulses for inclined cylindrical charges ($0°, 45°$ orientation, centrally detonated) for tests a) T024, b) T026 and c) T027, with d) showing a collation of the three tests. For each case, the perpendicular sensor array is presented in the left column, with the aligned array shown in the right column. Insets indicate the relative orientation of the charge and sensor configuration.

4.7 Cylindrical tests – Inclined (0°, 67.5°)

The following section presents the reflected pressure and specific impulse results obtained from cylindrical charges inclined at 67.5° to the reflecting plate, with the charge axis aligned, 0°, to the instrumented bar array. At this inclination angle, the charge approaches the axial orientation, with the measurement positions falling closer to the primary end ("axial") wave of the charge than in the preceding configurations. The loading characteristics are therefore expected to reflect a transition towards the axial blast environment, but strongly in the bridging and reflected wave region.

4.7.1 Test Results

The results are presented in the same format as the preceding inclined tests in Section 4.6, with individual test figures arranged as a matrix of four rows and two columns, with the left column presenting the perpendicular array results and the right column presenting the parallel array results. The comparative figures follow the same four-row arrangement, with rows a), b), and c) corresponding to Tests T028, T030, and T031 respectively, and row d) presenting the cross-test mean or compiled results as appropriate.

T028

The reflected pressure histories recorded during Test T028 are presented in Figure 4.50, using the same array configuration and subplot arrangement as described for the preceding tests. The central bar trace is included in all subplots as a consistent spatial reference when available. It is noted that a significant number of bars did not record valid pressure traces during this test, specifically one bar at the 25 mm, 50 mm, and 75 mm perpendicular positions and one bar at the 25 mm parallel position, all of which are represented as zero-value flat lines in the figure.

The surviving perpendicular traces at 25 mm, 50 mm, and 75 mm present good pressure records. The 25 mm perpendicular trace exhibits a notable early pressure pulse arriving prior to the central bar arrival time, which is distinct and fully resolved before the main shock front arrives. This feature is not observed in any other trace and is tentatively attributed to the detonator bouncing off the reflecting plate, though this remains unconfirmed. At 100 mm, one perpendicular bar records a good pressure trace with a considerably delayed arrival (∼0.1 ms), whilst the other records a low pressure response with no discernible shock front, consistent with the anomalous 100 mm behaviour observed in the preceding inclined tests.

The parallel results exhibit low pressure traces at both the 25 mm and 50 mm positions. At 75 mm and 100 mm, one bar at each position records a low pressure trace, whilst the other records a higher pressure trace with a later arrival, similar to T024 but delayed about 0.05ms to the central bar.

The specific impulse histories for Test T028 are presented in Figure 4.51. As noted for the

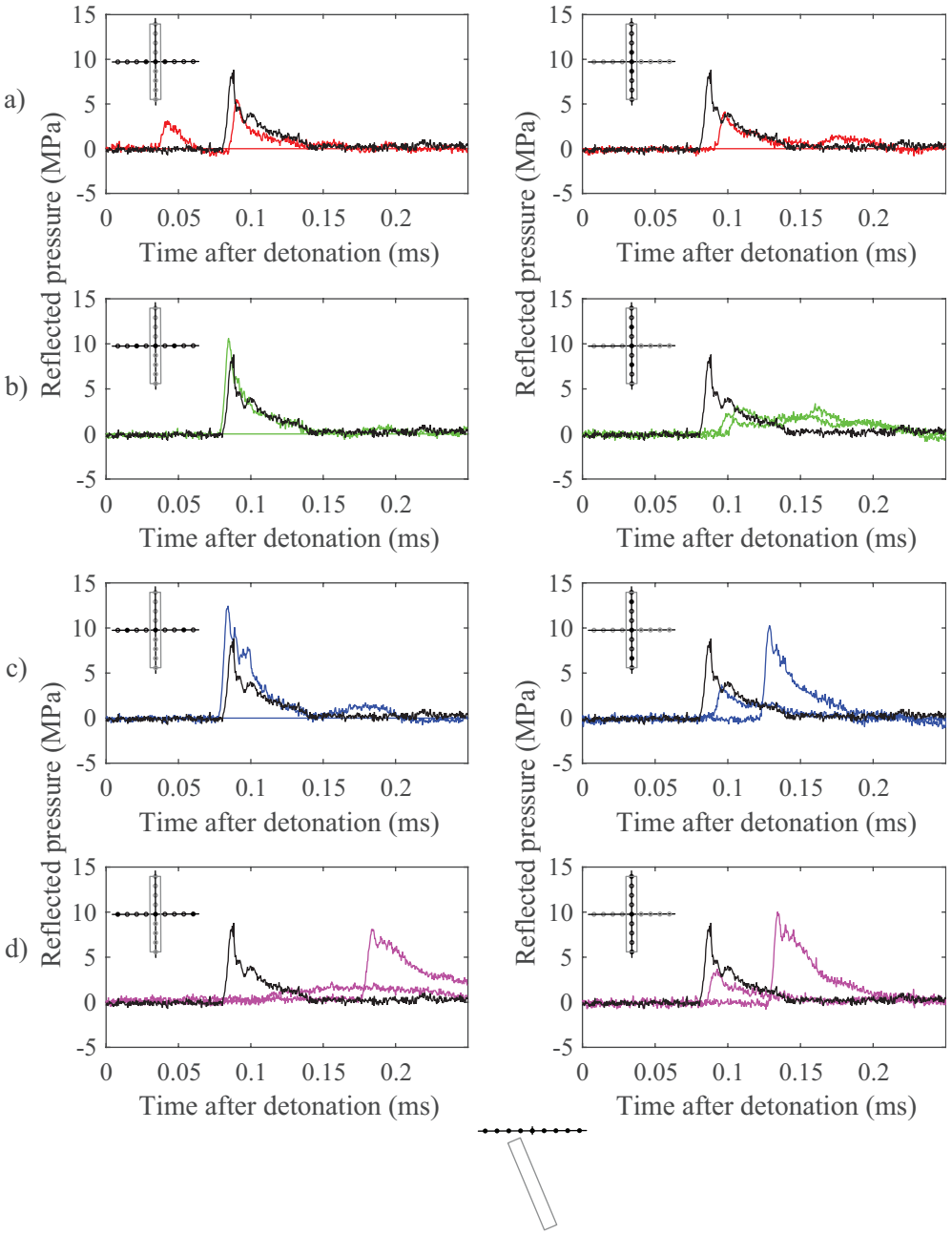


Figure 4.50: Reflected pressure time histories for test T028 (inclined cylindrical charge, $0°, 67.5°$ orientation, centrally detonated). Results are shown for radial offsets of (a) 25 mm (red), (b) 50 mm (green), (c) 75 mm (blue), and (d) 100 mm (magenta), compared against the central reference measurement (0 mm, black). For each radial position, measurements are presented for perpendicular sensor arrays (left column) and aligned sensor arrays (right column). Insets indicate the relative orientation of the charge and sensor configuration.

preceding tests in this orientation, instrumentation noise influences the computed specific impulse prior to shock arrival and should be borne in mind in the interpretation of the results. The early pressure pulse observed in the 25 mm perpendicular trace is visible in the corresponding impulse history as an initial rise prior to the main shock contribution. The 50 mm and 75 mm perpendicular impulse results present good profiles consistent with their

pressure observations. At 100 mm, the two perpendicular traces exhibit markedly different impulse characteristics; one records a low but continuously increasing trace consistent with the broad pressure hump observed in the pressure data, whilst the other records a well-defined impulse profile commencing only at approximately 0.18 ms after detonation, consistent with the shock arrival at this position. The parallel impulse results at 25 mm and 50 mm exhibit profiles consistent with low peak pressure long duration waves, accumulating impulse gradually over the period of interest. At 75 mm and 100 mm, one bar at each position exhibits the same gradual accumulation characteristic, whilst the other records a later but more conventional impulse rise profile, reflecting the higher pressure and delayed arrival of the corresponding trace.

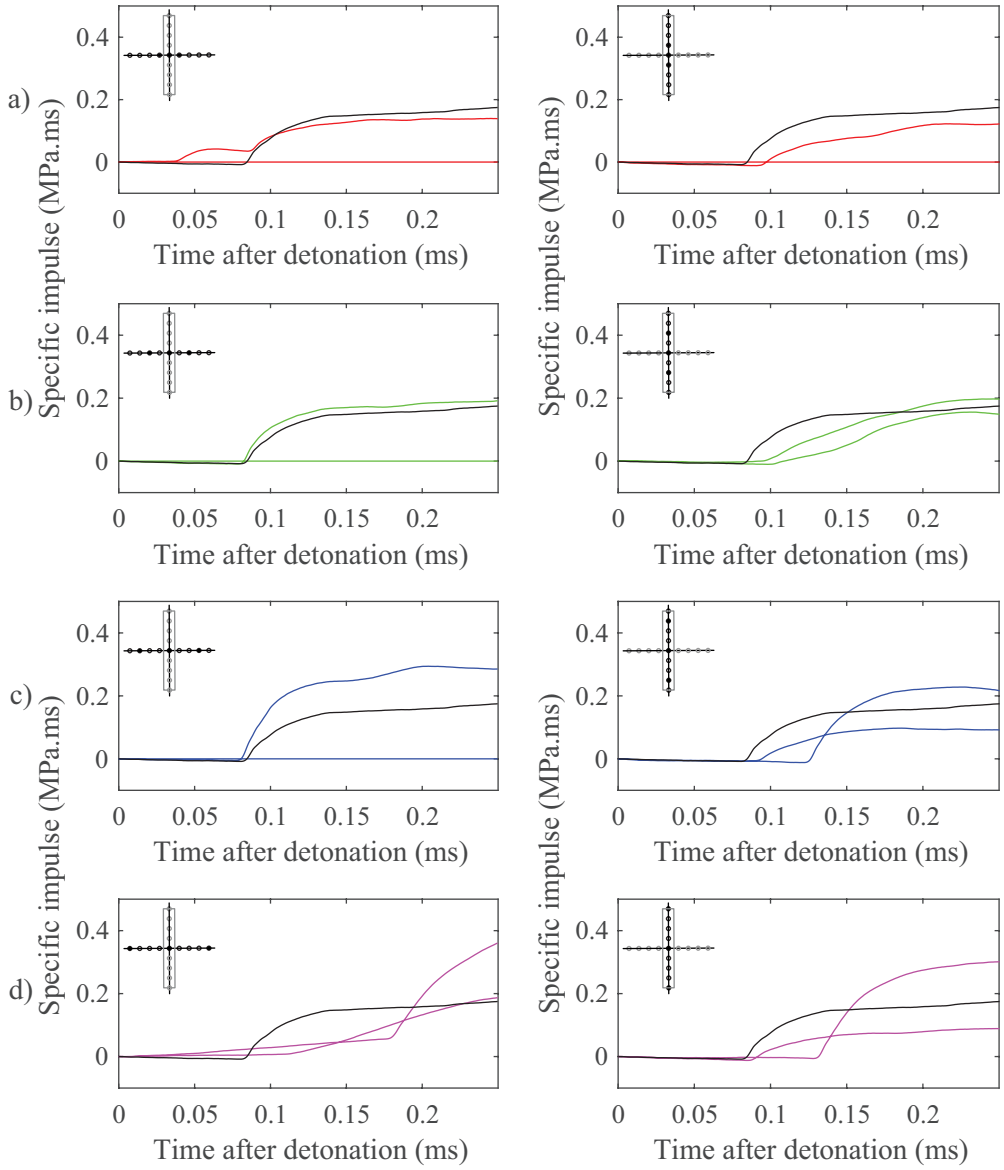


Figure 4.51: Specific impulse time histories for test T028 (inclined cylindrical charge, $0°, 67.5°$ orientation, centrally detonated). Results are shown for radial offsets of a) 25 mm (red), b) 50 mm (green), c) 75 mm (blue), and d) 100 mm (magenta), compared against the central reference measurement (0 mm, black). For each radial position, measurements are presented for perpendicular sensor arrays (left column) and aligned sensor arrays (right column). Insets indicate the relative orientation of the charge and sensor configuration.

T030

The reflected pressure histories recorded during Test T030 are presented in Figure 4.52, using the same array configuration and subplot arrangement as described for the preceding tests. A significant number of bars did not record valid pressure traces during this test, including the central bar, one bar at the 25 mm, 50 mm, and 75 mm perpendicular positions, and one bar at the 25 mm and 100 mm parallel positions, all of which are represented as zero-value flat lines in the figure. The absence of the central bar reference trace is noted; as no substitute reference is available. Instrumentation noise is prominent across a number of traces in this test, which is attributed to the low pressure magnitudes recorded at this orientation rendering the signal-to-noise ratio of the CoBL apparatus less favourable; the pressure axis is correspondingly more tightly scaled than in the preceding tests, spanning −2.5 to 10 MPa, which further accentuates the visual prominence of the noise.

The surviving perpendicular traces at 25 mm, 50 mm, and 75 mm present good pressure records broadly consistent with the equivalent surviving traces observed in Test T028. At 100 mm, the two perpendicular bars exhibit the same trend as T028, with one recording a considerably delayed good pressure trace and the other a low pressure response with a weak shock front. The parallel results exhibit broadly similar characteristics to those observed in Test T028 across all surviving positions, with low pressure traces at the 25 mm and 50 mm positions and the divergent low early arriving and high late arriving pattern at 75 mm and 100 mm.

The specific impulse histories for Test T030 are presented in Figure 4.53. The results exhibit very similar trends to those observed in Test T028, with the instrumentation noise influencing the computed specific impulse prior to shock arrival across a number of traces. The early pressure pulse feature observed in the 25 mm perpendicular trace of Test T028 is absent in the corresponding T030 trace, and the impulse profile at this position follows the conventional accumulation pattern from the main shock arrival onwards. All other impulse characteristics are consistent with the observations documented for Test T028.

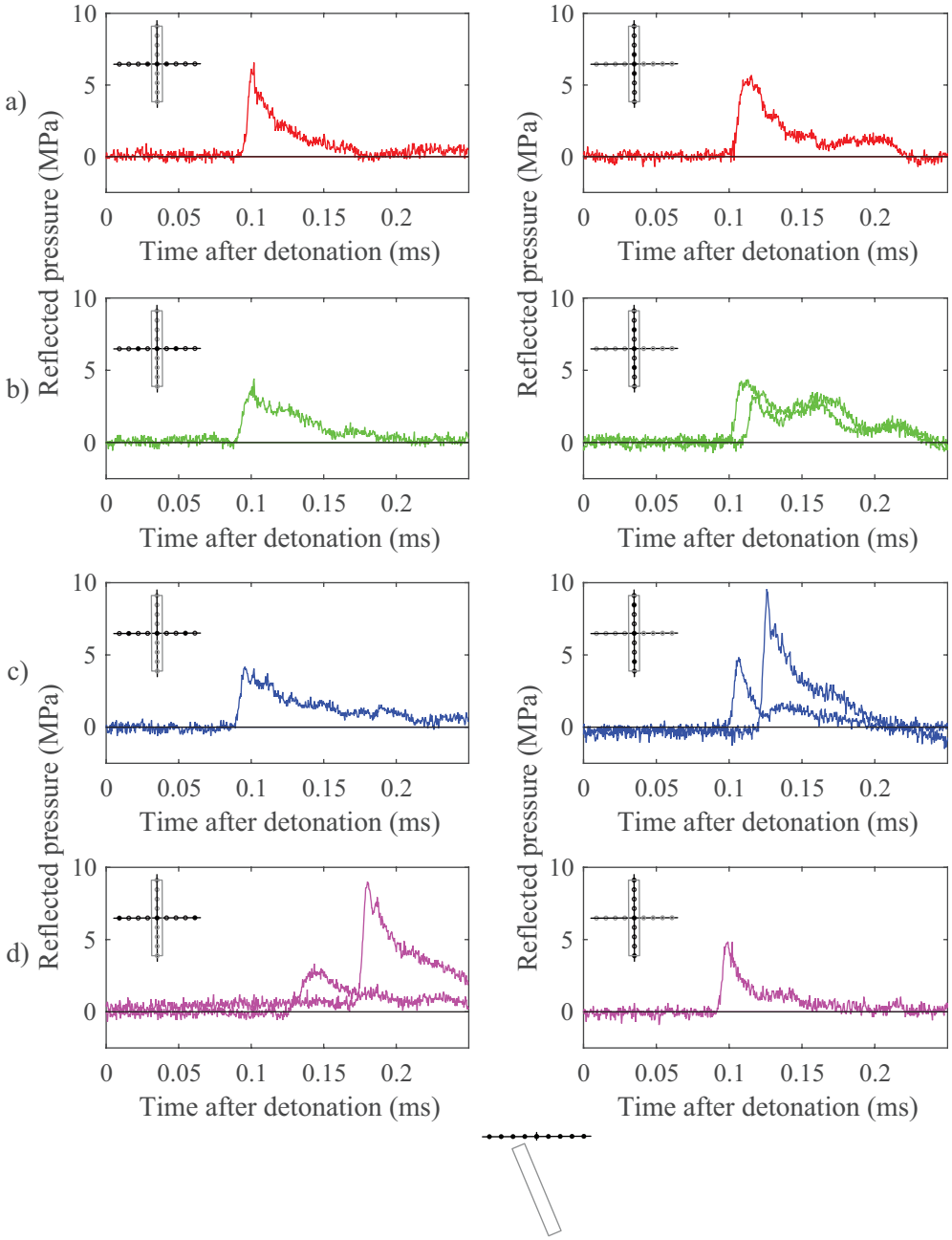


Figure 4.52: Reflected pressure time histories for test T030 (inclined cylindrical charge, $0°, 67.5°$ orientation, centrally detonated). Results are shown for radial offsets of (a) 25 mm (red), (b) 50 mm (green), (c) 75 mm (blue), and (d) 100 mm (magenta), compared against the central reference measurement (0 mm, black). For each radial position, measurements are presented for perpendicular sensor arrays (left column) and aligned sensor arrays (right column). Insets indicate the relative orientation of the charge and sensor configuration.

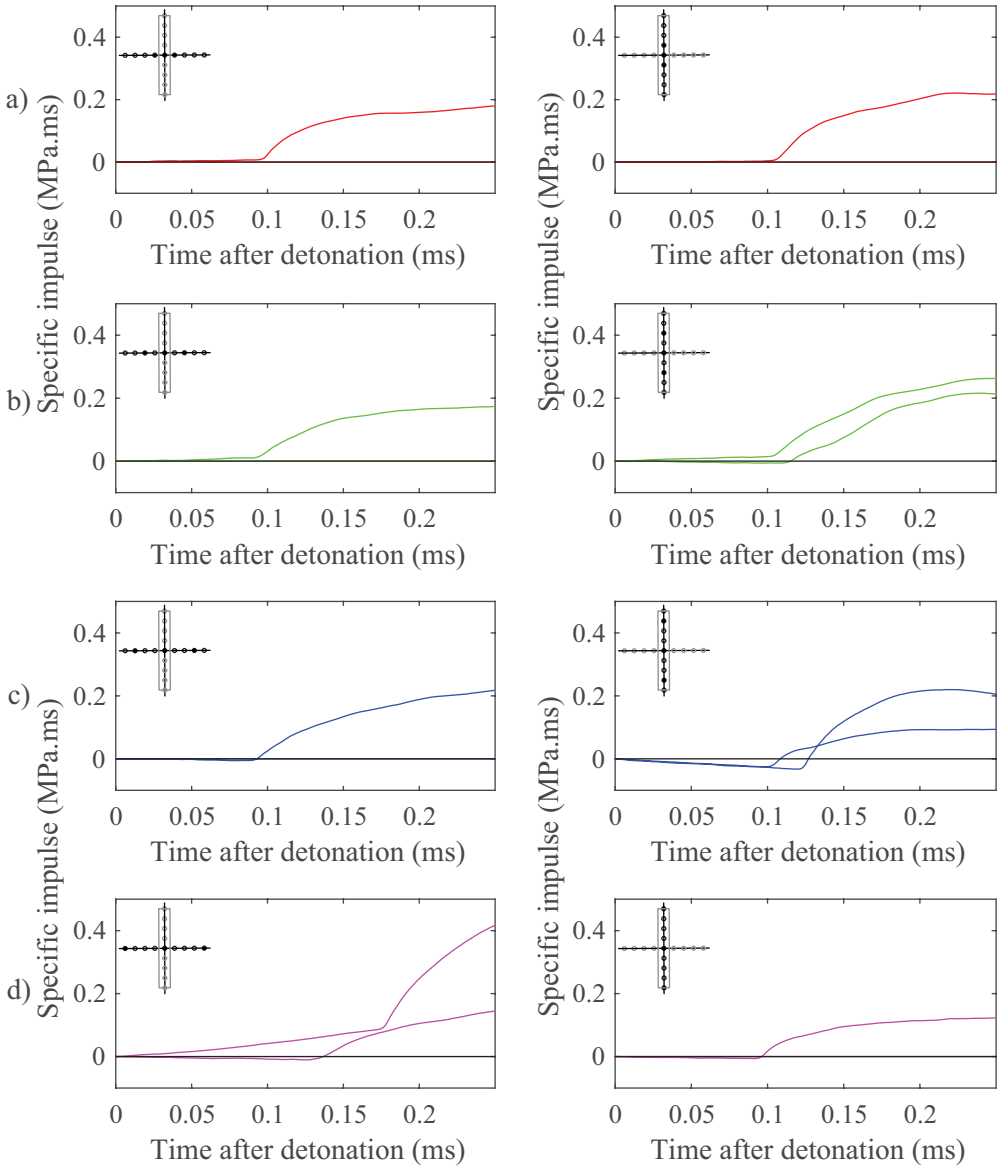


Figure 4.53: Specific impulse time histories for test T030 (inclined cylindrical charge, 0°, 67.5° orientation, centrally detonated). Results are shown for radial offsets of a) 25 mm (red), b) 50 mm (green), c) 75 mm (blue), and d) 100 mm (magenta), compared against the central reference measurement (0 mm, black). For each radial position, measurements are presented for perpendicular sensor arrays (left column) and aligned sensor arrays (right column). Insets indicate the relative orientation of the charge and sensor configuration.

T031

The reflected pressure histories recorded during Test T031 are presented in Figure 4.54, using the same array configuration and subplot arrangement as described for the preceding tests. As with Test T030, the central bar did not record a valid pressure trace and is represented as a zero-value flat line in the figure. Additionally, one bar at the 25 mm, 50 mm, and 75 mm perpendicular positions and one bar at the 25 mm and 100 mm parallel positions did not record valid traces and are represented accordingly.

The surviving perpendicular traces at 25 mm, 50 mm, and 75 mm exhibit pressure magnitudes and waveform shapes broadly consistent with those observed in Test T030. A discernible secondary pressure feature is observed in all these traces following the completion of the initial wave, which is tentatively attributed to a reflected end wave from the cylindrical charge. At 100 mm, the two perpendicular bars exhibit the same trend as the preceding tests, with one recording a considerably delayed pressure trace and the other a low pressure response with no discernible shock front.

The parallel results exhibit broadly similar low pressure responses at the 25 mm, 50 mm, and 100 mm positions, with a secondary pressure feature observed in the 25 mm, 50 mm, and 75 mm traces, consistent with the reflected end wave tentatively identified in the perpendicular results. The 75 mm parallel position is notable in recording the only well-defined shock front in the parallel array, arriving after an initial lower pressure wave in a pattern similar to that observed in Test T030.

The specific impulse histories for Test T031 are presented in Figure 4.55. The majority of the impulse histories exhibit low and gradually accumulating profiles, reflecting the weak pressure loading across most of the array with a gentle step up when the secondary wave arrives. The exceptions are the 100 mm perpendicular and 75 mm parallel positions, both of which record notably more active impulse profiles with a higher peak specific impulse values, consistent with the more prominent pressure features observed in the pressure data.

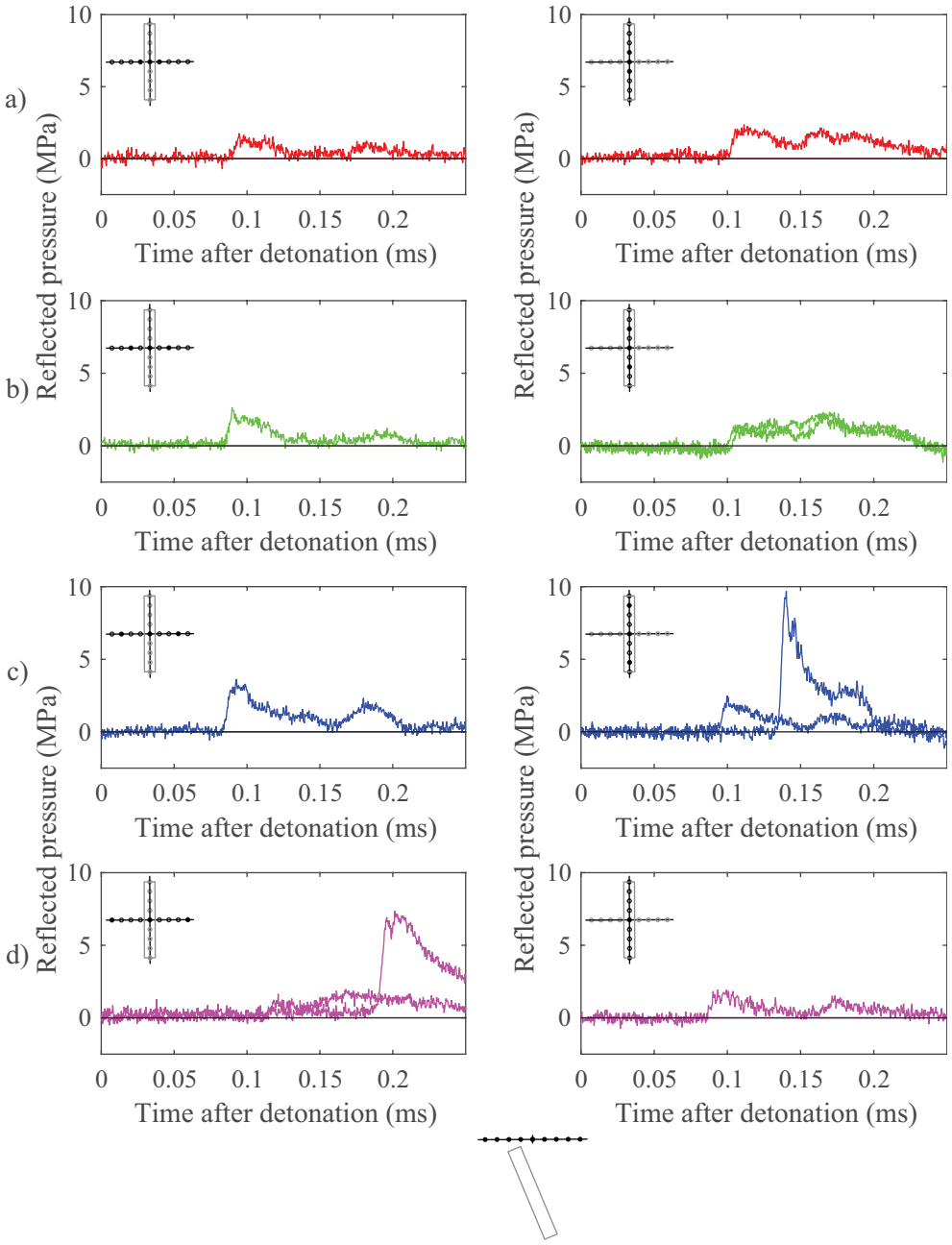


Figure 4.54: Reflected pressure time histories for test T031 (inclined cylindrical charge, 0°, 67.5° orientation, centrally detonated). Results are shown for radial offsets of (a) 25 mm (red), (b) 50 mm (green), (c) 75 mm (blue), and (d) 100 mm (magenta), compared against the central reference measurement (0 mm, black). For each radial position, measurements are presented for perpendicular sensor arrays (left column) and aligned sensor arrays (right column). Insets indicate the relative orientation of the charge and sensor configuration.

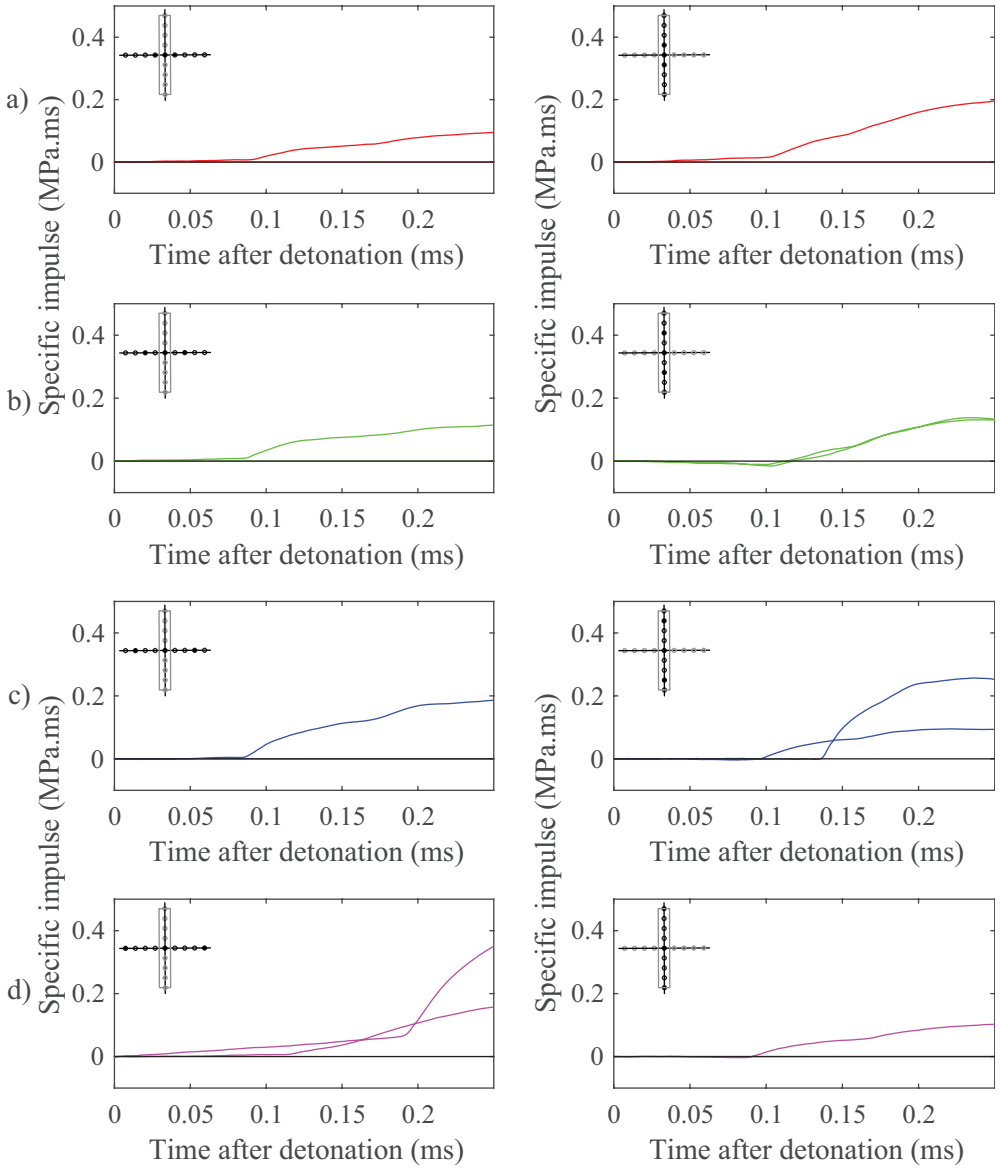


Figure 4.55: Specific impulse time histories for test T031 (inclined cylindrical charge, $0°, 67.5°$ orientation, centrally detonated). Results are shown for radial offsets of a) 25 mm (red), b) 50 mm (green), c) 75 mm (blue), and d) 100 mm (magenta), compared against the central reference measurement (0 mm, black). For each radial position, measurements are presented for perpendicular sensor arrays (left column) and aligned sensor arrays (right column). Insets indicate the relative orientation of the charge and sensor configuration.

4.7.2 Compiled results

The reflected pressure histories from Tests T028, T030, and T031 are presented collectively in Figure 4.56, following the same subplot arrangement as described for Figure 4.46, with rows a), b), and c) corresponding to Tests T028, T030, and T031 respectively, and row d) presenting the unweighted cross-test mean. The absence of the central bar reference trace in Tests T030 and T031 is reflected in the corresponding rows of the figure. The alignment of the timing for the averaging of the tests was conducted using the +75 mm parallel trace as it showed the most consistency across all the available traces. The + and − notation is applied consistently with the preceding inclined tests, with the charge elevated on the − side of the array.

The late arrival of the 100 mm perpendicular trace is a consistent and prominent feature across all three tests, remaining clearly visible in the cross-test mean in row d). The early pressure pulse observed in the 25 mm perpendicular trace is exclusive to Test T028. The long, late loading at the −50 mm parallel position is consistent across all three tests and is well preserved in the cross-test mean. The elevated peak pressures are concentrated towards the positive end of the parallel array, with the +75 mm position recording prominent peaks in all three tests. The +100 mm position recorded an elevated peak in Test T028, and this is mirrored in the cross-test mean for this location.

The specific impulse histories from Tests T028, T030, and T031 are presented in Figure 4.57, following the same arrangement as Figure 4.56. Considerable variability is present across the impulse traces, reflecting the complex and asymmetric loading environment of the 67.5° inclined configuration and the influence of instrumentation noise at these low pressure levels. The +75 mm parallel position exhibits the steepest impulse rise of any position in the array, and this feature is well preserved in the cross-test mean, although the +100 mm bar showed the highest peak impulse in the parallel array but could not be repeated due to the bars not recording for subsequent tests. The late arriving 100 mm perpendicular trace is seen to continue rising beyond the period of interest, indicating that the peak specific impulse has not been achieved. The 75 mm perpendicular trace for test T028 shows a peak specific impulse similar to the adjacent 100 mm bars but with a contrasting profile, highlighting the difference in loading type over a short distance.

The peak reflected pressures from Tests T028, T030, and T031 are presented in Figure 4.58. The perpendicular results exhibit good consistency between Tests T030 and T031 across all radial positions, whilst Test T028 records higher peak pressures across the array. The exception is at the 100 mm position, where all three tests show good agreement in peak pressure, for the very different loading profiles recorded at nominally identical points. The parallel results exhibit a clear trend of increasing peak pressure towards the positive end of the array, consistent with the dominant loading features identified in the comparative pressure traces.

The peak specific impulse values from Tests T028, T030, and T031 are presented in Figure 4.59, following the same arrangement as Figure 4.58. The perpendicular results

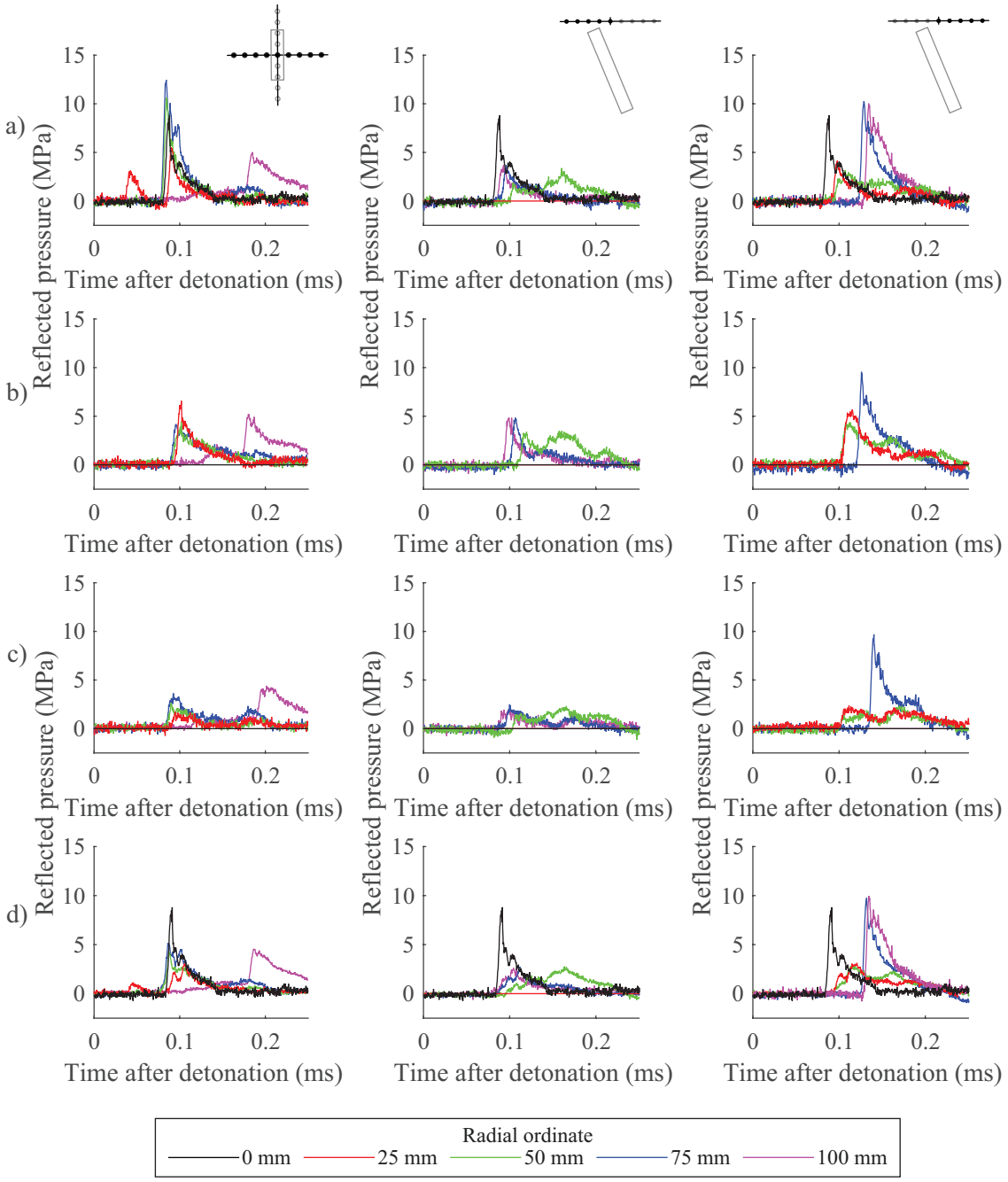


Figure 4.56: Reflected pressure time histories for inclined cylindrical charges ($0°, 67.5°$ orientation, centrally detonated) for tests a) T028, b) T030 and c) T031, with d) showing the average of the three tests, aligned by the arrival time at the central reference measurement (0 mm, black). Traces are shown for radial offsets of 0 mm (black), 25 mm (red), 50 mm (green), 75 mm (blue), and 100 mm (magenta). For each case, the perpendicular sensor array is presented in the left column, with the aligned array shown in the middle and right columns (opposing sides). Insets indicate the relative orientation of the charge and sensor configuration.

exhibit a general trend of increasing peak specific impulse with radial distance from the central bar outwards. The split in results at the 100 mm radial ordinate as also seen in the peak specific impulses. The parallel results display a broadly consistent trend of increasing peak specific impulse from the -100 mm to the $+100$ mm positions, with good consistency

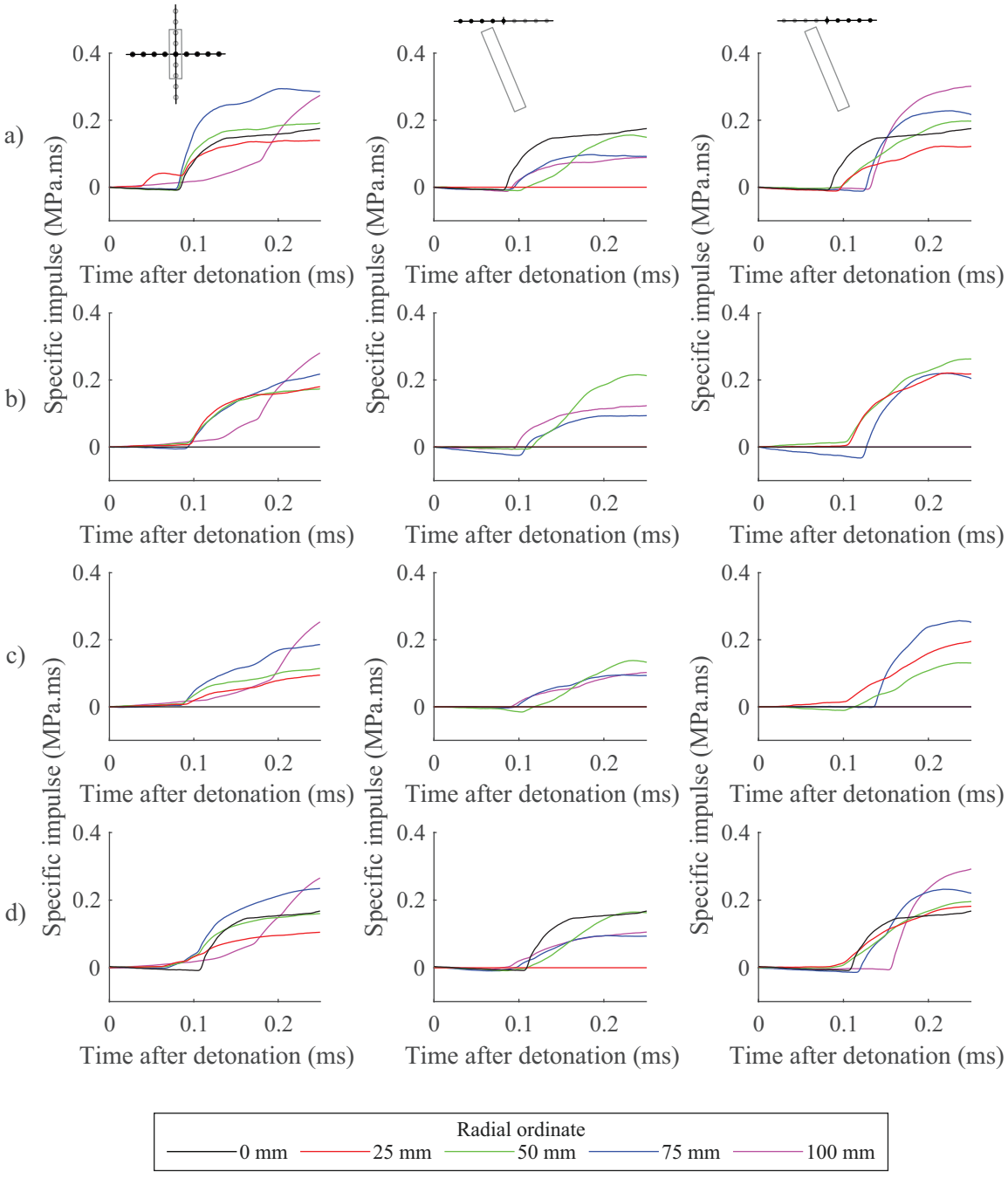


Figure 4.57: Specific impulse time histories for inclined cylindrical charges (0°, 67.5° orientation, centrally detonated) for tests a) T028, b) T030 and c) T031, with d) showing the average of the three tests, aligned by the arrival time at the central reference measurement (0 mm, black). Traces are shown for radial offsets of 0 mm (black), 25 mm (red), 50 mm (green), 75 mm (blue), and 100 mm (magenta). For each case, the perpendicular sensor array is presented in the left column, with the aligned array shown in the middle and right columns (opposing sides). Insets indicate the relative orientation of the charge and sensor configuration.

across all three tests. Particularly strong agreement between the three tests is observed at the −100 mm, −75 mm, and +75 mm positions, lending confidence that some repeatability of the experiments in the low-loading region in the near-field can be achieved.

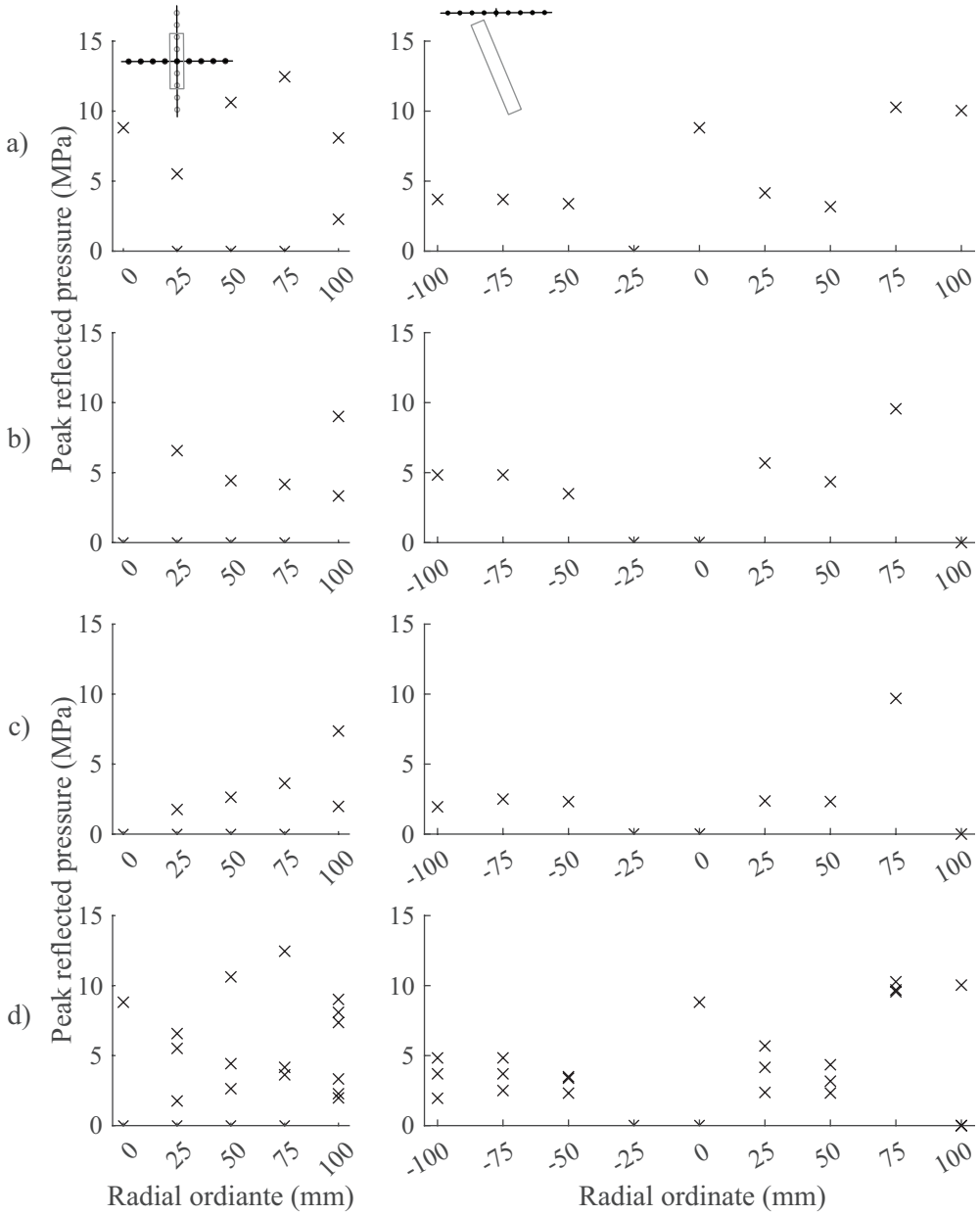


Figure 4.58: Peak reflected pressures for inclined cylindrical charges ($0°, 67.5°$ orientation, centrally detonated) for tests a) T028, b) T030 and c) T031, with d) showing a collation of the three tests. For each case, the perpendicular sensor array is presented in the left column, with the aligned array shown in the right column. Insets indicate the relative orientation of the charge and sensor configuration.

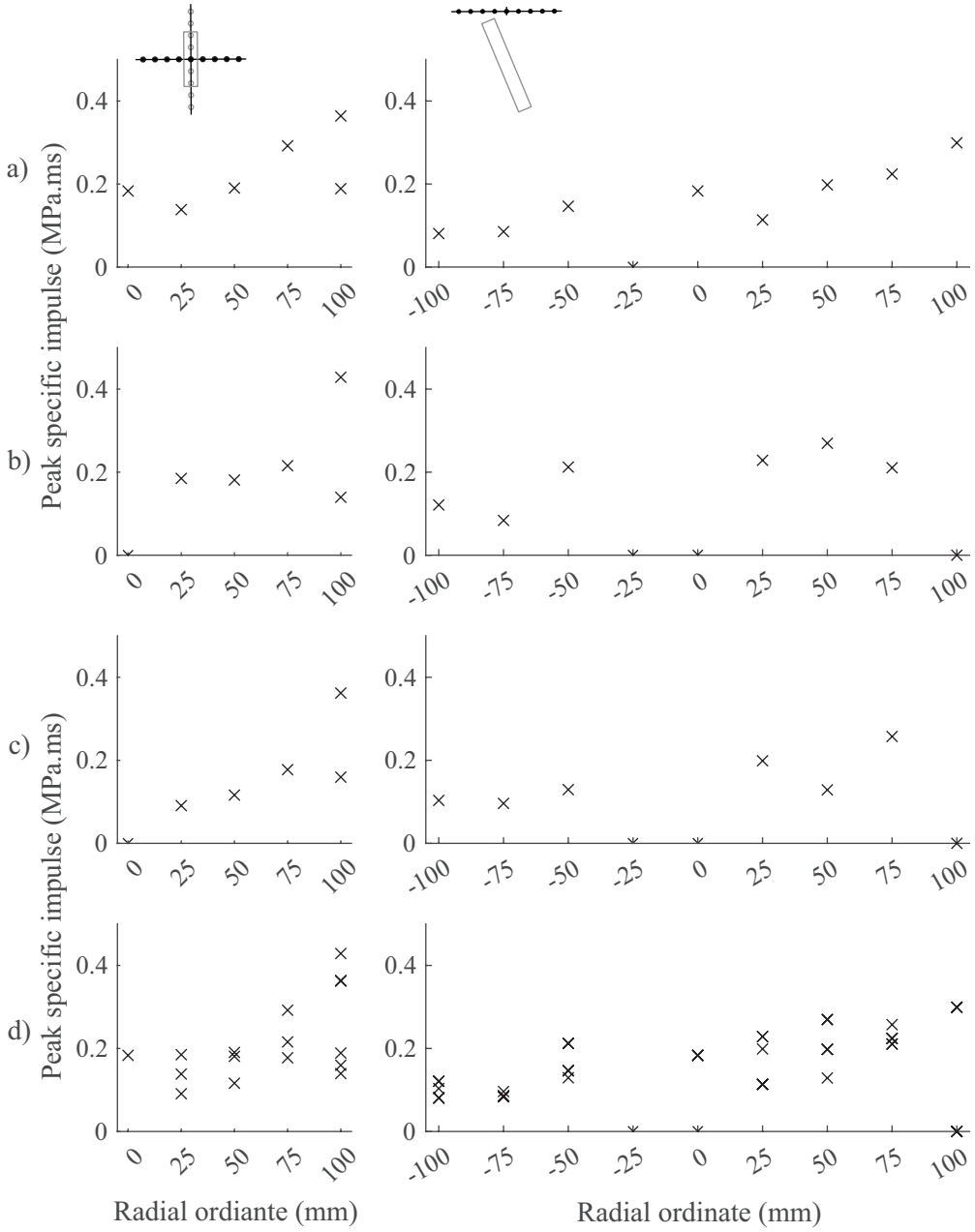


Figure 4.59: Peak specific impulses for inclined cylindrical charges ($0°, 67.5°$ orientation, centrally detonated) for tests a) T028, b) T030 and c) T031, with d) showing a collation of the three tests. For each case, the perpendicular sensor array is presented in the left column, with the aligned array shown in the right column. Insets indicate the relative orientation of the charge and sensor configuration.

4.8 Cylindrical tests – Axial (0°, 90°)

The following section presents the reflected pressure and specific impulse results obtained from cylindrical charges oriented axially, with the charge axis directed normal to the reflecting plate. With the charge axis directed normal to the reflecting plate, the axial blast wave is expected to be the dominant loading mechanism, with the reflected pressure and specific impulse distributions anticipated to reflect the characteristic spatial decay of the axial wave with increasing radial distance from the charge axis.

4.8.1 Test Results

In this configuration, both arrays are nominally identical in their geometric relationship to the charge, as the axial symmetry of the loading ensures that all bars at equivalent radial distances occupy equivalent positions relative to the charge axis. As a consequence, all bars at each radial distance are treated as repeat measurements of the same loading condition, yielding up to four repeat measurements per radial location across the two arrays. The results are presented using the same format as the 45° radial tests described in Section 4.4, with individual test figures arranged as a matrix of four subplots corresponding to radial offsets of 25 mm, 50 mm, 75 mm, and 100 mm, labelled a)–d) respectively, with the central bar trace included in each subplot as a consistent spatial reference. The comparative figures follow the same arrangement as the preceding sections, with rows a), b), and c) corresponding to Tests T016, T017, and T032 respectively, and row (d) presenting the cross-test mean or compiled results as appropriate.

T016

The reflected pressure histories recorded during Test T016 are presented in Figure 4.60, using the same array configuration and subplot arrangement as described for the axial tests. The central bar trace is included in all subplots as a consistent spatial reference. It is noted that one bar at the 50 mm position and two bars at the 75 mm position did not record valid pressure traces during this test and are represented as zero-value flat lines in the figure.

The central bar records the most Friedlander-like pressure trace observed across the experimental programme for centrally detonated charges, characterised by a sharp, high peak pressure followed by a rapid exponential decay. Oscillations are visible in the decay phase of the central bar trace; these are attributed to Pochhammer-Cree dispersion within the bar and are not considered representative of a physical feature of the blast wave. At 25 mm, one bar records a notably elevated peak pressure, whilst the remaining bars at this position record lower values that are nevertheless higher than those observed at the 75 mm and 100 mm positions, with considerable variability across the four traces. At 50 mm, one of the three surviving bars records a high pressure trace, whilst the remaining two record low values. At 75 mm and 100 mm, all surviving traces record low pressure values, consistent with the expected spatial decay of the axial blast wave with increasing radial

distance.

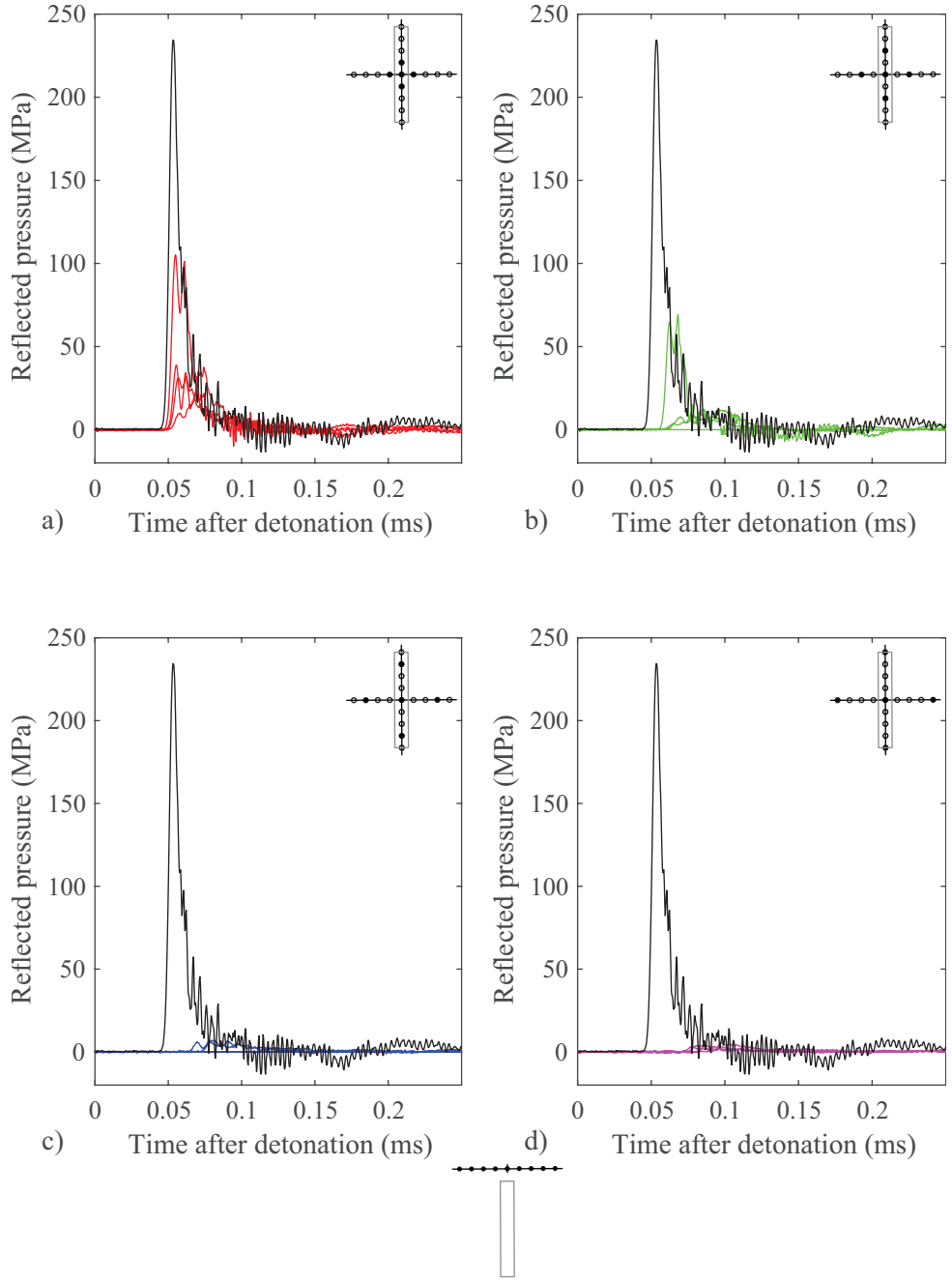


Figure 4.60: Reflected pressure time histories for test T016 (axial cylindrical charge, 0°, 90° orientation, centrally detonated). Results are shown for radial offsets of (a) 25 mm (red), (b) 50 mm (green), (c) 75 mm (blue), and (d) 100 mm (magenta), compared against the central reference measurement (0 mm, black). For each radial position, measurements are presented for perpendicular sensor arrays (left column) and aligned sensor arrays (right column). Insets indicate the relative orientation of the charge and sensor configuration.

The specific impulse histories for Test T016 are presented in Figure 4.61. The central bar records a strong impulse profile characterised by a fast rise and a rapid plateau to peak specific impulse, consistent with the sharp Friedlander-like pressure trace at this position. At 25 mm, the peak specific impulse exhibits approximately three-fold variability across

the four bars, with the spread distributed across the traces rather than being driven by a single outlier, whilst good repeatability is observed between the bars at either end of this range. Some variability is observed at 50 mm, whilst the 75 mm and 100 mm positions exhibit a close grouping of peak specific impulse values. A general trend of decreasing peak specific impulse with increasing radial distance from the central bar is discernible across the array, consistent with the expected dominance of the narrow axial blast wave jet.

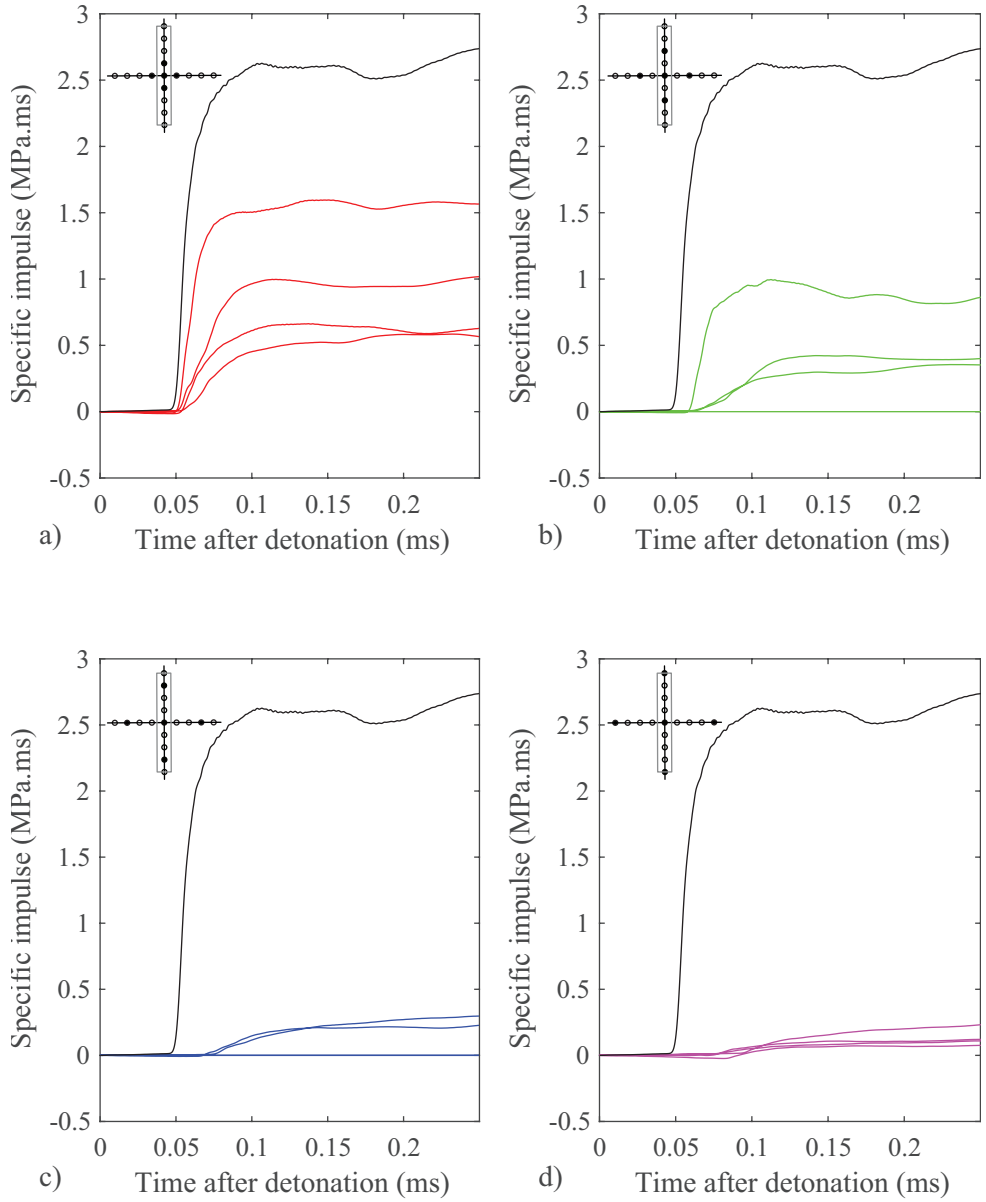


Figure 4.61: Specific impulse time histories for test T016 (axial cylindrical charge, 0°, 90° orientation, centrally detonated). Results are shown for radial offsets of a) 25 mm (red), b) 50 mm (green), c) 75 mm (blue), and d) 100 mm (magenta), compared against the central reference measurement (0 mm, black). For each radial position, measurements are presented for perpendicular sensor arrays (left column) and aligned sensor arrays (right column). Insets indicate the relative orientation of the charge and sensor configuration.

T017

The reflected pressure histories recorded during Test T017 are presented in Figure 4.62, using the same array configuration and subplot arrangement as described for Test T016. Three non-functioning bars were present, with one bar at the 50 mm position and two bars at the 75 mm position represented as zero-value flat lines in the figure, same as T016.

The results are broadly similar to those observed in Test T016. The central bar again records a strong Friedlander-like pressure trace with a sharp peak and rapid decay; Pochhammer-Cree dispersion oscillations are present in the decay phase, though less pronounced than in Test T016. At 25 mm, all four bars record broadly similar peak pressures, in contrast to the single notably elevated trace observed at this position in Test T016. At 50 mm, a mix of high and low pressure traces is again observed across the surviving bars, consistent with the pattern identified in T016. The 75 mm and 100 mm positions continue to record low pressure values across all surviving traces, consistent with the spatial decay of the axial blast wave with increasing radial distance.

The specific impulse histories for Test T017 are presented in Figure 4.63. The 25 mm bars exhibit a closer grouping of peak specific impulse values than observed in Test T016, consistent with the more uniform pressure traces at this position. At 50 mm, greater variability is observed, with two of the surviving bars recording peak specific impulse values mirroring those at the 25 mm position, consistent with the elevated pressure traces at this location. The 75 mm and 100 mm positions record low peak specific impulse values with a close grouping, consistent with the observations from Test T016.

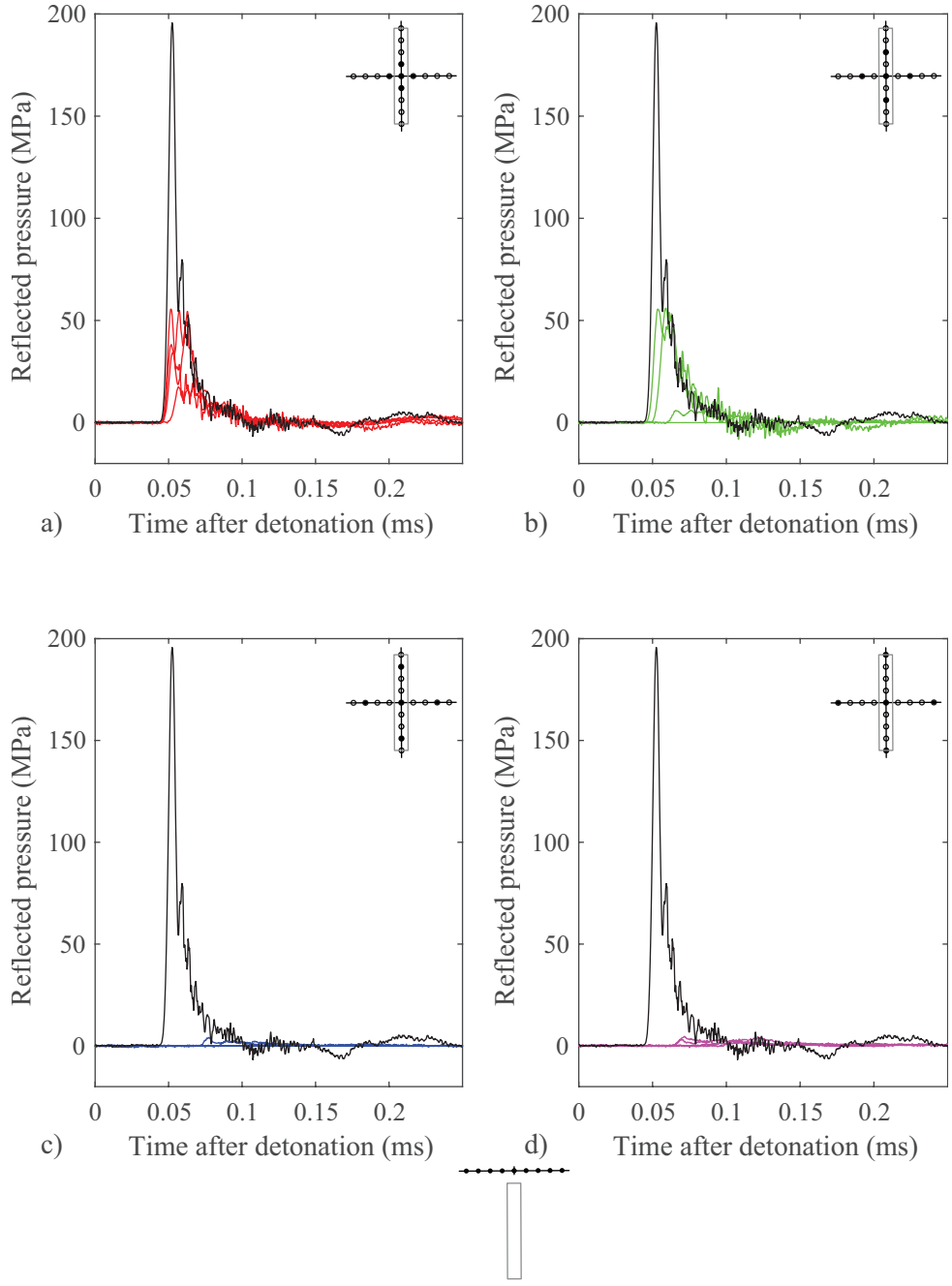


Figure 4.62: Reflected pressure time histories for test T017 (axial cylindrical charge, $0°, 90°$ orientation, centrally detonated). Results are shown for radial offsets of (a) 25 mm (red), (b) 50 mm (green), (c) 75 mm (blue), and (d) 100 mm (magenta), compared against the central reference measurement (0 mm, black). For each radial position, measurements are presented for perpendicular sensor arrays (left column) and aligned sensor arrays (right column). Insets indicate the relative orientation of the charge and sensor configuration.

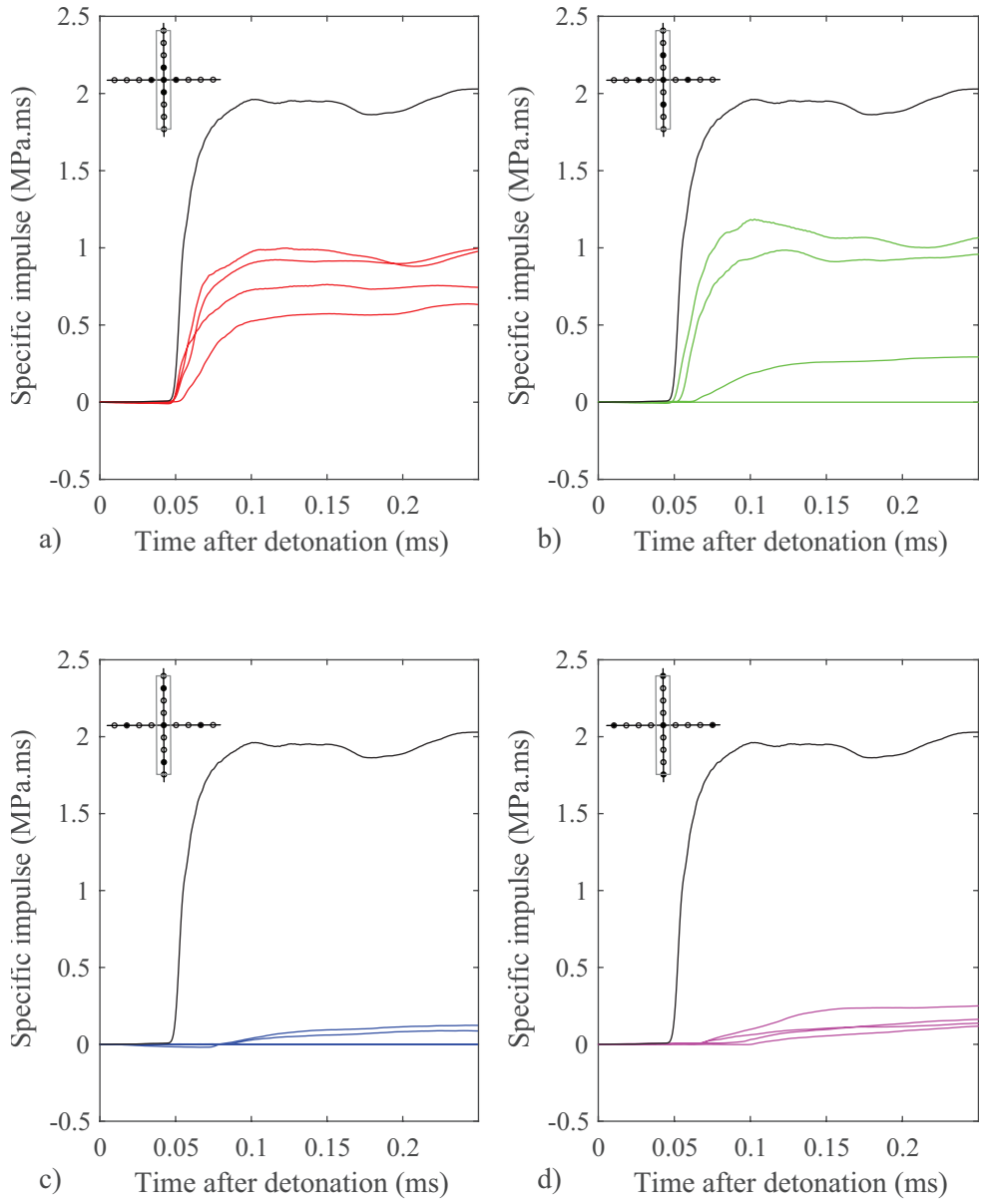


Figure 4.63: Specific impulse time histories for test T017 (axial cylindrical charge, 0°, 90° orientation, centrally detonated). Results are shown for radial offsets of a) 25 mm (red), b) 50 mm (green), c) 75 mm (blue), and d) 100 mm (magenta), compared against the central reference measurement (0 mm, black). For each radial position, measurements are presented for perpendicular sensor arrays (left column) and aligned sensor arrays (right column). Insets indicate the relative orientation of the charge and sensor configuration.

T032

The reflected pressure histories recorded during Test T032 are presented in Figure 4.64, using the same array configuration and subplot arrangement as described for the preceding axial tests. A significant number of bars did not record valid pressure traces during this test, including the central bar, two bars at the 25 mm position, one bar at the 50 mm position, one bar at the 75 mm position, and two bars at the 100 mm position, all of which are represented as zero-value flat lines in the figure. The absence of the central bar reference trace is noted throughout.

Of the two surviving traces at 25 mm, one records a strong shock consistent in character with the 25 mm results from Tests T016 and T017, whilst the other records a considerably reduced pressure, falling below the expectation established by the preceding tests at this position. The 50 mm surviving bars record low and mutually consistent pressure traces, broadly in line with the lower traces observed at this position in T016 and T017. At 75 mm, two of the three surviving bars record unusually elevated pressure traces, characterised by a lower peak pressure and longer positive phase duration than the Friedlander-like profiles observed in the central bar of the preceding tests; this departure from the expected spatial decay is tentatively attributed to either a slight misalignment of the charge or near-field variability, though no definitive cause has been identified. The third surviving 75 mm trace is more consistent with the low values recorded at this position in the preceding tests. At 100 mm, the two surviving bars record little to no discernible pressure, with the traces dominated by instrumentation noise.

The specific impulse histories for Test T032 are presented in Figure 4.65. The two surviving 25 mm traces exhibit vastly different peak specific impulse values, consistent with the strong and reduced pressure traces at this position. Good consistency is observed between the surviving 50 mm bars, reflecting the uniformity of the pressure traces at this location. The two questionably elevated 75 mm pressure traces produce peak specific impulse values considerably above the expectation from the preceding tests, whilst the third surviving trace at this position remains consistent with the T016 and T017 results. The 100 mm traces are predominantly influenced by instrumentation noise, with no meaningful specific impulse accumulation discernible above the noise baseline. Whilst the significant number of dead bars and the anomalous 75 mm results necessitate that the T032 data be interpreted with appropriate caution, the surviving traces nonetheless contribute additional data points to the cross-test averaging and compiled peak results presented in the subsequent comparative figures.

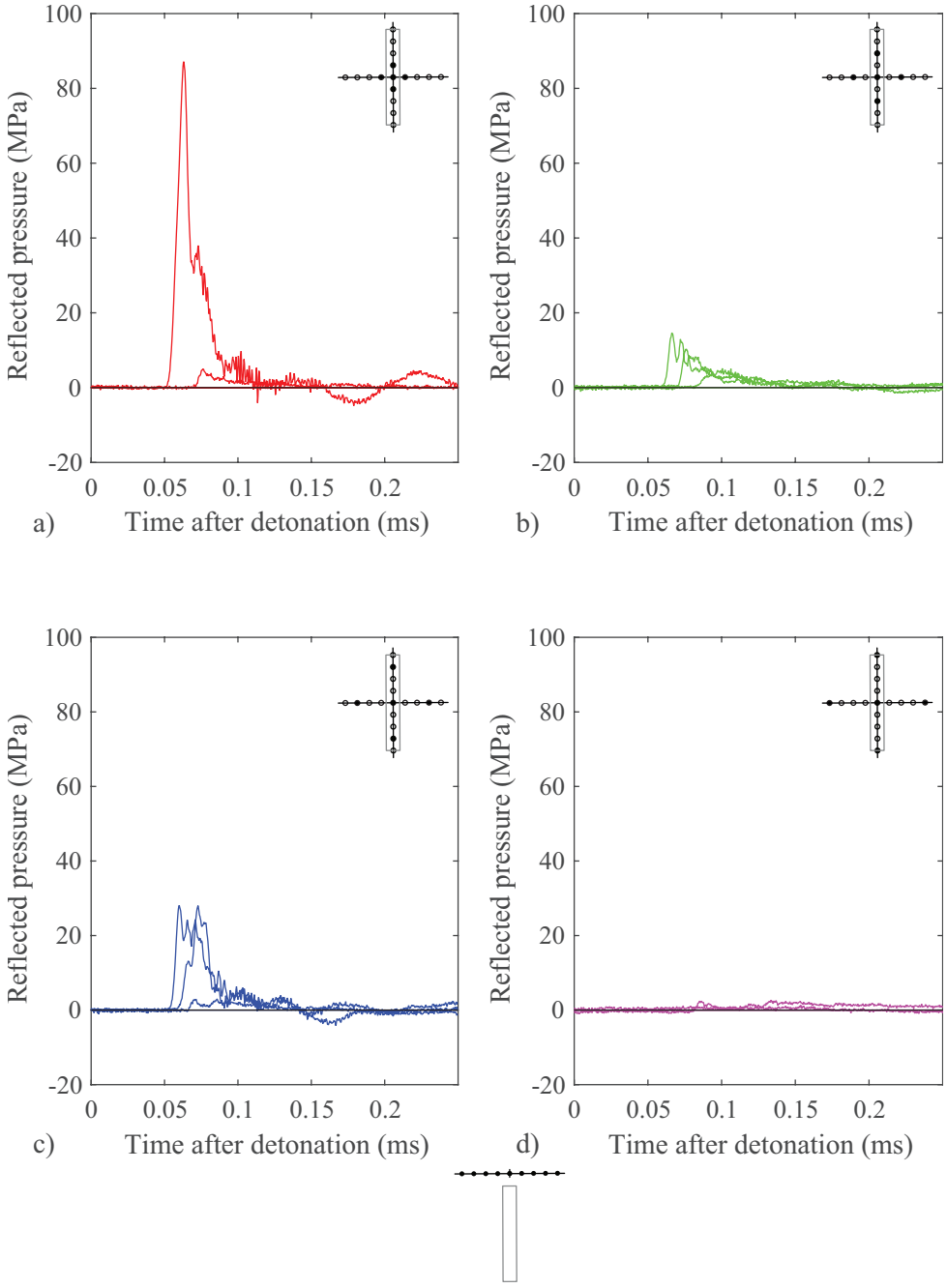


Figure 4.64: Reflected pressure time histories for test T032 (axial cylindrical charge, 0°, 90° orientation, centrally detonated). Results are shown for radial offsets of (a) 25 mm (red), (b) 50 mm (green), (c) 75 mm (blue), and (d) 100 mm (magenta), compared against the central reference measurement (0 mm, black). For each radial position, measurements are presented for perpendicular sensor arrays (left column) and aligned sensor arrays (right column). Insets indicate the relative orientation of the charge and sensor configuration.

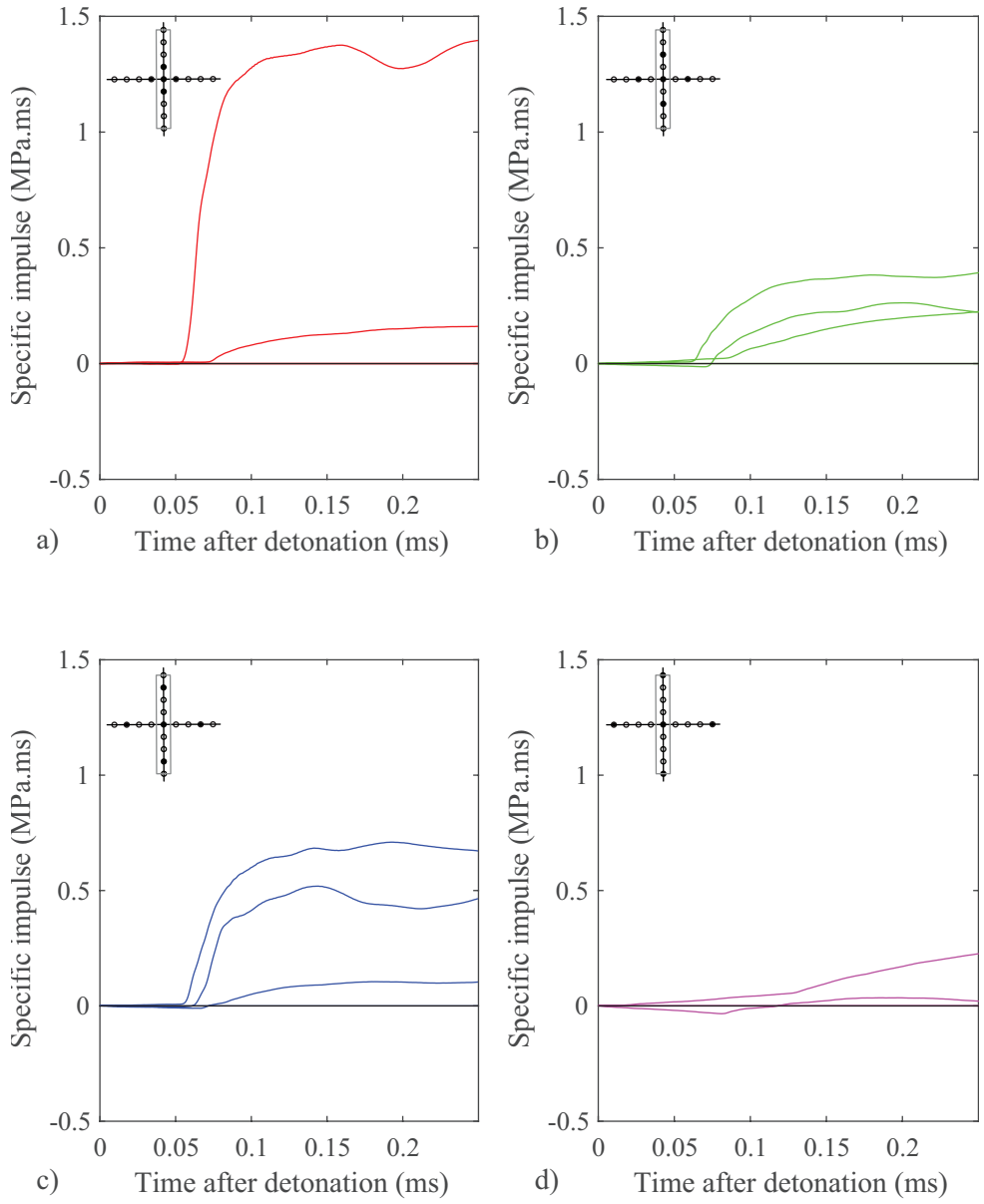


Figure 4.65: Specific impulse time histories for test T032 (axial cylindrical charge, 0°, 90° orientation, centrally detonated). Results are shown for radial offsets of a) 25 mm (red), b) 50 mm (green), c) 75 mm (blue), and d) 100 mm (magenta), compared against the central reference measurement (0 mm, black). For each radial position, measurements are presented for perpendicular sensor arrays (left column) and aligned sensor arrays (right column). Insets indicate the relative orientation of the charge and sensor configuration.

4.8.2 Compiled results

The reflected pressure histories from Tests T016, T017, and T032 are presented collectively in Figure 4.66, following the same subplot arrangement as described for Figure 4.26, with a), b), and c) corresponding to Tests T016, T017, and T032 respectively, and d) presenting the unweighted cross-test mean. As all bars at equivalent radial distances are nominally identical in this orientation, each trace represents the mean of the surviving bars at each radial position, with zero-value traces excluded from the averaging process prior to computation of the mean.

The central bar traces from Tests T016 and T017 exhibit consistent Friedlander-like characteristics and reproduce well in the cross-test mean in d), with the absence of the central bar in Test T032 noted but not significantly detracting from the averaged result. The 25 mm averaged trace from Test T032 complements the timing and magnitude of the equivalent traces from Tests T016 and T017, contributing positively to the cross-test mean at this position. The anomalous 75 mm traces from Test T032 are visible in c), recording higher averaged pressures than the 50 mm position, and their influence is reflected in the cross-test mean in d). The averaged traces in d) demonstrate a clear and progressive stepping down in pressure with increasing radial distance from the central bar, most clearly established in the cross-test mean where the inter-test variability at individual positions is mitigated by the averaging process.

The specific impulse histories from Tests T016, T017, and T032 are presented in Figure 4.67, following the same arrangement as Figure 4.66. The variability in the 25 mm and 50 mm impulse results observed in Tests T016 and T017 individually is mitigated in the cross-test mean, which produces an averaged impulse decay with radial distance consistent with both the pressure observations and the expected behaviour of the axial blast wave. Test T032 exhibits an order swap in peak specific impulse between the 50 mm and 75 mm positions, consistent with the anomalously elevated 75 mm pressure traces identified in that test. Despite this, the cross-test mean in d) presents a clear and consistent reduction in specific impulse with increasing radial distance.

The peak reflected pressures from Tests T016, T017, and T032 are presented in Figure 4.68. The compiled results demonstrate a clear trend of rapidly diminishing peak pressure with increasing radial distance from the central bar. The reduction in peak pressure between the central bar and the 25 mm position is particularly pronounced, with a greater than halving of peak pressure observed consistently across Tests T016 and T017, with the effect being even more pronounced in Test T017. This highlights both the strong spatial variation in the axial shock front and the good agreement between the first two experimental tests.

The peak specific impulse values from Tests T016, T017, and T032 are presented in Figure 4.69, following the same arrangement as Figure 4.68. The compiled results exhibit a similar spatial relationship to the peak pressure data, with a clear reduction in peak specific impulse with increasing radial distance from the central bar, though the rate of spatial variation is less pronounced than that observed in the peak pressure results. The

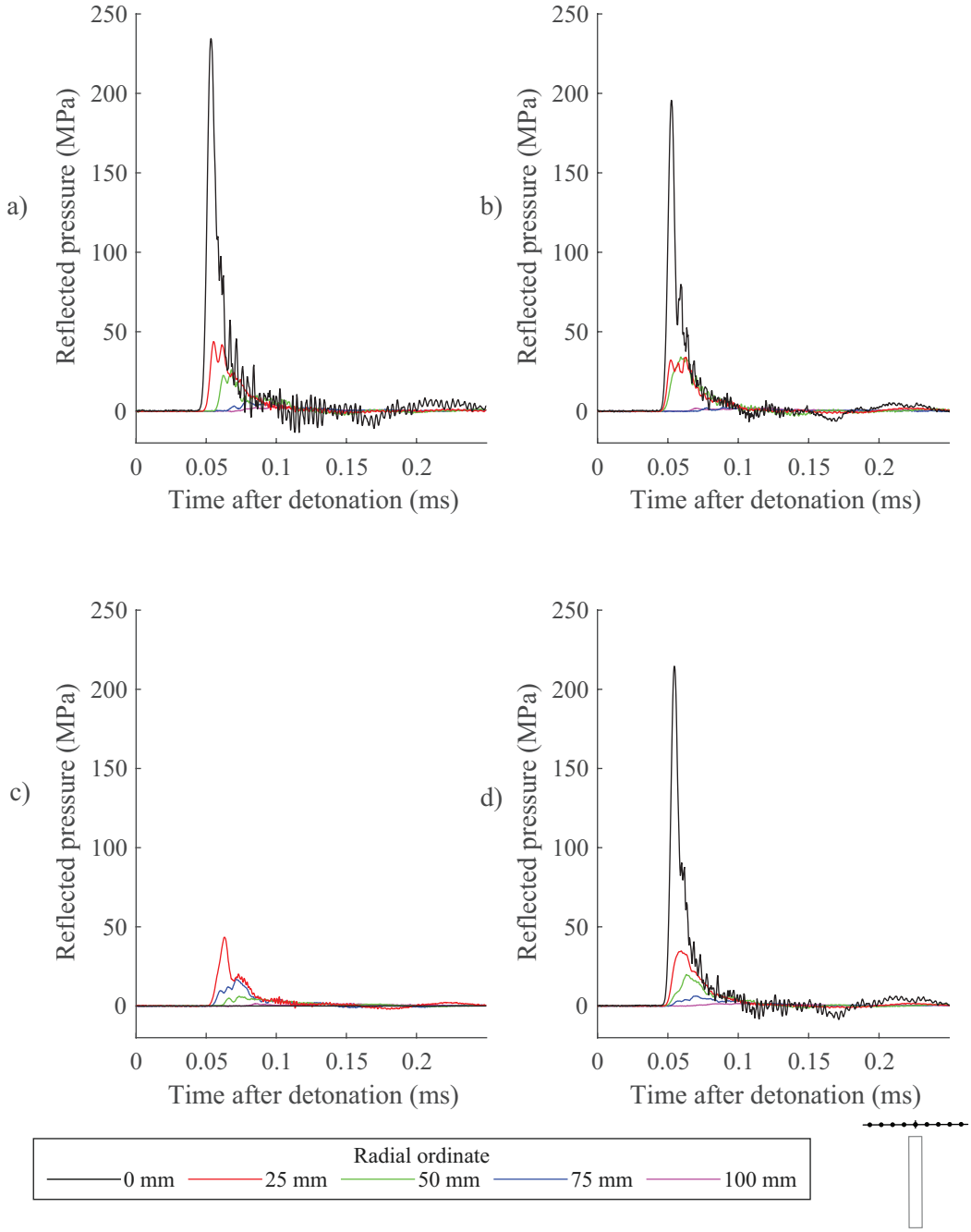


Figure 4.66: Reflected pressure time histories for axial cylindrical charges ($0°, 90°$ orientation, centrally detonated) for tests a) T016, b) T017 and c) T032, with d) showing the average of the three tests, aligned by the arrival time at the central reference measurement (0 mm, black). Traces are shown for radial offsets of 0 mm (black), 25 mm (red), 50 mm (green), 75 mm (blue), and 100 mm (magenta). For each case, the perpendicular sensor array is presented in the left column, with the aligned array shown in the middle and right columns (opposing sides). Insets indicate the relative orientation of the charge and sensor configuration.

overall trend remains clearly discernible despite the influence of the anomalous 75 mm results from Test T032, the elevated 50 mm results from Test T017, and one elevated 25 mm result from Test T016, all of which shift the upper bound of the data banding at their respective positions without obscuring the underlying decay trend.

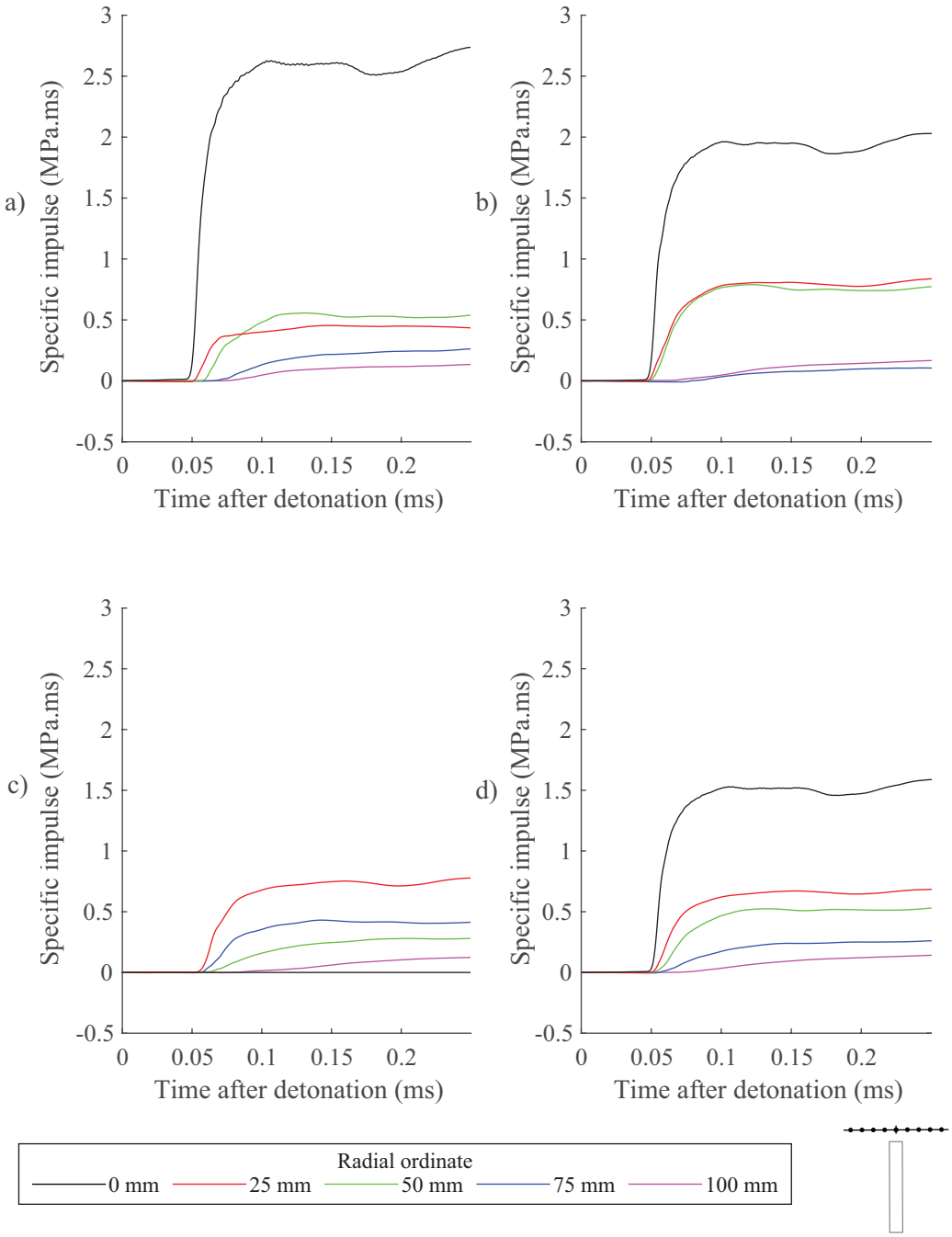


Figure 4.67: Specific impulse time histories for axial cylindrical charges (0°, 90° orientation, centrally detonated) for tests a) T016, b) T017 and c) T032, with d) showing the average of the three tests, aligned by the arrival time at the central reference measurement (0 mm, black). Traces are shown for radial offsets of 0 mm (black), 25 mm (red), 50 mm (green), 75 mm (blue), and 100 mm (magenta). For each case, the perpendicular sensor array is presented in the left column, with the aligned array shown in the middle and right columns (opposing sides). Insets indicate the relative orientation of the charge and sensor configuration.

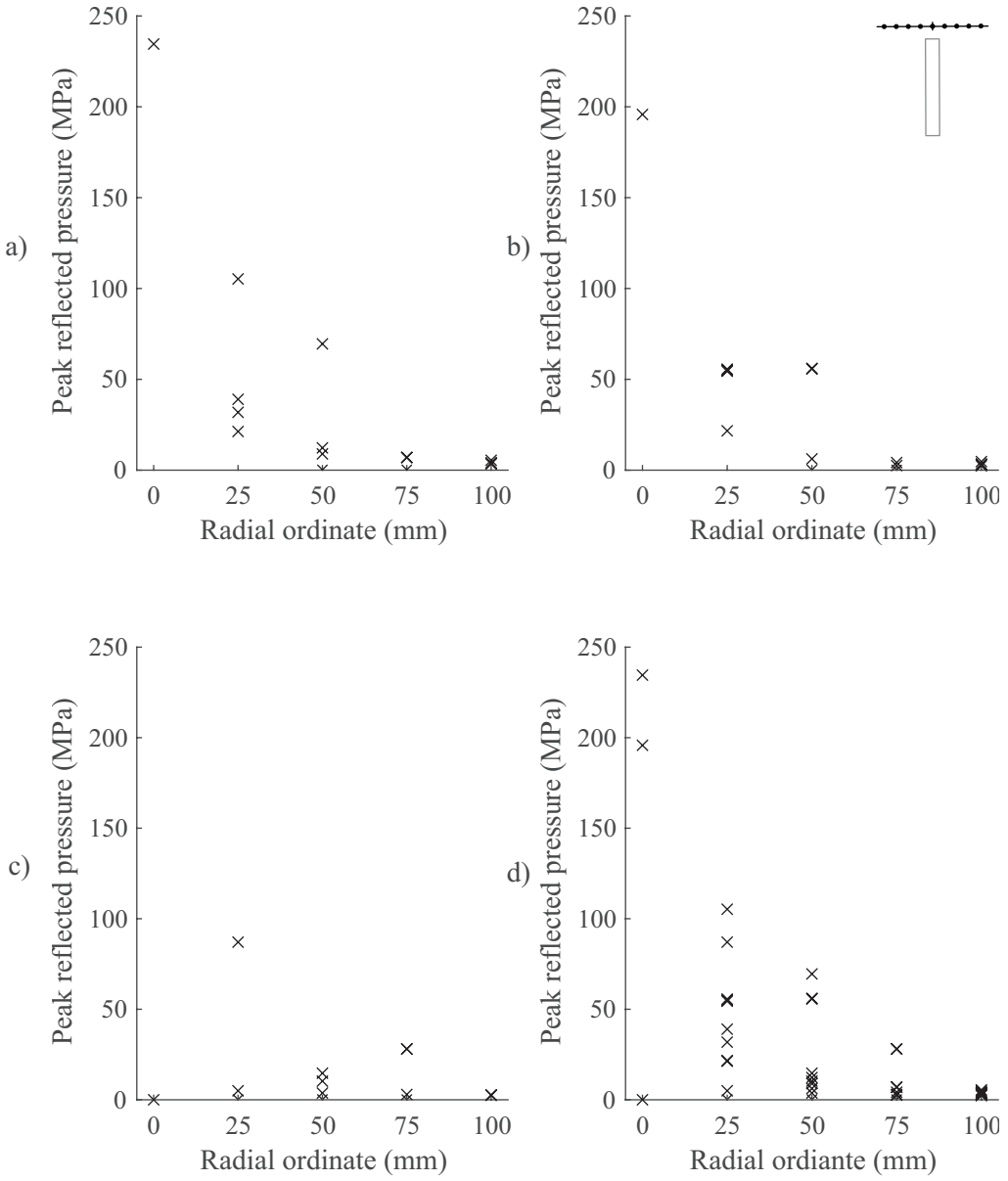


Figure 4.68: Peak reflected pressures for axial cylindrical charges ($0°, 90°$ orientation, centrally detonated) for tests a) T016, b) T017 and c) T032, with d) showing a collation of the three tests. For each case, the perpendicular sensor array is presented in the left column, with the aligned array shown in the right column. Insets indicate the relative orientation of the charge and sensor configuration.

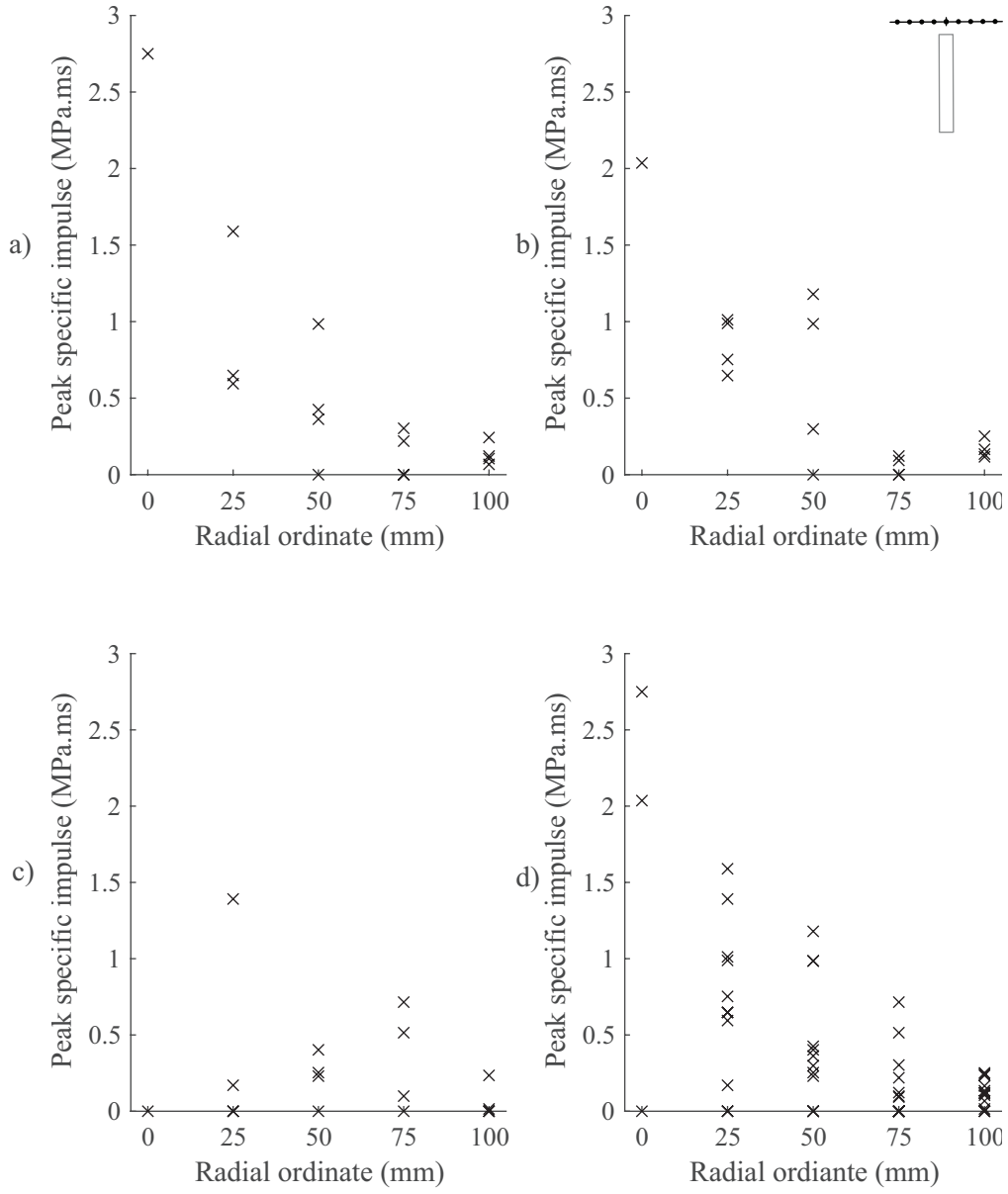


Figure 4.69: Peak specific impulses for axial cylindrical charges ($0°, 90°$ orientation, centrally detonated) for tests a) T016, b) T017 and c) T032, with d) showing a collation of the three tests. For each case, the perpendicular sensor array is presented in the left column, with the aligned array shown in the right column. Insets indicate the relative orientation of the charge and sensor configuration.

Three cylindrical tests with the symmetrical-axis of the charges aligned with the axis of the central bar, were conducted and results are presented alongside the results from spheres and radial cylinders in Figure 4.70.

Bars not recording data are removed from the data set, relying on the redundancy of four bars at each radial ordinate from which to calculate an average. If the central (0 mm) bar is non-functional a result cannot be given.

The reflected pressure and specific impulse histories, averaged at the matching radial ordinates, from the three tests and an average are presented in Figure 4.70. The experimental results exhibit good repeatability, characterised by consistently high peak pressure readings at the central bar and a rapid decline in pressure at larger radial ordinates. Signs of secondary shock waves are visible in the pressure traces around 0.01 ms after the initial shock front but the averaging of the data has removed some of the detail.

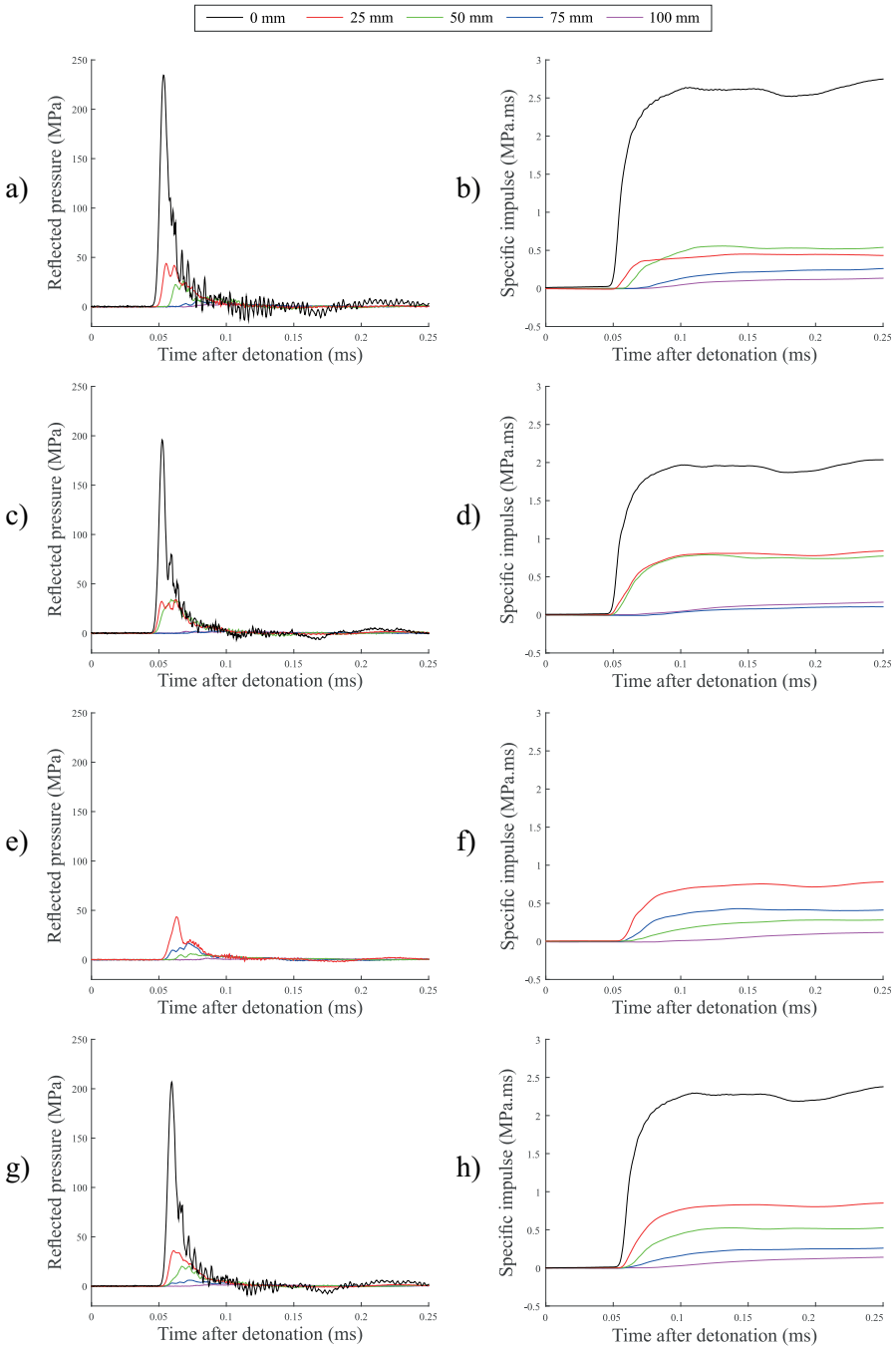


Figure 4.70: Reflected pressure (a, c, e, g) and specific impulse (b, d, f, h) traces averaged at the four symmetrical, non-central radial ordinate of axial cylindrical tests 1-3 (a,b, c,d, e,f respectively) and an average (g,h)

4.9 Cylindrical tests – Axial (0°, 90°) – End detonated

The following section presents the reflected pressure and specific impulse results obtained from cylindrical charges oriented axially and detonated at the end of the charge, with the charge axis directed normal to the reflecting plate. Whilst the end detonation point differs from the centrally detonated case, the axial orientation of the charge preserves the symmetry of the loading across the array.

4.9.1 Test Results

As with the centrally detonated axial tests presented in Section 4.8, the rotational symmetry of the configuration about the charge axis ensures that all bars at equivalent radial distances occupy nominally identical positions relative to the charge, yielding up to four repeat measurements per radial location across the two arrays. The results are presented in the same format as the centrally detonated axial tests, with individual test figures arranged as a matrix of four subplots corresponding to radial offsets of 25 mm, 50 mm, 75 mm, and 100 mm, labelled a)–d) respectively, with the central bar trace included in each subplot as a consistent spatial reference. The comparative figures follow the same three-row arrangement as the end detonated radial tests, with a) and b) corresponding to Tests T014 and T015 respectively, and c) presenting the cross-test mean or compiled results as appropriate.

T014

The reflected pressure histories recorded during Test T014 are presented in Figure 4.71, using the same array configuration and subplot arrangement as described for the axial tests. The central bar trace is included in all subplots as a consistent spatial reference. It is noted that one bar at the 50 mm position did not record a valid pressure trace during this test and is represented as a zero-value flat line in the figure.

The central bar records a good Friedlander-like pressure pulse, consistent in character with the central bar traces observed in the centrally detonated axial tests. At 25 mm, one bar records a peak pressure comparable in magnitude to the central bar, whilst the remaining bars at this position exhibit a large spread of lower values. Pochhammer-Cree dispersion oscillations are visible in the decay phase of the traces recording the highest peak pressures, consistent with the observations from Tests T016 and T017. At 50 mm, the three surviving bars record small but consistent pressure pulses across the position. At 75 mm and 100 mm, little to no loading is recorded consistently across all bars, representing the rapid spatial decay observed in the centrally detonated axial tests.

The specific impulse histories for Test T014 are presented in Figure 4.72. At 25 mm, a broad spread of peak specific impulse values is observed across all four bars, with one trace exceeding the central bar peak specific impulse. Despite this spread, a general trend of decreasing specific impulse with increasing radial distance is discernible across the array. The 50 mm positions record moderate specific impulse values, consistent with the small

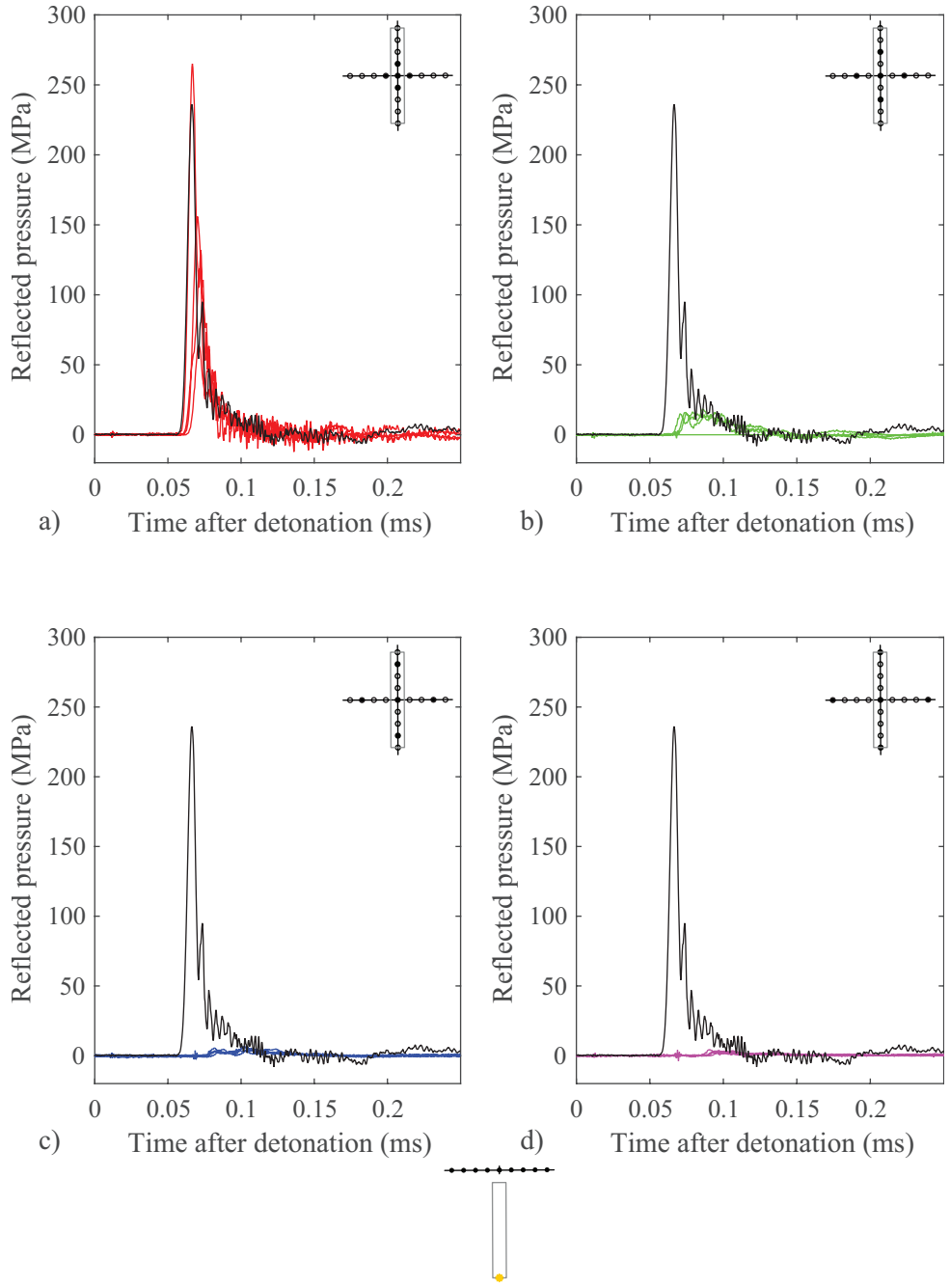


Figure 4.71: Reflected pressure time histories for test T014 (axial cylindrical charge, 0°, 90° orientation, end detonated). Results are shown for radial offsets of (a) 25 mm (red), (b) 50 mm (green), (c) 75 mm (blue), and (d) 100 mm (magenta), compared against the central reference measurement (0 mm, black). For each radial position, measurements are presented for perpendicular sensor arrays (left column) and aligned sensor arrays (right column). Insets indicate the relative orientation of the charge and sensor configuration.

pressure pulses observed at this location, whilst the 75 mm and 100 mm positions record little specific impulse accumulation, reflecting the negligible pressure loading at these distances. Noise in the signals is seen to affect three of the impulse traces at the 75 mm ordinate, having the effect of reducing the peak impulses recorded.

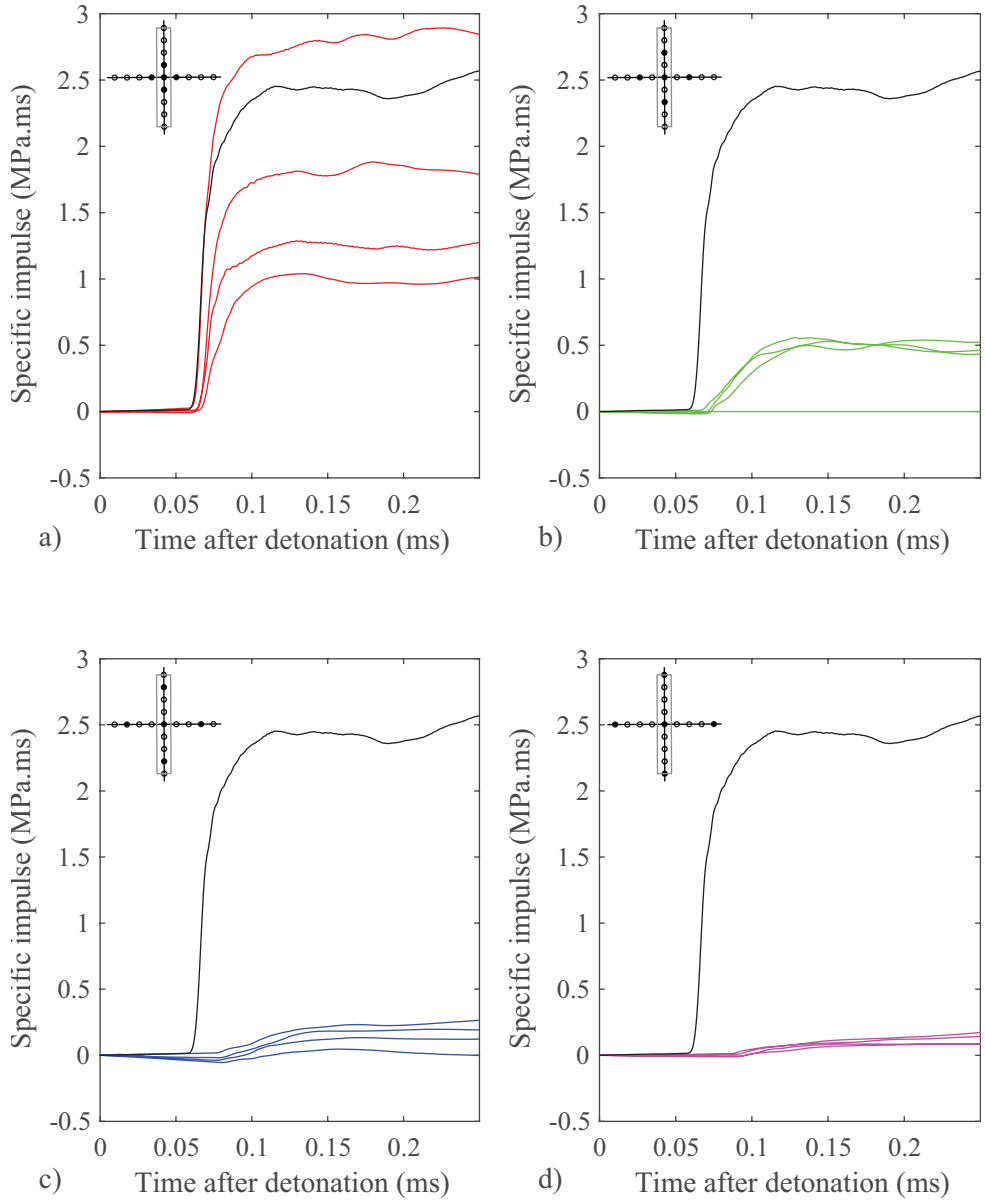


Figure 4.72: Specific impulse time histories for test T014 (axial cylindrical charge, 0°, 90° orientation, end detonated). Results are shown for radial offsets of a) 25 mm (red), b) 50 mm (green), c) 75 mm (blue), and d) 100 mm (magenta), compared against the central reference measurement (0 mm, black). For each radial position, measurements are presented for perpendicular sensor arrays (left column) and aligned sensor arrays (right column). Insets indicate the relative orientation of the charge and sensor configuration.

T015

The reflected pressure histories recorded during Test T015 are presented in Figure 4.73, using the same array configuration and subplot arrangement as described for the preceding axial tests. The central bar trace is included in all subplots as a consistent spatial reference. It is noted that one bar at the 50 mm position and one bar at the 75 mm position did not record valid pressure traces during this test and are represented as zero-value flat lines in the figure.

The central bar records the highest peak pressure observed across the entire experimental programme, representing a notable result for this charge orientation and detonation configuration. Pochhammer-Cree dispersion oscillations are present in the central bar decay phase, though not particularly prominent given the exceptional magnitude of the peak. At 25 mm, the four bars record lower peak pressures than the equivalent position in Test T014, but with considerably less variation between them; the repeatability is good across three of the four bars, with one recording a lower value. The 50 mm, 75 mm, and 100 mm positions record similarly low pressure values to those observed in Test T014, with the surviving bars at each position exhibiting results consistent with the spatial decay trend established across the axial tests.

The specific impulse histories for Test T015 are presented in Figure 4.74. The central bar records a very high peak specific impulse, consistent with the exceptional peak pressure at this position. The 25 mm bars exhibit a close grouping of peak specific impulse values across all four bars, representing a notably tighter spread than observed in Test T014. At 50 mm, one of the three surviving bars records a moderately elevated specific impulse, whilst the remaining two bars record values consistent with the expected range at this position, showing good mutual agreement. The 75 mm and 100 mm positions record little to no specific impulse accumulation, consistent with the negligible pressure loading at these distances.

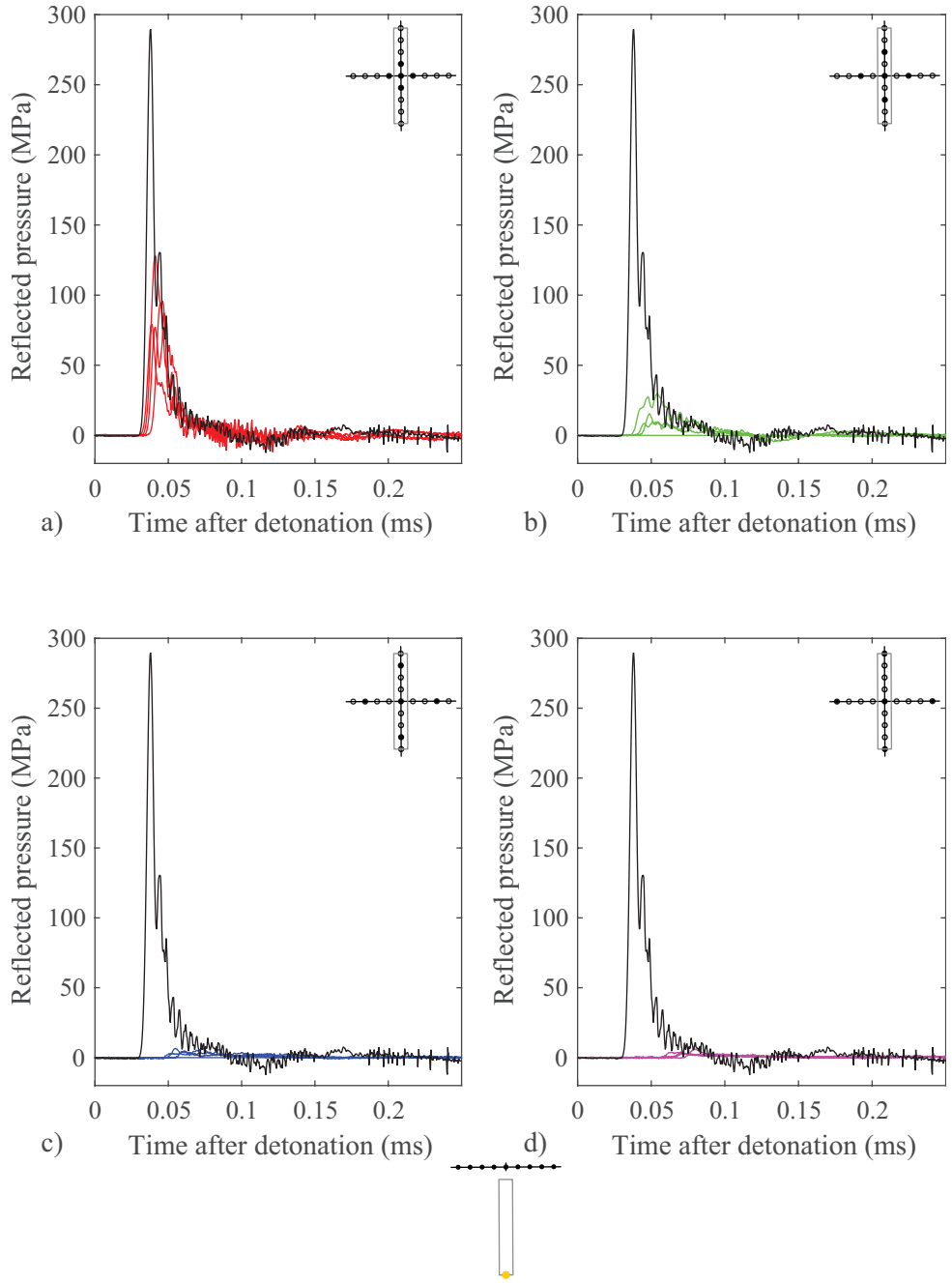


Figure 4.73: Reflected pressure time histories for test T015 (axial cylindrical charge, $0°, 90°$ orientation, end detonated). Results are shown for radial offsets of (a) 25 mm (red), (b) 50 mm (green), (c) 75 mm (blue), and (d) 100 mm (magenta), compared against the central reference measurement (0 mm, black). For each radial position, measurements are presented for perpendicular sensor arrays (left column) and aligned sensor arrays (right column). Insets indicate the relative orientation of the charge and sensor configuration.

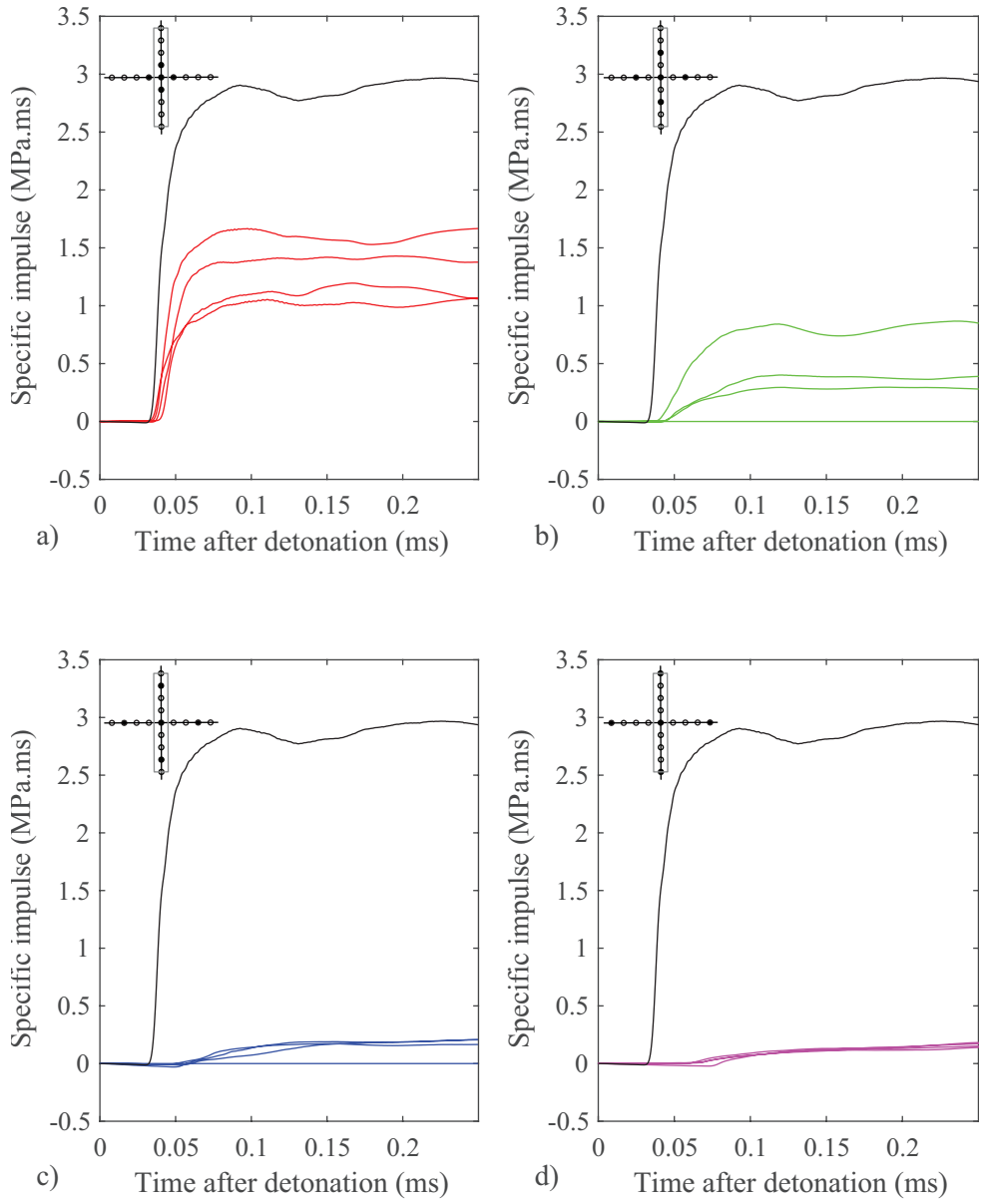


Figure 4.74: Specific impulse time histories for test T015 (axial cylindrical charge, 0°, 90° orientation, end detonated). Results are shown for radial offsets of a) 25 mm (red), b) 50 mm (green), c) 75 mm (blue), and d) 100 mm (magenta), compared against the central reference measurement (0 mm, black). For each radial position, measurements are presented for perpendicular sensor arrays (left column) and aligned sensor arrays (right column). Insets indicate the relative orientation of the charge and sensor configuration.

4.9.2 Compiled results

The reflected pressure histories from Tests T014 and T015 are presented collectively in Figure 4.75, following the same subplot arrangement as described for Figure 4.66, with the exception that only three rows are presented. Graph a) and b) correspond to Tests T014 and T015 respectively, and c) presents the unweighted cross-test mean. As with the centrally detonated axial tests, each trace represents the mean of the surviving bars at each radial position, with zero-value traces excluded from the averaging process prior to computation of the mean.

The central bar traces are the dominant feature of the comparative pressure results, consistent with the observations from the centrally detonated axial tests. The elevated 25 mm pressure values recorded in Test T014 are retained in the individual test average in a), but are diminished in the cross-test mean in c), where the lower 25 mm values of Test T015 pull the averaged trace down at this position. The reduction in pressure with increasing radial distance is clearly and consistently demonstrated across all traces in both individual tests and the cross-test mean, representing one of the clearest illustrations of spatial pressure decay observed across the entire experimental programme.

The specific impulse histories from Tests T014 and T015 are presented in Figure 4.76, following the same arrangement as Figure 4.75. The central bar impulse traces exhibit consistent behaviour between the two tests, with both recording strong and rapidly plateauing profiles. The 25 mm traces exhibit a large spread between the two tests, with the cross-test mean in c) sitting at the expected intermediate value. The results demonstrate a clear directionality of the blast loading, particularly in Test T015, where the concentration of specific impulse at the central bar position relative to the radial positions is especially pronounced, consistent with the exceptionally high central bar pressure recorded in that test.

The peak reflected pressures from Tests T014 and T015 are presented in Figure 4.77. The considerable variance in the T014 25 mm results is clearly visible in the compiled data and influences the spread of data points at this radial position. The T015 results, however, present a tight and clearly stepped or sloped series of peak pressures from the central bar outwards, with a prominent and consistent reduction in peak pressure with increasing radial distance that is readily discernible despite the influence of the T014 variance at 25 mm.

The peak specific impulse values from Tests T014 and T015 are presented in Figure 4.78, following the same arrangement as Figure 4.77. The influence of the T014 25 mm variance is again apparent in the compiled data at this position. The spatial variation in peak specific impulse with radial distance is less pronounced than that observed in the peak pressure data, consistent with the equivalent observation made for the centrally detonated axial tests in Section 4.8, where the impulse metric was found to exhibit a less steep decay with radial distance than the peak pressure.

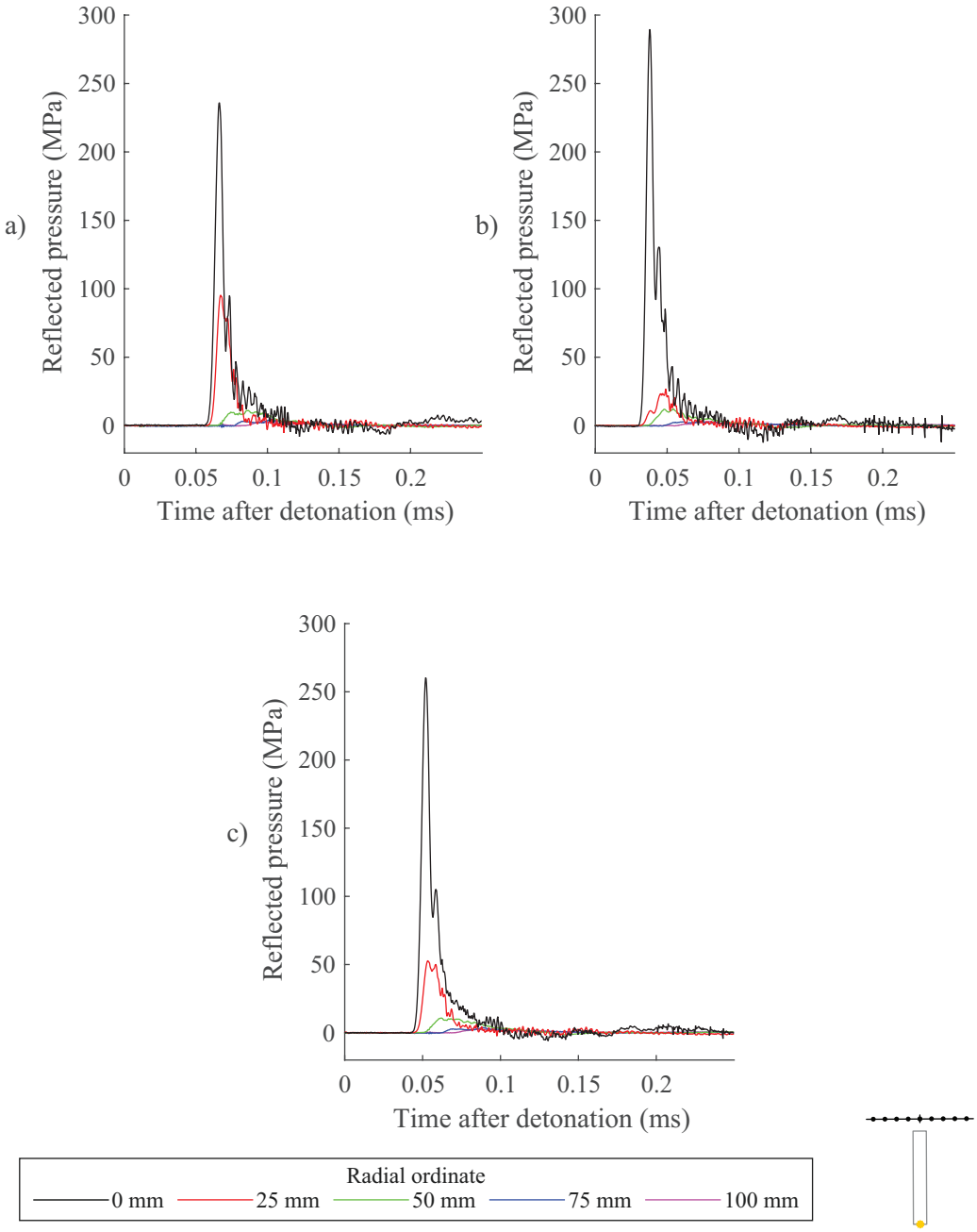


Figure 4.75: Reflected pressure time histories for axial cylindrical charges ($0°, 90°$ orientation, end detonated) for tests a) T014, b) T015, with c) showing the average of the two tests, aligned by the arrival time at the central reference measurement (0 mm, black). Traces are shown for radial offsets of 0 mm (black), 25 mm (red), 50 mm (green), 75 mm (blue), and 100 mm (magenta). For each case, the perpendicular sensor array is presented in the left column, with the aligned array shown in the middle and right columns (opposing sides). Insets indicate the relative orientation of the charge and sensor configuration.

4.10 Summary

The experimental results presented in this chapter document the reflected pressure and specific impulse loading produced by spherical charges and cylindrical charges across eight distinct orientations, spanning the full range from radial to axial configurations and

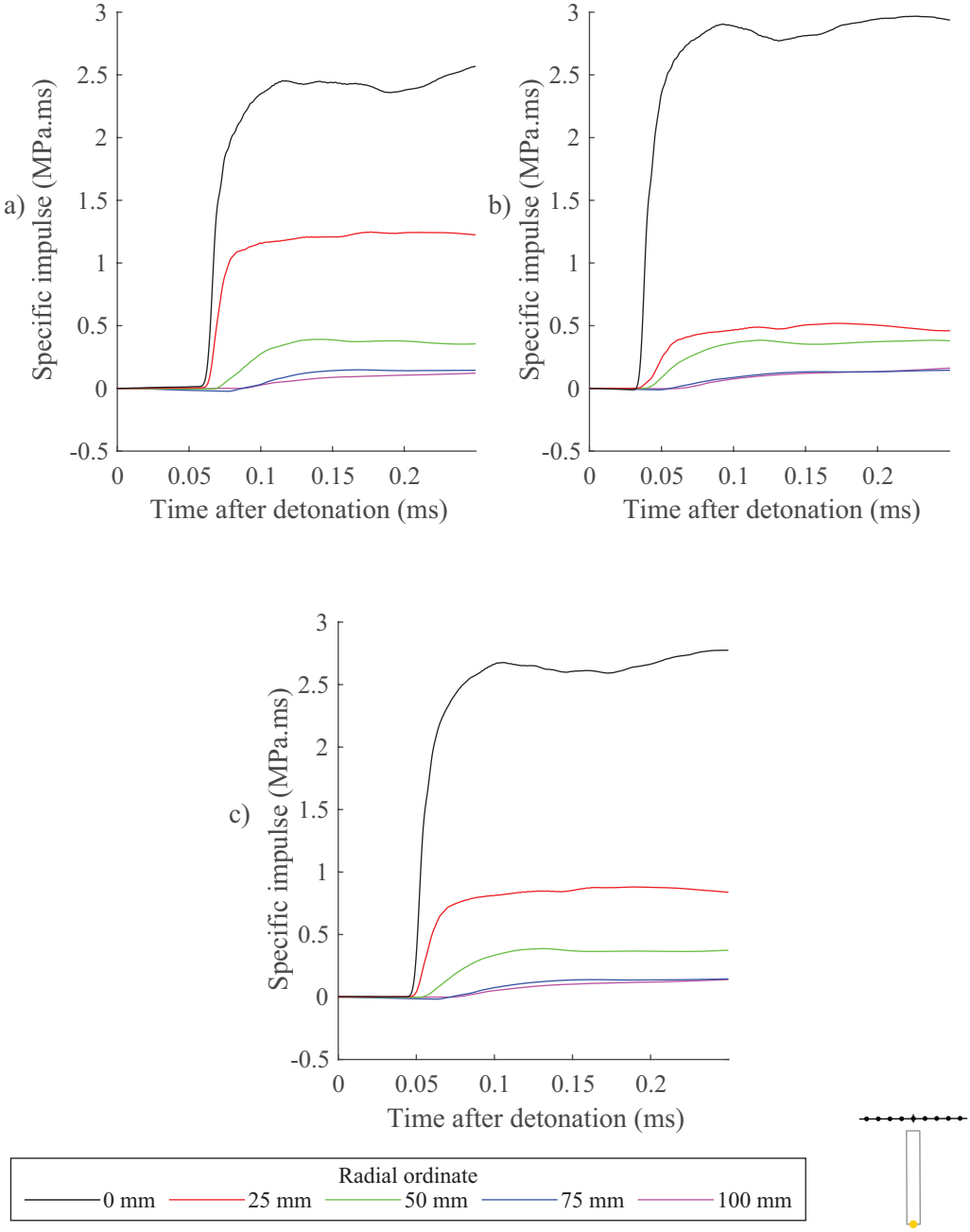


Figure 4.76: Specific impulse time histories for axial cylindrical charges (0°, 90° orientation, end detonated) for tests a) T014, b) T015, with c) showing the average of the two tests, aligned by the arrival time at the central reference measurement (0 mm, black). Traces are shown for radial offsets of 0 mm (black), 25 mm (red), 50 mm (green), 75 mm (blue), and 100 mm (magenta). For each case, the perpendicular sensor array is presented in the left column, with the aligned array shown in the middle and right columns (opposing sides). Insets indicate the relative orientation of the charge and sensor configuration.

including a series of intermediate inclined orientations. Across the programme, a total of thirty-two individual tests were conducted, twenty-three presented here, providing a substantial dataset from which consistent trends and loading characteristics have been identified.

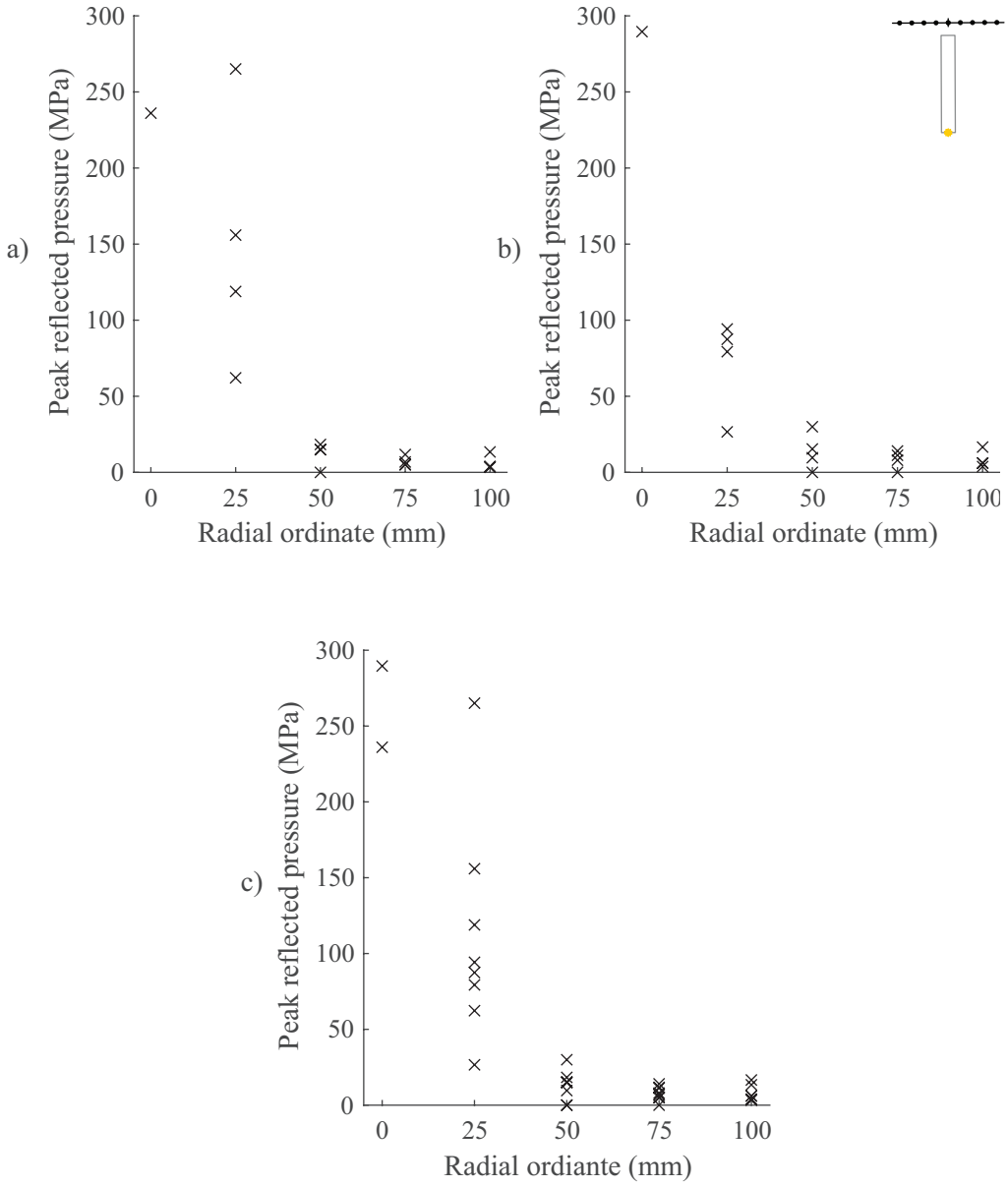


Figure 4.77: Peak reflected pressures for axial cylindrical charges ($0°, 90°$ orientation, end detonated) for tests a) T014, b) T015, with c) showing a collation of the two tests. For each case, the perpendicular sensor array is presented in the left column, with the aligned array shown in the right column. Insets indicate the relative orientation of the charge and sensor configuration.

In the radial orientation, the centrally detonated tests demonstrate clear and repeatable spatial loading distributions. The perpendicular array consistently exhibits pressure profiles closely resembling that of the central bar, with a gradual attenuation of peak reflected pressure with increasing radial distance. The parallel array produces a more varied response, with elevated peak pressures concentrated at the intermediate radial positions of 50 mm and 75 mm, accompanied by a Friedlander-like decay. The 100 mm parallel bars consistently record reduced responses across all radial tests, attributed to their geometric relationship with the end of the cylindrical charge. The end detonated radial tests broadly replicate these trends, with the asymmetry introduced by the detonation point manifesting most

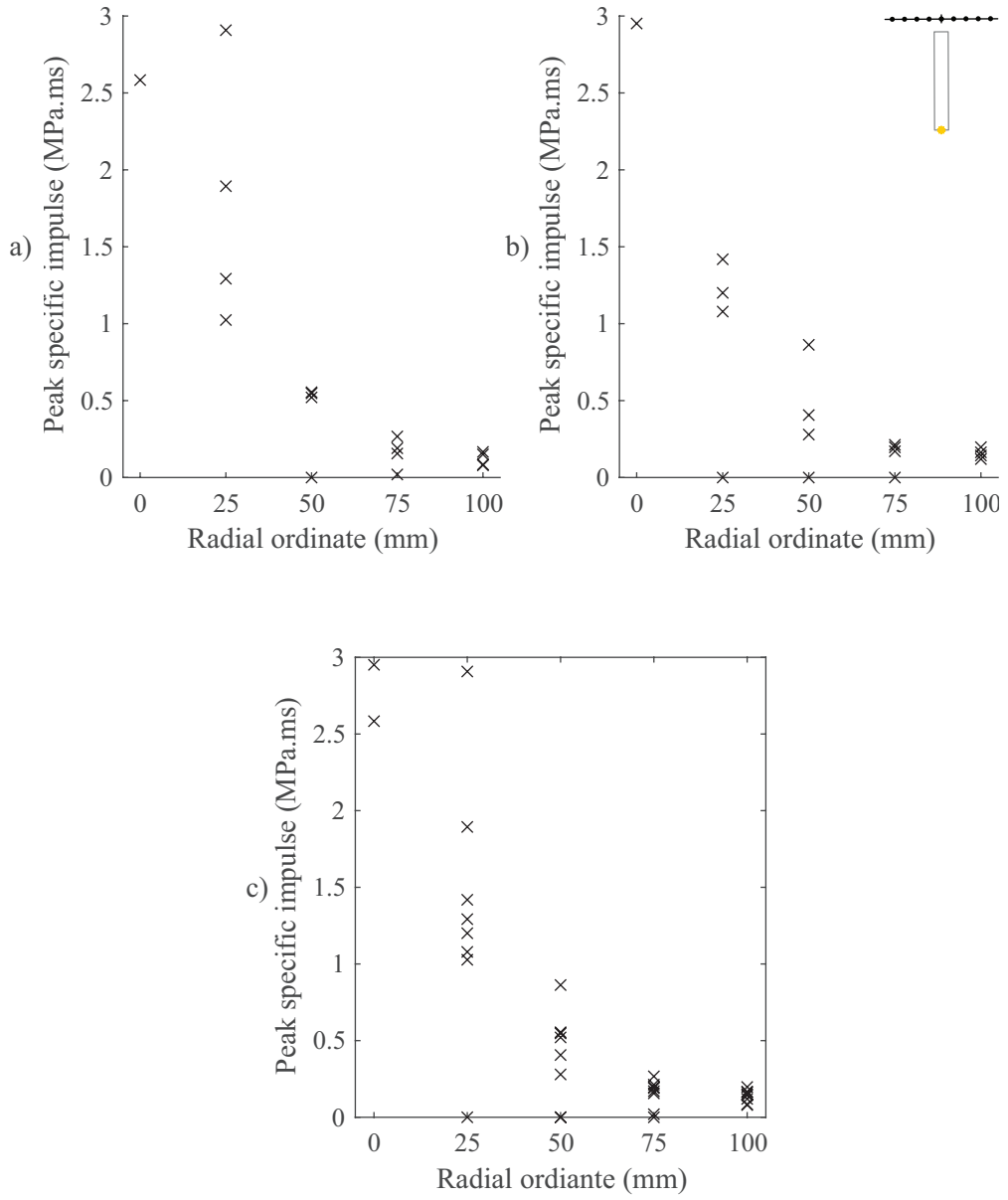


Figure 4.78: Peak specific impulses for axial cylindrical charges ($0°, 90°$ orientation, end detonated) for tests a) T014, b) T015, with c) showing a collation of the two tests. For each case, the perpendicular sensor array is presented in the left column, with the aligned array shown in the right column. Insets indicate the relative orientation of the charge and sensor configuration.

prominently in the parallel array. The specific impulse results across the radial orientations reflect the pressure observations, with the perpendicular array exhibiting closer agreement with the central bar and the parallel array showing greater spatial variation.

The 45° radial orientation, in which all bars occupy nominally identical positions relative to the charge axis, produces a loading character that combines features of both the parallel and perpendicular responses observed in the 0° radial tests. Elevated peak pressures are recorded at the outer radial positions, with a narrow window of high pressure followed by a diminishing tail consistent with a clearing effect propagating inwards from the edges of the array. The specific impulse, however, is concentrated towards the intermediate radial

positions of 25 mm and 50 mm, reflecting the combined influence of peak pressure magnitude and positive phase duration at these locations. Good repeatability is demonstrated between the two tests at this orientation, with the cross-test averages providing representative loading profiles.

The transition from radial to axial loading through the series of inclined orientations reveals a progressive evolution in the loading character of both arrays. At 22.5°, the perpendicular array retains a broadly radial character whilst the parallel array begins to exhibit asymmetric behaviour. At 45°, the asymmetry becomes more pronounced, with the loading concentrated towards the positive end of the parallel array and the perpendicular results exhibiting an increasing trend of peak specific impulse with radial distance. At 67.5°, the loading continues to decrease but the directionality is consistently seen along the parallel array. The instrumentation noise becomes increasingly prominent in the inclined orientations as the pressure magnitudes reduce, necessitating appropriate caution in the interpretation of the results.

In the fully axial orientation, the loading is dominated by the axial blast wave, with the central bar recording the highest peak pressures and specific impulses and a rapid spatial decay observed with increasing radial distance. The centrally detonated axial tests demonstrate a clear halving of peak pressure between the central bar and the 25 mm position, highlighting the strong spatial gradients characteristic of the axial blast environment. The end detonated axial tests produce broadly similar results, with the central bar again recording the highest loading. In both axial configurations, the spatial variation in peak specific impulse is less pronounced than that in peak pressure, consistent with the accumulation of impulse over the positive phase duration moderating the steep spatial gradients seen in the peak pressure data.

Across the full experimental programme, the repeatability of the results is generally good, particularly for the perpendicular arrays and for the centrally detonated radial tests. The parallel arrays and inclined orientations exhibit greater inter-test variability, reflecting the more complex and asymmetric loading environments at these configurations. The cross-test averaging produces representative loading profiles that are consistent with the physical expectations of each orientation.

The influence of the detonation point is demonstrated in the end detonated configurations, where the asymmetry introduced by the travelling detonation front produces distinct loading characteristics in the parallel array that differ to central detonation. The compiled blast loading data across all orientations provide basis for the characterisation of the spatial and temporal loading distributions produced by 7:1 cylindrical charges, forming a robust experimental basis for the analytical and numerical work presented in the subsequent chapters.

Chapter 5

Numerical modelling

A series of numerical simulations were conducted utilising the Multi-Material Eulerian/Arbitrary Lagrangian-Eulerian (MMALE) solver in in LS-DYNA (Hallquist 2006). It is noteworthy that LS-DYNA has undergone rigorous validation against experimental data, particularly in the context of near-field spherical and cylindrical blast scenarios (Rigby et al. 2018c).

5.1 2D Numerical model setup – Spherical

A 0.8 x 0.8 m computational domain was discretised into 2D axi-symmetric multi-material elements (*SECTION_ALE2D) with axisymmetric solid area-weighted element formulations (*ELFORM) with 1 mm side lengths. The boundary constraints along the top were set as rigid to model the target plate, with the two other (non-axis) sides set as transmission boundaries. The JWL parameters used for the EOS of C4 and surround air are listed in Table 2.2, (Dobratz & Crawford 1985).

The geometry of the spherical charge relating to 200g at a density of 1559 kg/m^3 (measured from the explosives used in the experimental tests) gave a diameter of 62.6 mm, centrally detonated at 0.281m from the target boundary. The spherical charge is represented in axi-symmetry as a semi-circle, described by *INITIAL_VOLUME_FRACTION_GEOMETRY. The charge is positioned 250 mm from the reflecting surface, the top of Figure 5.1.a.

5.1.1 Spherical results

Presented alongside in Figure 5.1 are three *D3PLOTs of spatial overpressure at three positions in time in the 0.8 m square domain.

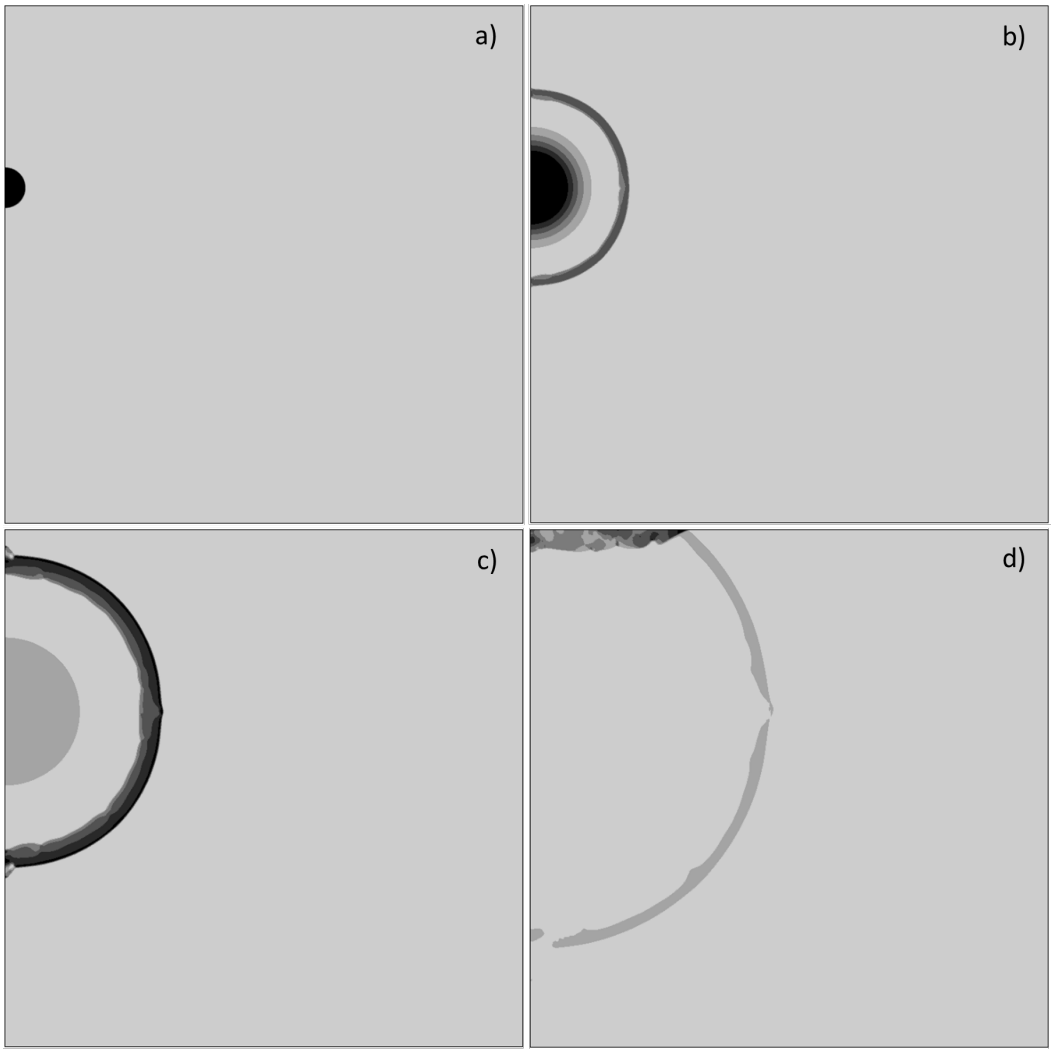


Figure 5.1: Spatial pressure plots from 2D numerical model of sphere at time a) 0, b) 0.03 ms, c) 0.06 ms, d) 0.12 ms

The theoretical spherical wave is modelled well except the visible erroneous peaks in the shock front at angles of 0°, 45° and 90°. These are results of numerical jetting as the pressure fronts move parallel to the cell boundaries, particularly along the mirror boundary (Rigby et al. 2018, 2021). This presents as an early arrival time and non-direct rise to the peak pressure. They are also seen more faintly at 45° from the point of detonation and show the numerical nuances of mesh-grid's effects on FEM.

The model was run for 150 μs to allow the primary positive phase duration to be completed on the reflecting surface. The reflected pressure and specific impulse recorded at the equivalent positions of the bars on CoBL, Figure 3.4, are presented in Figure 5.2. The pressure trace displays a more complex profile than the theoretical Friedlander decay due to

the interactions at the boundary as the blast wave reflects off the surface and the incoming pressure waves.

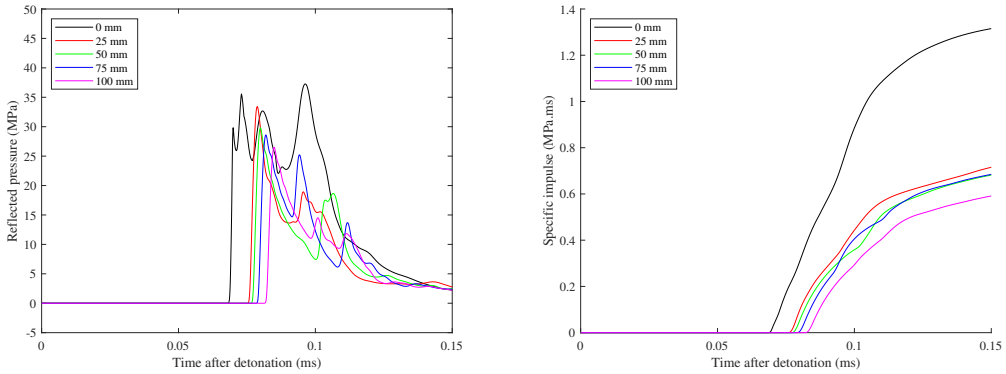


Figure 5.2: Reflected pressure and specific impulse of 2D axi-symmetric numerical model of spherical charge at five distances from the centre of a rigid reflecting plate

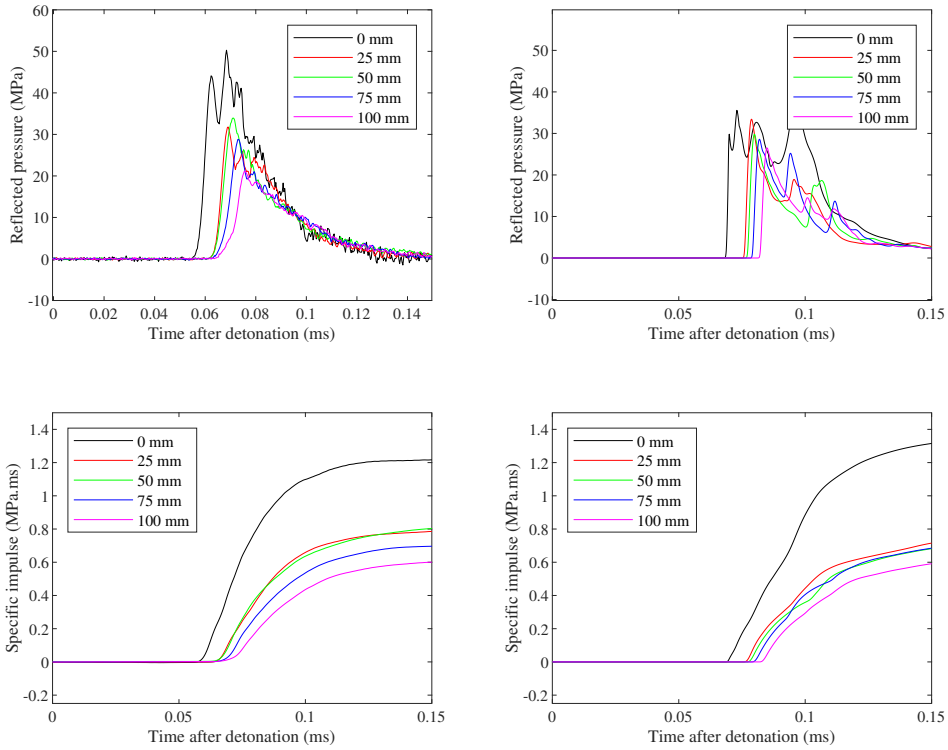


Figure 5.3: Reflected pressure and specific impulse of experimental tests (left) and 2D axi-symmetric numerical model (right) of spherical charge at five distances from the centre of a rigid reflecting plate

5.2 2D Numerical model setup – Radial

A domain of 0.4 m by 0.8 m was discretised into 0.5 mm square, volume-weighted 2D axi-symmetric elements. The domain was initially filled with air, modelled using the *MAT_NULL material model and linear polynomial equation of state (EOS). The initial specific internal energy was set as $E_0 = 253.4$ kPa to give an atmospheric pressure of 101.4 kPa. The explosive geometry was represented using *INITIAL_VOLUME_FRACTION_GEOMETRY by specifying a 200 mm long, 14.3 mm high rectangle, centred on the axis, which would represent a 28.6 mm diameter cylinder when rotated about the axis.

In this configuration, the 0° array is given by a line parallel to the symmetry axis, 264.3 mm from the charge centre. Whilst the 90° array is out-of-plane in the 2D model, its effective position can be mapped onto the 2D domain as a series of in-plane points, each with equal distance to the charge centre as the corresponding points in the 90° array. For example, the 100 mm bar in the 90° array is a total slant distance of $\sqrt{(264.3^2 + 100^2)} = 282.6$ mm from the centre of the charge (where 264.3 mm is the normal stand-off distance, and 100 mm is the lateral distance along the target). The general geometry of the numerical model is represented in the first image in Figure 5.4, with representative bar locations indicated by 'x' and 'o' markers for 0° and 90° arrays respectively. The axis of symmetry is also labelled, and the indicative position of the target plate is given as a horizontal line.

5.2.1 Radial results

Figure 5.4 shows fringe plots of material volume fraction (1.0 represents pure explosive detonation products, and 0.0 represents pure air), incident pressure, and resultant acceleration, which is analogous to the pressure gradient (Rigby et al. 2014c).

When considering the material volume fraction plots, at 0.01 ms, the detonation products have begun expanding in the radial direction whilst the detonation wave is still some distance from the axial end of the explosive, causing the detonation product breakout to be initially spherical in shape. As time progresses, the detonation products become increasingly prolate, until at approximately 0.05 ms after detonation when the explosive products become flat-topped with respect to the target plate. This continues until the detonation products and shock waves impinge on the target plate, which would occur between 0.07 and 0.09 ms had the problem not been modelled in axi-symmetry.

Numerical arrival times have been evaluated by taking the time at which the first non-zero pressure was recorded along an array of tracer particles representing the 0° and 90° arrays. Figure 5.5 shows a comparison of these numerical arrival times with the experimentally-recorded arrival times from Test 7. Here, the results are presented as relative arrival time, i.e. with the arrival time at the central bar subtracted, for ease of comparison between the two. It can be clearly seen that arrival times along the 0° array are reasonably consistent, whereas arrival times along the 90° increase with increasing radial ordinate. Numerical and experimental results are in good agreement, with a maximum variation of 5 μs between

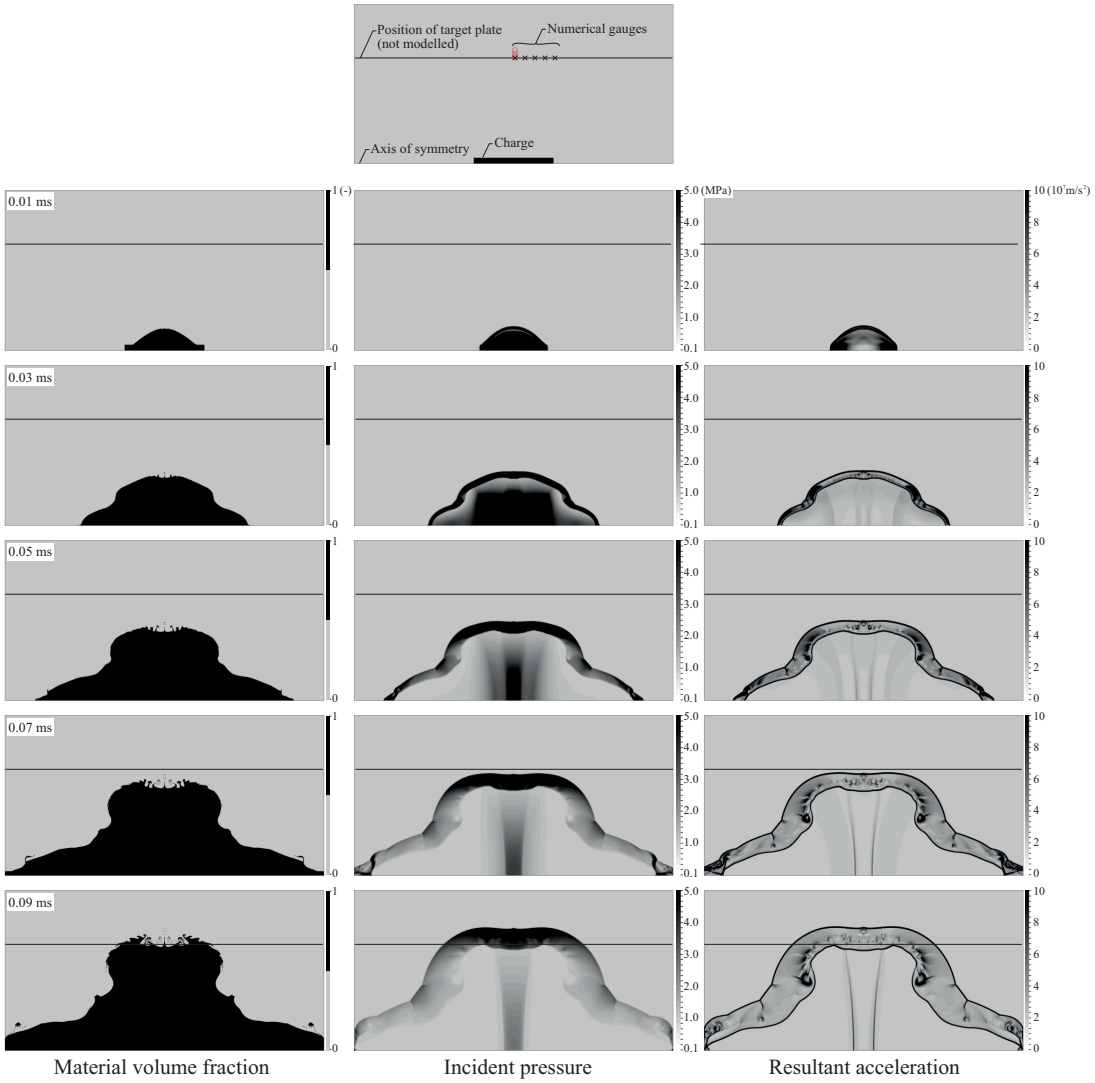


Figure 5.4: Fringe plots of volume fraction material (explosive detonation products), incident pressure, and resultant acceleration from detonation of 200 g $L/D = 7$ cylinders of C4 modelled. Representative bar locations are indicated by 'x' and 'o' markers for 0° and 90° arrays respectively. Note that target position is for indication only; an incident analysis was performed and the target itself was not explicitly modelled.

the numerical and experimental relative arrival times. It can be said with some confidence, therefore, that near-uniform arrival time of the shock front along the 0° array is as a result of the flat-topped nature of the expanding detonation product cloud.

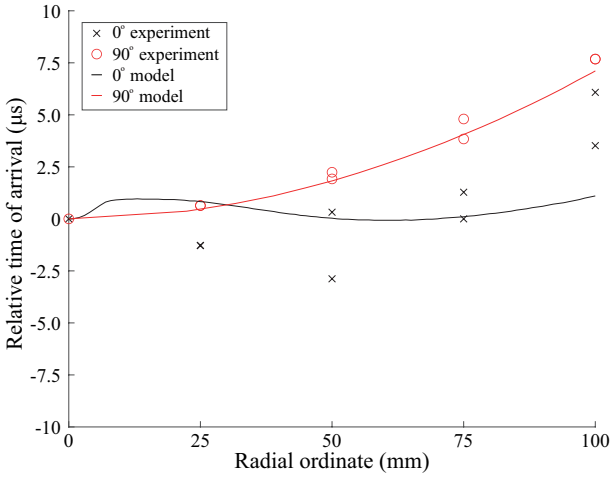


Figure 5.5: Relative time of arrival of the blast wave at radial ordinates for 0° and 90° arrays: numerical results (incident) compared against recorded arrival times in Test 7.

With reference to the pressure plots in Figure 5.4, the initial expansion of the shock front appears to be effectively spherical in nature. However, as the detonation wave progresses along the axis of the charge, more material becomes available to confine the expanding detonation products, and the shock front is subjected to increasing levels of lateral inertial confinement, as observed in Nurick et al. (2016). Hence, as the shock front continues to expand (i.e. between 0.05–0.07 ms), the highest pressures are not located directly in the centre of the detonation product cloud, but some position off-centre. The numerical and experimental results show that, for this geometry, the peak pressure acts on the target approximately 75 mm from the centre. The indicative modelling suggests that this is due to inertial self-confinement of the detonation products.

Finally, the resultant acceleration plots in Figure 5.4 reveal complex structures in the region between the shock front and detonation products. These are particularly prominent at later times, and are focussed around the region where the detonation products transition from flat-topped to rounded (approximately 75–100 mm from the charge centre for this geometry). These structures are evidence of complex interactions between the primary end waves and bridging waves, and give rise to more complex and variable behaviour at the remote bar locations.

5.3 2D Numerical modelling – Axial

2D axi-symmetric multi-material elements of 1 mm square were created in a 0.8 × 0.4 m computational domain. A rigid boundary was placed along the top edge of the domain, with the other two edges (excluding the axis of symmetry) retained as outflow boundaries. The geometry of the C4 was modelled to match the experimental charges to the effect of

a 200 × 14.3 mm rectangle along the axis of the axi-symmetric model. The charge was modelled using *INITIAL_VOLUME_FRACTION to represent a rectangle along the symmetry boundary, and detonated centrally on the axis with *INITIAL_DETONATION at time zero. Fixed-location tracer points (*DATABASE_TRACERS) were set at 1 mm increments from 0 to 100 mm from the axis of symmetry.

5.3.1 Axial results

The results of the numerical model are compared to the experimental tests in Figure 5.6. The numerical model over predicts the experimental peak pressure and specific impulse measured at the central bar by 59% and 79% respectively. However, model better predicts the experimental data at radial ordinates 25 mm and greater, with the radial ordinates 25 mm and above.

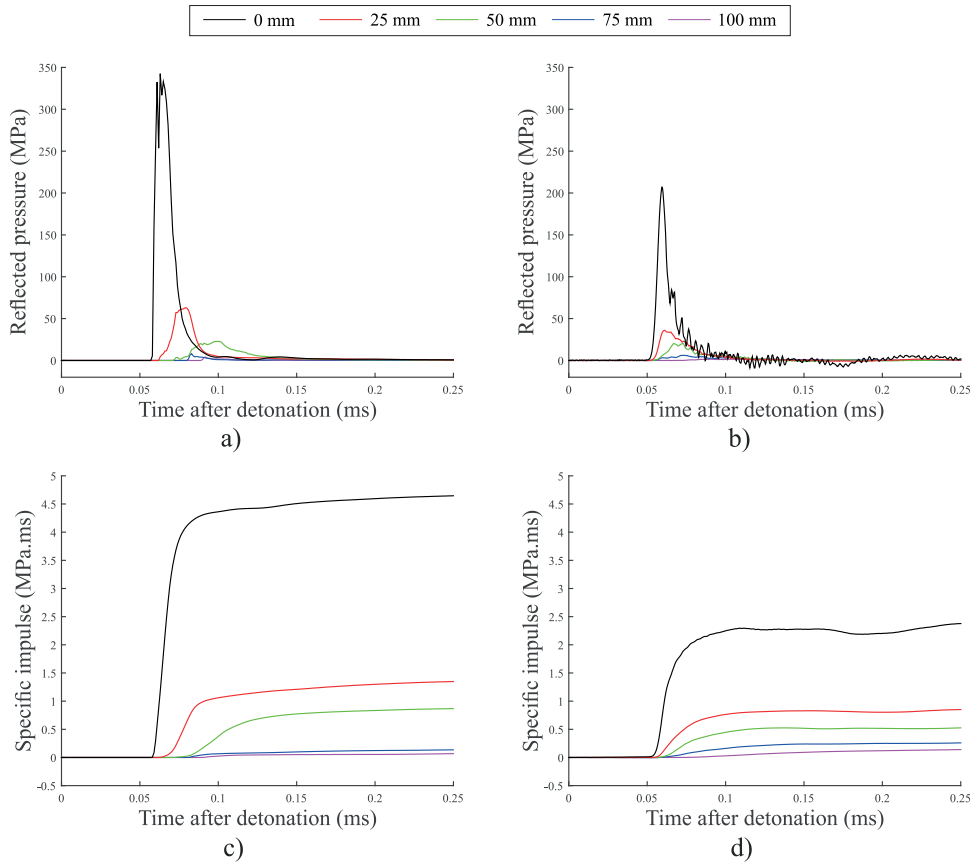


Figure 5.6: Reflected pressure (a-b) and specific impulse (c-d) of numerical model (a,c) and experimental (b,d) axial cylinder tests at five distances from the centre of a rigid reflecting plate

Figure 5.7 shows snapshots of the pressure distributions in the numerical model. Figure 5.7.c shows boundary effects along the axis of symmetry have may have resulted in the commonly observed "jetting" effect along the symmetry axis due to the reflecting boundary. This may be responsible for the over-prediction of the central loading. The pressure plot shows the axi-symmetric modelling is capturing the shockwave features expected from a cylindrical charge; radial front and two jets one from either end of the axial ends. Bridging waves can

also be seen to develop to connect the primary waves as described by Wisotski & Snyer (1965).

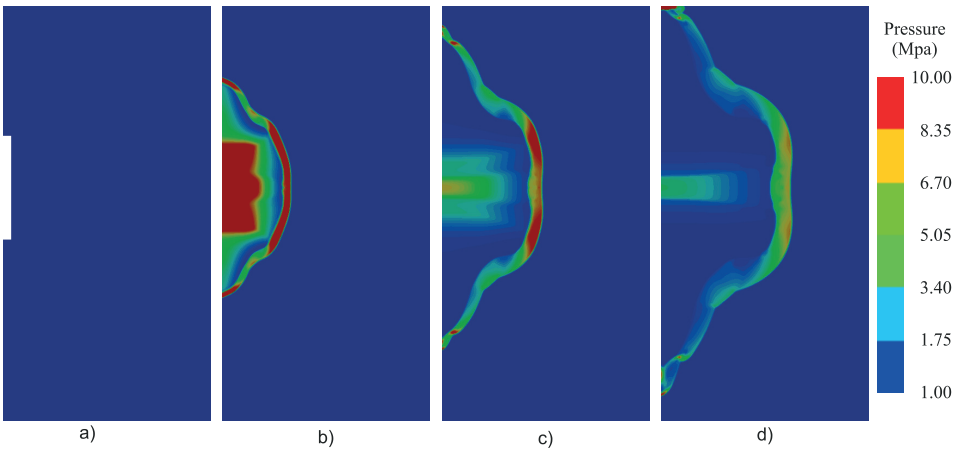


Figure 5.7: Pressure distribution plots from 2D numerical model of axial cylinder charge at time 0 (a), 0.03 ms (b), 0.05 ms (c) and 0.07 ms (d)

The 2D numerical modelling of the experimental configurations presented in this chapter is discussed in detail in Chapter 6, where the predicted loading distributions are compared directly against the experimental results. A sample keyword file for the numerical model is provided in Appendix 9.

5.4 3D Numerical Modelling

2D axi-symmetric ALE modelling accurately captures the experimental loading profile away from the axis of symmetry. 3D models have been run to remove the boundary effect and explore the accuracy and validity of the 3D ALE model in LS-DYNA.

Three-dimensional numerical modelling was conducted in *SECTION_SOLID with 1 point ALE multi-material element formulations. The domain was initially filled with air modelled with the same parameters as the 2D modelling, see Table 2.2. The initial specific internal energy was set as $E_0 = 253.4$ kPa to give an atmospheric pressure of 101.4 kPa.

The explosive parts were defined with *INITIAL_VOLUME_FRACTION_GEOMETRY, cylindrical containers of radius 0.0143m, 0.2500m length and centred in the domain. It was detonated at the beginning of the simulation with *INITIAL_DETONATION.

A solid reflecting boundary was set at the top of the model with *CONSTRAINED_GLOBAL restricting x, y and z rotations, to represent the rigid reflecting plate. All other domain edges were left open as transmission boundaries. 41 *DATABASE_TRACERS were positioned at 5 mm increments from one side of the instrumented area on the reflecting surface to the other covering the 200 mm of the x-axis. A further 20 tracers perpendicular to first line intersecting at the central of the domain with a common tracer at the centre. Set to sample at 1 μs for the length of the simulation.

Domain sizes from 1.0 × 1.0 × 1.0 m down to 0.4 × 0.4 × 0.65 m were discretised into cube elements of 10 mm down to 1.6 mm.

The 3D numerical modelling of the experimental configurations presented in this chapter is discussed in detail in Chapter 6, where the predicted loading distributions are compared directly against the experimental results. A sample keyword file for the numerical model is provided in Appendix 9.

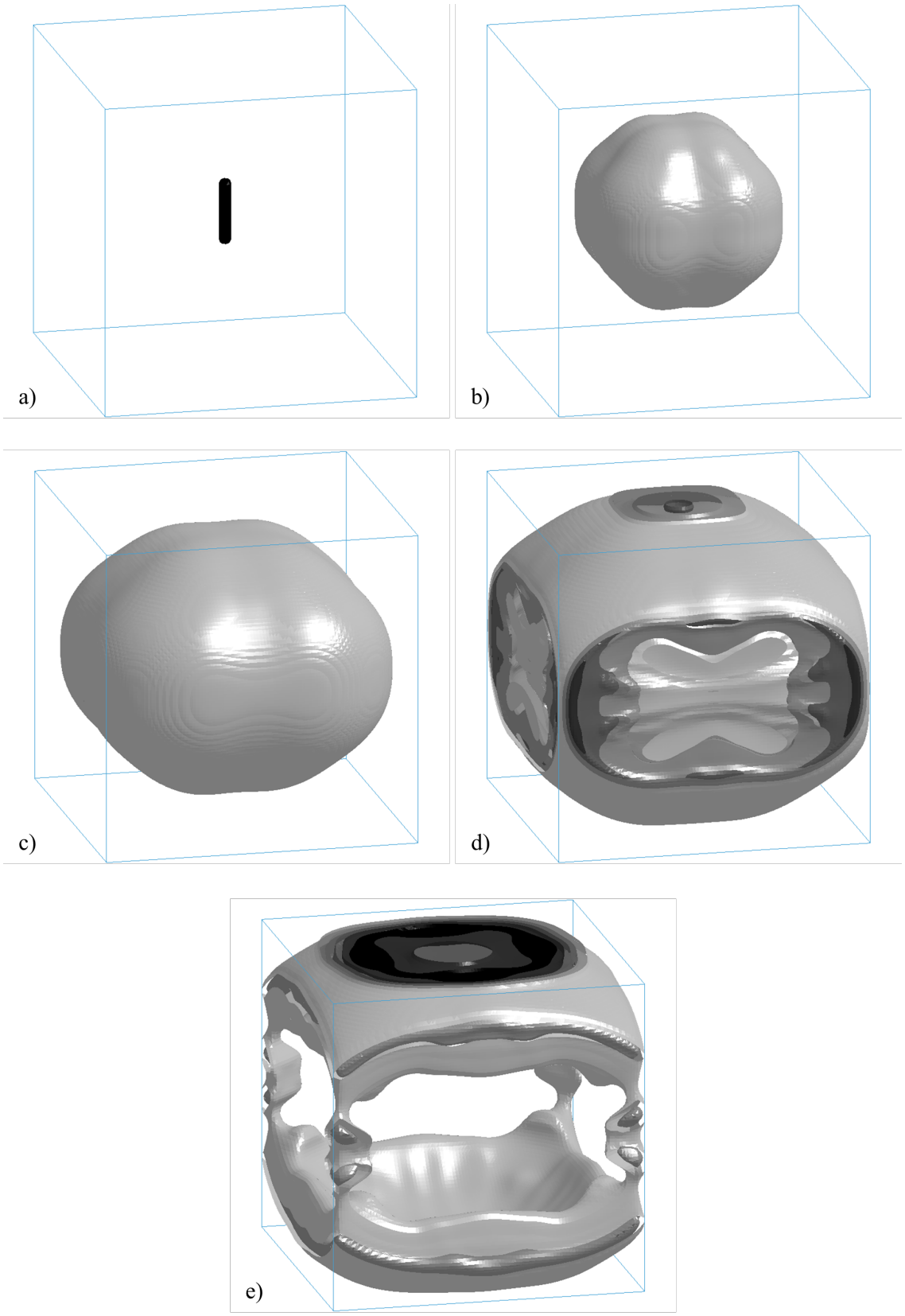


Figure 5.8: Pressure distribution plots from 3D numerical model of axial cylinder charge at time 0 (a), 0.01 ms (b), 0.02 ms (c), 0.3 ms (d) and 0.4 ms (e). The blue frame defines the domain and the reflecting surface is located at the top of each image and all 5 other boundaries are open.

Chapter 6

Discussion

6.1 Validity of experimental results

The data collected from the CoBL apparatus demonstrates several strengths and weaknesses in its ability to characterise near-field blast loading. One of the principal challenges is obtaining repeatable and consistent experimental data, as blast waves in the near-field are highly dynamic and subject to chaotic physical processes, including Rayleigh-Taylor and Richtmyer-Meshkov instabilities, that introduce inherent variability in the localised loading at individual measurement positions. The statistical analysis presented in Section 6.2 quantifies this variability through relative standard deviations calculated across all tested configurations, demonstrating that whilst local peak pressures and specific impulses exhibit considerable spread, the total impulse imparted to the measurement area is highly consistent across repeat tests. This two-level characterisation supports the conclusion that the variability is a physical characteristic of the blast environment rather than a limitation of the measurement methodology.

The use of Hopkinson pressure bars as pressure transducers introduces a number of measurement considerations. The finite diameter of the bars gives rise to Pochhammer-Chree dispersion, which manifests as spurious oscillations in the recorded pressure traces and a degradation of transient pressure features with durations less than 5 μs (Rigby et al. 2018a), as clearly visible in the highlighted region of the central bar pressure trace

from Test T004 (Figure 6.1). A frequency analysis of the central bar pressure trace from Test T004 demonstrates that the dominant blast signal energy is concentrated at a peak frequency of 3.99 kHz, with 50% of the signal energy below 7.98 kHz and 90% below 35.92 kHz. Using the Rayleigh correction for phase velocity dispersion in a cylindrical bar (Tyas & Pope 2005), the accumulated time shift error over the 250 mm gauge setback distance for the EN24(T) steel bars is 1.3 ns at the peak frequency and 104 ns at the 90% energy frequency, corresponding to 0.4% and 33% of a single sample interval respectively. The 90% energy frequency of 35.92 kHz lies below the normalised frequency threshold of $fd/c_0 = 0.1$ (50.5 kHz for a 10 mm diameter bar), above which Tyas & Pope (2005) identify dispersion corrections as becoming non-negligible. It is therefore concluded that whilst Pochhammer-Chree oscillations are visible in the pressure traces, the peak pressure and specific impulse values extracted from the recorded signals are not meaningfully affected by dispersion, and the general form of the pressure pulse and the temporal evolution of specific impulse remain representative of the true blast loading.

The form factor of the Hopkinson pressure bars introduces a further consideration in the spatial resolution of the measurements. Each bar records a spatially averaged pressure over its 10 mm diameter face, which acts as a low-pass spatial filter on the loading distribution. This is of particular relevance in the axial charge configurations, where steep spatial gradients in peak pressure are observed across the array, and the recorded values at intermediate radial positions may underestimate the true peak loading between bar positions. This limitation is inherent to the discrete point measurement approach and is acknowledged in the interpretation of the spatial loading distributions presented in Chapter 4.

Overall, whilst the CoBL apparatus provides valuable and repeatable insight into near-field blast load behaviour, its reliability is subject to the design and measurement limitations described above. Improvements to the design, materials and instrumentation have been incorporated into its successor, the Mechanisms and Characterisation of Explosions (MaCE) facility, which further develops the measurement technique (Barr et al. 2023*b*).

6.2 Variability of localised loading

From inspection of Figure 6.2, it is clear that the variations in near-field loading are considerably higher than the variations observed in the preliminary far-field testing (Figure 3.2), and the repeatability of near-field blast load measurement from cylindrical charges is dependent on both radial ordinate and orientation angle. For example, the range of peak reflected pressure at 75 mm in the perpendicular array of the radial (0°,0°) centrally detonated configuration is approximately ±35 MPa from the mean, whereas at the same radial ordinate in the perpendicular array the deviation is approximately ±10 MPa from the mean.

Table 6.1 presents the relative standard deviation (RSD, given as the standard deviation

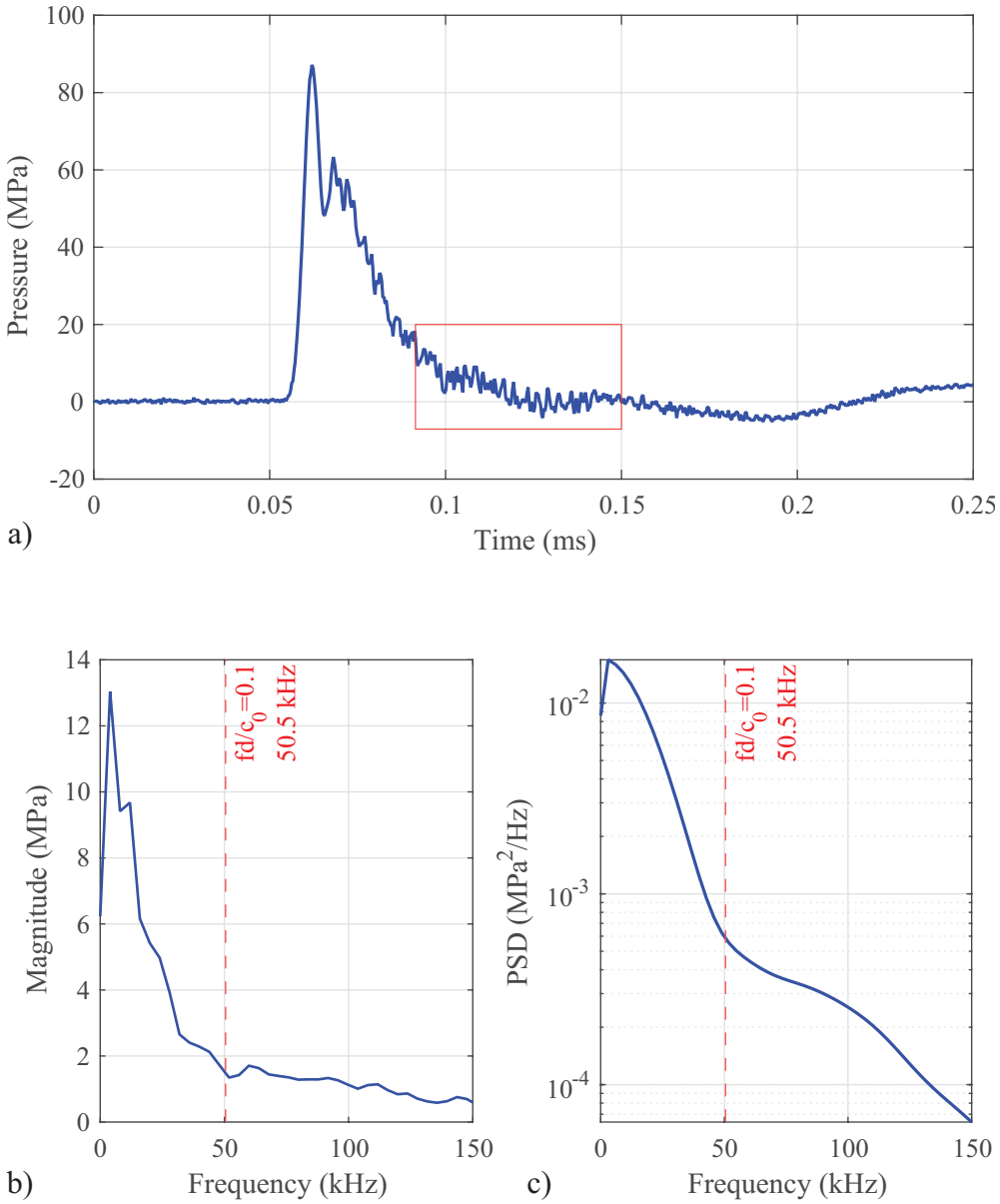


Figure 6.1: Frequency analysis of the central bar pressure trace from Test T004. a) recorded pressure history; the red box highlights the region between approximately 0.09 ms and 0.15 ms where Pochhammer-Chree dispersion oscillations are most prominent in the decay phase. b) FFT magnitude spectrum of the raw signal. c) power spectral density (PSD) of the raw signal. The red dashed line in both frequency domain plots denotes the normalised frequency threshold $fd/c_0 = 0.1$ (50.5 kHz), above which dispersion corrections become non-negligible (Tyas & Pope 2005).

normalised by the mean value, expressed as a percentage) of the peak reflected pressure and peak specific impulse measurements across all tested charge orientations, array types, and radial ordinates. Mean values of peak reflected pressure and peak specific impulse are also provided to contextualise the variability relative to the magnitude of loading at each position. For orientations with rotational symmetry about the charge axis — namely the spherical charges, the radial (45°,0°) configuration, and both axial configurations — all bars at each radial ordinate are treated as nominally identical and combined into a single row. For the remaining asymmetric configurations, the perpendicular and positive

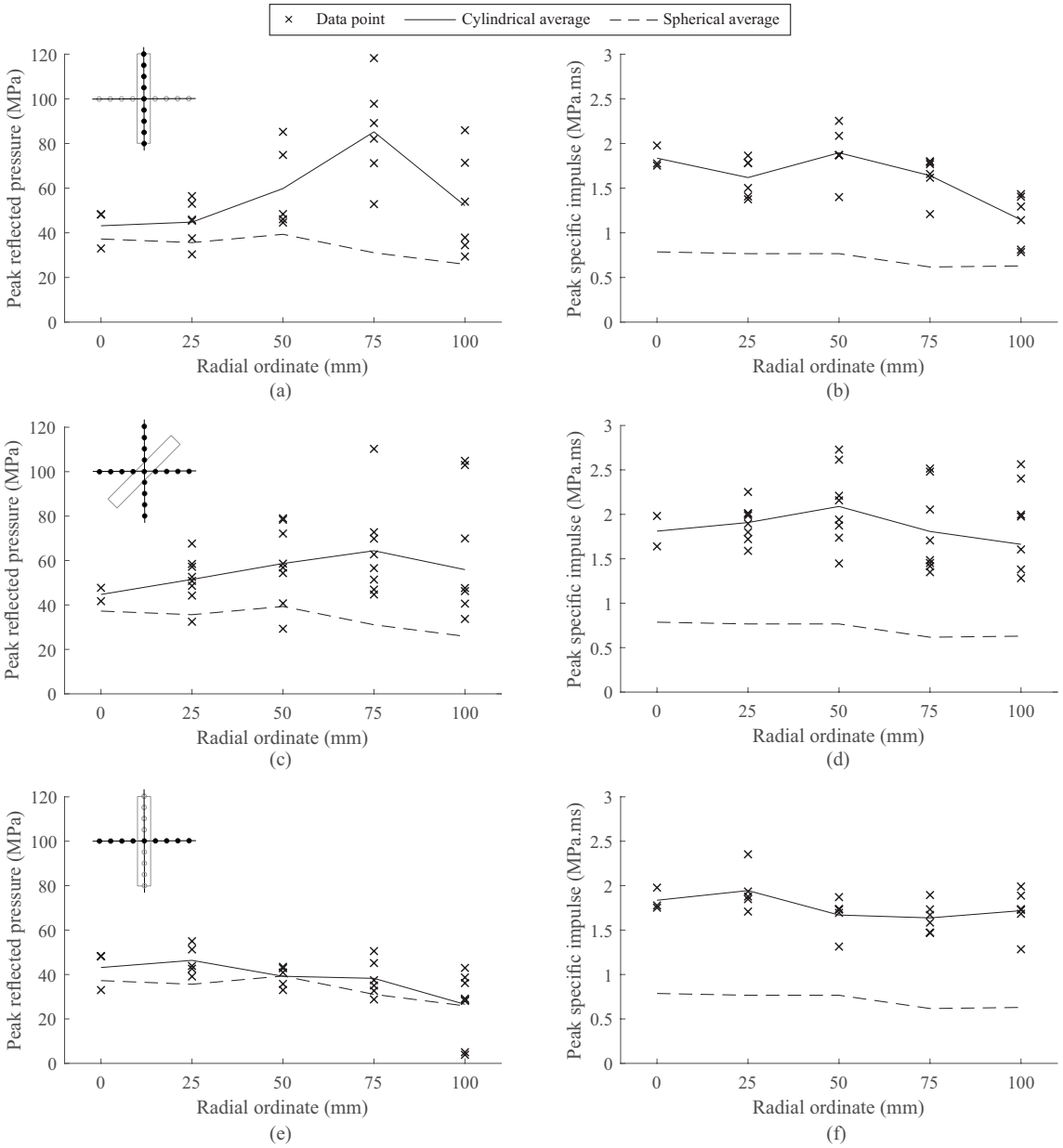


Figure 6.2: Compiled peak reflected pressure and peak specific impulse versus radial ordinate from detonation of 200 g $L/D = 7$ horizontal cylinders of C4 and 200 g spheres of C4 at 250 mm clear stand-off: (a–b) 0°; (c–d) 45°, and; (e–f) 90°. Alignment is indicated in on the respective row.

and negative parallel arrays are presented separately. Dead bars are excluded from all calculations, and entries with fewer than two valid data points are denoted by —.

Table 6.1: Relative standard deviation (RSD, %) of peak reflected pressure (P) and peak specific impulse (I) across all tested charge orientations, array types, and radial ordinates. Dead bars are excluded. Mean values of peak reflected pressure (MPa) and peak specific impulse (MPa·ms) are also provided. For symmetrical configurations (Spherical, Radial (45°,0°), and Axial), all bars at each radial ordinate are combined into a single row. Entries marked — indicate fewer than two valid data points.

Orientation	**Array**	**Ord. (mm)**	**Mean P (MPa)**	**P RSD (%)**	**Mean I (MPa·ms)**	**I RSD (%)**
Spherical	Central	0	62.2	56.7	1.2	47.4
	All bars	25	35.6	18.8	0.8	19.8
	All bars	50	39.3	19.9	0.8	38.7
	All bars	75	31.1	21.0	0.7	16.0
	All bars	100	25.9	22.0	0.7	17.1
Radial (0°,0°) Central	Central	0	41.5	27.9	1.6	16.0
	Perp	25	48.7	28.2	1.8	16.7
	Perp	50	46.4	38.9	1.6	9.8
	Perp	75	42.0	18.4	1.5	9.9
	Perp	100	34.8	16.1	1.5	11.4
	Para (−)	25	40.6	21.8	1.4	4.8
	Para (−)	50	55.7	30.0	1.9	6.4
	Para (−)	75	78.3	33.9	1.8	8.2
	Para (−)	100	32.9	9.4	1.0	47.6
	Para (+)	25	49.0	20.5	1.6	6.0
	Para (+)	50	66.8	39.0	1.6	16.1
	Para (+)	75	80.8	41.8	1.5	17.1
	Para (+)	100	59.3	41.3	1.2	8.8
Radial (0°,0°) End	Central	0	58.4	5.3	1.5	6.2
	Perp	25	72.2	24.0	1.7	17.8
	Perp	50	85.4	35.8	1.9	26.3
	Perp	75	52.3	54.8	1.4	33.2
	Perp	100	55.8	73.7	1.4	48.0
	Para (−)	25	52.9	8.0	1.6	11.3
	Para (−)	50	71.7	5.1	1.7	11.8
	Para (−)	75	35.1	10.1	1.3	21.1
	Para (−)	100	45.0	48.7	1.1	40.1
	Para (+)	25	64.2	29.6	1.7	2.3
	Para (+)	50	84.7	49.0	2.0	40.4
	Para (+)	75	47.2	16.9	1.5	14.6
	Para (+)	100	49.4	22.4	1.3	0.6
Radial (45°,0°)	Central	0	44.7	9.5	1.6	8.8
	All bars	25	51.5	20.3	1.7	15.3
	All bars	50	58.7	30.2	1.8	15.1
	All bars	75	64.4	32.8	1.6	20.1
	All bars	100	63.7	46.6	1.5	27.1
Inclined (0°,22.5°)	Central	0	47.0	34.3	0.8	41.4
	Perp	25	38.7	30.9	0.7	19.5
	Perp	50	35.7	29.3	0.6	26.5
	Perp	75	30.5	27.9	0.6	12.9
	Perp	100	25.3	37.3	0.6	23.1

Continued on next page

Table 6.1 continued from previous page

Orientation	Array	Ord. (mm)	Mean P (MPa)	P RSD (%)	Mean I (MPa·ms)	I RSD (%)
	Para (−)	25	23.3	26.0	0.5	32.0
	Para (−)	50	15.0	48.7	0.4	16.4
	Para (−)	75	16.3	12.9	0.3	11.4
	Para (−)	100	13.2	33.5	0.3	23.3
	Para (+)	25	74.1	78.2	1.4	47.5
	Para (+)	50	—	—	—	—
	Para (+)	75	23.2	18.8	0.9	13.8
	Para (+)	100	30.7	21.3	1.2	17.6
Inclined (0°,45°)	Central	0	10.0	17.3	0.4	81.4
	Perp	25	8.4	23.9	0.2	24.6
	Perp	50	8.0	35.8	0.2	26.5
	Perp	75	9.7	13.1	0.3	22.4
	Perp	100	10.2	46.4	0.3	34.3
	Para (−)	25	6.6	49.7	0.2	28.5
	Para (−)	50	7.3	28.2	0.3	26.8
	Para (−)	75	7.8	42.8	0.2	31.0
	Para (−)	100	7.4	30.9	0.2	18.4
	Para (+)	25	11.6	7.7	0.3	25.6
	Para (+)	50	8.6	2.9	0.2	26.2
	Para (+)	75	13.6	30.8	0.2	17.6
	Para (+)	100	17.6	34.6	0.3	23.6
Inclined (0°,67.5°)	Central	0	8.8	—	0.2	—
	Perp	25	4.6	54.8	0.1	30.7
	Perp	50	5.9	71.1	0.2	25.5
	Perp	75	6.7	73.3	0.2	23.8
	Perp	100	5.3	59.1	0.3	44.5
	Para (−)	25	—	—	—	—
	Para (−)	50	3.1	21.2	0.2	24.0
	Para (−)	75	3.7	31.7	0.1	1.6
	Para (−)	100	3.5	41.6	0.1	16.4
	Para (+)	25	4.1	40.8	0.2	28.7
	Para (+)	50	3.3	30.9	0.2	33.4
	Para (+)	75	9.8	3.9	0.2	8.3
	Para (+)	100	10.0	—	0.3	—
Axial (0°,90°) Central	Central	0	215.2	12.7	2.4	21.1
	All bars	25	47.6	64.7	0.8	63.5
	All bars	50	26.4	98.7	0.6	65.8
	All bars	75	11.4	101.1	0.3	79.7
	All bars	100	3.6	27.9	0.1	48.1
Axial (0°,90°) End	Central	0	262.8	14.4	2.8	10.1
	All bars	25	102.2	81.1	1.2	77.7
	All bars	50	17.2	39.9	0.5	36.2
	All bars	75	5.7	19.8	0.2	39.5
	All bars	100	4.0	24.1	0.1	26.5

Peak pressure RSDs are larger than peak specific impulse RSDs in the majority of configurations, with this pattern consistent across nearly all tested orientations and radial positions. The mean pressure RSD across all radial positions ranges from 20.4% for the spherical charges to 73.1% for the axial (0°,90°) centrally detonated configuration, whilst the corresponding mean impulse RSDs range from 13.6% to 64.3%. The two exceptions are the spherical charges, where the mean impulse RSD (22.9%) marginally exceeds the mean pressure RSD (20.4%), and the axial end detonated configuration (41.2% pressure, 45.0% impulse), where the sharp spatial gradient in loading means that small variations in the precise position of the peak pressure between tests accumulate into the impulse more significantly than in other configurations. This indicates that the complex features causing variability in the pressure histories, such as the primary side and end wave interaction and the bridging wave effects described previously, have a lesser influence on the development of peak specific impulse across the majority of configurations. This finding is consistent with observations from experiments quantifying the output from buried explosives (Rigby et al. 2016), and supports the conclusion that specific impulse is a more stable and repeatable measure of blast loading than peak pressure across most tested configurations.

For the asymmetric configurations, the perpendicular array generally exhibits lower mean pressure RSDs than the parallel array in the radial orientations, with values of 25.4% and 29.7% respectively for the radial (0°,0°) centrally detonated case, consistent with the perpendicular array lying within the more uniform primary side wave region. However, this relationship reverses for the inclined orientations at 45° and 67.5°, where the perpendicular array exhibits higher mean pressure RSDs (29.8% and 64.6% respectively) than the parallel array (28.5% and 28.3%), reflecting the increasingly complex loading environment experienced by the perpendicular array as the charge approaches the axial orientation and the end and bridging wave effects become more prominent at those positions.

The trend of pressure RSD with radial distance varies systematically with both orientation and array type. For the symmetric configurations, the spherical charges show a broadly flat distribution of RSDs across radial ordinates (18.8% at 25 mm to 22.0% at 100 mm), consistent with the spatially uniform character of the spherical blast wave. The radial (45°,0°) configuration shows a clear increasing trend (20.3% to 46.6%), attributed to the greater influence of end and bridging wave interactions at larger radial distances. Both axial configurations exhibit a decreasing trend with radial distance, with the centrally detonated case showing a sharp reduction from 64.7% at 25 mm to 27.9% at 100 mm, driven in part by the anomalous T032 results at the intermediate radial positions discussed in Section 4.8. For the asymmetric configurations, the perpendicular array of the radial (0°,0°) centrally detonated case shows a decreasing trend (28.2% to 16.1%), whilst the end detonated radial and all inclined configurations show increasing trends, consistent with the findings of Rigby et al. (2016) and Rigby et al. (2018b) for buried explosive tests. The 67.5° inclined configuration exhibits the highest mean perpendicular array pressure RSDs of any asymmetric orientation (64.6%), reflecting both the complex loading environment in the bridging wave zone and the reduced number of valid data points at certain positions

due to the high incidence of dead bars in this test series.

Together, these observations confirm that the local variability observed in the near-field loading is an inherent physical characteristic of the blast environment produced by non-spherical charges, strongly dependent on the geometric relationship between the measurement position and the charge geometry. The relationship between this local variability and the consistency of the total impulse imparted to the measurement area is explored in Section 6.3.1, where it is demonstrated that the variability is driven by the spatial and temporal redistribution of energy rather than inconsistency in the total energy released by the detonation.

6.3 Consistency of experimental data

The reliability of experimental data obtained from ostensibly straightforward configurations involving spherical and hemispherical charges in the far-field has been a subject of contention within the scientific community. The highly cited paper, Formby & Wharton (1996), notably reported substantial variations in nominally identical tests conducted in the far-field. Considering the inherent physics of the problem at hand, a chemical reaction, it is expected that the energy release should remain constant when employing highly controlled commercial high explosives sourced from the same batch. This inconsistency prompted some researchers to question whether the observed variations stem from inherent characteristics of the explosive event or are instead consequences of potential user errors during the testing procedures.

Other researchers however, notably Rickman & Murrell (2006) and Farrimond et al. (2023) have reported excellent consistency of far field blast parameters from nominally identical test arrangements. Additionally, their results correlated very well with predictions from semi-empirical fast-running engineering models (FREMs). These results imply strongly that far-field blast parameters from spherically-shaped charges of standard HEs are in fact consistent and predictable. This might be expected from a simple first order assessment of how far-field blast waves are formed. In the far-field, we are essentially so far from the detonation in time and space that the precise mechanisms of detonation are insignificant. What matters is that a given amount of energy has been released at a point in time and space, resulting in disturbance in the surrounding air which produces the blast wave. All other things being equal, if the same energy is released in two detonations, we might expect, as Rickman & Murrell (2006) and Farrimond et al. (2023) find, that the resulting far field blast waves will be highly consistent.

Alternatively, the high consistency of the blast waves recorded by these authors may be read as implying that there is a consistent release of energy from a given mass of well-controlled HE. Those studies used commercially available RDX and PETN-based plastic explosives, manufactured to well controlled tolerances. And it is in fact to be expected that there would be a high degree of consistency of the chemical composition, and hence, the energy

released on detonation.

Although only 3 far field tests were conducted with the RDX-based C4 plastic explosive used throughout this study, the results agreed strongly with those of Rickman & Murrell (2006) and Farrimond et al. (2023). This gives confidence that the C4 used was consistent in its chemical constituents and detonation parameters.

In the near field conditions of interest in this study, the precise mechanisms of the detonation process are more likely to affect the resulting blast loading. As well as the effect of the precise position of the detonation, and that of the charge relative to the target, issues such as Rayleigh-Taylor and Richtmyer–Meshkov instabilities discussed in Chapter 2 have been shown to greatly influence the local features of the near field blast load (Tyas et al. 2015). Nevertheless, as Tyas indicated in that work, it appeared that, despite very large local variations in peak pressure and specific impulse, when the impulse was integrated over the entire 200mm diameter recording face of the CoBL facility, the results for spherical charges were highly consistent.

This suggests that we might expect consistency of results on a meso-length scale, (because the average energy release is consistent) whilst variations of load might be expected locally. A major strength of the CoBL facility is precisely that it enables the user to investigate the loading on a range of scales. With this background, we will investigate in the subsequent sections, the variability the blast loads captured in the experimental tests.

6.3.1 Total impulse

In previous experimental investigations, spherical charges have demonstrated a remarkable degree of consistency in the total impulse imparted to the measured area of the CoBL apparatus, as highlighted by Tyas et al. (2015). Even in more complex near-field scenarios, these experiments revealed minimal variation in total impulse between repeat tests, typically within $\pm 5\%$ across five tests, as illustrated in Figure 2.4. Whilst peak total impulse represents a simplified aggregation of the spatial data, it serves as a valuable singular metric for characterising the temporal and spatial variations across the 17 measurement locations, providing a concise overview of the loading history and energy imparted.

Total impulse is computed as the integral of specific impulse with respect to the area of the measurement array, evaluated at each timestep using an area-weighted linear interpolation of the specific impulse distributions sampled at 1 mm increments of radial ordinate. This yields the temporal development of total impulse over the positive phase duration, offering insight into the cumulative evolution of the blast loading and the relative contributions of peak pressure magnitude and positive phase duration to the total energy imparted to the array.

Where one or more bars did not record a valid trace, the affected locations are excluded from the total impulse calculation prior to integration. For symmetrical array configurations, the missing location is removed from the averaging process. For non-symmetrical configurations,

where nominally identical repeat measurements are not available at each location, the missing data are accounted for by interpolating across the remaining valid measurements in the array.

Spheres

The total impulse histories for the two spherical charge tests are presented in Figure 6.3, providing a baseline assessment of experimental consistency prior to the analysis of the cylindrical charge orientations. The results demonstrate a remarkable degree of repeatability, with peak total impulse values of 23.75 Ns and 23.88 Ns recorded for Tests 4 and 5 respectively, representing a variation of just ±0.3% between the two tests. This is consistent with the findings reported by Tyas et al. (2015) for equivalent spherical charge configurations, and serves to validate the experimental methodology employed throughout this programme. The ability to reproduce previously published results with such fidelity reinforces the robustness of the CoBL apparatus as a platform for characterising blast loading, and lends confidence to the comparative analyses of the cylindrical charge orientations presented in the subsequent sections.

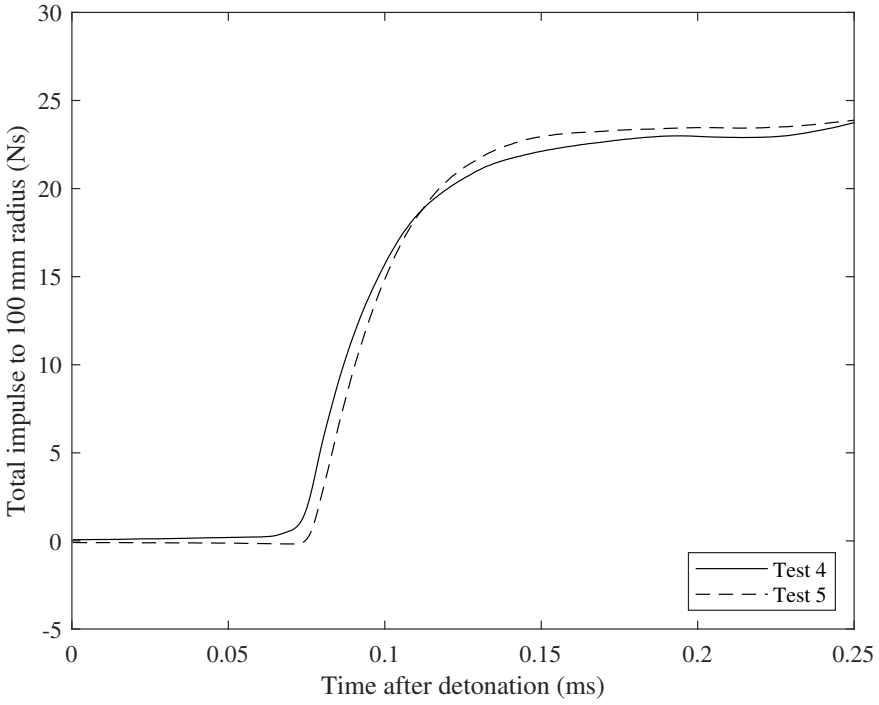


Figure 6.3: Total impulse development of spherical blast tests on a 200 mm diameter instrumented area.

Radial (0°, 0°)

Centrally detonated The radial cylindrical charge orientation presents a distinct challenge for the total impulse calculation, as the absence of axi-symmetry about the normal to the reflecting plate means that the two instrumented arrays — parallel and

perpendicular to the charge axis — produce distinct specific impulse profiles. This is accommodated in the total impulse calculation by attributing equal weighting to each array, with each contributing half of the total observed area.

The temporal total impulse histories for the centrally detonated radial tests are presented in Figure 6.4, alongside the constituent contributions from the parallel and perpendicular specific impulse profiles. The peak total impulse across the three tests varies within ±3.6% of the cross-test mean of 47.31 Ns, demonstrating a level of consistency that is notably higher than might be anticipated from the literature for near-field non-spherical charges. Examination of the constituent components reveals that the parallel and perpendicular arrays contribute equally to the peak total impulse, each providing approximately half of the total. The parallel component consistently dominates the early-time loading, exhibiting a higher rate of impulse accumulation in the initial phase; however, in Tests T006 and T007 the perpendicular component surpasses the parallel at a consistent time of 0.134–0.135 ms after detonation, after which both components contribute comparably to the total. In Test T019, the parallel and perpendicular components exhibit an identical profile throughout the loading history, with no crossover observed between the two constituents.

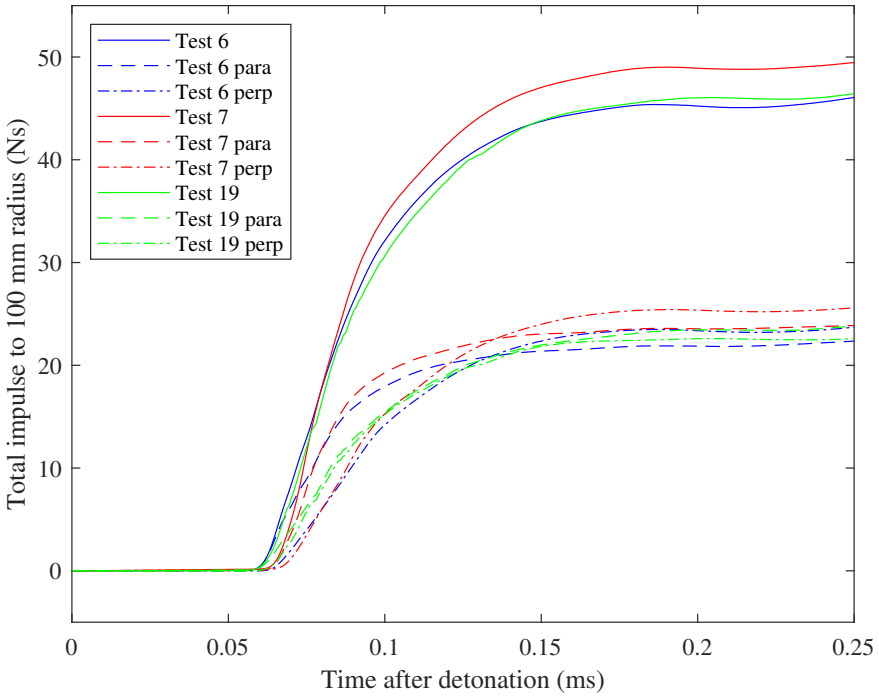


Figure 6.4: Total impulse development of aligned cylindrical blast tests on a 200 mm diameter instrumented area. The 'para' and 'perp' refer to the parallel (0°) and perpendicular (90°) loading integrated over half the swept area. The total test data is the sum of the corresponding two parts.

End detonated The temporal total impulse histories for the end detonated radial tests are presented in Figure 6.5. The profiles are broadly similar in shape across the two tests, with peak total impulse values varying within ±4.8% of the cross-test mean of 45.3 Ns.

This level of consistency is comparable to that observed in the centrally detonated radial tests, and the peak total impulse is of a similar magnitude to the 47.31 Ns recorded for the centrally detonated configuration, suggesting that the detonation point has a limited influence on the total impulse imparted to the measurement array for this charge orientation.

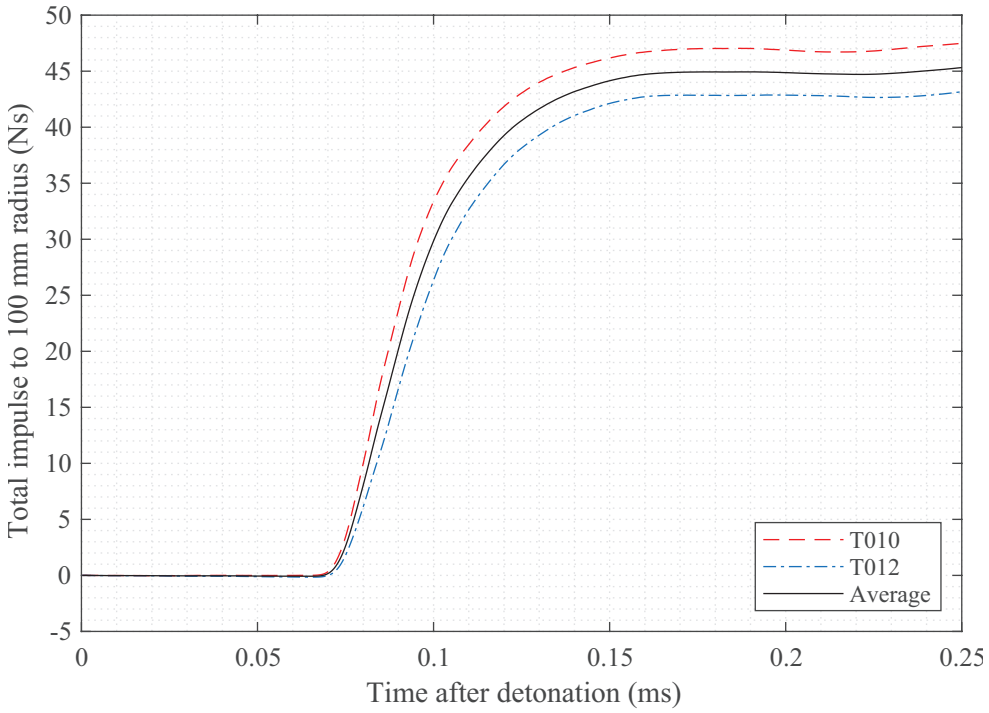


Figure 6.5: Total impulse development of radial cylindrical blast tests (0°, 0°), end detonated, on a 200 mm diameter instrumented area. Tests T010 and T012 are displayed in red and blue respectively, and an average of them in black.

Radial (45°, 0°)

The 45° radial orientation introduces axi-symmetry about the normal to the reflecting plate, enabling the use of a singular loading profile for the total impulse calculation, consistent with the approach employed for the spherical charges. In addition to this computational simplification, the rotation of the charge relative to the instrumented arrays provides additional measurement locations compared to the aligned configuration for an otherwise identical explosive test, as illustrated in Figure 3.4, enhancing the spatial characterisation of the loading and aiding in the identification of potential hot spots in the pressure and impulse distributions.

The total impulse histories for all five centrally detonated radial cylindrical tests are presented collectively in Figure 6.6, encompassing both the aligned and 45° orientations. The peak total impulse exhibits a variation of ±7.5% about a cross-test mean of 48.34 Ns, well within the range considered indicative of good experimental consistency in blast testing. Notably, no apparent distinction is observed between the aligned and 45° orientations in the total impulse profiles, suggesting that the rotational approach angle of the charge

relative to the instrumented array has a negligible influence on the total impulse imparted to the measurement area when the data are spatially averaged. This observation further supports the validity of the equal area weighting assumption employed in the total impulse calculation for the aligned configuration, in which half of the observed area is attributed to each of the parallel and perpendicular loading profiles.

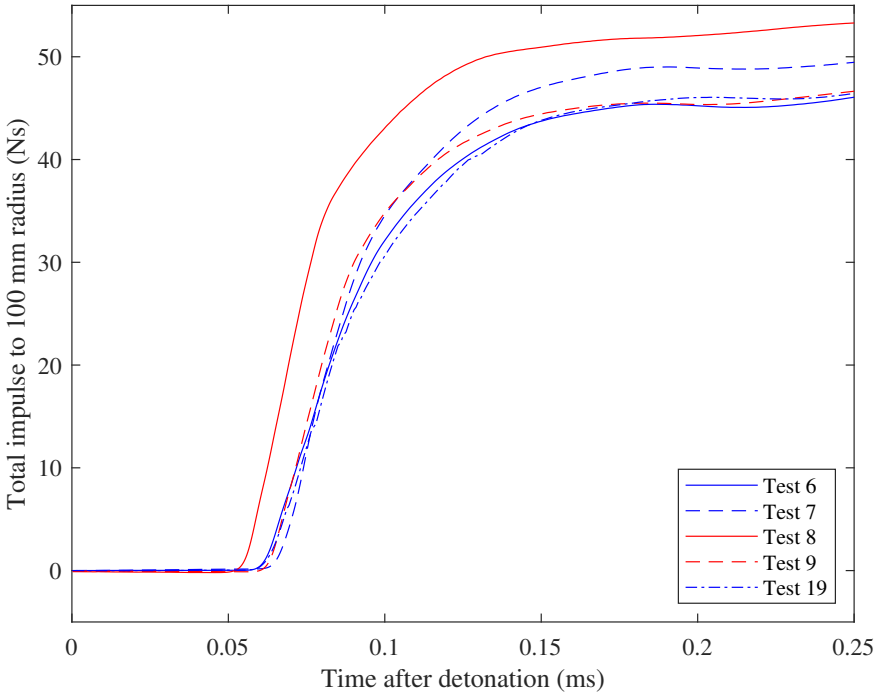


Figure 6.6: Total impulse development of radial cylindrical blast tests on a 200 mm diameter instrumented area. Aligned 0° cylinders are presented in blue and 45° orientated cylinders are presented in red.

Inclined

Inclined (0°, 22.5°) The temporal total impulse histories for the 22.5° inclined tests are presented in Figure 6.7. The three profiles exhibit good consistency in shape, although the peak total impulse values display a higher degree of inter-test variability than observed in the preceding orientations, with peak values of 19.84 Ns, 23.46 Ns, and 19.12 Ns recorded for Tests T020, T021, and T023 respectively, giving a cross-test mean of 20.81 Ns and a variation of ±12.7%. The elevated peak total impulse recorded in Test T021 is consistent with the exceptionally strong central bar pressure and the significantly elevated peak pressure at the +25 mm parallel position identified in that test, both of which contribute to the total impulse calculation. This influence is further exacerbated by the absence of a valid trace at the +50 mm parallel position across all three tests, such that the interpolation of the total impulse calculation over this region is dominated by the elevated +25 mm values, amplifying its contribution to the integrated total. This inter-test variability is reflected in the averaged specific impulse and peak specific impulse distributions presented in Figures 4.37 and 4.39 respectively, where the influence of the Test T021 results on the cross-test mean is clearly apparent.

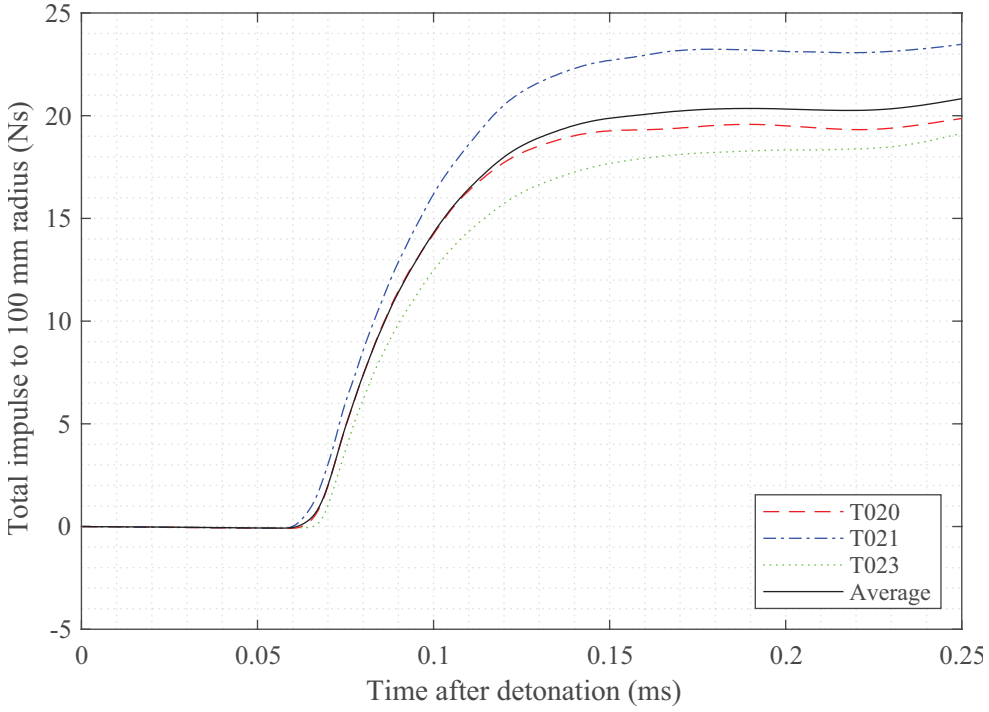


Figure 6.7: Total impulse development of inclined cylindrical blast tests (0°, 22.5°) on a 200 mm diameter instrumented area. Tests T020, T021 and T023 are displayed in red, blue and green respectively, and an average of them in black.

Inclined (0°, 45°) The temporal total impulse histories for the 45° inclined tests are presented in Figure 6.8. The profiles exhibit a different character to those observed in the preceding orientations, with all three traces following an S-curve development rather than the sharper initial rise seen at lower inclination angles. This change in profile shape is

consistent with the lower peak pressures recorded at this orientation and the shift of the dominant loading towards the later positive phase, as the measurement positions fall within the transitional region between the radial and axial blast zones where the initial shock is weaker and the majority of the impulse accumulates progressively over a longer duration. A slight difference in the time of arrival of the total impulse between the three tests is observed, with Test T024 arriving later than Tests T026 and T027, which contributes to the visual difference of the three tests. Peak total impulse values of 7.38 Ns, 8.30 Ns, and 8.52 Ns are recorded for Tests T024, T026, and T027 respectively, giving a cross-test mean of 8.06 Ns and a variation of ±7%, which is considered acceptable given the complexity of the loading environment at this orientation.

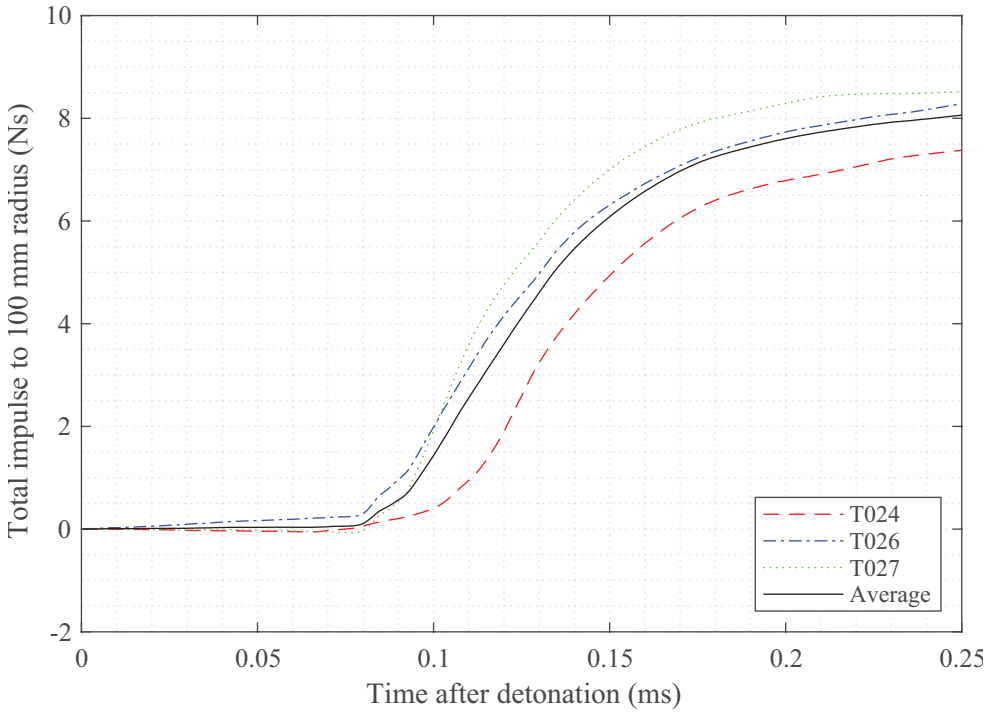


Figure 6.8: Total impulse development of inclined cylindrical blast tests (0°, 45°) on a 200 mm diameter instrumented area. Tests T024, T025 and T027 are displayed in red, blue and green respectively, and an average of them in black.

Inclined (0°, 67.5°) The temporal total impulse histories for the 67.5° inclined tests are presented in Figure 6.9. The profiles exhibit a further evolution in shape from the S-curve observed at 45°, transitioning to an adjusted S-curve characterised by an initial rise, a sustained approximately constant gradient, and a gradual tapering off towards the peak total impulse. This shape is consistent across all three tests and reflects the increasingly complex and late-dominated loading character of the blast environment at this orientation. It is noted that the instrumentation noise discussed in the individual test sections manifests in the total impulse profiles prior to shock arrival, producing a spurious negative gradient in the pre-arrival region for Tests T028 and T030, and a slight positive gradient for Test T031; these pre-arrival features are not representative of a physical loading characteristic. Peak total impulse values of 6.30 Ns, 6.30 Ns, and 5.80 Ns are recorded for Tests T028,

T030, and T031 respectively, giving a cross-test mean of 6.13 Ns. The consistency between Tests T028 and T030 is particularly notable, with the slightly lower value recorded in Test T031 contributing to a modest overall variation across the three tests.

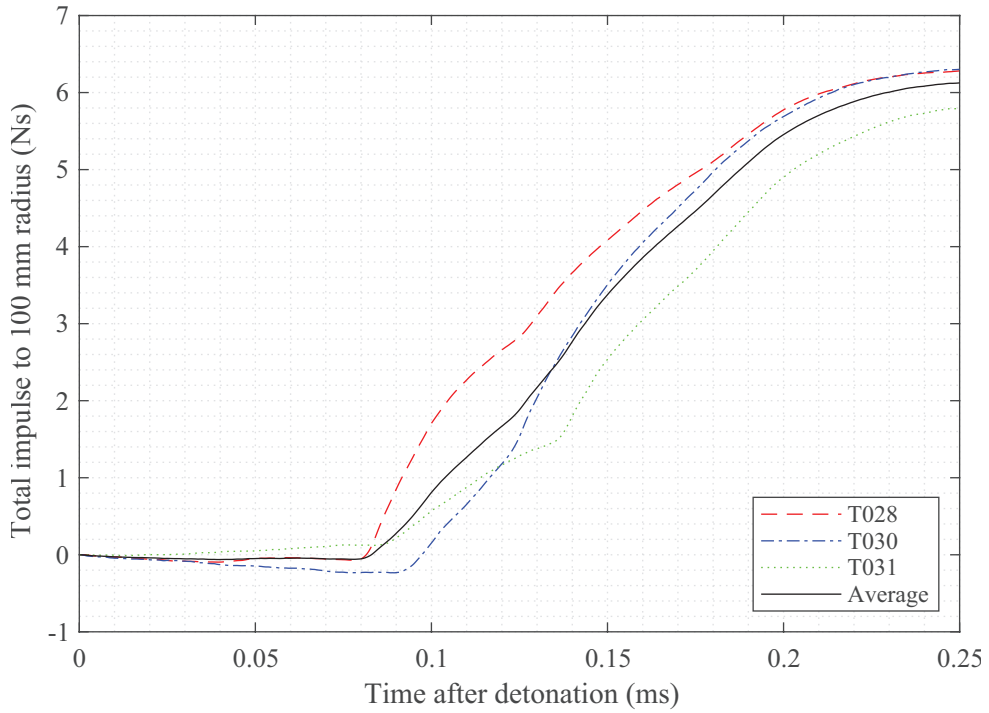


Figure 6.9: Total impulse development of inclined cylindrical blast tests (0°, 67.5°) on a 200 mm diameter instrumented area. Tests T028, T030 and T031 are displayed in red, blue and green respectively, and an average of them in black.

Axial (0°, 90°)

Centrally detonated In the axial orientation, the rotational symmetry of the loading about the charge axis allows the total impulse to be calculated from measurements at equivalent radial ordinates, following the same methodology applied to the spherical and 45° radial cylindrical tests. In instances where one or more bars did not record valid traces, the redundancy afforded by multiple nominally identical sensing locations is exploited, with the mean of the remaining valid traces used in place of the missing data.

Test T032 presents a particular challenge in this regard, as the central bar did not record a valid trace during this test. The other tests missing a central bar use an interpolated value from the other data sets in the array but the localised peak in the axial tests would be missed with this approach; necessitating substituting in the mean of the equivalent traces from Tests T016 and T017. Given that the central bar measurement point contributes only 6.25% of the total area in the linear interpolation scheme, this substitution is considered acceptable and allows the remaining valid data from Test T032 to be fully represented in the total impulse calculation.

The temporal total impulse histories for the three axial tests are presented in Figure 6.10. The results demonstrate good consistency, with peak total impulse values varying within

±5.0% of the cross-test mean of 13.12 Ns. This level of repeatability is encouraging for near-field testing of a complex charge geometry, and underscores the reliability and reproducibility of the experimental methodology. The observed variability is considered inherent to the spatial and temporal distribution of the blast loading rather than indicative of inconsistency in the energy released by the detonation, and does not significantly affect the broader understanding of the loading dynamics across the measurement area.

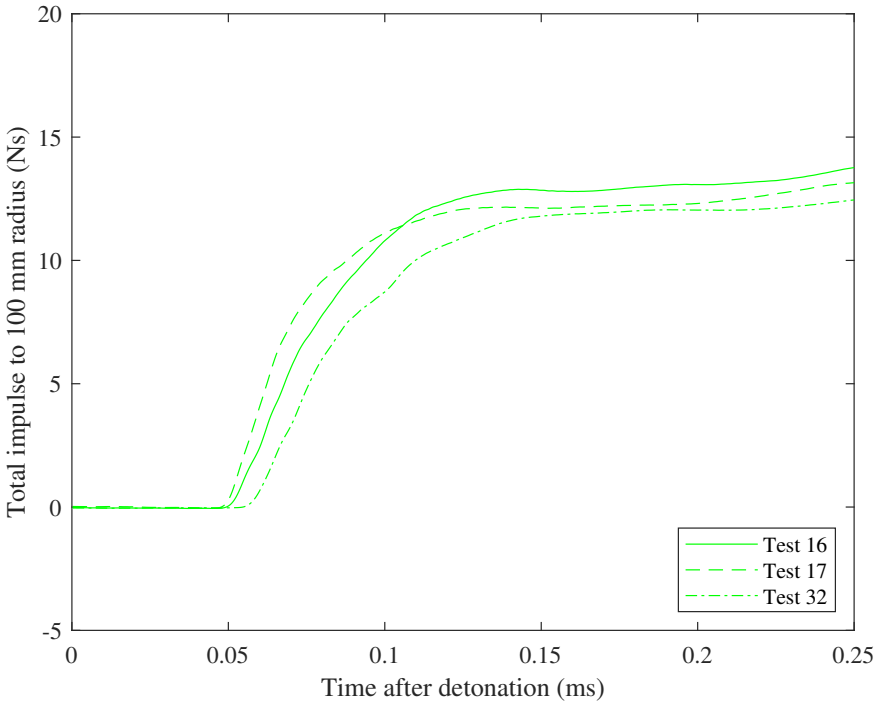


Figure 6.10: Total impulse development of axial cylindrical blast tests on a 200 mm diameter instrumented area. Test 32 has an artificial central loading trace applied from the average of tests 16 and 17.

End detonated The temporal total impulse histories for the end detonated axial tests are presented in Figure 6.11. The two profiles exhibit a consistent shape broadly similar to that observed in the centrally detonated axial tests, though with a higher degree of inter-test variation, with peak total impulse values of 15.82 Ns and 12.57 Ns recorded for Tests T014 and T015 respectively, giving a cross-test mean of 14.20 Ns and a variation of ±11.5%.

The considerably lower peak total impulse recorded in Test T015 is noteworthy given that this test produced the highest central bar peak pressure observed across the entire experimental programme. This apparent contradiction is explained by the rapid spatial decay of the loading with radial distance identified in the individual test results; whilst the central bar records an exceptional peak pressure, the sharp attenuation at the 25 mm and beyond positions means that the elevated central bar loading contributes only marginally to the total impulse, as the central bar measurement point accounts for just 6.25% of the

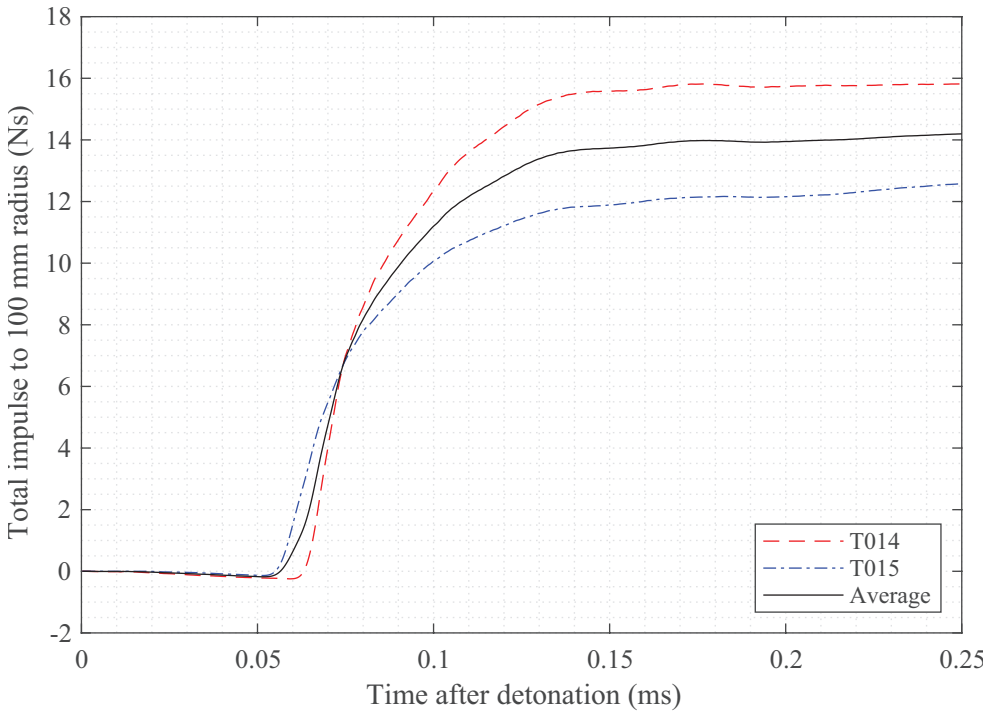


Figure 6.11: Total impulse development of axial cylindrical blast tests (0°, 90°), end detonated, on a 200 mm diameter instrumented area. Tests T014 and T014 are displayed in red and blue respectively, and an average of them in black.

total area in the linear interpolation scheme. The considerably larger area attributed to the 25 mm and outer radial positions, where the loading in Test T015 is comparatively modest, therefore dominates the total impulse calculation, resulting in a lower peak total impulse than might otherwise be anticipated from the central bar pressure alone.

Comparison

The experimental results across all charge configurations demonstrate internal consistency, providing reliable results within each orientation. However, a significant distinction emerges when comparing the configurations against one another. All tests involve the detonation of 200 g of C4 at a cleared standoff distance of 250 mm, maintaining an identical cleared scaled distance. The variables across the experiments are the charge shape and its orientation relative to the reflecting surface, with the cleared standoff distance adopted in preference to the to-centre scaled distance to account for the considerable variation in geometric charge length between the spherical and cylindrical configurations, and detonation point.

The average total impulse traces for all charge orientations are presented in Figure 6.12e. The radially oriented cylindrical charges, encompassing both the aligned (0°, 0°) and (45°, 0°) configurations as well as their end detonated equivalents, produce broadly consistent peak total impulse values in the range of 45–48 Ns, with the end detonation point having little influence on the total impulse for the radial orientation.

The axially oriented cylindrical charges, both centrally and end detonated, produce peak

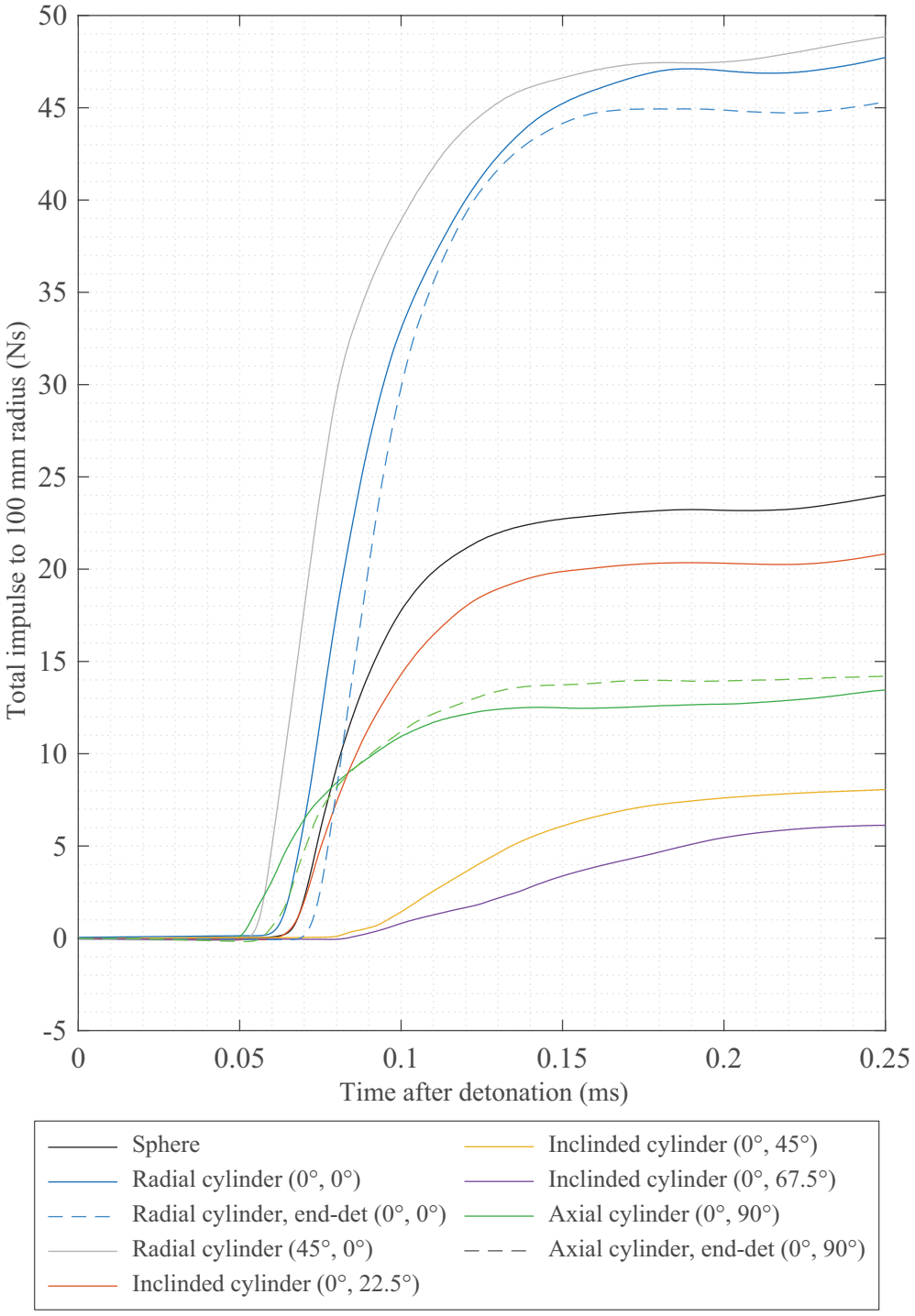


Figure 6.12: Temporal development of total impulse for all charge configurations, presented as cross-test averages. Spherical charges are shown in black; radial cylindrical charges at (0°, 0°) in blue and (45°, 0°) in grey; inclined cylindrical charges at (0°, 22.5°) in red, (0°, 45°) in orange, and (0°, 67.5°) in purple; and axial cylindrical charges at (0°, 90°) in green. End detonated configurations are denoted by dashed lines.

total impulse values of approximately 13–14 Ns, with the difference between the two detonation configurations considered within experimental variability. The spherical charges produce a peak total impulse of approximately 23.8 Ns, sitting between the radial and

axial extremes.

The inclined cylindrical orientations occupy a transitional region between the radial and axial extremes, with peak total impulse values of 20.81 Ns, 8.06 Ns, and 6.13 Ns recorded at inclination angles of 22.5°, 45°, and 67.5° respectively. Notably, the 45° and 67.5° orientations produce lower peak total impulse values than the axial configuration, rather than following a simple monotonic transition between the radial and axial extremes. This is attributed to the measurement positions at these inclination angles falling within the bridging wave zone, between the primary side and end wave regions of the cylindrical charge, where the loading is characterised by lower peak pressures and a more gradual impulse accumulation than experienced in either the purely radial or purely axial configurations.

From the comparative data, a clear and striking relationship between the charge orientations emerges:

1. Radially oriented cylindrical charges impart approximately **twice** the total impulse on the 200 mm observed area compared to the spherical equivalent charge.
2. Axially oriented cylindrical charges impart approximately **half** the total impulse on the 200 mm observed area compared to the spherical equivalent charge, or approximately **one quarter** of the total impulse produced by the radially oriented cylindrical charges.

This clear relationship underscores the profound influence of charge orientation on the resulting blast loading, with a four-fold difference in total impulse observed between the radial and axial extremes of an otherwise identical explosive configuration. Whilst the variation in to-centre scaled distance between the configurations is acknowledged, the use of a consistent cleared standoff distance is considered insufficient to account for the magnitude of the differences recorded, reinforcing the conclusion that charge orientation is the dominant factor governing the total impulse imparted to the target.

Experimental robustness

The instrumented area of approximately 0.0314 m^2 represents only around $\frac{1}{30}$th of the total theoretical surface area of a sphere at the cleared standoff distance of the charge, such that the measurements capture a small but representative fraction of the total blast energy. The few percentage points of variation in total impulse observed within each charge configuration across repeat tests underscore the remarkable spatial consistency with which the explosive energy is distributed, lending confidence to the representativeness of the instrumented area as a sampling region.

Whilst total impulse provides a valuable high-level metric for characterising and comparing the blast loading across configurations, it represents an aggregation of the spatial and temporal distribution of the loading. The peak pressure and specific impulse temporal histories presented in the preceding sections offer a more detailed interrogation of the loading characteristics, and it is through the combination of these metrics that a comprehensive

understanding of the influence of charge shape and orientation on blast loading can be developed.

6.3.2 Experimental spatial variation of loading

Spherical

The spherical charge tests revealed a considerable disparity in peak reflected pressure at the central bar position, representing an anomalous result that is attributed to a localised pressure plume in the blast wave impinging directly on the end of the bar. Whilst spatial variability in peak pressure across the target face is an expected feature of near-field blast loading, the magnitude of the central bar measurement in this instance significantly exceeded expectations. High-speed video recording would have been invaluable in confirming this interpretation; however, similar phenomena have been observed and explained in an equivalent manner by Tyas et al. (2015), lending support to the proposed explanation.

Removing the anomalous data point from the set gives a more representative distribution of the loading expected from previous studies and is shown by the average trace line. The adjusted average is identified when it is used for comparison going forward.

The variability of peak reflected pressure and peak specific impulse is consistent across the radial ordinates 25-50 mm and relatively large at $\pm 30 - 35\%$.

Cylindrical

Figure 6.14 presents the peak reflected pressure and peak specific impulse of the two orientations of cylinders with the average of the spheres. This highlights the spatial distribution of both the pressure and impulse compared to the relatively uniform spheres and radial cylinders. The maximum peak specific impulse of the axial cylinders fall below the minimum of the radial cylinders at the 50, 75 and 100 mm ordinates which has a great effect on the total impulse due to the swept area that these radial ordinates cover.

This has enabled the localisation of the loading to be quantified. Peak reflected pressures have been found to decay by more than 80% between the point on the target co-axial with the charge axis and a point radially offset by 25mm, with the equivalent specific impulses falling by around 60%.

The spread of peak pressures and specific impulses, reaching as much as 100% of the mean value in some cases, highlights the considerable variability inherent in near-field blast testing. However, this variability has been demonstrated to be localised in nature, with the total impulse imparted to the measurement area remaining highly consistent across repeat tests, confirming that it is the spatial distribution of the loading rather than the overall energy delivery that is the source of the observed inconsistency. The variability appears to increase with radial ordinate, although the limited number of data points at the central bar position may obscure the true extent of the spread at that location.

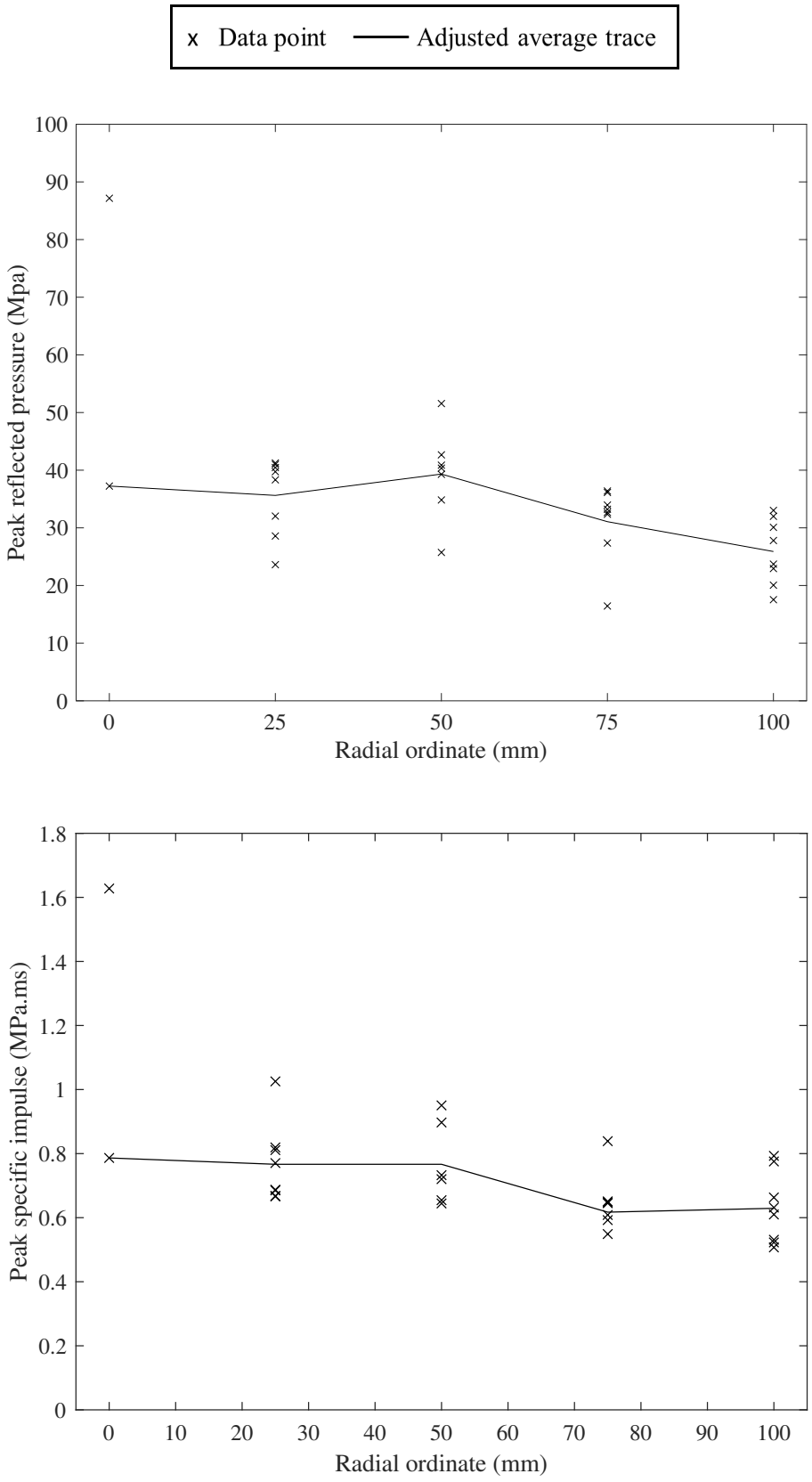


Figure 6.13: Peak reflected pressure and peak specific impulse from spherical blast tests and average profile, excluding anomalous result

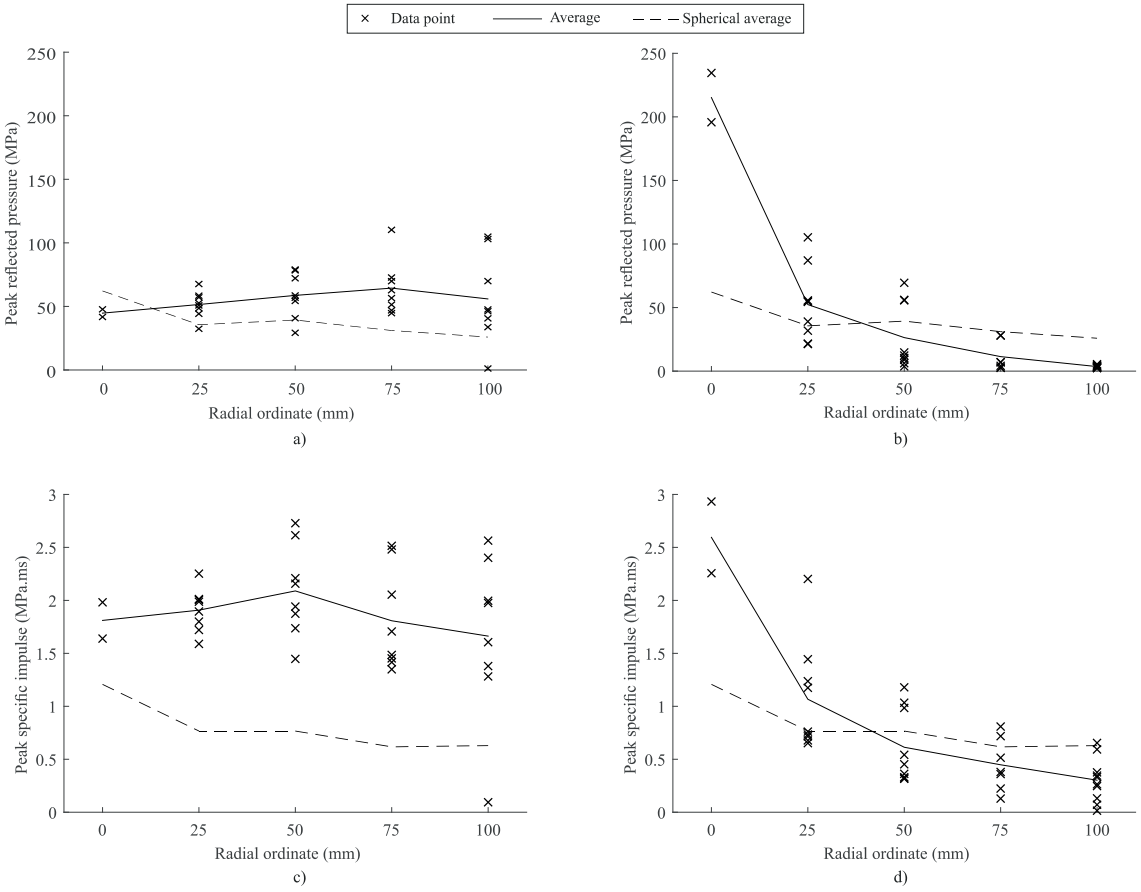


Figure 6.14: Peak reflected pressure (a-b) and peak specific impulse (c-d) of radial cylinder (a,c) and axial cylinder (b,d) blast tests with spherical comparison (dashed line)

The cylindrical peak pressure at the target centre (invariant of orientation angle since the cylinders are rotated about this point) is approximately equal to the epicentral peak pressure from the spherical charge, however the corresponding specific impulse value is approximately twice that from the spherical charge. At 0° and 45° the maximum pressure is clearly non-central (at 75 mm in both cases). This is also observed in the specific impulse distributions for these two orientations, albeit to a lesser extent, which both demonstrate a higher specific impulse at 50 mm than the epicentral value. It is suggested that this behaviour is due to the complex interactions between the target plate and the coalescence of the primary waves from the axial faces ('end') and radial ('side') of the charge and the bridging wave between the two.

The peak reflected pressures at 90° orientation generally follow the cylindrical peak pressure distributions, however the peak specific impulse is again approximately twice the spherical values. Whilst the specific impulse distribution at 0° appears to reduce with distance on account of the reduction of the 100 mm bar impulse due to localised clearing as explained previously, the 45° and 90° specific impulse distributions appear relatively uniform with radial ordinate.

6.3.3 Impulse distributions

Figure 6.15 shows quarter-symmetric surface plots of the distributed specific impulse from the spherical and cylindrical charges. Linear interpolation was used to map the mean specific impulse distributions from Figure 6.2 onto a regular Cartesian grid at 0.5 mm spacing. The spherical data utilised 1D interpolation as a function of radial ordinate, whereas the cylindrical data required interpolation in 2D as a function of radial ordinate and orientation with respect to the longitudinal axis of the cylinder. Linear interpolation was used throughout, and is considered adequate here for illustrative purposes.

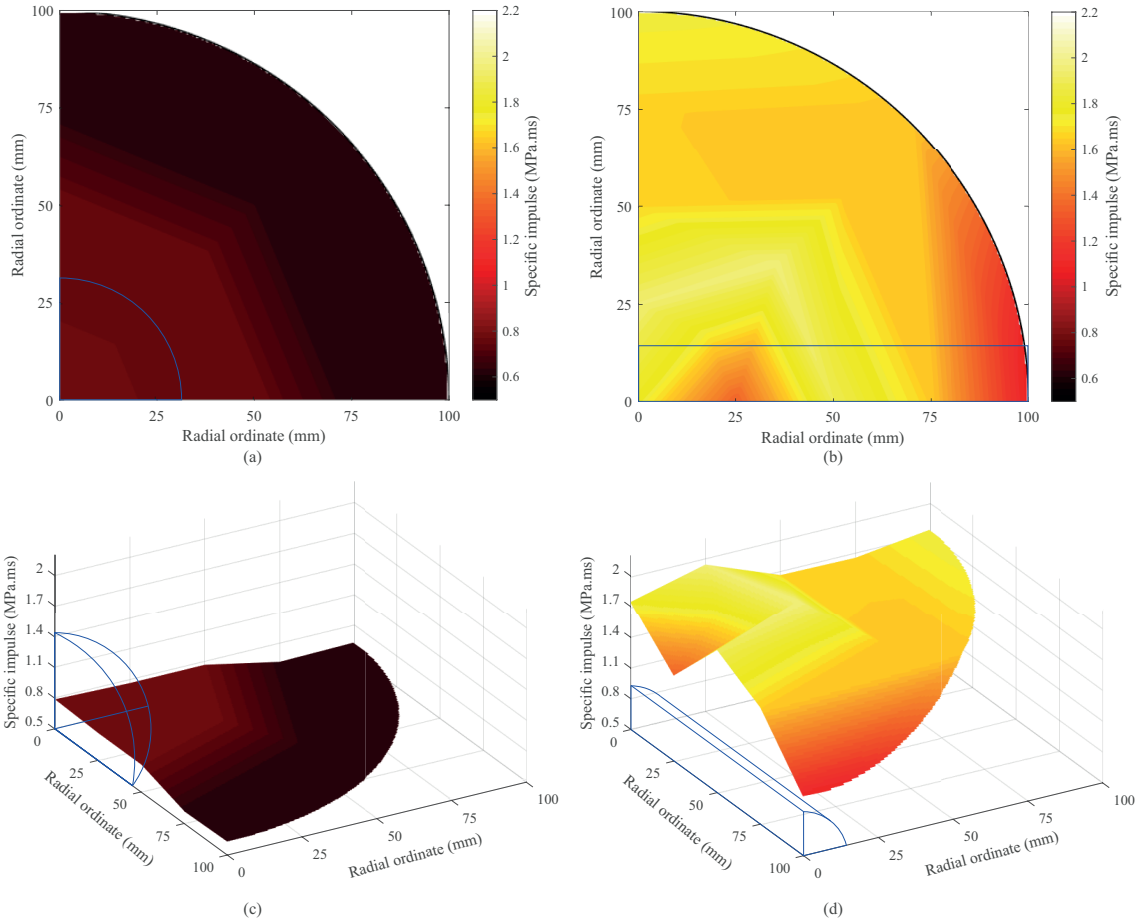


Figure 6.15: Interpolated peak specific impulse surface plots for spherical (with adjusted average) [left] and radial cylindrical [right] charges. Blue outline represents 1/8 charge shape/orientation.

The enhancement provided by the cylindrical charges is immediately apparent, i.e. the loading is less regular across the target face, it decays in a less consistent manner with radial ordinate, and is considerably higher in magnitude throughout. These surface plots also provide a clear visualisation of the effects of the complex side, end, and bridging wave interaction phenomena occurring at approximately 50–75 mm from the centre of the cylinder as described previously. Finally, the rapid reduction in loading towards the end of the cylinder (100 mm radial ordinate at 0° orientation) is clearly visible.

The data from Figure 6.15 is presented again in Figure 6.16 alongside the axial equivalent.

The spherical data is presented this time with the non-corrected average, note the scales are vary for each orientation to facilitate displaying the detail of the distributions.

6.4 Numerical modelling

6.4.1 Axial

Development of total impulse

Experimentally, the voltage recordings captured by the oscilloscopes were converted to reflected pressure histories using the known strain gauge calibration factors and the Young's modulus of the bar material, with the stress pulses in the Hopkinson bars taken as representative of the applied reflected pressure, as described in Section 2.2.9. The temporal integration of the reflected pressure traces yields the specific impulse at each measurement location, from which the total impulse imparted to the instrumented area is computed using an area-weighted linear interpolation of the specific impulse distributions. Full details of the total impulse calculation methodology are provided in Section 6.3.1. Figure 6.20 presents the temporal evolution of the total impulse delivered to the central 200 mm diameter instrumented area of the target.

Figure 6.17 presents the computed total impulse from both axial experimental tests and numerical modelling. The axi-symmetric numerical simulations exhibit a good correlation, albeit with a slight tendency toward over predicting the peak total impulse as the mesh size is reduced.

Conversely, the 3D numerical traces show a lack of correlation with the experimental data, suggesting that the model fails to accurately capture the underlying mechanisms driving the explosion. In particular, there is an overestimation of both the rate of and the peak total impulse. The decreasing mesh size also suggests that the correlation would be achieved at higher total impulse although this assumption remains speculative due to limitations in running finer meshes on the available computing systems.

The 2D axi-symmetric modelling is a considered a good representation of the experimental data, especially considering that total impulse often serves as a solitary metric by which numerous testing setups can measure. Therefore, there is neither a reason nor the capability to investigate further and the other characteristics are taken as writ. On the other hand, the inadequacy of the 3D modelling to achieve a correlation is rationalised by the inherent challenge in achieving a sufficiently small mesh resolution capable of accurately capturing the intricate energy flow within the model.

Spatial specific impulse

The CoBL apparatus, coupled with its spatial sampling capabilities, facilitates a detailed examination of the loading characteristics. This allows for a nuanced analysis by comparing the experimental data with numerical simulations by multiple metrics, shedding light on

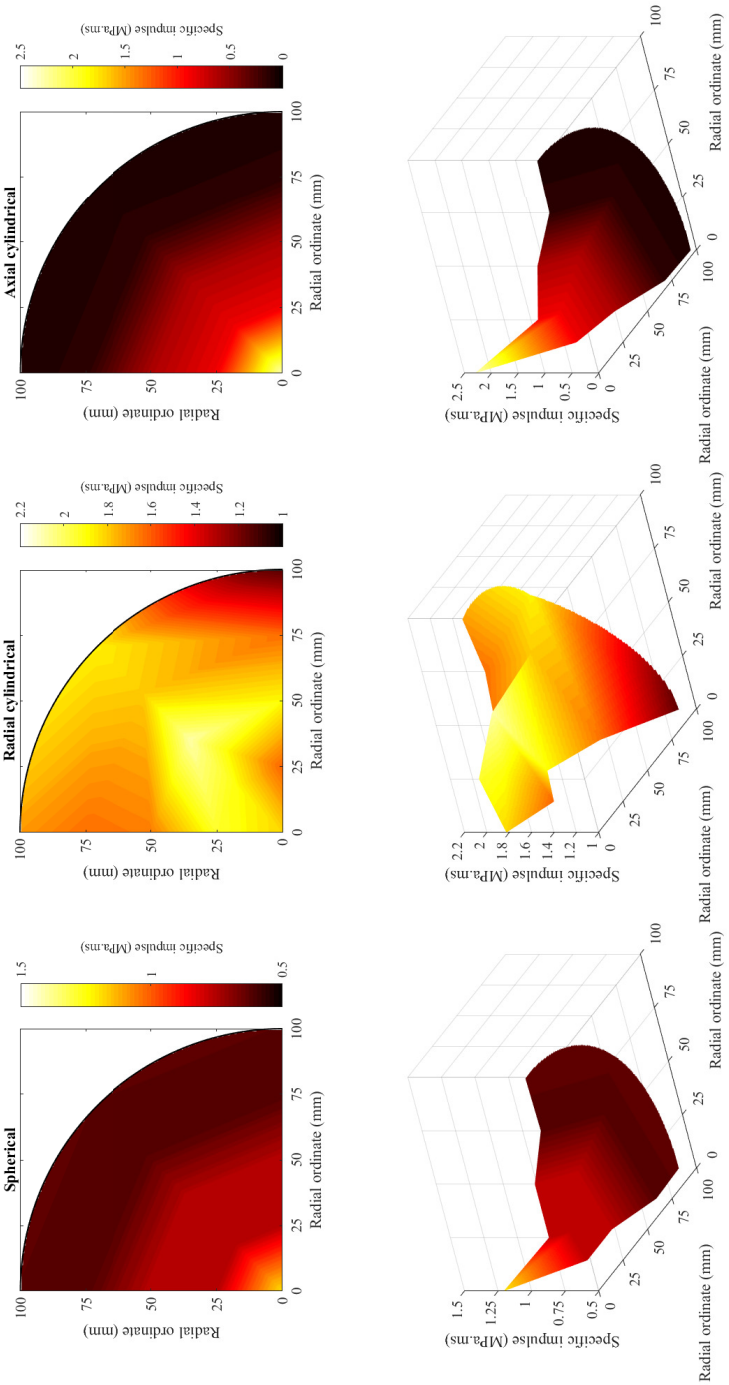


Figure 6.16: Interpolated peak specific impulse surface plots for spherical [left], radial cylindrical [middle] and axial cylindrical [right] charges.

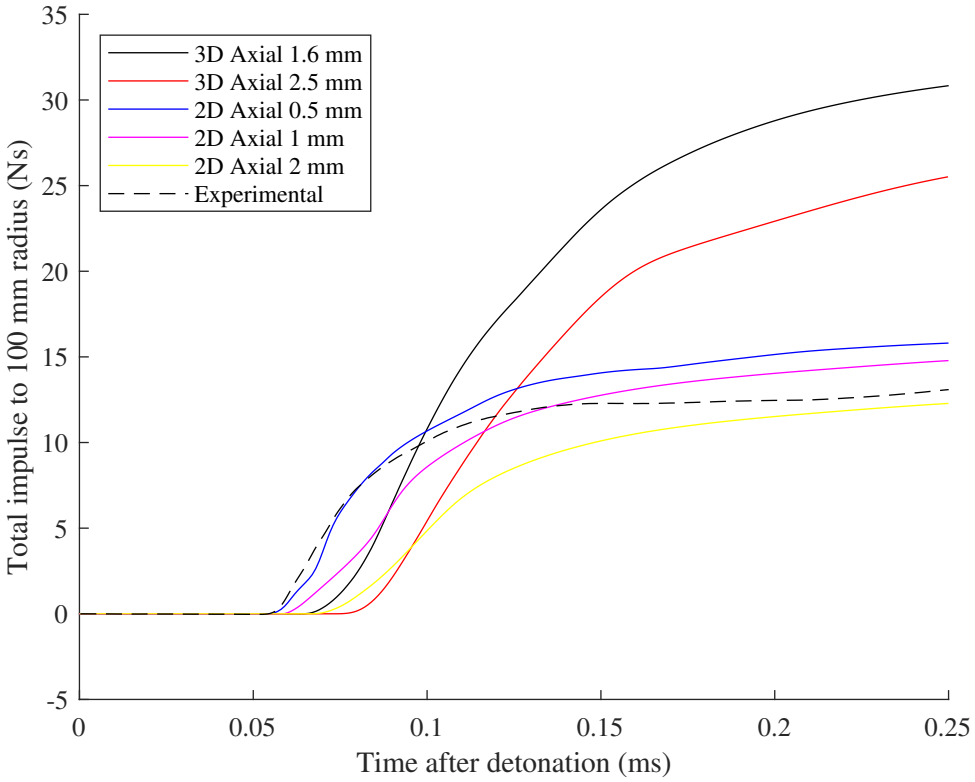


Figure 6.17: Temporal development of total impulse on a 200 mm diameter instrumented area for experimental and numerically modelled axial cylinders.

where the model accurately captures reality and identifying instances where errors may accumulate, potentially resulting in correct outcomes obtained through incorrect means. This capability to drill down into the details of loading behaviour provides valuable insights for refining and validating numerical models.

The peak values of specific impulse for nominally identical radial ordinates from blast tests are marked on Figure 6.18, maximum of four points for the radial ordinates $25 - 100$ mm for the three tests. The 'experimental' line plotted are the peak values of the averaged signal for the three tests at the five measurement locations and not the averages of the peaks. This is an average trace and the peak values indicate a boundary incorporating the blast variability.

The 2D numerical modelling with finer meshes exhibits a significant over-prediction of the central loading and an under-prediction at the outer radial ordinates. The greater influence of larger radial ordinates on the total impulse, attributed to the increased swept area at greater radii, biases the influence of total impulse towards the extremities of the observed area. This bias is evident in Figure 6.17, where the substantial over-prediction in the centre offsets the total impulse. The 2 mm mesh shows a highly consistent specific impulse distribution with the experimental data in the central half (up to 50 mm radial ordinate) but exhibits a drop-off in the second half. This alignment at the centre is likely

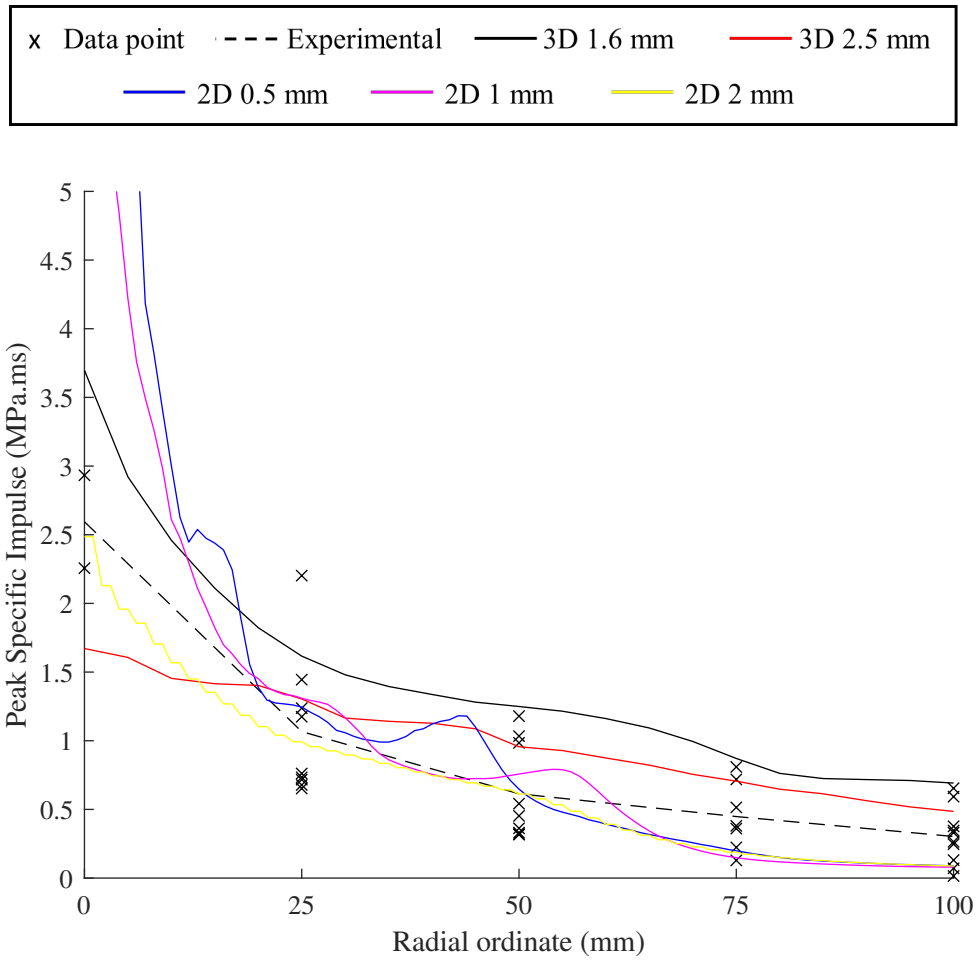


Figure 6.18: Peak specific impulse of axial cylindrical blast tests, average and numerical modelling

to be coincidental as the coarse mesh is tempering the axial shock wave while the numerical jetting is exacerbating it, a balancing of errors.

On the other hand, the specific impulse distribution of the 3D numerical models align more closely with the experimental profile, as illustrated in Figure 6.18. The 1.6 mm mesh consistently registers $0.5 - 1$MPa.ms higher than the experimental values across the observed radius, contributing to the high total impulse depicted in Figure 6.17. The profile of the fine 3D model suggests that the numerical analysis is capable of capturing the mechanisms driving the axial shock wave, despite the magnitude being incorrect.

Peak pressure distribution

The peak pressure distributions show a similar story to the peak impulses, as shown in Figure 6.19. The peak pressures of the 2D axi-symmetric models suffer from numerical jetting, significantly over-predicting the central pressures. This over-prediction limits their representativeness beyond identifying high spatial variability favouring the centre. The orders of magnitude difference in peak pressure across the instrumented area (100mm) versus the stand-off (250mm) illustrates the directionality of the axial shock front, which is

consistently predicted, measured, and modelled.

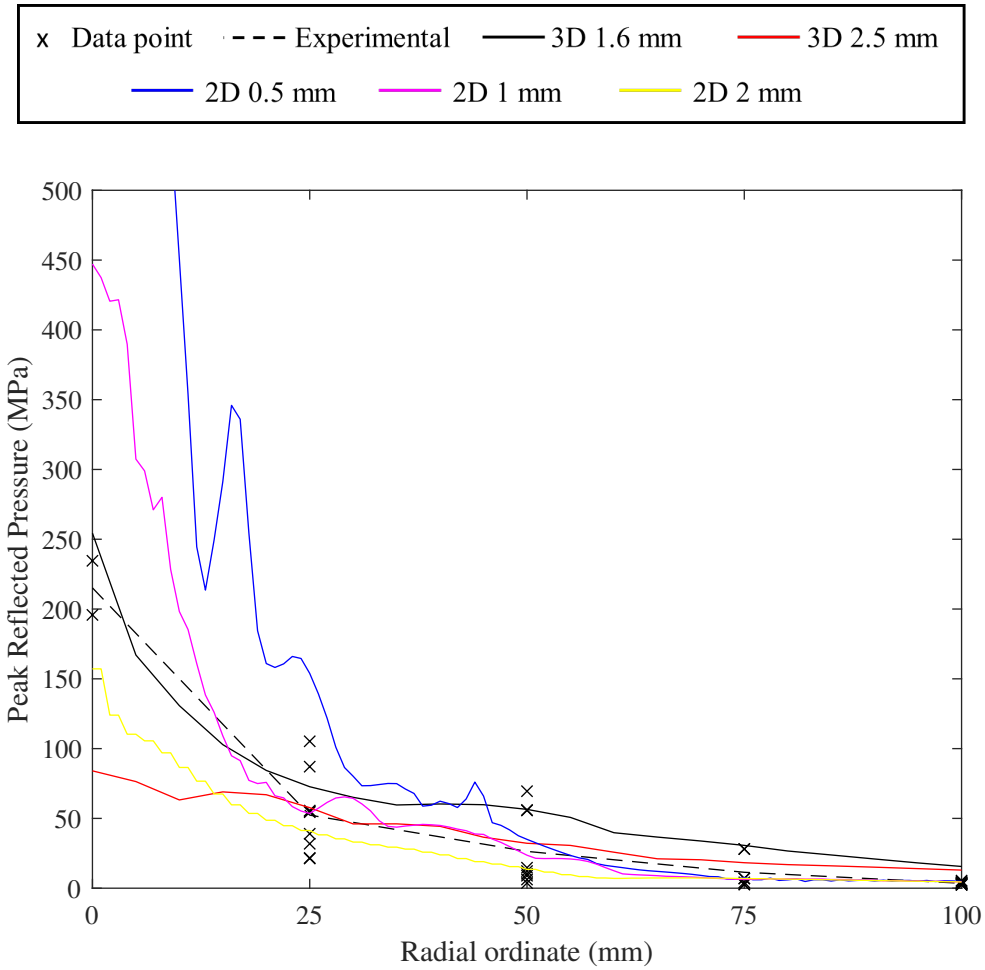


Figure 6.19: Peak reflected pressure of axial cylindrical blast tests, average and numerical modelling

The 3D numerical model in a 1.6 mm mesh accurately tracks the experimental profile and is within 10% of the peak recorded pressures across all radial ordinates, as illustrated in Figure 6.19. This high level of correlation instils confidence in the capability of 3D ALE models to accurately capture the intricate mechanisms that sustain the shock fronts in the plume.

The various numerical modelling techniques employed in this study showcase unique strengths in predicting different blast parameters. However, it is essential to emphasise that determining the correctness of these predictions requires validation against appropriate experimental data. Without such validation, it remains challenging to definitively identify the accuracy of each modelling approach in representing the complex physics involved in blast events.

6.4.2 Radial

Figure 6.20 shows the temporal development of total impulse imparted to the central 200 mm diameter instrumented area of the target. Total impulse is calculated at each

timestep using an area-weighted linear interpolation of the specific impulse distributions, sampled at 1 mm increments of radial ordinate. The 45° orientation loading has been integrated over the entire instrumented area, whereas the 0° and 90° orientation loadings have each been integrated over half the swept area to separate total impulse into parallel and perpendicular components. 'Total aligned cylinder' is given by the summation of the parallel and perpendicular components of total impulse.

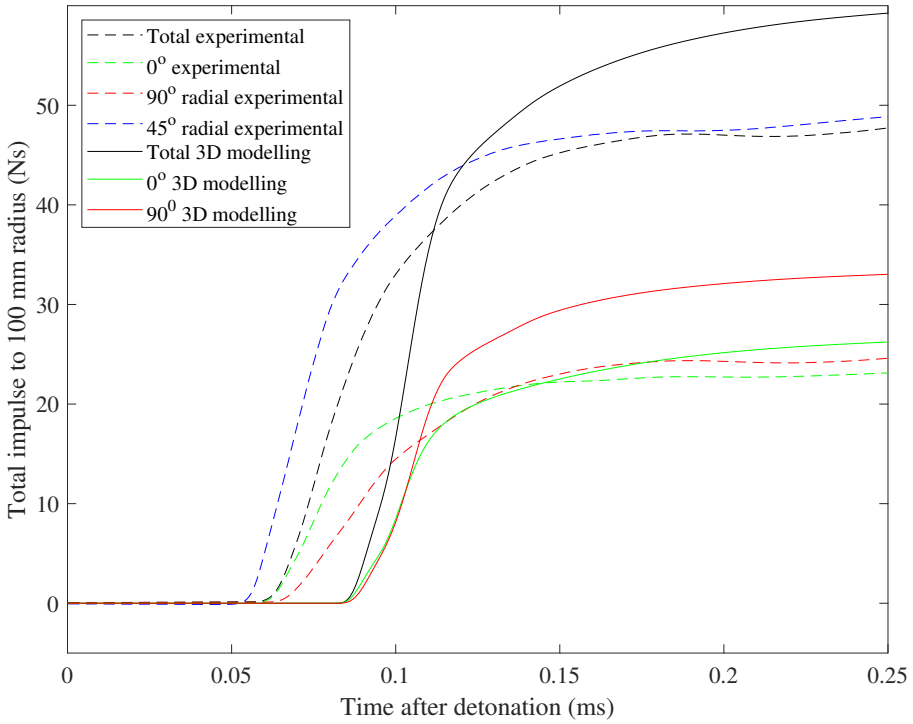


Figure 6.20: Temporal development of total impulse for experimental and numerical modelling of radial cylinders. 45° cylinder loading integrated over the entire area, whereas 0° and 90° orientation loading integrated over half the swept area. These two combined give the 'Total aligned cylinder' trace.

The perpendicular component is predicted very well but an over-prediction in the parallel component causes the total loading to be significantly higher than the experimental data.

The staggered shock front arrival time along the 90° array results in a more gradual development of total impulse when compared to the 0° orientation loading, which demonstrates a sharper rise on account of the concurrent shock front arrival times seen in Figure 4.9(a). Despite differences in the temporal development of total impulse, both components result in a similar final value which, when these two components are superimposed, results in a similar total impulse to the 45° loading. This suggests that, whilst there are clearly two distinct mechanisms governing load development along the parallel and perpendicular arrays, this results in notable differences in *specific* impulse distribution along a particular array but the development of *total* impulse appears invariant of charge orientation.

Peak loading distribution

The peak reflected pressure distributions and peak specific impulse distributions are presented in Figures 6.21 and 6.22 alongside the experimental data and experimental average.

The parallel predictions from the model do not capture the peak reflected pressure distribution in the centre of the measured area, but the 75-100 mm radial ordinates are close to the average. This impacts the peak specific impulse distribution were the central loading is over-predicted but comes within range earlier from the 50 mm ordinate. The peak reflected pressure does not capture the notable feature of the non-centralise loading as seen in the experimental data, Figure 6.21.

The significant over-prediction of the peak pressure in the perpendicular orientation is not far outside the highest pressures seen in one test, but the profile is similar in shape if not magnitude, Figure 6.22. The peak specific impulse equally shows a similarly correct trend but at an elevated magnitude, Figure 6.22.

In total the near consistent over-predictions, especially in the perpendicular orientation, does not reflect equally in the total impulse seen. This suggest that the model is capturing the energy correctly, which includes the significantly greater total impulse than the equivalent spherical charge as demonstrated by the experimental data.

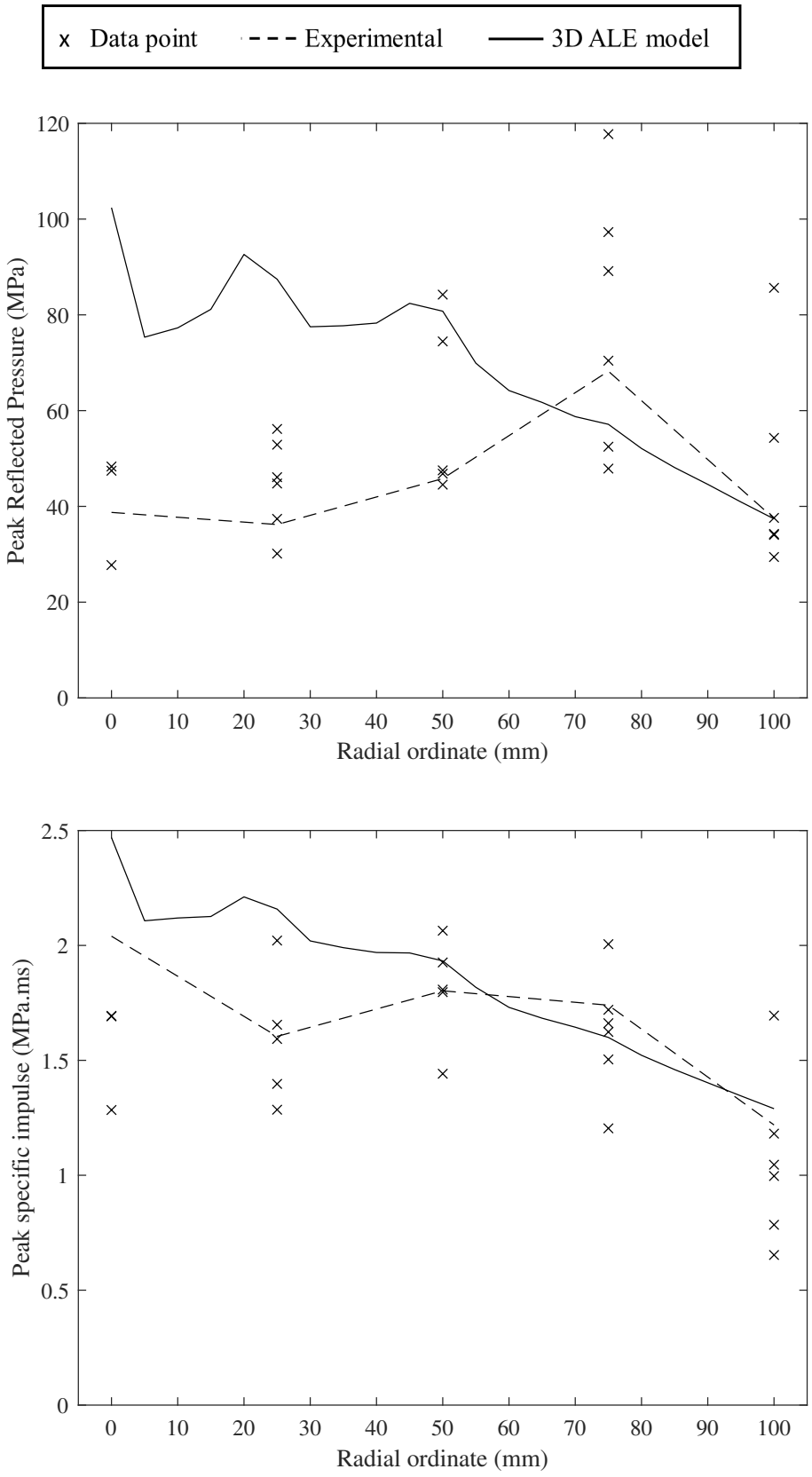


Figure 6.21: Peak reflected pressure and peak specific impulse of 0° ('parallel') radial cylindrical blast tests and numerical modelling.

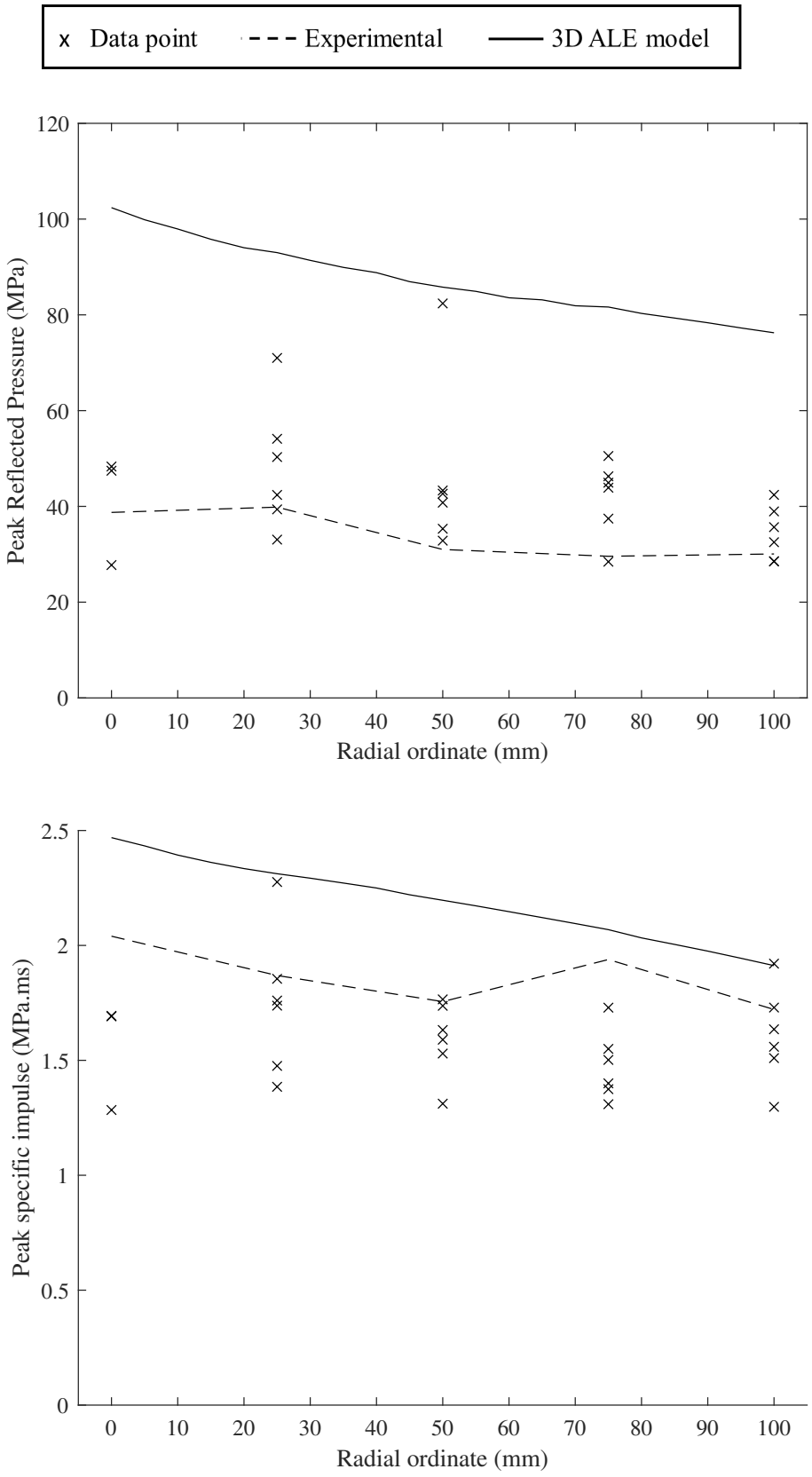


Figure 6.22: Peak reflected pressure and Peak specific impulse of 90° ('perpendicular') radial cylindrical blast tests and numerical modelling.

Chapter 7

Conclusions

The thesis presents experimental and numerical modelling studies aimed at characterising near-field blast loading from 200g spheres and 200g cylinders (L / D = 7) of C4 bare HE charges placed at 250 mm clear stand-off from a rigid target. A number of observations and conclusions from this work are presented below.

1. Novelty of the work
   For the first time, detailed experimental spatial and temporal records have been obtained of blast loads in the very near-field from highly non-spherical explosive charges. This has been supported by numerical modelling analysis of the same events, which consequently represents the first models of such events conducted and analysed in the light of detailed experimental validation data.

2. Consistency of experimental data

   (a) Far-field
   A short, informative preliminary series of far-field testing confirmed that the measured far-field loading parameters correlated very closely with those predicted by a semi-empirical FREM, supporting the conclusion that, for simple geometrical scenarios, such models are capable of accurately predicting far-field loading. It is therefore concluded that far-field blast loading from simple spherically-based shaped explosives is highly consistent and predictable, and

that FREMs represent a reliable tool for its characterisation.

(b) Near-field

Whilst the near-field experimental results demonstrated a high degree of consistency when assessed using total impulse as a global metric, this measure conceals considerable variation in peak loading at nominally identical points on the target between repeat tests. It is concluded that the applicability of a deterministic FREM for near-field load prediction is contingent upon the nature of the target: for large, ductile structures that respond primarily to total impulse, such an approach may be viable. For lightweight, brittle targets sensitive to spatial variations in loading, however, the chaotic processes governing local load distribution — including Rayleigh-Taylor and Richtmyer-Meshkov instabilities — render the development of a reliable deterministic FREM for non-spherical charges inherently difficult with current understanding.

3. Features of near-field loading from cylindrical and spherical charges

(a) Radial orientation

The detonation of cylindrical charges in the radial orientation produces loading that differs markedly in magnitude, form, and spatial distribution from that of equivalent spherical charges. It is concluded that, at the standoff distance employed in this work, a radially oriented cylindrical charge consistently imparts approximately twice the total impulse to the 200 mm measurement area compared to an equivalent spherical charge. Furthermore, it is concluded that the spatial distribution of the time-averaged specific impulse from a radially oriented cylindrical charge is, to a good approximation, dependent only on radial distance from the centre of the target and not on angular position, such that the loading is effectively axi-symmetric when averaged across nominally identical measurement locations.

(b) Axial orientation

The axial orientation produces the highest local specific impulse at the centre of the target of any configuration investigated; however, the dramatic attenuation of loading with radial distance results in a peak total impulse of only approximately half that of the equivalent spherical charge, and one quarter of that produced by the radially oriented cylindrical charge. It is concluded that the axial orientation represents the least efficient configuration for delivering total impulse to an extended target area, despite producing the most intense localised loading at the point of closest approach.

(c) Inclined orientations

The inclined cylindrical charge orientations between 22.5° and 67.5° produce a progressive transition in loading character between the radial and axial extremes, with the degree of asymmetry between the two parallel arrays increasing with inclination angle. It is concluded that at inclination angles of 45° and 67.5°, the

measurement positions fall within the bridging wave zone between the primary radial and end wave regions of the charge, producing loading characteristics that are distinct from both limiting configurations and result in peak total impulse values lower than those of even the axial orientation. This non-monotonic behaviour of total impulse with inclination angle is a significant finding, demonstrating that the relationship between charge orientation and blast loading cannot be characterised by simple interpolation between the radial and axial extremes. It is further concluded that the spatial and temporal complexity of the loading at inclined orientations, combined with the asymmetry inherent to these configurations, renders the development of a deterministic FREM for inclined cylindrical charges a considerably more challenging prospect than for either the radial or axial cases.

(d) End detonated configurations
It is concluded that the detonation point has a negligible influence on the total impulse imparted to the measurement area for radially oriented cylindrical charges, with end and central detonation producing broadly equivalent peak total impulse values. However, the detonation point is found to have a significant influence on the spatial distribution of loading in the parallel array, where the geometric asymmetry introduced by the travelling detonation front produces markedly divergent pressure and impulse responses between nominally equivalent bar positions. For the axially oriented charge, end detonation produces broadly equivalent total impulse to central detonation, but results in the highest peak reflected pressure recorded across the entire experimental programme at the central bar position, confirming that the detonation configuration can have a profound influence on localised peak loading even when the global energy delivery remains comparable.

4. Numerical modelling
The finite element modelling programme found different approaches were able to predict the features revealed by the experimental loading. The 2D analysis was able to capture the total loading but the spatial pressure and impulse predictions were not representative. The computational efficiency of modelling axi-symmetric problems in two dimensions makes it appealing for structure-blast analysis calculations, but it has been shown to not apprehend the pressure discontinuity along the reflecting boundary, and the correct total impulse is achieved at the cost of spatial accuracy.

Modelling in three dimensions removes the numerical jetting and the pressure and impulse spatial profiles are more representative of the experimental observations, even at a coarser mesh resolution than is achievable in two dimensions. The computational cost of high fidelity modelling in 3D makes it currently prohibitive for frequent analysis and, as demonstrated, it is unable to accurately reproduce the total energy distributions for the axial shock wave of cylindrical charges.

The use of numerical modelling remains a key tool in blast analysis; however, caution should be exercised when non-spherical charges are considered in the near-field. This further highlights the dependence of our understanding of explosions on meticulously executed experimental tests to validate the mathematical interpretations of the underlying physical mechanisms.

Chapter 8

Recommendations for future work

The findings of this experimental and numerical programme have advanced the understanding of near-field blast loading from non-spherical charges considerably; however, they have also identified a number of avenues warranting further investigation. The following recommendations are proposed to build upon the work presented in this thesis.

1. Extension of the parameter space
   The trends identified in this work, including the orientation-dependent loading distributions and the non-monotonic behaviour of total impulse with inclination angle, have been established at a single cleared standoff distance of 250 mm. It is recommended that future experimental programmes extend this investigation across a range of standoff distances and charge geometric ratios to determine the consistency and limits of the observed trends. Of particular interest is the identification of the scaled distance at which non-spherical cylindrical charges can be considered equivalent to spherical charges for the purposes of load prediction, effectively defining the boundary of applicability of spherical FREMs for non-spherical charge geometries. Establishing this equivalence threshold would represent a significant practical contribution to the field of near-field blast load characterisation.

2. Charge geometry and explosive material parametric study
   The experimental programme presented in this work has been conducted using C4

charges of a fixed length-to-diameter ratio. It is recommended that future work extend this to charges of varying L/D ratios, progressing towards a long rod geometry that approaches an effectively infinite length. This would isolate the influence of charge length on the side wave loading and provide insight into the asymptotic behaviour of the radial blast wave as the end effects of the charge become negligible. Extension of the programme to alternative explosive materials would further establish the generality of the observed trends beyond C4, and determine the extent to which the loading characteristics are governed by charge geometry rather than explosive composition.

3. High-speed video diagnostics
   The absence of high-speed video recording in the present experimental programme was identified as a limitation in the interpretation of certain features of the results, particularly in relation to the detonation product expansion geometry and the development of the bridging wave in the inclined charge orientations. It is recommended that future experimental campaigns incorporate high-speed video recording to enable direct observation of the fireball and shock front geometry, the shock wave mechanics identified in the inclined orientation results, and the clearing effects observed in the radial tests. This would provide a means of directly comparing the experimentally observed blast phenomena with the numerical predictions, significantly enhancing the validation and interpretability of both the experimental and modelling results.

4. Alternative numerical modelling platforms
   The numerical modelling programme identified limitations in the ability of the current modelling approach to accurately reproduce the total energy distributions for the axial shock wave of cylindrical charges, and highlighted the trade-off between spatial accuracy and computational efficiency in two- and three-dimensional analyses. It is recommended that future modelling work investigate alternative hydrocode platforms, such as Apollo or Viper, applied to the same experimental validation dataset. A comparative study of different solvers would provide valuable insight into the source of the discrepancies identified in the present work and the relative capabilities of available modelling tools for near-field non-spherical charge problems, contributing to the development of more reliable numerical methods for blast load prediction.

5. Minimum representative measurement area
   The observation that near-field blast loading exhibits considerable local variability at nominally identical measurement points, yet demonstrates strong consistency when aggregated over a sufficiently large area, raises an important practical question regarding the minimum measurement area required to achieve representative total impulse results. Until the sources of local variability are better understood, this is best addressed experimentally, through a systematic reduction of the instrumented area and quantification of the point at which the total impulse becomes sensitive to the spatial arrangement of the loading. Establishing an appropriate measurement

length scale for near-field blast loading would provide valuable guidance for the design of future experimental programmes and the interpretation of their results.

6. Artificial intelligence for pattern recognition in experimental data
   The extensive dataset of spatially discrete pressure-time histories generated by the CoBL apparatus presents both an opportunity and a challenge for data analysis. Whilst the present work has identified a number of consistent trends through manual interrogation of the data, the volume and complexity of the dataset means that concealed patterns and relationships may remain undetected. It is recommended that future work investigate the application of artificial intelligence and machine learning techniques to systematically analyse the dataset, with potential applications including automated anomaly detection in individual pressure traces, pattern recognition across orientations and charge geometries, the automated classification of waveform features, and the development of regression-based predictive models for blast wave parameters as a step towards data-driven load prediction for non-spherical charge geometries. Leveraging these capabilities could unlock insights that are not readily accessible through conventional analysis methods and contribute to a more comprehensive understanding of the complex dynamics captured in near-field experimental data.

Bibliography

Anderson, J., Parry, S. & Ritzel, D. (2016), 'Time dependent blast wave properties from shock wave tracking with high speed video', *24th military aspects of blast and shock, Halifax, Nova Scotia, Canada* .

Army Matriel Command Alexandria VA (1974), 'Engineering design handbook. explosions in air. part one'.

Artero-Guerrero, J., Pernas-Sánchez, J. & Teixeira-Dias, F. (2017), 'Blast wave dynamics: The influence of the shape of the explosive', *Journal of Hazardous Materials* **331**, 189–199.

Barr, A. D., Rigby, S. E., Clarke, S. D., Farrimond, D. & Tyas, A. (2023*a*), 'Temporally and spatially resolved reflected overpressure measurements in the extreme near field', *Sensors* **23**(2), 964.

Barr, A., Rigby, S., Clarke, S., Farrimond, D. & Tyas, A. (2023*b*), Measurements of reflected overpressure in the extreme near field, *in* 'Proceedings of the 26th International Symposium on Military Aspects of Blast and Shock (MABS26)', Military Aspects of Blast and Shock (MABS).

Biss, M. M. & McNesby, K. L. (2014), 'Optically measured explosive impulse', *Experiments in fluids* **55**, 1–8.

Bogosian, D., Ferritto, J. & Shi, Y. (2002), Measuring uncertainty and conservatism in simplified blast models, *in* '30th explosives safety seminar', Vol. 26, Department of Defense Explosives Safety Board.

Bogosian, D., Powell, D. & Ohrt, A. (2019), Consequences of applying objective methods

for selecting peak pressure from experimental data, *in* 'Internationl symposium of the interaction of effects of munitions with structures (ISIEMS), Panama City, Florida', pp. 21–25.

Bogosian, D., Yokota, M. & Rigby, S. (2016), TNT equivalence of C-4 and PE4: A review of traditional sources and recent data, *in* 'Proceedings of the 24$^{\text{th}}$ International Symposium on Military Aspects of Blast and Shock (MABS24), Halifax, Nova Scotia, Canada'.

Bogosian, D., Yu, A., Dailey, T. et al. (2014), 'Statistical variation in reflected airblast parameters from bare charges in: 23rd international symposium on military aspects of blast and shock'.

Borenstein, E. & Benaroya, H. (2009), 'Sensitivity analysis of blast loading parameters and their trends as uncertainty increases', *Journal of sound and vibration* **321**(3-5), 762–785.

Carter, S., Ned, A., Chivers, J. & Bemis, A. (2016), 'Selecting piezoresistive vs. piezoelectric pressure transducers', *Application Note: AN-102, Industry/Kulite General Overview* .

Chiquito, M., Castedo, R., López, L. M., Santos, A. P., Mancilla, J. M. & Yenes, J. I. (2019), 'Blast wave characteristics and tnt equivalent of improvised explosive device at small-scaled distances', *Defence Science Journal* **69**(4), 328–335.

Chree, C. (1889), 'The equations of an isotropic elastic solid in polar and cylindrical co-ordinates their solution and application', *transactions of the Cambridge Philosophical Society* **14**, 250.

Clarke, S. D., Fay, S. D., Warren, J. A., Tyas, A., Rigby, S. E. & Elgy, I. (2015), 'A large scale experimental approach to the measurement of spatially and temporally localised loading from the detonation of shallow-buried explosives', *Measurement Science and Technology* **26**, 015001.

Cranz, C. (1926), *Lehrbuch der Basllistik*, Springer, Berlin, Germany.

Curry, R. & Langdon, G. (2017), 'Transient response of steel plates subjected to close proximity explosive detonations in air', *International Journal of Impact Engineering* **102**, 102–116.

Departments of the Army, Navy, Air Force, and the Defense Special Weapons Agency (1998), 'Design and analysis of hardened structures to conventional weapons effects tm5-855-1.', *US Army, Navy and Air Force, US Government Printing Office, Washington DC* .

Dewey, J. (1971), 'The properties of a blast wave obtained from an analysis of the particle trajectories', *Proceedings of the Royal Society of London. A. Mathematical and Physical Sciences* **324**(1558), 275–299.

Dewey, J. M. (1964), 'The air velocity in blast waves from tnt explosions', *Proceedings of the Royal Society of London. Series A. Mathematical and Physical Sciences* **279**(1378), 366–385.

Dobratz, P. & Crawford, B. (1985), *LLNL Explosives handbook – Properties of chemical explosives and explosive simulants*, Lawrence Livermore National Laboratory, CA, US.

Draganić, H., Varevac, D. & Lukić, S. (2018), 'An overview of methods for blast load testing and devices for pressure measurement', *Advances in civil engineering* **2018**(1), 3780482.

Esparza, E. D. (1986*a*), Airblast measurements and equivalency for spherical charges at small scaled distances, *in* 'Proceedings of the 22nd Department Defense Safety Seminar', pp. 2029–2057.

Esparza, E. D. (1986*b*), 'Blast measurements and equivalency for spherical charges at small scaled distances', *International Journal of Impact Engineering* **4**(1), 23–40.

Esparza, E. D. (1992), Spherical equivalency of cylindrical charges in free-air, *in* '25th Department of Defense Explosives Safety Seminar, Anaheim, CA, USA'.

Farrimond, D. G., Rigby, S. E., Clarke, S. D. & Tyas, A. (2022), 'Time of arrival as a diagnostic for far-field high explosive blast waves', *International Journal of Protective Structures* **13**(2), 379–402.

Farrimond, D. G., Woolford, S., Tyas, A., Rigby, S. E., Clarke, S. D., Barr, A., Whittaker, M. & Pope, D. J. (2023), 'Far-field positive phase blast parameter characterisation of rdx and petn based explosives', *International Journal of Protective Structures* p. 20414196221149752.

Farrimond, D. G., Woolford, S., Tyas, A., Rigby, S. E., Clarke, S. D., Barr, A., Whittaker, M. & Pope, D. J. (2024), 'Far-field positive phase blast parameter characterisation of rdx and petn based explosives', *International Journal of Protective Structures* **15**(1), 141–165.

Fay, S., Clarke, S., Warren, J. A., Tyas, A., Bennett, T., Reay, J., Elgy, I. & Gant, M. (2013), Capturing the spatial and temporal variations in impulse from shallow buried charges, *in* 'Proceedings of The 15th International Symposium on the Interaction of the Effects of Munitions with Structures (ISIEMS15), Potsdam, Germany'.

Formby, S. & Wharton, R. (1996), 'Blast characteristics and tnt equivalence values for some commercial explosives detonated at ground level', *Journal of Hazardous materials* **50**(2-3), 183–198.

Friedlander, F. G. (1946), 'The diffraction of sound pulses. I. Diffraction by a semi-infinite plane', *Proceedings of the Royal Society A: Mathematical, Physical and Engineering Sciences* **186**(1006), 322–344.

Hallquist, J. O. (2006), *LS-DYNA Theory Manual*, Livermore Software Technology Corporation, CA, USA.

Hargather, M. (2013), 'Background-oriented schlieren diagnostics for large-scale explosive testing', *Shock waves* **23**(5), 529–536.

Hargather, M. J. & Settles, G. S. (2007), 'Optical measurement and scaling of blasts from gram-range explosive charges', *Shock waves* **17**, 215–223.

Held, M. (1999), 'Impulse method for the blast contour of cylindrical high explosive charges', *Propellants, Explosives, Pyrotechnics* **24**(1), 17–26.

Hopkinson, B. (1914), 'A method of measuring the pressure produced in the detonation of high explosives or by the impact of bullets', *Philiosophical Transactions of the Royal Society of London. Series A, Containing Papers of a Mathematical or Physical Character* **213**(1914), 437–456.

Hopkinson, B. (1915), *British Ordnance Board Minutes, 13565*, British Ordnance.

Hu, Y., Chen, L., Fang, Q. & Xiang, H. (2018), 'Blast loading model of the rc column under close-in explosion induced by the double-end-initiation explosive cylinder', *Engineering Structures* **175**, 304–321.

Hyde, D. W. (1991), *Conventional Weapons Effect Program (ConWep)*, U.S Army Waterways Experimental Station, Vicksburg, MS, USA.

Hyde, D. W. et al. (1988), 'Microcomputer programs conwep and funpro, applications of tm 5-855-1,'fundamentals of protective design for conventional weapons'(user's guide)', *US Army Engineer Waterways Experiment Station* .

Jenkins, C. M., Ripley, R. C., Wu, C.-Y., Horie, Y., Powers, K. & Wilson, W. H. (2013), 'Explosively driven particle fields imaged using a high speed framing camera and particle image velocimetry', *International journal of multiphase flow* **51**, 73–86.

Kaufmann, R., Olufsen, S. N., Fagerholt, E. & Aune, V. (2023), 'Reconstruction of surface pressures on flat plates impacted by blast waves using the virtual fields method', *International Journal of Impact Engineering* **171**, 104369.
URL: *https://www.sciencedirect.com/science/article/pii/S0734743X2200210X*

Kingery, C. N. & Bulmash, G. (1984), *Airblast Parameters from TNT Spherical Air Burst and Hemispherical Surface Burst*, ARBRL-TR-02555, US Army Ballistic Research Laboratory, Aberdeen Proving Ground, MD, USA.

Kinney, G. F. & Graham, K. J. (1985), *Explosive shocks in air*, Springer Science, NY, USA.

Knock, C. & Davies, N. (2011a), 'Predicting the impulse from the curved surface of detonating cylindrical charges', *Propellants, Explosives, Pyrotechnics* **36**(2), 105–109.

Knock, C. & Davies, N. (2011b), 'Predicting the peak pressure from the curved surface of detonating cylindrical charges', *Propellants, Explosives, Pyrotechnics* **36**(3), 203–209.

Knock, C. & Davies, N. (2013), 'Blast waves from cylindrical charges', *Shock Waves* **23**, 337–343.

Knock, C., Davies, N. & Reeves, T. (2015), 'Predicting blast waves from the axial direction of a cylindrical charge', *Propellants, Explosives, Pyrotechnics* **40**(2), 169–179.

Kuznetsov, V. & Bennetts, S. P. (2013), 'Development of photon doppler velocimeter for explosives research', *Defence Science and Technologoy Organisation* .

Langdon, G. S. & Shekhar, V. (2020), 'The effect of the bend radius on the impulse transfer characteristics of v-hulls: Numerical simulations', *International Journal of Protective Structures* **11**(1), 69–89.

Langran-Wheeler, C., Rigby, S., Clarke, S., Tyas, A., Stephens, C. & Walker, R. (2021), 'Near-field spatial and temporal blast pressure distributions from non-spherical charges: Horizontally-aligned cylinders', *International Journal of Protective Structures* **12**(4), 492–516.

Langran-Wheeler, C., Tyas, A., Rigby, S. E., Stephens, C. S., Clarke, S. & Warren, J. (2017), Characterisation of reflected blast loads in the very-near field from non-spherical explosive charges, *in* 'Proceedings of The 17th International Symposium for the Interaction of Munitions with Structures (ISIEMS17), Bad Neuenahr, Germany'.

Langran-Wheeler, C., Tyas, A., Rigby, S., Stephens, C. S., Clarke, S. & Walker, R. E. (2019), Reflected blast loads from long cylinders in the near-field, *in* 'Proceedings of The 18th International Symposium for the Interaction of Munitions with Structures (ISIEMS18), Panama City, FL, USA'.

Lee, E. L., Hornig, H. C. & Kury, J. W. (1968), Adiabatic expansion of high explosive detonation products, Technical Report TID 4500-UCRL 50422, Lawrence Radiation Laboratory, University of California, CA, USA.

Lord Rayleigh (1882), 'Investigation of the character of the equilibrium of an incompressible heavy fluid of variable density', *Proceedings of the London Mathematical Society* **4**(1), 170–177.

McNesby, K. L., Biss, M. M., Benjamin, R. A. & Thompson, R. A. (2014), 'Optical measurement of peak air shock pressures following explosions', *Propellants, Explosives, Pyrotechnics* **39**(1), 59–64.

McNesby, K. L., Homan, B. E., Benjamin, R. A., Boyle, V. M., Densmore, J. M. & Biss, M. M. (2016), 'Quantitative imaging of explosions with high-speed cameras', *Review of scientific instruments* **87**(5).

Meshkov, E. E. (1969), 'Instability of the interface of two gases accelerated by a shock wave', *Fluid Dynamics* **4**, 101–104.

Mizukaki, T., Wakabayashi, K., Matsumura, T. & Nakayama, K. (2014), 'Background-oriented schlieren with natural background for quantitative visualization of open-air explosions', *Shock Waves* **24**(1), 69–78.

Netherton, M. D. & Stewart, M. G. (2010), 'Blast load variability and accuracy of blast load prediction models', *International Journal of Protective Structures* **1**(4), 543–570.

Nurick, G. N., Mahoi, S. & Langdon, G. S. (2016), 'The response of plates subjected to loading arising from the detonation of different shapes of plastic explosive', *International Journal of Impact Engineering* **89**, 102–113.

Ohashi, K., Kleine, H. & Takayama, K. (2001), 'Characteristics of blast waves generated by milligram charges', *Proc. ISSW23* .

Pierron, F. & Grédiac, M. (2012), *The virtual fields method: extracting constitutive mechanical parameters from full-field deformation measurements*, Springer Science & Business Media.

Plooster, M. N. (1978), *Blast front pressure from cylindrical charges of high explosives*, TM 3631, Naval Weapons Center, Denver Research Institute, China Lake, CA, USA.

Plooster, M. N. (1982), *Blast effects from cylindrical explosive charges: experimental measurements*, NWC TP 6382, Naval Weapons Center, Denver Research Institute, China Lake, CA, USA.

Pochhammer, L. (1876), 'Ueber die fortpflanzungsgeschwindigkeiten kleiner schwingungen in einem unbegrenzten isotropen kreiscylinder.'.

Richtmyer, R. D. (1960), 'Taylor instability in a shock acceleration of compressible fluids.', *Communications on Pure and Applied Mathematics* **13**, 297–319.

Rickman, D. D. & Murrell, D. W. (2006), 'Development of an Improved Methodology for Predicting Airblast Pressure Relief on a Directly Loaded Wall', *Journal of Pressure Vessel Technology* **129**(1), 195–204.

Rigby, S., Barr, A. & Clayton, M. (2018a), 'A review of Pochhammer-Chree dispersion in the Hopkinson bar', *Proceedings of the Institution of Civil Engineers: Engineering and Computational Mechanics* **171**(1), 3–13.

Rigby, S. & Clarke, S. (2015), 'Characterisation of blast loading – current research at the university of sheffield', *Explosives Engineering* **March/April**, 14–17.

Rigby, S. E., Fay, S. D., Tyas, A., Warren, J. A. & Clarke, S. D. (2015b), 'Angle of incidence effects on far-field positive and negative phase blast parameters', *International Journal of Protective Structures* **6**(1), 23–42.

Rigby, S. E., Fuller, B. J. & Tyas, A. (2018c), Validation of near-field blast loading in LS-DYNA, *in* 'Proceedings of the 5th International Conference on Protective Structures (ICPS5), Poznan, Poland'.

Rigby, S. E., Knighton, R., Clarke, S. D. & Tyas, A. (2020), 'Reflected near-field blast pressure measurements using high speed video', *Experimental Mechanics* **60**(7), 875–888.

Rigby, S. E., Osborne, C., Langdon, G. S., Cooke, S. B. & Pope, D. J. (2021), 'Spherical equivalence of cylindrical explosives: effect of charge shape on deflection of blast-loaded plates', *Submitted for publication in International Journal of Impact Engineering* .

Rigby, S. E., Tyas, A., Bennett, T., Clarke, S. D. & Fay, S. D. (2014a), 'The negative phase of the blast load', *International Journal of Protective Structures* **5**(1), 1–20.

Rigby, S. E., Tyas, A., Bennett, T., Fay, S. D., Clarke, S. D. & Warren, J. A. (2014c), 'A numerical investigation of blast loading and clearing on small targets', *International Journal of Protective Structures* **5**(3), 253–274.

Rigby, S. E., Tyas, A., Clarke, S. D., Fay, S. D., Reay, J., Warren, J. A., Elgy, I. & Gant, M. (2015a), 'Observations from preliminary experiments on spatial and temporal pressure measurements from near-field free air explosions', *International Journal of Protective Structures* **6**(2), 175–190.

Rigby, S. E., Tyas, A., Curry, R. J. & Langdon, G. S. (2019a), 'Experimental measurement of specific impulse distribution and transient deformation of plates subjected to near-field explosive blasts', *Experimental Mechanics* **59**(2), 163–178.

Rigby, S., Fay, S., Clarke, S., Tyas, A., Reay, J., Warren, J., Gant, M. & Elgy, I. (2016), 'Measuring spatial pressure distribution from explosives buried in dry Leighton Buzzard sand', *International Journal of Impact Engineering* **96**, 89–104.

Rigby, S., Fay, S., Tyas, A., Clarke, S., Reay, J., Warren, J., Gant, M. & Elgy, I. (2018b), 'Influence of particle size distribution on the blast pressure profile from explosives buried in saturated soils', *Shock Waves* **28**(3), 613–626.

Rigby, S., Fuller, B. & Tyas, A. (2018), Validation of near-field blast loading in ls-dyna, *in* 'Proceedings of the 5th International Conference on Protective Structures', International Association of Protective Structures.

Rigby, S. & Gitterman, Y. (2016), Secondary shock delay measurements from explosive trials, *in* 'Proceedings of the 24$^{\text{th}}$ International Symposium on Military Aspects of Blast and Shock (MABS24), Halifax, Nova Scotia, Canada'.

Rigby, S., Tyas, A., Clarke, S., Fay, S., Reay, J., Warren, J. & Pope, D. (2015), A review of UFC-3–340–02 blast wave clearing predictions, *in* 'Proceedings of The 16th International Symposium for the Interaction of Munitions with Structures (ISIEMS16), Halifax, Nova Scotia, Canada'.

Rigby, S., Tyas, A., Fay, S., Clarke, S. & Warren, J. (2014), Validation of semi-empirical blast pressure predictions for far field explosions – is there inherent variability in blast wave parameters?, *in* 'Proceedings of the 6th International Conference on Protection of Structures against Hazards'.

Schlöffel, G., Bastide, M., Bachmann, S., Mundt, C. & Seiler, F. (2009), 'Investigation of

the acceleration of aluminum particles behind a shock wave using instantaneous laser doppler velocimetry', *Shock Waves* **19**, 125–134.

Sherkar, P., Shin, J., Whittaker, A. & A, A. (2016), 'Influence of charge shape and point of detonation on blast-resistant design', *Journal of Structural Engineering* **142**(2), 04015109.

Shi, Y. & Stewart, . G. (2015), 'Damage and risk assessment for reinforced concrete wall panels subjected to explosive blast loading', *International Journal of Impact Engineering* **85**, 5–19.

Simoens, B. & Lefebvre, M. (2015), 'Influence of the shape of an explosive charge: quantification of the modification of the pressure field', *Central European Journal of Energetic Materials* **12**, 195–213.

Smith, P., Rose, T., Saotonglang, E. & Conwep (1999), 'Clearing of blast waves from building facades.', *Proceedings of the institution of civil engineers-structures and buildings* **134**(2), 193–199.

Stoner, R. G. & Bleakney, W. (1948), 'The attenuation of spherical shock waves in air', *Journal of Applied Physics* **19**(7), 670–678.

Swizdak, M. M. (1982), *Explosion effects and properties, Part 1 – Explosion effects in air*, Report NSWC/WOL/TR 75-116, Naval Surface Weapons Report, White Oak, MD, USA.

Tang, L., Bird, D., Rigby, S., Tyas, A. & Warren, J. (2017), Reflections on variability of blast pressure measurement at different scales, *in* '17th international symposium on the interaction of the effects of munitions with structures', Bad Neuenahr-Ahrweiler, Germany', pp. 16–20.

Taylor, G. I. (1950), 'The instability of liquid surfaces when accelerated in a direction perpendicular to their planes. I', *Proceedings of the Royal Society A: Mathematical, Physical and Engineering Sciences* **201**(1065), 192–196.

Tyas, A. (2019), Blast loading from high explosive detonation: what we know and what we don't know, *in* '13th International Conference on Shock and Impact Loads on Structures, Guangzhou, China'.

Tyas, A. & Pope, D. (2005), 'Full correction of first-mode pochammer–chree dispersion effects in experimental pressure bar signals', *Measurement Science and Technology* **16**, 642.

Tyas, A., Reay, J. J., Fay, S. D., Clarke, S. D., Rigby, S. E., Warren, J. A. & Pope, D. J. (2016), 'Experimental studies of the effect of rapid afterburn on shock development of near-field explosions', *International Journal of Protective Structures* **7**(3), 456–465.

Tyas, A., Reay, J., Warren, J., Rigby, S., Clarke, S., Fay, S. & Pope, D. (2015), Experimental studies of blast wave development and target loading from near-field spherical petn

explosive charges, *in* '16th international symposium for the interaction of the effects of munitions with structures'.

Tyas, A., Warren, J., Bennett, T. & Fay, S. (2011), 'Prediction of clearing effects in far-field blast loading of finite targets', *Shock Waves* **21**(2), 111–119.

Tyas, A. & Watson, A. J. (2001), 'An investigation of frequency domain dispersion correction of pressure bar signals', *International Journal of Impact Engineering* **25**(1), 87–101.

US Army Engineers Waterways Experiment Station (1986), 'Tm5-855-1 fundamentals of protective design for conventional weapons', *US Army, Navy and Air Force, US Government Printing Office, Washington DC* .

US Department of Defence (2008), *Structures to resist the effects of accidental explosions*, US DoD, Washington DC, USA, UFC-3-340-02.

Wisotski, J. & Snyer, W. H. (1965), *Characteristics of blast waves obtained from cylindrical high explosive charges*, University of Denver, Denver Research Institute, CO, USA.

Wu, C., Fattori, G., Whittaker, A. & Oehlers, D. J. (2010), 'Investigation of air-blast effects from spherical-and cylindrical-shaped charges', *International Journal of Protective Structures* **1**(3), 345–362.

Xiao, W., Andrae, M. & Gebbeken, N. (2020a), 'Effect of charge shape and initiation configuration of explosive cylinders detonating in free air on blast-resistant design', *Journal of Structural Engineering* **146**(8), 04020146.

Xiao, W., Andrae, M. & Gebbeken, N. (2020b), 'Influence of charge shape and point of detonation of high explosive cylinders detonated on ground surface on blast-resistant design', *International Journal of Mechanical Sciences* **181**, 105697.

Chapter 9

Appendix

1. Peak reflected pressures, Peak specific impulses and Time to peak pressure data for all tests
2. Peak total impulse for all tests
3. Sample keyword entry (.k) file for 2D ALE LS-DYNA model of 200g 7/1 cylinder
4. Sample keyword entry (.k) file for 3D ALE LS-DYNA model of 200g 7/1 cylinder

Table 9.1: Summary of peak reflected pressure, peak specific impulse and time to peak pressure for all experimental tests.

Test	Channel	Location (X, Y) (mm)	Peak Reflected Pressure (MPa)	Peak Specific Impulse (MPa·ms)	Time to Peak Pressure (ms)
	1	(−100, 0)	30.088	0.708	0.079
	2	(−75, 0)	36.390	0.637	0.073
	3	(−50, 0)	39.282	0.216	0.068
	4	(−25, 0)	40.995	1.181	0.079
	5	(0, 0)	87.166	1.630	0.062
	6	(25, 0)	28.584	0.902	0.068
	7	(50, 0)	34.833	0.769	0.071
	8	(75, 0)	27.370	0.639	0.075
T004	9	(100, 0)	33.022	0.843	0.073
	10	(0, −100)	27.800	0.588	0.076
	11	(0, −75)	33.224	0.684	0.073
	12	(0, −50)	25.734	1.082	0.071
	13	(0, −25)	38.327	0.708	0.071
	14	(0, 25)	32.035	0.733	0.083
	15	(0, 50)	42.661	0.719	0.070
	17	(0, 75)	33.951	0.655	0.072
	18	(0, 100)	20.055	0.574	0.075
	1	(−100, 0)	32.002	0.922	0.079
	2	(−75, 0)	36.139	0.862	0.069
	3	(−50, 0)		—	
	4	(−25, 0)	41.248	0.935	0.068
	5	(0, 0)	37.246	0.811	0.068
	6	(25, 0)	39.742	0.819	0.069
	7	(50, 0)	40.354	0.680	0.072
	8	(75, 0)	16.443	0.483	0.076
T005	9	(100, 0)	23.706	0.664	0.083
	10	(0, −100)	17.538	0.645	0.085
	11	(0, −75)	32.360	0.709	0.073
	12	(0, −50)	40.869	1.097	0.067
	13	(0, −25)	23.613	0.711	0.068
	14	(0, 25)	40.454	0.708	0.068
	15	(0, 50)	51.557	0.985	0.069
	17	(0, 75)	32.681	0.754	0.071
	18	(0, 100)	22.941	0.731	0.074
	1	(−100, 0)	29.144	1.510	0.066
	2	(−75, 0)	28.776	1.324	0.096
	3	(−50, 0)	35.757	1.613	0.092
	4	(−25, 0)	39.103	1.819	0.066
	5	(0, 0)	48.151	1.753	0.075
	6	(25, 0)	42.621	1.791	0.065
	7	(50, 0)	42.827	1.582	0.068
	8	(75, 0)	37.424	1.381	0.086
T006	9	(100, 0)	38.678	1.569	0.094
	10	(0, −100)	29.381	0.647	0.066
	11	(0, −75)	89.150	1.723	0.064

Continued on next page

Table 9.1 continued from previous page

Test	Channel	Location (X, Y) (mm)	Peak Reflected Pressure (MPa)	Peak Specific Impulse (MPa·ms)	Time to Peak Pressure (ms)
	12	(0, −50)	44.589	1.867	0.083
	13	(0, −25)	45.424	1.402	0.071
	14	(0, 25)	53.027	1.597	0.065
	15	(0, 50)	48.376	1.443	0.065
	17	(0, 75)	71.181	1.617	0.072
	18	(0, 100)	37.869	1.114	0.065
	1	(−100, 0)	42.970	1.636	0.076
	2	(−75, 0)	45.166	1.538	0.073
	3	(−50, 0)	40.942	1.724	0.076
	4	(−25, 0)	54.985	2.239	0.084
	5	(0, 0)	48.313	1.664	0.087
	6	(25, 0)	51.278	1.846	0.068
	7	(50, 0)	43.475	1.630	0.085
	8	(75, 0)	50.538	1.722	0.087
T007	9	(100, 0)	28.590	1.289	0.075
	10	(0, −100)	34.418	0.791	0.074
	11	(0, −75)	97.793	1.625	0.075
	12	(0, −50)	74.878	2.032	0.065
	13	(0, −25)	45.924	1.373	0.067
	14	(0, 25)	56.451	1.672	0.073
	15	(0, 50)	85.215	1.813	0.074
	17	(0, 75)	118.233	1.689	0.074
	18	(0, 100)	85.940	1.300	0.076
	1	(−100, 0)		—	
	2	(−75, 0)	69.855	1.538	0.071
	3	(−50, 0)	79.027	1.970	0.067
	4	(−25, 0)	57.194	2.000	0.059
	5	(0, 0)	47.731	1.707	0.075
	6	(25, 0)	50.821	1.909	0.058
	7	(50, 0)	40.707	1.673	0.073
	8	(75, 0)	56.576	1.474	0.068
T008	9	(100, 0)	102.992	2.039	0.068
	10	(0, −100)	104.882	1.590	0.065
	11	(0, −75)	46.915	1.326	0.059
	12	(0, −50)	78.370	2.332	0.062
	13	(0, −25)	52.634	1.805	0.075
	14	(0, 25)	48.620	1.580	0.059
	15	(0, 50)	58.605	1.768	0.074
	17	(0, 75)	110.264	2.257	0.062
	18	(0, 100)	40.592	1.229	0.071
	1	(−100, 0)	46.241	1.258	0.073
	2	(−75, 0)	44.707	1.402	0.067
	3	(−50, 0)	29.289	1.403	0.078
	4	(−25, 0)	32.456	1.577	0.081
	5	(0, 0)	41.714	1.508	0.084
	6	(25, 0)	58.463	1.753	0.070
	7	(50, 0)	56.830	1.733	0.078

Continued on next page

T009

Table 9.1 continued from previous page

Test	Channel	Location (X, Y) (mm)	Peak Reflected Pressure (MPa)	Peak Specific Impulse (MPa·ms)	Time to Peak Pressure (ms)
	8	(75, 0)	51.404	1.299	0.065
	9	(100, 0)	33.699	0.926	0.069
	10	(0, −100)	69.940	1.953	0.069
	11	(0, −75)	62.775	1.784	0.076
	12	(0, −50)	72.140	1.671	0.074
	13	(0, −25)	67.625	1.280	0.079
	14	(0, 25)	44.225	1.363	0.065
	15	(0, 50)	54.340	1.754	0.066
	17	(0, 75)	72.764	1.471	0.073
	18	(0, 100)	47.602	1.415	0.068
	1	(−100, 0)	29.469	0.787	0.097
	2	(−75, 0)	32.567	1.102	0.083
	3	(−50, 0)	69.106	1.530	0.078
	4	(−25, 0)	49.923	1.491	0.073
	5	(0, 0)	60.649	1.454	0.078
	6	(25, 0)	77.617	1.777	0.084
	7	(50, 0)	55.336	1.454	0.089
	8	(75, 0)	52.784	1.375	0.086
T010	9	(100, 0)	57.264	1.318	0.084
	10	(0, −100)	113.741	2.321	0.077
	11	(0, −75)	93.886	2.119	0.082
	12	(0, −50)	79.432	1.855	0.084
	13	(0, −25)	52.394	1.376	0.081
	14	(0, 25)	84.810	1.698	0.082
	15	(0, 50)	118.503	2.495	0.076
	17	(0, 75)	45.536	1.204	0.075
	18	(0, 100)	34.587	1.062	0.079
	1	(−100, 0)	60.461	1.410	0.087
	2	(−75, 0)	37.560	1.489	0.076
	3	(−50, 0)	74.254	1.809	0.082
	4	(−25, 0)	55.884	1.751	0.090
	5	(0, 0)	56.235	1.587	0.098
	6	(25, 0)	50.743	1.721	0.072
	7	(50, 0)	114.095	2.616	0.078
	8	(75, 0)	41.535	1.691	0.083
T012	9	(100, 0)	41.597	1.306	0.082
	10	(0, −100)	20.134	0.784	0.082
	11	(0, −75)	28.446	1.110	0.089
	12	(0, −50)	58.316	1.483	0.080
	13	(0, −25)		—	
	14	(0, 25)	79.363	1.976	0.091
	15	(0, 50)		—	
	17	(0, 75)	41.395	1.241	0.102
	18	(0, 100)	54.820	1.405	0.087
	1	(−100, 0)	3.359	0.143	0.094
	2	(−75, 0)	6.821	0.134	0.102
	3	(−50, 0)	15.048	0.539	0.071

Continued on next page

T014

Table 9.1 continued from previous page

Test	Channel	Location (X, Y) (mm)	Peak Reflected Pressure (MPa)	Peak Specific Impulse (MPa·ms)	Time to Peak Pressure (ms)
	4	(−25, 0)	155.937	1.883	0.070
	5	(0, 0)	236.044	2.571	0.067
	6	(25, 0)	118.877	1.288	0.072
	7	(50, 0)	18.323	0.557	0.086
	8	(75, 0)	4.884	0.197	0.124
	9	(100, 0)	3.412	0.084	0.096
	10	(0, −100)	3.754	0.088	0.107
	11	(0, −75)	4.151	0.047	0.105
	12	(0, −50)	14.869	0.529	0.075
	13	(0, −25)	5.842	0.000	0.151
	14	(0, 25)	265.103	2.892	0.067
	15	(0, 50)		—	
	17	(0, 75)	6.551	0.266	0.101
	18	(0, 100)	4.223	0.173	0.090
T015	1	(−100, 0)	6.111	0.140	0.079
	2	(−75, 0)	6.464	0.208	0.055
	3	(−50, 0)	9.623	0.296	0.051
	4	(−25, 0)	79.302	1.195	0.039
	5	(0, 0)	289.604	2.968	0.038
	6	(25, 0)	94.237	1.069	0.045
	7	(50, 0)	15.358	0.402	0.049
	8	(75, 0)		—	
	9	(100, 0)	2.947	0.182	0.072
	10	(0, −100)	3.909	0.152	0.063
	11	(0, −75)	6.668	0.173	0.074
	12	(0, −50)	29.968	0.867	0.054
	13	(0, −25)	10.894	0.000	0.090
	14	(0, 25)	87.430	1.429	0.047
	15	(0, 50)		—	
	17	(0, 75)	4.620	0.206	0.060
	18	(0, 100)	4.144	0.172	0.071
T016	1	(−100, 0)	5.452	0.233	0.098
	2	(−75, 0)	7.073	0.298	0.082
	3	(−50, 0)	8.944	0.355	0.077
	4	(−25, 0)	21.277	0.585	0.069
	5	(0, 0)	234.557	2.739	0.053
	6	(25, 0)	31.829	0.663	0.062
	7	(50, 0)	69.500	0.996	0.068
	8	(75, 0)		—	
	9	(100, 0)	3.402	0.110	0.077
	10	(0, −100)	3.904	0.076	0.087
	11	(0, −75)		—	
	12	(0, −50)	12.274	0.423	0.085
	13	(0, −25)	38.993	0.000	0.056
	14	(0, 25)	105.252	1.596	0.055
	15	(0, 50)		—	
	17	(0, 75)	6.901	0.228	0.091

Continued on next page

Table 9.1 continued from previous page

Test	Channel	Location (X, Y) (mm)	Peak Reflected Pressure (MPa)	Peak Specific Impulse (MPa·ms)	Time to Peak Pressure (ms)
	18	(0, 100)	3.951	0.121	0.081
T017	1	(−100, 0)	3.235	0.163	0.098
	2	(−75, 0)	4.194	0.124	0.078
	3	(−50, 0)	6.211	0.294	0.076
	4	(−25, 0)	21.670	0.637	0.068
	5	(0, 0)	195.792	2.029	0.052
	6	(25, 0)	54.963	0.999	0.057
	7	(50, 0)	55.684	1.185	0.053
	8	(75, 0)		—	
	9	(100, 0)	3.335	0.137	0.069
	10	(0, −100)	4.720	0.251	0.072
	11	(0, −75)		—	
	12	(0, −50)	56.055	0.985	0.059
	13	(0, −25)	54.460	0.997	0.063
	14	(0, 25)	55.619	0.763	0.051
	15	(0, 50)		—	
	17	(0, 75)	2.535	0.089	0.089
	18	(0, 100)	2.382	0.119	0.102
T019	1	(−100, 0)	33.003	1.674	0.072
	2	(−75, 0)	43.872	1.541	0.075
	3	(−50, 0)	33.003	1.321	0.067
	4	(−25, 0)	32.696	1.489	0.079
	5	(0, 0)	28.149	1.281	0.076
	6	(25, 0)	71.364	1.414	0.081
	7	(50, 0)	82.155	1.770	0.073
	8	(75, 0)	46.059	1.390	0.067
	9	(100, 0)	36.143	1.282	0.074
	10	(0, −100)	35.041	1.522	0.072
	11	(0, −75)	48.041	1.907	0.066
	12	(0, −50)	47.540	1.795	0.079
	13	(0, −25)	30.344	1.277	0.090
	14	(0, 25)	37.553	1.482	0.083
	15	(0, 50)		—	
	17	(0, 75)	52.845	1.212	0.081
	18	(0, 100)	53.943	1.127	0.067
T020	1	(−100, 0)	30.391	0.602	0.076
	2	(−75, 0)	26.700	0.490	0.073
	3	(−50, 0)	53.920	0.881	0.069
	4	(−25, 0)	39.783	0.694	0.071
	5	(0, 0)	40.011	0.669	0.068
	6	(25, 0)	32.318	0.525	0.069
	7	(50, 0)	32.510	0.485	0.070
	8	(75, 0)	39.251	0.638	0.073
	9	(100, 0)	21.292	0.512	0.073
	10	(0, −100)	17.922	0.323	0.085
	11	(0, −75)	18.650	0.338	0.082
	12	(0, −50)	13.459	0.319	0.075

Continued on next page

Table 9.1 continued from previous page

Test	Channel	Location (X, Y) (mm)	Peak Reflected Pressure (MPa)	Peak Specific Impulse (MPa·ms)	Time to Peak Pressure (ms)
	13	(0, −25)	21.668	0.344	0.069
	14	(0, 25)	48.524	1.113	0.065
	15	(0, 50)		—	
	17	(0, 75)	27.972	1.029	0.072
	18	(0, 100)	30.988	1.145	0.078
T021	1	(−100, 0)	37.240	0.848	0.073
	2	(−75, 0)	18.506	0.660	0.072
	3	(−50, 0)	36.040	0.712	0.071
	4	(−25, 0)	36.251	0.876	0.066
	5	(0, 0)	65.407	1.227	0.068
	6	(25, 0)	25.752	0.672	0.069
	7	(50, 0)	37.148	0.796	0.072
	8	(75, 0)	41.411	0.737	0.074
	9	(100, 0)	14.722	0.556	0.074
	10	(0, −100)	12.531	0.281	0.087
	11	(0, −75)	15.662	0.293	0.081
	12	(0, −50)	8.531	0.374	0.085
	13	(0, −25)	30.025	0.644	0.067
	14	(0, 25)	140.437	2.197	0.068
	15	(0, 50)		—	
	17	(0, 75)	19.374	0.875	0.084
	18	(0, 100)	24.065	1.022	0.091
T023	1	(−100, 0)	32.783	0.574	0.076
	2	(−75, 0)	28.088	0.602	0.074
	3	(−50, 0)	32.519	0.522	0.071
	4	(−25, 0)	61.063	0.889	0.073
	5	(0, 0)	35.481	0.598	0.069
	6	(25, 0)	37.238	0.652	0.072
	7	(50, 0)	21.853	0.490	0.071
	8	(75, 0)	29.027	0.646	0.071
	9	(100, 0)	15.637	0.453	0.075
	10	(0, −100)	9.147	0.200	0.088
	11	(0, −75)	14.594	0.271	0.080
	12	(0, −50)	22.869	0.443	0.076
	13	(0, −25)	18.228	0.445	0.073
	14	(0, 25)	33.297	0.956	0.075
	15	(0, 50)		—	
	17	(0, 75)	22.292	0.785	0.072
	18	(0, 100)	37.133	1.434	0.080
T024	1	(−100, 0)	9.311	0.250	0.127
	2	(−75, 0)	9.056	0.217	0.121
	3	(−50, 0)	3.480	0.137	0.130
	4	(−25, 0)	5.344	0.304	0.114
	5	(0, 0)	10.062	0.242	0.113
	6	(25, 0)	11.043	0.291	0.116
	7	(50, 0)	10.931	0.289	0.118
	8	(75, 0)	11.253	0.372	0.123

Continued on next page

Table 9.1 continued from previous page

Test	Channel	Location (X, Y) (mm)	Peak Reflected Pressure (MPa)	Peak Specific Impulse (MPa·ms)	Time to Peak Pressure (ms)
	9	(100, 0)	6.917	0.197	0.127
	10	(0, −100)	5.969	0.205	0.070
	11	(0, −75)	4.997	0.146	0.080
	12	(0, −50)	5.285	0.217	0.095
	13	(0, −25)	4.497	0.233	0.107
	14	(0, 25)	12.638	0.366	0.115
	15	(0, 50)		—	
	17	(0, 75)	8.874	0.188	0.106
	18	(0, 100)	10.895	0.226	0.102
T026	1	(−100, 0)	6.173	0.269	0.109
	2	(−75, 0)		—	
	3	(−50, 0)	8.995	0.245	0.115
	4	(−25, 0)	9.255	0.239	0.111
	5	(0, 0)	8.208	0.222	0.097
	6	(25, 0)	6.968	0.159	0.095
	7	(50, 0)	7.226	0.218	0.095
	8	(75, 0)	8.367	0.313	0.095
	9	(100, 0)	17.086	0.478	0.132
	10	(0, −100)	6.259	0.183	0.099
	11	(0, −75)	6.897	0.174	0.101
	12	(0, −50)	7.321	0.312	0.106
	13	(0, −25)	4.982	0.133	0.107
	14	(0, 25)	10.933	0.227	0.090
	15	(0, 50)	8.451	0.256	0.098
	17	(0, 75)	16.897	0.247	0.083
	18	(0, 100)	22.808	0.360	0.083
T027	1	(−100, 0)	6.529	0.257	0.108
	2	(−75, 0)		—	
	3	(−50, 0)		—	
	4	(−25, 0)	9.501	0.258	0.100
	5	(0, 0)	11.650	0.849	0.094
	6	(25, 0)	8.589	0.180	0.095
	7	(50, 0)	9.562	0.190	0.095
	8	(75, 0)	10.219	0.271	0.094
	9	(100, 0)	14.897	0.391	0.132
	10	(0, −100)	10.089	0.260	0.097
	11	(0, −75)	11.481	0.261	0.100
	12	(0, −50)	9.430	0.378	0.105
	13	(0, −25)	10.447	0.229	0.098
	14	(0, 25)	11.340	0.259	0.091
	15	(0, 50)	8.810	0.176	0.096
	17	(0, 75)	14.954	0.267	0.083
	18	(0, 100)	18.952	0.343	0.082
T028	1	(−100, 0)	2.276	0.187	0.156
	2	(−75, 0)		—	
	3	(−50, 0)		—	
	4	(−25, 0)		—	

Continued on next page

Table 9.1 continued from previous page

Test	Channel	Location (X, Y) (mm)	Peak Reflected Pressure (MPa)	Peak Specific Impulse (MPa·ms)	Time to Peak Pressure (ms)
	5	(0, 0)	8.811	0.175	0.088
	6	(25, 0)	5.513	0.140	0.090
	7	(50, 0)	10.621	0.192	0.085
	8	(75, 0)	12.455	0.294	0.084
	9	(100, 0)	8.089	0.362	0.184
	10	(0, −100)	3.698	0.089	0.093
	11	(0, −75)	3.696	0.097	0.096
	12	(0, −50)	3.385	0.156	0.160
	13	(0, −25)		—	
	14	(0, 25)	4.160	0.122	0.098
	15	(0, 50)	3.173	0.198	0.107
	17	(0, 75)	10.276	0.228	0.129
	18	(0, 100)	10.036	0.301	0.134
	1	(−100, 0)	3.333	0.144	0.144
	2	(−75, 0)		—	
	3	(−50, 0)		—	
	4	(−25, 0)		—	
	5	(0, 0)		—	
	6	(25, 0)	6.571	0.180	0.102
T030	7	(50, 0)	4.425	0.174	0.102
	8	(75, 0)	4.163	0.218	0.096
	9	(100, 0)	9.014	0.417	0.180
	10	(0, −100)	4.833	0.123	0.099
	11	(0, −75)	4.837	0.094	0.107
	12	(0, −50)	3.493	0.216	0.157
	13	(0, −25)		—	
	14	(0, 25)	5.687	0.221	0.115
	15	(0, 50)	4.346	0.263	0.112
	17	(0, 75)	9.558	0.220	0.126
	18	(0, 100)		—	
	1	(−100, 0)	1.978	0.158	0.168
	2	(−75, 0)		—	
	3	(−50, 0)		—	
	4	(−25, 0)		—	
	5	(0, 0)		—	
	6	(25, 0)	1.759	0.095	0.095
T031	7	(50, 0)	2.636	0.114	0.090
	8	(75, 0)	3.628	0.186	0.093
	9	(100, 0)	7.362	0.351	0.202
	10	(0, −100)	1.950	0.102	0.093
	11	(0, −75)	2.504	0.095	0.100
	12	(0, −50)	2.319	0.138	0.165
	13	(0, −25)		—	
	14	(0, 25)	2.368	0.196	0.111
	15	(0, 50)	2.325	0.131	0.170
	17	(0, 75)	9.694	0.257	0.140

Continued on next page

Table 9.1 continued from previous page

Test	Channel	Location (X, Y) (mm)	Peak Reflected Pressure (MPa)	Peak Specific Impulse (MPa·ms)	Time to Peak Pressure (ms)
	18	(0, 100)		—	
	1	(−100, 0)	2.414	0.036	0.085
	2	(−75, 0)		—	
	3	(−50, 0)		—	
	4	(−25, 0)		—	
	5	(0, 0)		—	
	6	(25, 0)	4.966	0.161	0.076
T032	7	(50, 0)	14.680	0.393	0.066
	8	(75, 0)	28.099	0.710	0.060
	9	(100, 0)	2.708	0.227	0.133
	10	(0, −100)		—	
	11	(0, −75)	28.031	0.519	0.073
	12	(0, −50)	10.309	0.263	0.075
	13	(0, −25)		—	
	14	(0, 25)	87.067	1.396	0.063
	15	(0, 50)	3.721	0.225	0.094
	17	(0, 75)	2.927	0.105	0.072
	18	(0, 100)		—	

Table 9.2: Summary of peak total impulse for all experimental tests.

Test	**Orientation**	**Peak Total Impulse (Ns)**
T004	Spherical	23.75
T005	Spherical	23.88
T006	Radial (0°, 0°) – Centrally detonated	46.04
T007	Radial (0°, 0°) – Centrally detonated	49.46
T008	Radial (45°, 0°)	53.28
T009	Radial (45°, 0°)	46.63
T010	Radial (0°, 0°) – End detonated	47.49
T012	Radial (0°, 0°) – End detonated	43.17
T014	Axial (0°, 90°) – End detonated	15.82
T015	Axial (0°, 90°) – End detonated	12.57
T016	Axial (0°, 90°) – Centrally detonated	13.76
T017	Axial (0°, 90°) – Centrally detonated	13.15
T019	Radial (0°, 0°) – Centrally detonated	44.29
T020	Inclined (0°, 22.5°)	19.84
T021	Inclined (0°, 22.5°)	23.46
T023	Inclined (0°, 22.5°)	19.12
T024	Inclined (0°, 45°)	7.38
T026	Inclined (0°, 45°)	8.30
T027	Inclined (0°, 45°)	8.52
T028	Inclined (0°, 67.5°)	6.30
T030	Inclined (0°, 67.5°)	6.30
T031	Inclined (0°, 67.5°)	5.80
T032	Axial (0°, 90°) – Centrally detonated	12.45

```
*KEYWORD memory = 100000000
*INCLUDE
mesh.k
*ALE_MULTI-MATERIAL_GROUP
$      SID    IDTYPE
         1         1
         2         1
*CONTROL_ALE
$      DCT      NADV      METH      AFAC      BFAC      CFAC      DFAC      EFAC
        -1         1         2
$    START       END     AAFAC     VFACT      PRIT       EBC      PREF   NSIDEBC
         0   1.0e+20         1   1.0e-06       0.0         0  1.0136E5
$Atmospheric pressure applied to boundary of ALE domain
*CONTROL_BULK_VISCOSITY
$       Q1        Q2      type
  6.000000  0.500000         2
*CONTROL_TERMINATION
$   ENDTIM    ENDCYC     DTMIN    ENDENG    ENDMAS
      5E-4
*DATABASE_TRHIST
$       DT    BINARY      LCUR     IOOPT     DTHFF     BINHF
      1E-6
*DATABASE_BINARY_D3PLOT
$  DT/CYCL   LCDT/NR      BEAM     NPLTC    PSETID
      1E-4
*CONTROL_ENERGY
$     HGEN      RWEN    SLNTEN     RYLEN
         2         1         2         2
*MAT_NULL
$      MID        RO        PC        MU     TEROD     CEROD        YM        PR
         2     1.225
*EOS_LINEAR_POLYNOMIAL
$ AIR
$    EOSID        CO        C1        C2        C3        C4        C5        C6
         2         0         0         0         0       0.4       0.4         0
$       E0        V0
   2.534E5         1
*MAT_HIGH_EXPLOSIVE_BURN
$      MID        RO         D       PCJ      BETA         K         G      SIGY
         1      1559      8193    2.8E10 0.000E+00
*EOS_JWL
$ C4
$    EOSID         A         B        R1        R2      OMEG        E0        V0
         1 6.0977E11  12.950E9      4.50      1.40     0.250   9.0E+09      1.00
*SECTION_ALE2D
$    SECID   ALEFORM       AET    ELFORM
         1        11         0        14
*SECTION_ALE2D
$    SECID   ALEFORM       AET    ELFORM
         2        11         0        14
*PART
$      PID     SECID       MID     EOSID      HGID      GRAV    ADPOPT      TMID

         1         1         1         1
*PART
$      PID     SECID       MID     EOSID      HGID      GRAV    ADPOPT      TMID

         2         2         2         2
*SET_PART
$      SID       DA1       DA2       DA3       DA4
         4     0.000     0.000     0.000     0.000MECH
$     PID1      PID2      PID3      PID4      PID5      PID6      PID7      PID8
         1         2
*CONSTRAINED_GLOBAL
$       TC        RC       DIR         X         Y         Z
         7         7         2     0.000     0.800     0.000
*INITIAL_DETONATION
$      PID         X         Y         Z        LT
         1     0.000     0.450     0.000         0
```

```
70  *INITIAL_VOLUME_FRACTION_GEOMETRY
71  $     FMSID    FMIDTYP     BAMMG    NTRACE
72            4          0         2         3
73  $   CONTTYP   FILLOPT     FAMMG
74            5          0         1
75  $        X0         Y0        Z0        X1        Y1        Z1
76       0.000      0.350     0.000    0.0143     0.550     0.000
77  *END
```

```
*KEYWORD memory = 2100000000
*INCLUDE
mesh3D.k
*ALE_MULTI-MATERIAL_GROUP
$      SID    IDTYPE
         1         1
         2         1
*CONTROL_ALE
$      DCT      NADV      METH      AFAC      BFAC      CFAC      DFAC      EFAC
        -1         1         2
$    START       END     AAFAC     VFACT      PRIT       EBC      PREF   NSIDEBC
         0   1.0e+20         1   1.0e-06       0.0         0  1.0136E5
$Atmospheric pressure applied to boundary of ALE domain
*CONTROL_BULK_VISCOSITY
$       Q1        Q2      type
  6.000000  0.500000         2
*CONTROL_TERMINATION
$   ENDTIM    ENDCYC     DTMIN    ENDENG    ENDMAS
    2.5E-4
*DATABASE_TRHIST
$       DT    BINARY      LCUR     IOOPT     DTHFF     BINHF
      1E-6
*DATABASE_BINARY_D3PLOT
$  DT/CYCL   LCDT/NR      BEAM     NPLTC    PSETID
      1E-4
*CONTROL_ENERGY
$     HGEN      RWEN    SLNTEN     RYLEN
         2         1         2         2
*SECTION_SOLID
$    SECID    ELFORM       AET
         1        11
*SECTION_SOLID
$    SECID    ELFORM       AET
         2        11
*PART
C4
$      PID     SECID       MID     EOSID      HGID      GRAV    ADPOPT      TMID
         1         1         1         1
*MAT_HIGH_EXPLOSIVE_BURN
$      MID        RO         D       PCJ      BETA         K         G      SIGY
         1      1601      8193    2.8E10 0.000E+00
*EOS_JWL
$    EOSID         A         B        R1        R2      OMEG        E0        V0
         1 6.0977E11  12.950E9      4.50      1.40     0.250   9.0E+09      1.00
*PART
AIR
$      PID     SECID       MID     EOSID      HGID      GRAV    ADPOPT      TMID
         2         2         2         2
*MAT_NULL
$      MID        RO        PC        MU     TEROD     CEROD        YM        PR
         2     1.225
*EOS_LINEAR_POLYNOMIAL
$    EOSID        CO        C1        C2        C3        C4        C5        C6
         2         0         0         0         0       0.4       0.4         0
$       E0        V0
   2.534E5         1
*SET_PART
$      SID       DA1       DA2       DA3       DA4
         4     0.000     0.000     0.000     0.000MECH
$     PID1      PID2      PID3      PID4      PID5      PID6      PID7      PID8
         1         2
*CONSTRAINED_GLOBAL
$       TC        RC       DIR         X         Y         Z
         7         7         3     0.000     0.000     0.650
*INITIAL_DETONATION
$      PID         X         Y         Z        LT
         1     0.200     0.200     0.300         0
*INITIAL_VOLUME_FRACTION_GEOMETRY
$    FMSID   FMIDTYP     BAMMG    NTRACE
```

```
         4         0         2         3
$  CONTTYP    FILLOPT     FAMMG
         4         0         1
$       X0        Y0        Z0        X1        Y1        Z1        R1        R2
     0.200     0.200     0.200     0.200     0.200     0.400    0.0143    0.0143
*DATABASE_TRACER
$     TIME     TRACK         X         Y         Z
         0         1     0.200     0.200  0.649999
         0         1     0.205     0.200  0.649999
         0         1     0.210     0.200  0.649999
         0         1     0.215     0.200  0.649999
         0         1     0.220     0.200  0.649999
         0         1     0.225     0.200  0.649999
         0         1     0.230     0.200  0.649999
         0         1     0.235     0.200  0.649999
         0         1     0.240     0.200  0.649999
         0         1     0.245     0.200  0.649999
         0         1     0.250     0.200  0.649999
         0         1     0.255     0.200  0.649999
         0         1     0.260     0.200  0.649999
         0         1     0.265     0.200  0.649999
         0         1     0.270     0.200  0.649999
         0         1     0.275     0.200  0.649999
         0         1     0.280     0.200  0.649999
         0         1     0.285     0.200  0.649999
         0         1     0.290     0.200  0.649999
         0         1     0.295     0.200  0.649999
         0         1     0.300     0.200  0.649999
         0         1     0.200     0.205  0.649999
         0         1     0.200     0.210  0.649999
         0         1     0.200     0.215  0.649999
         0         1     0.200     0.220  0.649999
         0         1     0.200     0.225  0.649999
         0         1     0.200     0.230  0.649999
         0         1     0.200     0.235  0.649999
         0         1     0.200     0.240  0.649999
         0         1     0.200     0.245  0.649999
         0         1     0.200     0.250  0.649999
         0         1     0.200     0.255  0.649999
         0         1     0.200     0.260  0.649999
         0         1     0.200     0.265  0.649999
         0         1     0.200     0.270  0.649999
         0         1     0.200     0.275  0.649999
         0         1     0.200     0.280  0.649999
         0         1     0.200     0.285  0.649999
         0         1     0.200     0.290  0.649999
         0         1     0.200     0.295  0.649999
         0         1     0.200     0.300  0.649999
*END
```